TESIS DE LA UNIVERSIDAD DE ZARAGOZA

2025 129

Raúl Hoffrén Mansoa

Emerging multiscale and 3D remote sensing systems for improved estimation of fuels in Mediterranean forests

Director/es

Riva Fernández, Juan Ramón de la

Lamelas Gracia, María Teresa

ISSN 2254-7606

Prensas de la Universidad Universidad Zaragoza

Universidad de Zaragoza
Servicio de Publicaciones

ISSN 2254-7606

Universidad Zaragoza
1542

Tesis Doctoral

EMERGING MULTISCALE AND 3D REMOTE SENSING SYSTEMS FOR IMPROVED ESTIMATION OF FUELS IN MEDITERRANEAN FORESTS

Autor

Raúl Hoffrén Mansoa

Director/es

Riva Fernández, Juan Ramón de la
Lamelas Gracia, María Teresa

UNIVERSIDAD DE ZARAGOZA
Escuela de Doctorado

2025

Universidad Zaragoza
1542

Tesis Doctoral

Emerging multiscale and 3D remote sensing systems for improved estimation of fuels in Mediterranean forests

Autor

Raúl Hoffrén Mansoa

Directores

Juan de la Riva Fernández

María Teresa Lamelas Gracia

Departamento de Geografía y Ordenación del Territorio

Facultad de Filosofía y Letras

2024

The author of this PhD Thesis was supported by the Spanish Ministry of Science, Innovation, and Universities through an FPU predoctoral contract (FPU18/05027). Furthermore, the work was supported by the Spanish Ministry of Science, Innovation, and Universities through the projects SERGISAT (CGL2014-57013-C2) and FIREPATHS (PID2020-116556RA-I00); by the Government of Aragón (Geoforest S51_20R and Geoforest S51_23R, co-financed with FEDER "Construyendo Europa desde Aragón"); by the University Institute for Research in Environmental Sciences of Aragón (IUCA) of the University of Zaragoza, and by Centro Universitario de la Defensa, Academia General Militar, through the project GEDIFUEL (CUD2020-07).

The only way to discover the limits of the possible
is to go beyond them into the impossible.
(Arthur C. Clarke)

Raúl Hoffrén Mansoa
Emerging multiscale and 3D remote sensing systems for improved estimation of fuels in Mediterranean forests
326 pages.

PhD Thesis, University of Zaragoza, Spain (2024).
With abstract and conclusions in English and Spanish.

All figures made by Raúl Hoffrén Mansoa except for Figure 1.3 (left photograph by David Monniaux and right-above photograph by Wikimedia Commons) and Figures 2.8 and 2.9 (reproduced from Dubayah *et al*., 2020).

The present PhD Thesis is developed as compendium of papers according to the Doctoral program in Land and Environmental Management of the University of Zaragoza. The PhD candidate, Raúl Hoffrén, is the first author and responsible for each and every article listed below. The references of the works that constitute the PhD Thesis body are the following:

1. **Hoffrén, R.**, Lamelas, M.T., de la Riva, J., Domingo, D., Montealegre, A.L., García-Martín, A., and Revilla, S., 2023. Assessing GEDI-NASA system for forest fuels classification using machine learning techniques. *International Journal of Applied Earth Observation and Geoinformation* 116, 103175. https://doi.org/10.1016/j.jag.2022.103175.
2. **Hoffrén, R.**, Lamelas, M.T., and de la Riva, J., 2023. UAV-derived photogrammetric point clouds and multispectral indices for fuel estimation in Mediterranean forests. *Remote Sensing Applications: Society and Environment* 31, 100997. https://doi.org/10.1016/j.rsase.2023.100997.
3. **Hoffrén, R.**, Lamelas, M.T., and de la Riva, J., 2024. Evaluation of handheld mobile laser scanner systems for the definition of fuel types in structurally complex Mediterranean forest stands. *Fire* 7 (2), 59, https://doi.org/10.3390/fire7020059.
4. **Hoffrén, R.**, Lamelas, M.T., and de la Riva, J., 2024. Classification and mapping of fuels in Mediterranean forest landscapes using a UAV-LiDAR system and integration possibilities with handheld mobile laser scanner systems. *Remote Sensing* 16 (18), 3536. https://doi.org/10.3390/rs16183536.

ACKNOWLEDGEMENTS

The years of the thesis have been very intense but rewarding. I take with me an unforgettable experience and a lot of new knowledge and skills, personally, academically, and professionally. Many people have been part of this process and I would like to express my gratitude to them in the following lines.

First of all, I would like to thank my thesis supervisors, Juan de la Riva and María Teresa Lamelas. I am grateful for the opportunity you gave me to conduct this research and for your continuous support and guidance, which has enabled me to complete the thesis. I also appreciate the time you dedicated to addressing my questions and issues over the last years, as well as your advice regarding the academic and scientific world.

I also thank researchers of the Geoforest Group for their valuable ideas and recommendations for my thesis development. Thank you, Fernando Pérez Cabello and Marcos Rodrigues, for allowing me to collaborate in your respective research, which helped me gain a deeper understanding of forest ecosystems and remote sensing. I also express my gratitude to the Geoforest Group for the funding provided in this final year and for supporting my PhD stay at SLU in Umeå.

I would also like to extend my gratitude to María Begoña García from the Pyrenean Institute of Ecology (IPE-CSIC). Thank you for giving me the opportunity to continue my research during these years on the fascinating topic of climatic microrefugia for biodiversity, which I began during my Master's thesis. Although this research did not follow the main line of the thesis, it helped me learn several aspects that would later become important, such as optical UAV data acquisition and processing. I am also grateful for your support during the final stages of the thesis.

Thank you, Laura Duncanson, for accepting my request to join the GEDI team at the University of Maryland for a PhD stay during the fall of 2021, even though it ultimately could not take place due to ongoing COVID-19 restrictions. I also appreciate your valuable recommendations for the treatment and processing of GEDI data, which were of great help for the research.

Thank you, Rubén Valbuena, for welcoming me to your team in the Division of Forest Remote Sensing at SLU in Umeå and for introducing me to new ideas for my thesis development. My gratitude extends to all researchers in the division and other departments at SLU for your ideas and recommendations and for

always making me feel like part of the family. It was a pleasure to pursue my other line of research and to support researchers Anneli Ågren and Caroline Greiser in downloading microclimatic data in the Krycklan Catchment Study. Field work in the Swedish boreal forests was a unique experience. I cannot forget all the predoctoral fellows I met in Umeå. Thank you for your closeness and friendliness, and for the many great moments we shared, including padel matches, BBQs, beers, bike rides, and frustrated attempts to see northern lights.

Finally, I would like to express my gratitude to everyone who has contributed, in one way or another, to my growth not only as a researcher but also as a geographer. In particular, I extend my thanks to the professors and researchers of the Department of Geography and Land Management at the University of Zaragoza for the valuable discussions, debates, and knowledge you have generously shared with me in your respective areas of expertise. To my predoctoral fellows in the department, thank you for the wonderful times and experiences we have shared over the past years.

Thank you all.

ABSTRACT

Forests constitute one of the most valuable ecosystems on Earth, functioning as major carbon reservoirs, habitats for a vast array of biodiversity, and providers of essential services for human populations. These ecosystems are, however, susceptible to a range of natural and anthropogenic disturbances, which can lead to significant degradation when they occur with high frequency. Among these disturbances, wildfires are particularly impactful, especially in Mediterranean environments where climatic conditions, vegetation types, and cultural practices related to fire exacerbate the risk of fire. A critical component of wildfire prevention is the accurate identification of forest fuels, as this enables a better understanding of the potential trajectory and velocity of fire spread within a forest stand. Remote sensing technologies have demonstrated considerable utility in the identification of forest fuels. However, there is a pressing need for further research to explore the capabilities of emerging remote sensing systems, alongside advancements in their processing and analytical tools, to enhance fuel identification. This is particularly crucial in the context of escalating challenges posed by climate change.

The present PhD Thesis investigates the potential of novel remote sensing systems across various spatial scales, with the objective of evaluating their capabilities in improving the identification of fuel types, as defined by the Prometheus classification, in Mediterranean forest environments. This research has assessed four remote sensing systems with the ability of generating three-dimensional information: The NASA's *Global Ecosystem Dynamics Investigation* (GEDI) Satellite Laser Scanner system, optical (*eBee Classic*) and LiDAR (*DJI Matrice 300 RTK + DJI Zenmuse L1*) Unmanned Aerial Vehicles (UAVs), and *GeoSLAM ZEB-Horizon* Handheld Mobile Laser Scanner (HMLS) system. Additionally, the potential of integrating three-dimensional data with optical imagery obtained from both satellite and UAV platforms, as well as the synergistic use of three-dimensional data from different systems, has been examined. Data processing has facilitated the derivation of variables related to the structural, textural, spectral, volumetric, and diversity characteristics of forest vegetation. These variables have served as independent predictors for the final identification of fuel types, which has been conducted using two techniques: machine learning classification models –specifically, *Random Forest* (RF) and *Support Vector Machine* with linear (SVM-L) and radial (SVM-R) kernels– and the quantification of vegetation volume at very high spatial

resolution to delineate the vertical distribution of fuels for the different Prometheus fuel types.

The findings of this research show that the UAV-LiDAR system is particularly effective to classify and map the Prometheus fuel types. Moreover, the integration of UAV-LiDAR and HMLS data has yielded the highest classification accuracies for the Prometheus fuel types. The study has also observed favorable outcomes when variables derived from laser and photogrammetric systems are combined with optical imagery. In particular, GEDI has demonstrated significant capabilities in fuel type classification when its data have been integrated with vegetation indices derived from Landsat-8 OLI multispectral imagery. Similarly, the optical UAV system has produced the best results in fuel type classification when its three-dimensional data has been combined with multispectral imagery from the UAV itself, although with slightly lower accuracies compared to the UAV-LiDAR system. In all cases, the fuel types were classified equally or better using RF than SVM-L and SVM-R. Lastly, the extremely dense point cloud generated from the HMLS system has enabled precise quantification of vegetation volume at a very high spatial resolution. This has facilitated the accurate delineation of homogeneous distributions for the different Prometheus fuel types in forest plots characterized by high structural heterogeneity, where the predominant fuel type may otherwise be difficult to discern. While satellite data provide a comprehensive overview of fuel distribution over large areas, UAVs enable fuel estimation at more local scales with a very high level of detail. Their data could serve as ground-truth for expanding results across larger areas using ALS systems, which operate at a more effective scale for forest fuel management. Lastly, the potential of HMLS systems would lie in their highly accurate data for enhancing ground-truth, which would serve to improve fuel estimation using other remote sensing systems.

RESUMEN

Los bosques constituyen uno de los ecosistemas más valiosos de la Tierra, ya que son los principales reservorios de carbono, hogar de una gran biodiversidad y fuente de servicios para las sociedades humanas. Estos espacios se encuentran expuestos a numerosas perturbaciones naturales y antropogénicas que pueden producir deterioros en el ecosistema cuando su recurrencia es elevada. Los incendios forestales son una de las perturbaciones más importantes de los ecosistemas forestales, especialmente en los ambientes mediterráneos debido a las características del clima, la vegetación y la cultura del fuego. Una de las principales tareas para prevenir los incendios forestales es la identificación de los combustibles forestales, pues permiten conocer la trayectoria y velocidad de propagación del fuego en una masa forestal. La teledetección ha demostrado ser una herramienta de gran utilidad para identificar combustibles forestales. Sin embargo, es necesario seguir investigando en las capacidades de los nuevos sistemas de teledetección y de sus herramientas de procesado y análisis para mejorar la identificación de los combustibles forestales con el fin de establecer mecanismos más eficientes de prevención de incendios forestales, especialmente en el contexto de los actuales retos que plantea el cambio climático.

Esta tesis evalúa nuevos sistemas de teledetección a varias escalas espaciales con el objetivo de conocer sus capacidades para la mejora en la identificación de tipos de combustible, según la clasificación Prometheus, en ambientes forestales mediterráneos. Para ello, se han evaluado cuatro sistemas de teledetección con capacidad para generar información tridimensional: el sistema láser satelital *Global Ecosystem Dynamics Investigation* (GEDI) de la NASA, los vehículos aéreos no tripulados (UAVs) óptico (*eBee Classic*) y LiDAR (*DJI Matrice 300 RTK* + *DJI Zenmuse L1*), y el sistema láser escáner portátil (HMLS) *GeoSLAM ZEB-Horizon*. Además, se ha examinado el potencial de integración de los datos tridimensionales con imágenes ópticas obtenidas tanto desde satélite como desde plataforma UAV, así como el uso sinérgico de datos tridimensionales procedentes de diferentes sistemas. El procesado de los datos ha facilitado la obtención de variables relacionadas con las características estructurales, texturales, espectrales, volumétricas y de diversidad de la vegetación forestal. Estas variables han servido como predictoras independientes para la identificación final de los tipos de combustible, que se ha realizado mediante dos técnicas: modelos de clasificación *machine learning* –en concreto, *Random Forest* (RF) y *Support Vector Machine* de *kernel* lineal (SVM-L) y radial (SVM-R)– y a partir de la cuantificación a muy alta resolución espacial del volumen de

la vegetación para la definición de la distribución vertical del combustible para los distintos tipos Prometheus.

Los resultados de la investigación muestran que el sistema UAV-LiDAR es particularmente eficaz para clasificar y cartografiar los tipos de combustible Prometheus. Además, la integración de los datos UAV-LiDAR y HMLS ha proporcionado las mayores precisiones de clasificación de los tipos de combustible Prometheus. Se han observado asimismo buenos resultados cuando los datos procedentes de los sistemas láser y fotogramétricos han sido integrados con imágenes ópticas. En particular, GEDI ha demostrado buenas capacidades en la clasificación de los tipos de combustible cuando sus datos se han integrado con índices de vegetación derivados de imágenes multiespectrales de Landsat-8 OLI. Del mismo modo, el UAV fotogramétrico ha producido los mejores resultados en la clasificación de los tipos de combustible cuando sus datos tridimensionales se han combinado con imágenes multiespectrales del propio UAV, aunque con precisiones ligeramente inferiores en comparación con el sistema UAV-LiDAR. En todos los casos, los tipos de combustible se clasificaron igual o mejor usando RF que SVM-L y SVM-R. Finalmente, la extrema densidad de la nube de puntos derivada del sistema HMLS ha permitido cuantificar de manera precisa el volumen de la vegetación a muy alta resolución espacial y definir distribuciones homogéneas para los distintos tipos de combustible Prometheus en parcelas forestales de alta heterogeneidad estructural, donde el tipo de combustible predominante puede ser difícil de distinguir. Mientras que los datos obtenidos por satélite proporcionan una visión general de la distribución del combustible en grandes áreas, los UAVs permiten estimar el combustible a escalas más locales con un nivel de detalle muy elevado. Sus datos podrían servir de verdad-terreno para ampliar los resultados a zonas más extensas utilizando sistemas ALS, que operan a una escala más eficaz para la gestión de los combustibles forestales. Por último, el potencial de los sistemas HMLS residiría en sus datos altamente precisos para perfeccionar la verdad-terreno, lo que serviría para mejorar la estimación de los combustibles utilizando otros sistemas de teledetección.

CONTENTS

CHAPTER 1

BACKGROUND
AND RESEARCH JUSTIFICATION

1.1. WILDFIRES IN MEDITERRANEAN ECOSYSTEMS

Forest ecosystems cover 31% of the total surface area of planet Earth, which in absolute terms represents 4.06 billion hectares (FAO and UNEP, 2020). These areas play a pivotal role in the environment, serving as carbon sinks and havens for biodiversity. Forests also supply essential resources to human societies, such as timber and fuel, contribute to rural development, and offer recreational and leisure opportunities. These valuable ecosystems have been subjected to natural and anthropogenic disturbances throughout the history, but several recent processes are exerting greater pressure on them. Since 1990, about 420 million hectares of forests have been lost, primarily due to the change in land use, and more than 100 million hectares of forests have been affected by wildfires, diseases and other adverse events (FAO and UNEP, 2020).

Wildfires are one of the main disturbances of forest ecosystems. They constitute a primary process that is part of the natural dynamic of forests. Fire is the main source of forest regeneration, influences vegetation composition and structure, clears soils of undergrowth and dead matter, and facilitates the natural recycling of essential nutrients. However, when become recurrent, fire can cause devastating effects on forest ecosystems. In this sense, Rowell and Moore (2000) described fire as a paradox, as it can produce extensive ecological damages while simultaneously serves as a means of recycling and regenerating ecosystems. Wildfires can occur either because of natural or anthropogenic causes, albeit human activities represent the predominant ignition source in forests (San-Miguel-Ayanz *et al*., 2023). Furthermore, anthropogenic factors are contributing to the increase in the intensity and frequency of wildfires in last decades, such as land use changes (Ascoli *et al*., 2021; Braun *et al*., 2021a) or inadequate reforestation policies (Peñuelas and Sardans, 2021; Papatheodorou *et al*., 2023). In addition, processes derived from climate change, such as the increase in extreme temperatures, convective storms, and periods of drought, can further amplify the risk of wildfires and intensify their adverse effects on ecosystems (Dupuy *et al*., 2020; Jones *et al*., 2020; Abram *et al*., 2021; Pausas and Keeley, 2021).

Fire is a global issue as it affects almost all ecosystems (Chuvieco, 2009). The Mediterranean Basin represents one of the most fire-prone regions in the world, with about 90% of the total burned area in Europe (Pyne, 2009). It includes more than 25 million hectares of forests, about 10% of its total land cover (FAO and Plan Bleu, 2018). Mediterranean-type vegetation is determined by the fire regime and many species exhibit adaptations to fire. For instance, certain species

demonstrate passive resistance to wildfires, enabling survival during fire events, like cork oaks (*Quercus suber* L.). Other species possess the ability to rapidly resprout post-fire, such as holm oaks (*Quercus ilex* L.), Portuguese oaks (*Quercus faginea* Lam.), and junipers (*Juniperus oxycedrus* L.), while some others are able to disperse seeds capable of withstanding fire for subsequent germination, such as rosemary (*Rosmarinus officinalis* L.) and the majority of pines (e.g., *Pinus halepensis* Mill., *Pinus nigra* L., *Pinus pinaster* Aiton). The frequent occurrence of wildfires in the Mediterranean region is intricately tied to the prevalent climatic conditions. The equinoctial rainfall regime, particularly during spring, favors the growth of forest vegetation, which becomes susceptible to combustion when high temperatures and drought occur in the summer season. Furthermore, fire has been a valuable traditional resource for many Mediterranean societies to remove stubble or dead matter and to fertilize soil nutrients, which implies an additional risk of wildfires. In last decades the burned area and the number of fires has decreased in the Mediterranean Basin overall (Turco *et al*., 2016), probably due to improved forest management strategies supported by new technologies (Ruffault and Mouillot, 2015; Fréjaville and Curt, 2017). However, the size and severity of wildfires are expected to increase in the future, particularly in Mediterranean environments (González de Vega *et al*., 2016). Mediterranean climate shows trends towards greater aridity (Sillmann *et al*., 2013; MedECC, 2020) and increasingly high average temperatures (MedECC, 2020; Pastor *et al*., 2020) together with a more unpredictable rainfall regime, which makes this region one of the most vulnerable by climate change (MedECC, 2020; Ruffault *et al*., 2020). Additionally, progressive land abandonment may favor, more significantly than climate, the growth of wild vegetation and the emergence of new forests (Améztegui *et al*., 2010) producing an alteration of the fire regime as continuity of forest fuel may increase facilitating fire spread (Pausas and Fernández-Muñoz, 2012; MedECC, 2020). In this context, it is necessary to continue improving fire management in Mediterranean forests to minimize the adverse effects of wildfires on the territory.

Forest fire management involves actions taken both pre- and post-fire. Before fire occurrence, forecasting plans enable the assessment of fire risk in a given area, the identification of ignition sources, and the prediction of fire spread and intensity. Prevention plans include structural actions to reduce fire risk and vulnerability, such as thinning and periodic clearing, as well as non-structural actions like environmental education. On the other hand, after a fire event it is essential to assess its impact on ecosystems, evaluate the resilience of the affected plant communities, and understand the factors that govern post-fire

recovery (Rodrigues *et al*., 2024). One of the most critical components of fire management forecasting is the identification of forest fuels, as they provide insight into fire behavior in a forest mass. They are part of the so-called "fire triangle", together with the heat source and oxygen, but it is the only one that can be managed (Johnson and Peterson, 2005; Xanthopoulos *et al*., 2006; Stephens *et al*., 2009; Stephens *et al*., 2012; Ascoli *et al*., 2022). Forest fuels encompass all living or dead matter (e.g., branches, leaves, grasses, firewood, small shrubs) present in a forest that is available for combustion in case of fire. They are distributed across all stratum of the forest: on the ground (organic matter, roots), the lower surfaces (grass, shrubs, stumps), and the aerial part (trunks, branches, and crowns). There are several factors that can affect the flammability of fuels, such as humidity or the type of plant matter. The lower the moisture content, the more readily forest fuels will ignite and the faster the fire will spread. In this sense, the type of fuel material will determine the amount of moisture they can absorb. In addition, the gaps between tree canopies can have an impact on the amount of fuel moisture, as those located in shaded areas tend to dry more slowly than those exposed to open areas. Wildfires often start in surface fuels, and in this case, they are of low to moderate intensity. Crown fires reach greater intensities but are less likely to ignite. However, in forest stands with dense fuel, there may exist vertical continuity between surface and aerial fuels, causing a fire that started on the ground to reach the canopy. In such cases, fire intensity could reach its peak, making fires extremely challenging to control. Therefore, identifying the structure of forest fuels is a crucial first step towards improving fire management, particularly in Mediterranean ecosystems, which are seriously impacted by recurrent wildfires.

1.2. FOREST FUEL CLASSIFICATION SYSTEMS

The complex spatial distribution and the wide range of physical characteristics of forest fuels present significant challenges for accurate fuel quantification (Abdollahi and Yebra, 2023). To synthesize this complexity, several fuel classification systems have been developed over the past decades. They consider the most relevant features for estimating fire risk, categorizing fuels into types based on distinctive elements, shapes, sizes, and continuity, which exhibit similar behavior in the presence of fire (Merril and Alexander, 1987).

Table 1.1 summarizes the main fuel classification systems developed until date. One of the first widely used globally is the Rothermel's fire spread model (Rothermel, 1972). This model is based on heat balance concepts from Frandsen (1971), experiments with artificial fuel beds (Rothermel and Anderson, 1966),

and the fuel types developed by McArthur in Australia (McArthur, 1967). The Rothermel model is divided into 11 fuel types that synthesize a broad portion of forests, shrublands, and grasslands of the temperate areas of North America. It served as the basis for the development of the United States' National Fire Danger Rating System (NFDRS) (Deeming *et al*., 1972; Deeming *et al*., 1977), a seasonal weather system that, in combination with satellite imagery, allow deriving 20 fuel types (Arroyo *et al*., 2008; Abdollahi and Yebra, 2023). In addition, Albini (1976) adapted Rothermel's model to develop the Northern Forest Fire Laboratory (NFFL) fuel classification, including 13 fuel types and giving managers the option to develop their own fuel types (Arroyo *et al*., 2008). Furthermore, the Canadian Forest Fire Behavior Prediction System (FBP) provides estimates of fire behavior organized into five major vegetation groups discretized in 16 fuel types (Taylor *et al*., 1996). In Europe, the Prometheus fuel classification system (Prometheus, 1999) was created with the aim to be better adapted to fuels found in Mediterranean forests (Arroyo *et al*., 2008). It is an adaptation of the NFFL classification and comprises 7 fuel types grouped in three major vegetation classes. At the beginning of the 21st century, the Fuel Characteristics Classification System (FCCS) was developed in the United States to create fuel beds and classify them for their capacity to support fire and consume fuel (Sandberg *et al*., 2001; Ottmar *et al*., 2007). It uses a total of 216 fuel beds that represent the major vegetation types of the United States although the conceptual framework can be applicable worldwide (Ottmar *et al*., 2007). Finally, Scott and Burgan (2005) developed the Standard Fire Behavior Fuel Models (SFBFMs), which encompasses 45 fuel types, of which five are non-combustible. The SFBFMs system was designed to represent fuel characteristics, considering factors such as fuel load, fuel particle size, and moisture content (Carbone *et al*., 2023).

Although the objective of fuel classification systems is to facilitate the estimation, quantification, and mapping of forest fuels by synthesizing their high structural heterogeneity, certain limitations exist as described by Arroyo *et al*. (2008). For instance, fuel classifications have a strong dependence on specific environments, so it turns challenging when using them in other locations (Fogarty *et al*., 1998). Furthermore, difficulties arise in the classification of fuel types due to their complex structure and variability in physical attributes, making it sometimes difficult to assign a specific fuel type. Also, fuel classification systems are not useful for predicting fire effects, which are dependent on other factors. Finally, the spatial and temporal variability of fuels make them very difficult to estimate and map for effective fire management.

Table 1.1. The main fuel type classification systems.

Fuel classification system	Fuel types	Country	References
McArthur's grassland fire danger rating system	2	Australia	McArthur (1967)
Rothermel's fire spread model	11	USA	Rothermel (1972)
NFDRS	20	USA	Deeming *et al*. (1972)
NFFL	13	USA	Albini (1976)
FBP	16	Canada	Taylor *et al*. (1996)
Prometheus	7	Mediterranean Europe	Prometheus (1999)
FCCS	216	USA	Sandberg *et al*. (2001), Ottmar *et al*. (2007)
SFBFMs	45	USA	Scott and Burgan (2005)

Indeed, estimating forest fuels is not straightforward. However, technological advancements in recent decades can help overcome these limitations, especially with the continued development of the Earth observation systems supported by remote sensing and geographic information systems. In this context, the increasing number of instruments available for earth observation, the higher resolutions achievable by remote sensing sensors, the enhanced data processing capacity, the improved accessibility to processing tools, and the integration possibilities between different platforms and sensors may significantly enhance the identification of forest fuels. This may lead to more efficient forest fire management, especially in fire-prone regions like Mediterranean.

1.3. THE ROLE OF REMOTE SENSING IN FOREST FUEL MANAGEMENT

Remote sensing is a fundamental tool for the systematic monitoring of forests, the estimation of structural parameters of forest vegetation, and the mapping of a wide range of forest variables (Lechner *et al*., 2020). Moreover, it has enabled the identification and mapping of forest fuels with greater success than

traditional fieldwork methods (Abdollahi and Yebra, 2023). Much of the success of remote sensing, not only in forest ecosystems but also in other environments, relies on the free and open access to remote sensing data, which provides information across a wide range of spatial resolutions and spatiotemporal scales (Lechner *et al*., 2020). Additionally, continuous technological advancements in remote sensing facilitate the improvement of the assessment and monitoring of forest ecosystems at different scales (Calders *et al*., 2020a). Remote sensing can utilize both passive and active sensors. Passive sensors collect information across various regions of the electromagnetic spectrum, beyond just the visible light, providing valuable insights for studying forest and wildfires (Chuvieco, 2008). Active sensors include two technologies: LiDAR (*Light Detection and Ranging*) and radar (*Radio Detection and Ranging*), specifically SAR (*Synthetic Aperture Radar*) systems. They differ from passive sensors in their ability to emit their own energy rather than depending on energy reflected by another agent (i.e., the Sun). SAR systems emit microwave beams, while LiDAR sensors emit optical light beams, usually in the visible and infrared spectral regions of the electromagnetic spectrum. Both systems operate by measuring the distance between the emission of a microwave/laser pulse and its return to the sensor after being reflected by elements of the surface. This capability enables three-dimensional modelling of objects and terrain.

Early methods of forest fuel identification through remote sensing began in the late 1970s and 1980s using Landsat-MSS optical imagery (e.g., Cosentino, 1977; Kourtz, 1977; Rabii, 1979; Benson *et al*., 1982; Burgan and Shasby, 1984; Miller and Johnston, 1985). Landsat TM and SPOT (*Satellite Pour l'Observation de la Terre*) optical data were also used to identify fuels in late 1980s and during 1990s (e.g., Chuvieco and Congalton, 1989; Cohen, 1989; Chuvieco and Salas, 1996). In the 1980s, the potential of LiDAR technology for forestry applications began to emerge, such as for estimating forest canopy (Nelson *et al*., 1984), height and density of forest stands (Aldred and Bonnor, 1985), gross-merchantable timber volume (Maclean and Krabill, 1986), or volume and biomass of forests (Nelson *et al*., 1987). Forestry research utilizing LiDAR systems became well-established in the 1990s (e.g., Nilsson *et al*., 1996; Næsset, 1997; Nelson *et al*., 1997; Lefsky *et al*., 1998; Lefsky *et al*., 1999), when technology, computing processes and software experienced substantial progress. At the beginning of 21st century, the potential of LiDAR data for identifying forest fuels began to be recognized (e.g., Seielstad, 2003; Andersen *et al*., 2005; Peterson, 2005). Nowadays, LiDAR systems are on the most widely used remote sensing technologies for forest structure and forest fuel estimation (Wulder *et al*., 2008; Hudak *et al*., 2016; Beland *et al*., 2019; Xu *et al*., 2021).

LiDAR sensors are usually classified into two main groups according to the way they store distances: full-waveform and discrete-return systems (Figure 1.1). Full-waveform systems consist of the emission of a complete laser signal or backscattered full-continuous waveform, in which different peaks or energy returns are generated by the interaction of the waveform with the surface elements (Hermosilla *et al*., 2014). These systems have the capability to provide a precise and detailed depiction of vegetation structure (Bretar *et al*., 2008), although some challenges arise regarding the availability of tools capable of processing the complex and extensive information they generate (Ruiz *et al*., 2018). Discrete-return LiDAR systems does not record the full waveform but the points where the laser interacts with surface elements or with the terrain, resulting in a three-dimensional point cloud that reproduces the elements reflected by the laser in the x, y, and z coordinates. Of particular interest is the ability of discrete-return LiDAR systems to penetrate through the forest canopy, reaching down to lower strata and even the ground. In addition, LiDAR discrete pulses can be multi-registered; i.e., after interacting with some part of the vegetation, part of the pulse beam returns to the sensor while another part continues its journey to return later after several interactions, normally a maximum of 3 to 5 returns per pulse in Earth observation applications. These dual capabilities allow for a complete three-dimensional characterization of forest structure, making discrete-return LiDAR systems a highly valuable tools for forestry applications. Furthermore, the integration of LiDAR data with information provided by other remote sensing systems, primarily optical, enables the enhancement of the estimation of forest fuels. Some examples include the combination of LiDAR data with multispectral indices from satellite imagery (Marino *et al*., 2016; Adhikari *et al*., 2020; Domingo *et al*., 2020; Crespo-Calvo *et al*., 2023), hyperspectral imaging from planes (Romero-Ramírez *et al*., 2018), and satellite SAR systems (Kumar *et al*., 2018) together with optical imagery (Mulatu *et al*., 2019; Mihajlovski *et al*., 2023).

LiDAR systems can be attached to four main remote sensing platforms: satellites, planes, unmanned aerial vehicles, and ground-based. Furthermore, as will be explained later, unmanned aerial vehicles enable obtaining results comparable to LiDAR using optical sensors.

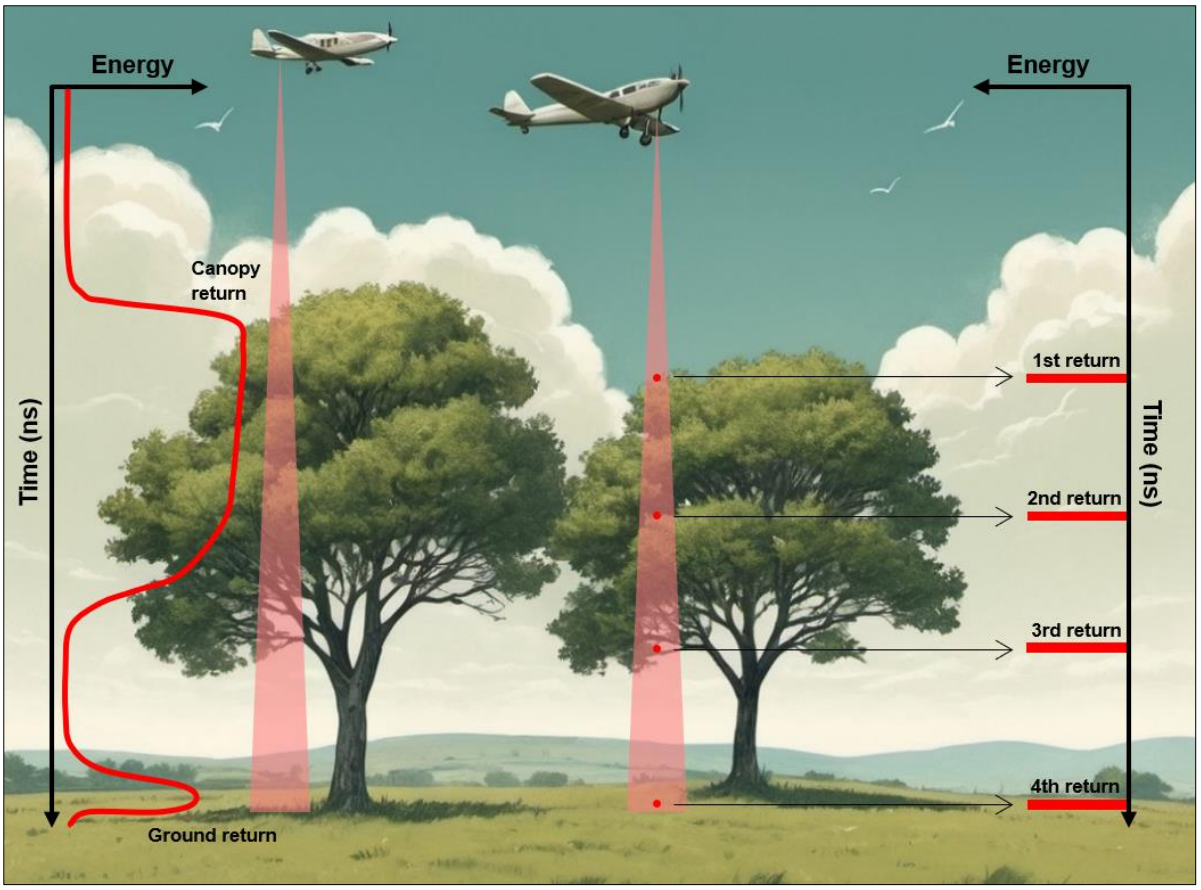

Figure 1.1. Two types of store distances from LiDAR sensors: full-waveform (left) and discrete-return (right) LiDAR systems.

1.3.1. Satellite Laser Scanners

Satellite Laser Scanners (SLS) provide information systematically on a global scale at medium-high spatial resolution. Data are registered in discrete circular footprints spaced several meters apart due to the considerable distance between the sensor and the Earth's surface, resulting in data gaps due to the lack of spatial continuity. They are less common than other LiDAR platforms but currently two SLS systems are operational: The *Global Ecosystem Dynamics Investigation* (GEDI) on board the International Space Station (ISS) and the *Advanced Topographic Laser Altimeter System* (ATLAS) attached to the ICESat-2 satellite. Both systems were launched by NASA on 2018. GEDI utilizes full waveform system to record information and is specifically designed for analysis in forest ecosystems (Dubayah *et al*., 2020). Numerous forestry studies have utilized GEDI data, primarily focusing on the estimation of vegetation structural parameters (e.g., Dhargay *et al*., 2022; Marselis *et al*., 2022; Wang *et al*., 2024) and forest biomass (e.g., Saarela *et al*., 2018; Qi *et al*., 2019; Duncanson *et al*., 2022), albeit it also shows promising capabilities for identifying forest fuels (Leite *et al*., 2022; Myroniuk *et al*., 2023). ICESat-2/ATLAS system operates

with a photon-counting sensor and can be used for forestry applications although its primary objective is the study of ice masses and glaciers on a global scale. A few studies have employed ICESat-2/ATLAS to estimate structural attributes of vegetation (e.g., Narine *et al.*, 2019; Neuenschwander *et al.*, 2020; Nandy *et al.*, 2021), but to date, it does not appear applicable for fuel identification. In the past, the *Geoscience Laser Altimeter System* (ICESat/GLAS), in operation between 2003 and 2009, constituted the first SLS system with global coverage. GLAS demonstrated capabilities to analyze wildfire effects (Ranson *et al.*, 2004) and identify forest fuels (Ashworth *et al.*, 2010; García *et al.*, 2012; Peterson *et al.*, 2013). In the near future, the currently under development NASA's EDGE (*Earth Dynamics Geodetic Explorer*) SLS system will complement data obtained from GEDI and ICESat-2/ATLAS. EDGE will focus on analyzing terrestrial ecosystems, ice masses and glaciers. Among the primary objectives related to terrestrial ecosystems include the quantification of forest structure and aboveground biomass changes due to natural and human-induces disturbances, the assessment of forest structure and its relationship with habitats and biodiversity, and the measure of carbon fluxes from woody vegetation and their potential sequestration in response to climate change.

1.3.2. Airborne Laser Scanners

Airborne Laser Scanners (ALS) operate on smaller scales than SLS, albeit data are registered with a higher spatial resolution. This makes them particularly well-suited for forest fuel management at local and regional scales. ALS consist of two main components: the laser sensor, which captures the data and is attached to the platform, and the navigation system, which includes the Global Navigation Satellite System (GNSS) and the Inertial Measurement Unit (IMU). The laser system continuously sends pulses towards the surface as the aircraft flies over the study area. Some ALS operate in full waveform (Means *et al.*, 1999; Höfle *et al.*, 2008; Hollaus *et al.*, 2013; Crespo-Peremarch *et al.*, 2018) but the predominant method of scanning is discrete-return systems. GNSS provides the geopositioning of the aircraft while the IMU enables its precise movement, allowing three-dimensional georeferenced data. The support of ground GNSS stations serves to improve the precision of the aircraft's GNSS and ensure that data is georeferenced with sub-meter accuracies (Vosselman and Maas, 2010). ALS provide great capabilities on the study of wildfires (Magnussen and Wulder, 2012; Gajardo *et al.*, 2013; Klauberg *et al.*, 2019) and forest fuels (Marino *et al.*, 2016; García-Cimarras *et al.*, 2021; Labenski *et al.*, 2023). Some countries have national-scale non-commercial ALS dataset which are freely accessible to users, such as Spain (PNOA: https://pnoa.ign.es/), Finland (MML:

https://maanmittauslaitos.fi/), the Netherlands (AHN: https://ahn.nl/), or Estonia (Maa-Amet: https://geoportaal.maaamet.ee/). Nationwide LiDAR datasets typically have low point density (<10 p/m^2) but have proven effective for wildfire assessments (Montealegre *et al.*, 2014), biomass quantification (Domingo *et al.*, 2018), and forest fuels identification (Domingo *et al.*, 2020).

1.3.3. Unmanned Aerial Vehicles

In the field of proximal remote sensing platforms, Unmanned Aerial Vehicles (UAVs), also referred to as Remotely Piloted Aircrafts (RPAs), Unmanned Aerial Systems (UAS), Remotely Piloted Aircraft Systems (RPAS), or just "drones", are nowadays among the most commonly used for forestry applications. UAVs provide information with very high spatial resolution, although on a smaller spatial scale compared to ALS. Their functioning is similar to ALS and involves the same main components to obtain georeferenced data with sub-meter accuracies. The primary difference is that UAV flights are unmanned and autonomously managed from the ground by an operator. Additionally, because UAVs fly at a much lower altitude than ALS, the resulting three-dimensional point clouds are typically of higher density, providing more detailed information on forest vegetation and fuels.

Studies involving UAVs in forest ecosystems began in the early 21st century (Olsson *et al.*, 2005), primary focusing on forest fire monitoring (e.g., Casbeer *et al.*, 2005; Ollero *et al.*, 2006; Sujit *et al.*, 2007). Further interest arose in the following decade as UAV technology advanced significantly. UAVs can generate three-dimensional point clouds not only from LiDAR systems but from passive sensors. This is achieved through photogrammetric processes using optical images captured by UAVs with a high degree of overlap (Figure 1.2). *Structure from Motion* (SFM) is currently one of the most widely used photogrammetric techniques among UAV image processing software. SFM is a computer vision technique based on traditional stereo photogrammetry, which relies on the geometry of the objects captured in multiple overlapping images from different angular viewpoints (Snavely *et al.*, 2008; Remondino *et al.*, 2014; Puliti *et al.*, 2015). It involves extracting various features from two-dimensional images (e.g., points or lines), estimating motion during data acquisition and calibrating the sensor to reconstruct the three-dimensional point clouds (Özyeşil *et al.*, 2017). UAV photogrammetric point clouds generated from high-resolution optical images are typically denser than those from LiDAR. They are considered indicated to estimate canopy height and coverage (Wallace *et al.*, 2016; Shin *et al.*, 2018). However, in dense forest environments, optical UAVs are unable to capture the vegetation beneath the canopy or the ground (White *et*

al., 2016; Guerra-Hernández *et al*., 2018; Salach *et al*., 2018; Cao *et al*., 2019; Lamping *et al*., 2021), even with very high overlaps between photographs (Wallace *et al*., 2016). This could potentially pose a challenge in estimating shrub and herbaceous fuels. UAV-LiDAR systems offer an advantage over optical UAVs by enabling laser pulses to penetrate through the canopy. This capability allows for the acquisition of data across all forest strata and even the ground (Hillman *et al*., 2021). UAV-LiDAR systems have been utilized to fuel management (Rodríguez-Puerta *et al*., 2020) and to characterize canopy fuels (Arkin *et al*., 2021). Nevertheless, the economic cost of UAV-LiDAR systems is usually considerably higher than that of optical UAVs. As a result, the latter are more accessible to users and thus can serve as an affordable alternative to UAV-LiDAR systems (Wallace *et al*., 2016).

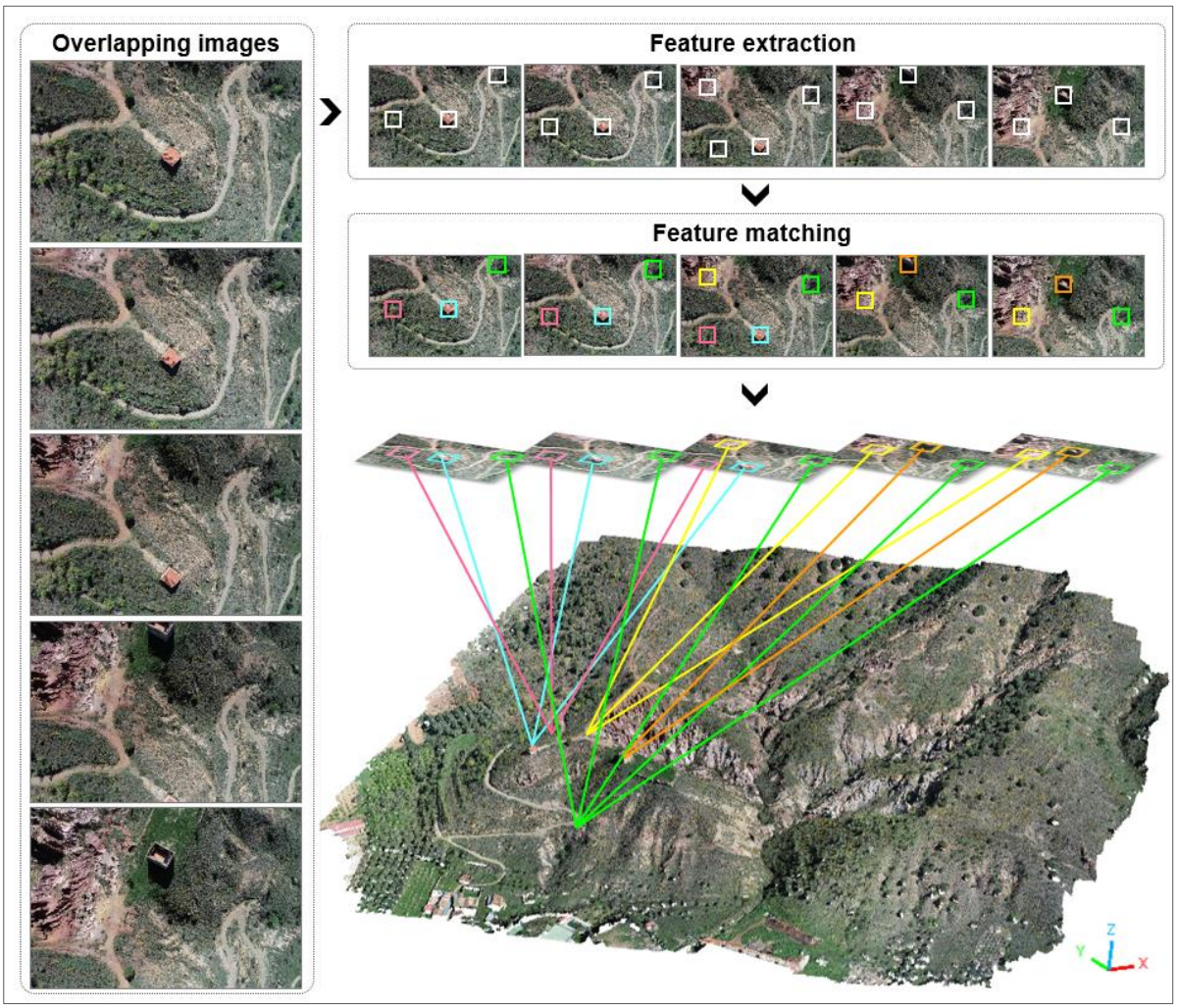

Figure 1.2. Graphic scheme of the photogrammetric process using highly overlapping images captured by optical UAVs to provide three-dimensional point clouds.

1.3.4. Ground-based laser scanners

Ground-based laser scanner systems are typically operated from three different platforms (Figure 1.3): static tripods (TLS: Terrestrial Laser Scanners), mobile platforms (MLS: Mobile Laser Scanners), and handheld or portable devices (HMLS: Handheld Mobile Laser Scanners). These systems commonly record data using panoramic and spherical scanners, which rotates horizontally 360º and vertically 80-90º while continuously sending out laser pulses (Vosselman and Maas, 2010). Data acquisition methods vary depending on the type of platform used. TLS systems require multiple acquisitions from different observation points to ensure thorough scanning of the entire area, avoid occlusions, and achieve accurate georeferencing of the data (Torralba *et al*., 2022; Vandendaele *et al*., 2022). This differs from MLS and HMLS platforms, where data is collected in motion, resulting in lower time cost (Tommaselli *et al*., 2014). Moreover, the integration of SLAM (*Simultaneous Localization and Mapping*) technology in MLS and HMLS platforms has improved the accuracy of object location estimation during data acquisition. Combined with the IMU, SLAM enables measurement of objects movement, rotation, and position change in the three-dimensional space, this improving mapping efficiency (Chen *et al*., 2016).

Data recorded with ground-based systems provide extremely dense point clouds (Crespo-Peremarch *et al*., 2020; Hillman *et al*., 2021; Wagers *et al*., 2021; Prendes *et al*., 2022; Torralba *et al*., 2022) and typically operate at a local scale, such as forest plots. Consequently, they are often used in detailed studies, providing estimates of tree height, crown volumes, basal diameter, and wood volume (Donager *et al*., 2021a; Vandendaele *et al*., 2022), as well as different parameters of forest fuels, such as tree trunks (Chen *et al*., 2016), fuel loads (Alonso-Rego *et al*., 2020), fuel biomass (Rowell *et al*., 2020), and the effects of logging on forest fuel structure (Wilson *et al*., 2021).

Figure 1.3. The three main platforms of ground-based laser scanner systems in forestry: TLS (left), MLS (above-right), and HMLS (below-right).

1.4. OBJECTIVES AND HYPOTHESES

Fire is a natural element on our planet. The climatic, biogeographic, and human characteristics of Mediterranean environments lead to a high prevalence of fire, posing great risks to both ecosystems and human populations. Fire must be considered an integral element to be managed within the territory, demanding policies that anticipate, prevent, and mitigate the negative effects of wildfires. The recurrence and intensity of fire result in the degradation of forest ecosystems and the loss of their natural, cultural, and economic heritage. The progressive abandonment of fields promotes natural wild reforestation, providing new fuel for wildfires and thus increasing fire risk. Additionally, the effects of climate change can exacerbate the risk of wildfires, making them more sever and harder to manage.

In response to this scenario, the Ministry for the Ecological Transition and Demographic Challenge of the Government of Spain developed the *Strategic Guidelines for the Management of Wildfires in Spain* (original title: *Orientaciones Estratégicas para la Gestión de Incendios Forestales en España*), which were approved by the Sectorial Environment Conference on July 28,

2022. Its general objective is to reduce the impacts and vulnerability to the social, economic, and environmental effects caused by wildfires in Spain. To this end, several priority lines of action were established based on seven specific objectives. One of these objectives is the reduction of the risk of wildfires and the adaptation of ecosystems and societies to their occurrence, whose lines of action aims to prevent the occurrence of fires or, at the very least, reduce their effects. It seeks to enhance ecosystems' capacity to face wildfire risk situations under favorable conditions, minimize the negative effects, and capitalize on the positive aspects. One line of action of this specific objective is land management at the meso- and macro-scale to reduce the load and continuity of forest fuels, thereby creating landscapes where the probability of wildfires is diminished. An additionally specific objective aims to integrate technological advancements in the prevention, detection, organization, and suppression of wildfires. In summary, both objectives emphasize the necessity of employing new technologies to mitigate the risk of wildfires, with a particular focus on the multiscale management of forest fuels in order to achieve efficient management of wildfires.

Fuel identification facilitates the development of structural wildfire mitigation plans. Therefore, tools and technology that have proven to be capable of estimating accurately different attributes of forest fuels are required. Among remote sensing systems, active LiDAR sensors enable precise estimation and mapping of forest structure and fuels across large areas. This capability holds whether used independently or in combination with other remote sensing data, and utilizing either full-waveform or discrete-return systems. The ongoing technological advancements in remote sensing underscore the importance of studying the capabilities of new systems for improved fuel identification. In this context, the evaluation of the potential of different novel remote sensing systems, considering their effective working scale, spatial and temporal resolution, data processing and analysis capacity, and overall accuracy in estimating forest fuels, are required. This assessment helps to understand the strengths, limitation, and potential synergies of each system for forest fuels identification, thus enabling more efficient wildfire management.

Based on this hypothesis, the main objective of this PhD Thesis is to evaluate novel remote sensing systems to improve forest fuel estimation in structurally heterogeneous Mediterranean forest environments. For fuel estimation, the Prometheus fuel classification has been utilized, as it is adapted to Mediterranean environments and the use of remote sensing techniques (Arroyo *et al.*, 2008). The evaluation considers various effective scales of work for forest fuel management in the context of the lines of action suggested in the strategic

guidelines for the management of wildfires in Spain. To this end, three remote sensing platforms have been analyzed: satellites, unmanned aerial vehicles, and ground-based platforms. Specifically, the instruments evaluated have been the GEDI SLS system, an optical UAV, a UAV-LiDAR system, and an HMLS system. LiDAR is the primary sensor evaluated in each of these platforms due to their demonstrated capacity to estimate forest fuels. Additionally, the capability of optical images, obtained from both satellite and airborne platforms in the visible and multispectral bands, to support LiDAR sensors in improving fuel identification is also assessed. ALS systems are not directly evaluated; instead, the extent of improvement resulting from their integration with data from other remote sensing platforms is yet analyzed.

The overarching objective includes several specific objectives, each accompanied by corresponding hypotheses, directly linked to the articles that form the primary outcomes of the research (Table 1.2), which comprise the core of the PhD Thesis.

a. Evaluate the performance of machine learning classification models for classifying Prometheus fuel types. The initial hypothesis posits that machine learning classification algorithms are effective for categorizing Prometheus fuel types based on data obtained from different remote sensing platforms.
b. Assess the capability of SLS systems to identify fuel types independently and in combination with optical images from satellites for improved fuel type classification. The initial hypothesis suggests that GEDI can independently identify fuel types. Furthermore, based on studies published during the development of the thesis, synergies observed with optical images from satellites are expected to enhance the classification accuracy of fuel types when combined with GEDI data.
c. Explore the potential of integrating Digital Elevation Models (DEMs) generated from ALS data to normalize the heights of UAV photogrammetric point clouds. The initial hypothesis postulates that the inability of photogrammetric point clouds to penetrate forest canopy can be addressed by leveraging high-resolution DEMs from ALS data, as noticed by previous studies. This integration enables the normalization of point cloud heights, facilitating the extraction of several forest variables.
d. Evaluate the capability of optical UAVs in identifying fuel types using structural, textural, and multispectral variables. The initial hypothesis proposes that three-dimensional point clouds derived from photogrammetric techniques enable the extraction of vegetation structure and texture variables for fuel type classification. Additionally, integrating non-structural

vegetation data acquired with the UAV, such as multispectral indices, is expected to enhance fuel classification accuracy.

e. Evaluate the effectiveness of HMLS systems in delineating fuel types within structurally complex forest stands. The initial hypothesis suggests that the very dense point cloud data are obtained from HMLS platforms enables precise capture of fuel structural heterogeneity, which is typical in Mediterranean forests. This capability facilitates detailed quantification of fuel volume across various height strata (e.g., the Prometheus model height strata) at exceptionally high resolution, thereby enabling the definition of fuel types in forest stands where the dominant type is uncertain.

f. Assess the efficacy of UAV-LiDAR systems in classifying and mapping fuel types and evaluate the integration of HMLS data. The initial hypothesis proposes that UAV-LiDAR systems, by virtue of their capability to characterize forest structure, can effectively classify fuel types and spatially map them over larger areas. Additionally, assuming some uncertainty of UAV-LiDAR systems in capturing understory fuels under dense forest canopy conditions, it is anticipated that HMLS data will improve differentiation between shrub and understory fuel types.

Finally, the evaluation of the four systems has served as a basis for a general discussion based on a comparative analysis between these systems and other remote sensing systems of significant interest for forest fuel estimation. The objective of this analysis is to assess the strengths and limitations of three-dimensional remote sensing systems at different scales for effective fuel management, considering the real scale of forest management work. The systems included in this analysis, but not directly evaluated within the core of this PhD Thesis, are the emerging SLS system ICESat-2/ATLAS, which is contemporary with GEDI, and ALS and TLS systems, due to their proven effectiveness in estimating forest fuels.

1.5. PHD THESIS STRUCTURE

The PhD Thesis, presented in the form of a compendium of articles, is structured as follows. Chapter 1 contextualizes the research framework of the thesis and outlines the objectives and hypotheses. Chapter 2 describes the study area and the materials and methods used to achieve the objectives. Chapters 3, 4, 5, and 6 comprise the research articles that form the core of the PhD Thesis, in which GEDI SLS, optical UAV, HMLS, and UAV-LiDAR systems constitute the main instruments assessed, respectively. Chapter 7 discusses the overall results and,

finally, Chapter 8 presents the conclusions. Additionally, the final appendix summarizes the metrics of the articles published as part of the thesis.

Figure 1.4 illustrates the development of the research conducted during the thesis, including research articles presented in Chapters 3 to 6 and their corresponding conference communications. It also includes the PhD stay at the *Sverige lantbruksuniversitet* (SLU) in Umeå, Sweden, which provided the opportunity to learn techniques for the acquisition, processing, and analysis of HMLS and UAV-LiDAR data. Additionally, Table 1.2 summarizes the contributing research articles and the corresponding specific objectives of the PhD Thesis listed in the previous section.

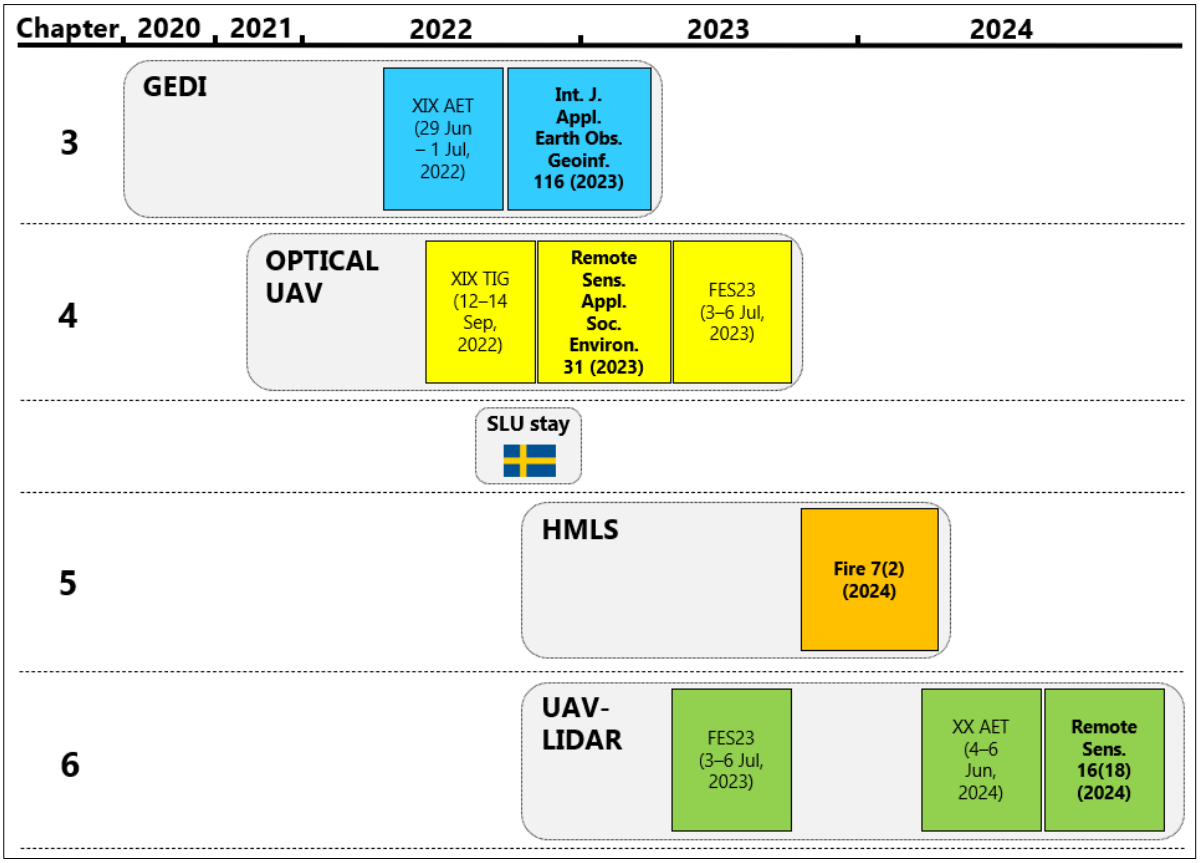

Figure 1.4. Research schedule and structure. Published articles are in bold, with the journal, issue number, and year of publication specified. Conference communications are in regular font, listing the name and date of the conference. The colors are grouped according to their respective chapters in the thesis.

Table 1.2. Summary of contributing research articles and their corresponding PhD Thesis' specific objectives.

Publication	Specific objectives
Hoffrén, R., Lamelas, M.T., de la Riva, J., Domingo, D., Montealegre, A.L., García-Martín, A., and Revilla, S., 2023. Assessing GEDI-NASA system for forest fuels classification using machine learning techniques. *International Journal of Applied Earth Observation and Geoinformation* 116, 103175. https://doi.org/10.1016/j.jag.2022.103175.	a. Evaluate the performance of machine learning classification models for classifying Prometheus fuel types. b. Assess the capability of SLS systems to identify fuel types independently and in combination with optical images from satellites for improved fuel type classification.
Hoffrén, R., Lamelas, M.T., and de la Riva, J., 2023. UAV-derived photogrammetric point clouds and multispectral indices for fuel estimation in Mediterranean forests. *Remote Sensing Applications: Society and Environment* 31, 100997. https://doi.org/10.1016/j.rsase.2023.100997.	a. Evaluate the performance of machine learning classification models for classifying Prometheus fuel types. c. Explore the potential of integrating Digital Elevation Models (DEMs) generated from ALS data to normalize the heights of UAV photogrammetric point clouds. d. Evaluate the capability of optical UAVs in identifying fuel types using structural, textural, and multispectral variables.
Hoffrén, R., Lamelas, M.T., and de la Riva, J., 2024. Evaluation of handheld mobile laser scanner systems for the definition of fuel types in structurally complex Mediterranean forest stands. *Fire* 7 (2), 59, https://doi.org/10.3390/fire7020059.	e. Evaluate the effectiveness of HMLS systems in delineating fuel types within structurally complex forest stands.
Hoffrén, R., Lamelas, M.T., and de la Riva, J., 2024. Classification and mapping of fuels in Mediterranean forest landscapes using a UAV-LiDAR system and integration possibilities with handheld mobile laser scanner systems. *Remote Sensing* 16 (18), 3536, https://doi.org/10.3390/rs16183536.	a. Evaluate the performance of machine learning classification models for classifying Prometheus fuel types. e. Evaluate the effectiveness of HMLS systems in delineating fuel types within structurally complex forest stands. f. Assess the efficacy of UAV-LiDAR systems in classifying and mapping fuel types and evaluate the integration of HMLS data.

CHAPTER 2

MATERIALS AND METHODS

2.1. STUDY AREA

The PhD Thesis has been developed in five forested sectors within the diverse Mediterranean landscapes of the Autonomous Community of Aragon, in northeastern Spain (Figure 2.1).

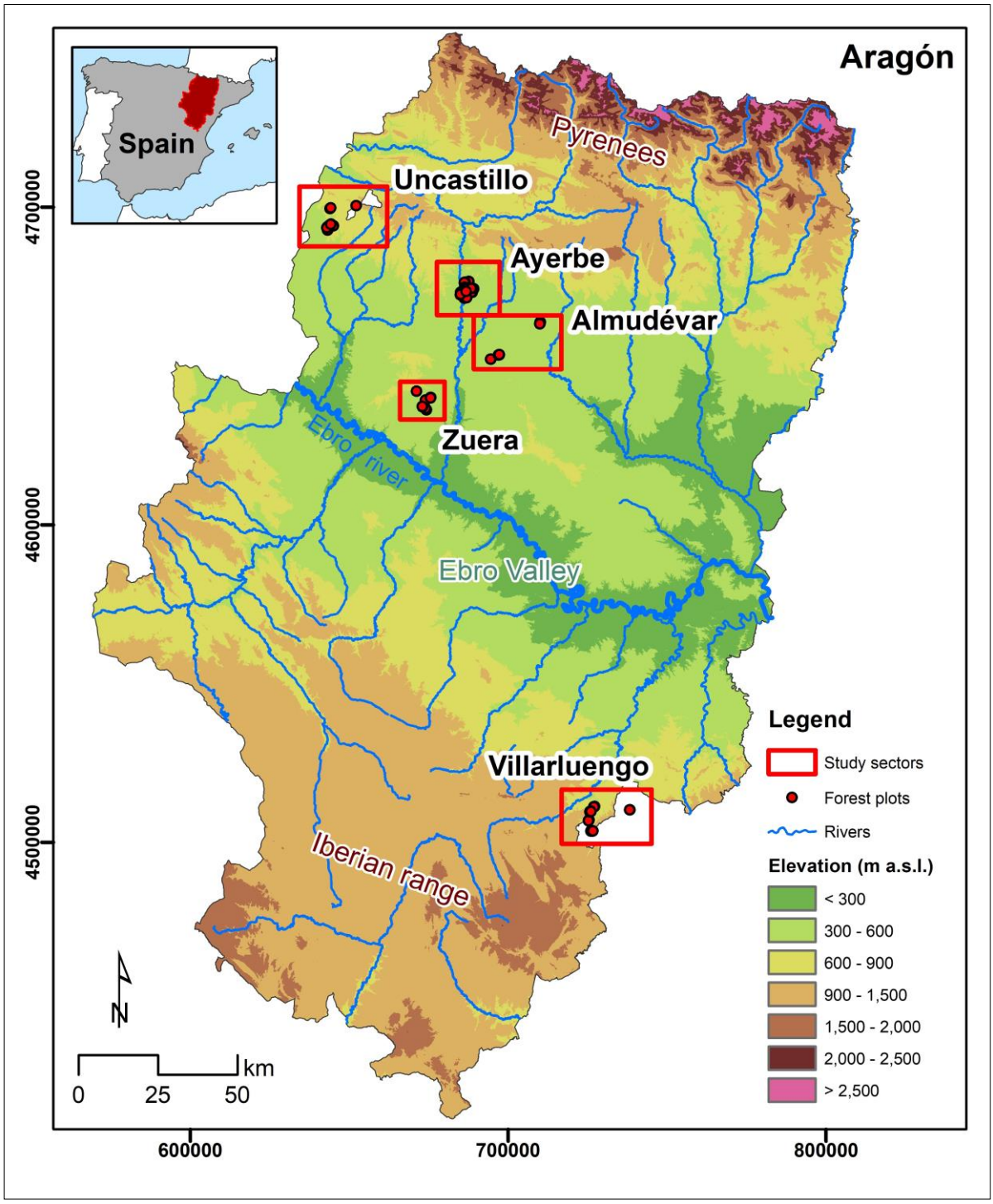

Figure 2.1. Main location of the five forest sectors studied for the development of the PhD Thesis within the Autonomous Community of Aragón, NE Spain.

2.1.1. General overview

The Autonomous Community of Aragon encompasses an area of 47,720.30 km^2, constituting 9.40% of the Spanish territory and ranking as the fourth largest region in the country. It comprises three provinces: Huesca, Zaragoza, and Teruel, arranged from north to south. Aragon shares borders with France to the north, Catalonia and Valencian Community to the east, Castile-La Mancha to the south, and Castile and León, La Rioja, and Navarre to the west. Viewed from north to south, the topographic profile of Aragon resembles a big basin, with the highest points situated at the northern (Pyrenees) and southern (Iberian Range) ends, and the lowest points in the center (Ebro Valley).

At the northernmost part lie the Pyrenees, a mountain range with an Armorican orientation formed during the Alpine orogeny, serving as the border between Spain and France. The highest altitudes are found in the Axial Pyrenees, located centrally within the mountain range, where Paleozoic materials and metamorphic and plutonic rocks associated with the Hercynian orogeny have resisted the intense erosion processes (Peña and Lozano, 2004). The tallest peaks include Aneto (3,404 m a.s.l.) and Posets (3,368 m a.s.l.). West of these mountain ranges lies another sector of high elevation formed by the Monte Perdido Massif, of karstic origin, with its highest point being Monte Perdido (3,355 m a.s.l.). To the south of the Pyrenees, and divided by perpendicular valleys, lie the *Sierras Exteriores*, also known as the Pre-Pyrenees. These series of mountain ranges configure the natural boundary between the Pyrenean sector to the north and the Ebro Valley to the south. Maximum altitudes of the Pre-Pyrenees typically range between 1,500 and 2,000 m a.s.l., with predominant materials originating from the Quaternary period, primarily composed of calcareous rocks, conglomerates, Oligocene molasses, and sandstones (Peña and Lozano, 2004).

South of the Pre-Pyrenees and occupying the central region of Aragon is the Ebro Valley, which was formed during the Cenozoic era, spanning from the Eocene to the Pliocene (Peña and Lozano, 2004). Its geological development is intertwined with the Alpine orogeny; however, unlike the Pyrenees, this area experienced a subsidence while the surrounding regions were uplifting. The outer regions of the valley are characterized by slightly elevated foothills, known as "*somontanos*", gently sloping flat lands of conglomeratic materials that connect the Pre-Pyrenees and the Iberian Range towards the center of the valley. Flowing through the center of the valley in a northwest to southeast direction is the Ebro River, Spain's longest river and the second longest in the Iberian Peninsula and the Mediterranean Basin. The river courses through various non-

consistent geological formations, including sandstones, marls, gypsum, limestone, and salts.

At the southern part of Aragon is located the Iberian Range, running in an Armorican orientation and formed during the Alpine orogeny. Its relief is less pronounced compared to the Pyrenees, with mean maximum altitudes rarely exceeding 2,000 m a.s.l. Within this range are various mountain systems separated by tectonic rifts, the most prominent being the *Sierra del Moncayo*, in the northwestern part, where the Iberian Range reaches its highest altitude (2,316 m a.s.l.), and the *Sierra de Gúdar* and *Sierra de Javalambre* in the southeastern end. The primary geological formations consist of sandstones, Paleozoic quartzites and slates, and Mesozoic limestones (Peña and Lozano, 2004).

The prevailing climate in Aragon is Mediterranean with continental influence. The region's extensive topographic variation leads to stark contrasts between different areas, ranging from steppe environments in the center of the Ebro Valley to a high mountain climate in the Pyrenees. Precipitation patterns are irregular throughout the year, although they tend to be concentrated during the equinoctial seasons, with slightly more rainfall in spring compared to autumn (Franco-Aliaga, 2010). Conversely, winters and summers are typically dry, particularly in the Ebro Valley, although convective storms are frequent in the end of spring and summer due to local air heating. According to the Climate Atlas of Aragon (Cuadrat *et al*., 2007), the average annual precipitation in Aragon is 548.80 mm, but its distribution across the region is highly heterogeneous. The Ebro Valley's central areas experience the lowest precipitation levels (<400 mm/year), which gradually increase towards the peripheral mountain systems. In the Iberian Range and the Pre-Pyrenees, the average annual precipitation is 800 mm/year, while in the Pyrenees, it exceeds 1,000-1,500 mm/year, with much of the precipitation occurring in winter in the form of snow. The average annual temperature in Aragon stands at 12ºC; however, as in precipitation, there is considerable spatial variability within the region. Generally, significant temperature variations occur throughout the year, with cold winters and warm summers, acting the equinoctial seasons as transitional periods. The Ebro Valley experiences the strongest thermal contrasts, especially in the central area, with extremely hot summers and cold winters. The peripheral mountain systems exhibit less pronounced thermal contrasts, with cooler summers, though winters tend to be very cold, particularly in the Pyrenees. Wind is a significant climatic factor in Aragon, particularly in the Ebro Valley. According to Cuadrat *et al*. (2007), the two prevailing wind regimes in the region are W-NW ("*cierzo*") and E-SE ("*bochorno*"). The "*cierzo*", which shares similarities with the French "*mistral*" wind, is a persistent

cold, dry wind throughout the year, capable of reaching very high speeds (>100 km/h) (Cuadrat, 2004). The "*bochorno*", which is less frequent and intense, is mild and humid in winter and spring, while dry in summer (Cuadrat, 2004).

Aragon is situated within two biogeographic regions of the Holarctic: The Eurosiberian and the Mediterranean. The Eurosiberian region, located in the northern part of Aragon, encompasses the alpine, subalpine, and montane bioclimatic zones. These areas are predominantly covered by forests and pastures, featuring vegetation dominated by alpine and boreoalpine species. The Mediterranean region comprises the Ebro Valley, the Pyrenean and Iberian "*somontanos*", and the moorlands of the province of Teruel (Longares, 2004). Here, medium and low shrubs such as rosemary (*Rosmarinus officinalis* L.), juniper (*Juniperus oxycedrus* L.), and boxwood (*Buxus sempervirens* L.) are prevalent. The vegetation in this region is well-adapted to gypsiferous and saline soils, high thermal contrasts, summer droughts, and the persistent "*cierzo*" drying wind. Forests are dominated by tree species such as Aleppo pine (*Pinus halepensis* Mill.), black pine (*Pinus nigra* L.), Scots pine (*Pinus sylvestris* L.), maritime pine (*Pinus pinaster* Aiton), and oaks (*Quercus ilex* L., *Quercus ilex* subsp. *rotundifolia* Lam., *Quercus coccifera* L.). According to the Spanish Forest Map (MFE, 2023), forested areas in Aragon represent 39.37% of the region's total land area and the most representative forest species are *Pinus halepensis* Mill. (21.46%), *Quercus ilex* L. (17.58%), and *Pinus sylvestris* L. (13.56%).

2.1.2. Study sectors and forest plots

The evaluation of GEDI SLS system was conducted across the entire area of the Zuera sector, while the UAVs and HMLS systems were evaluated at forest plot scale level, distributed among the five study sectors. Most of the plots were surveyed in earlier studies and only plots from the Almudévar sector, two from the Zuera sector (plots *zu201* and *zu202*), and all plots pertaining to the Prometheus model grass/herbaceous fuel type were included in the current PhD Thesis, in order to achieve a balanced representation of all Prometheus fuel types. Plots located in the Uncastillo and Villarluengo sectors were established within the framework of the SERGISAT project (CGL2014-57013-C2) of the Spanish Ministry of Economy and Competitiveness, which have been subject to prior research (e.g., Domingo *et al*., 2020; Rodrigues *et al*., 2024). Ayerbe plots were established within the context of research conducted by Domingo *et al*. (2017, 2018, 2019), while Zuera plots were established by Montealegre *et al*. (2016), excluding the aforementioned plots *zu201* and *zu202*. The center of each

forest plot was established with a *Leica VIVA*® GS15 CS10 GNSS real-time kinematic Global Positioning System with sub-meter accuracy.

Almudévar

The Almudévar sector is located at the north of the central area of the Ebro Valley, between the cities of Huesca and Zaragoza. It is formed by a total of 12 forest plots of 15-m circular radius (Figure 2.2). It predominantly consists of flat terrain, with elevations ranging from 350 to 440 m a.s.l., increasing away from the center of the valley towards the "*somontano*" to the north. The predominant land use is agricultural interspersed with patches of forest areas of *Pinus halepensis* Mill. and medium to high shrublands dominated by *Quercus ilex* L. The sector is delineated into three distinct study areas. The first area is located in the southernmost part of the sector, in a pine forest mass situated in the town of San Jorge. The second area is in the central part of the sector, in pine forest stands near the town of Almudévar. The third area is placed in two separated stands dominated by oak shrublands at the northern part of the sector.

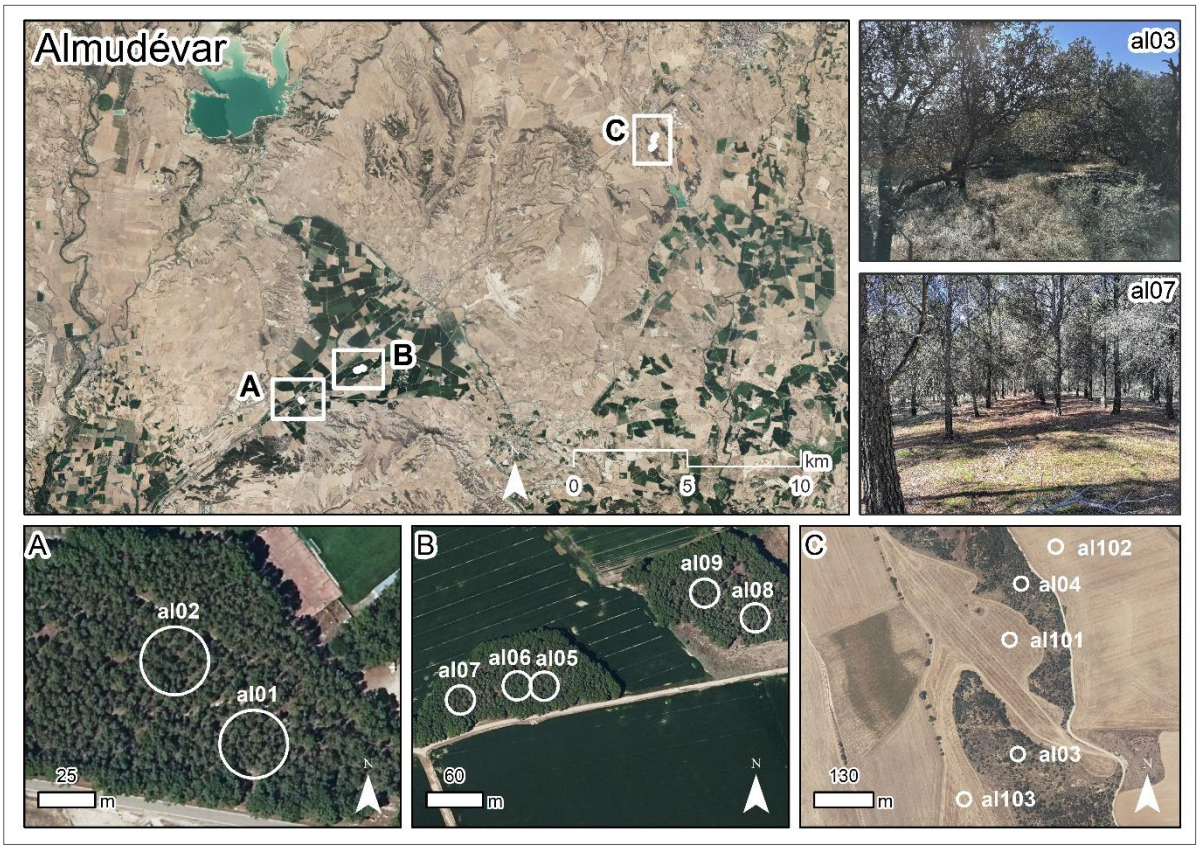

Figure 2.2. Location of the 12 forest plots (white dots) of the Almudévar sector distributed in the three study areas and photographs of two forest plots: *al03* and *al07*.

Ayerbe

The Ayerbe sector is situated to the north of the central Ebro Valley, close to the foothills of the Pre-Pyrenees. Comprising a total of 36 forest plots of 15-m circular radius (Figure 2.3), this area boasts an average elevation ranging from 410 to 550 m a.s.l. While certain zones exhibit rugged terrain, the overall landscape tends to be relatively flat, especially the areas closest to the Gállego river. The predominant land use is agriculture and forestry with *Pinus halepensis* Mill. as the prevailing forest vegetation type, although there are also forest stands dominated by *Populus x canadensis*. It is a very sparsely populated area, with the near towns being Ardisa, Biscarrués, and the main municipality, Ayerbe. Some areas of this sector were affected by two wildfires in 1991, burning approximately 600 hectares in total.

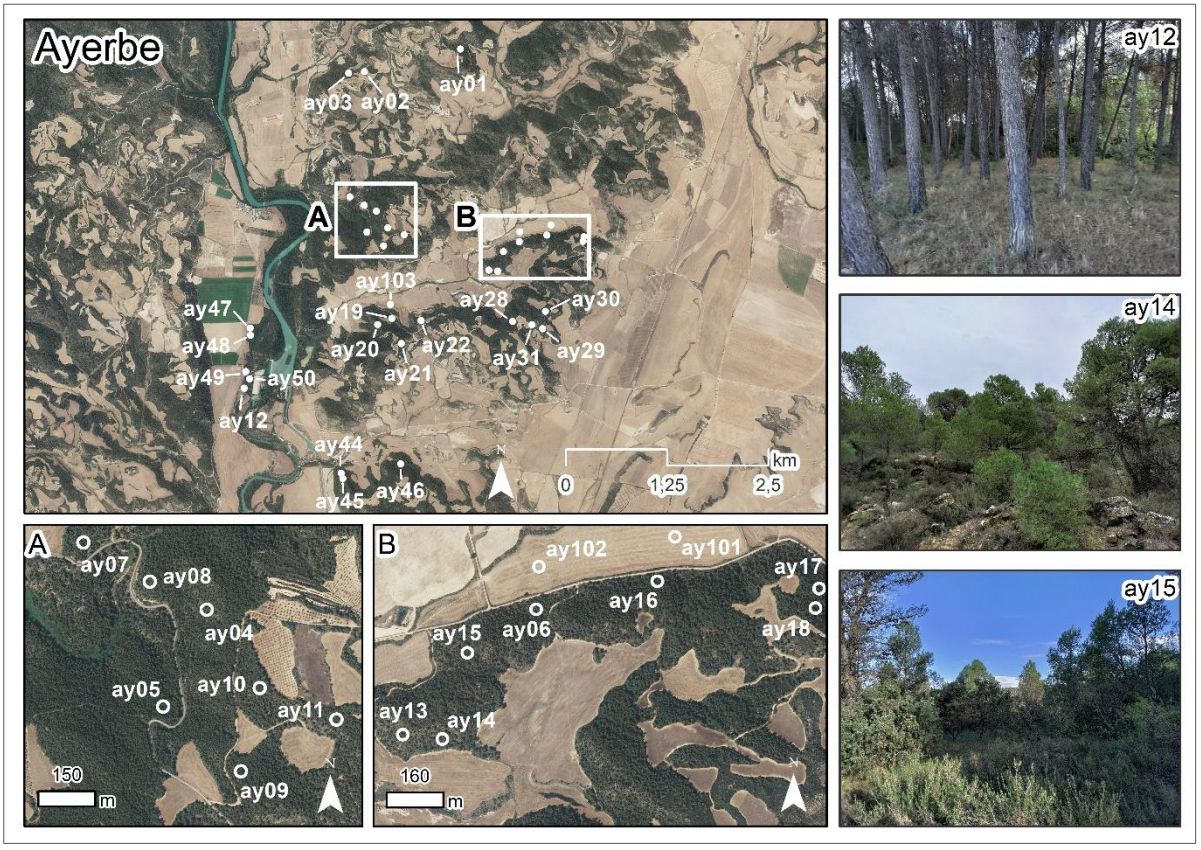

Figure 2.3. Location of the 36 forest plots (white dots) of the Ayerbe sector, detailed location of 16 plots from two areas, and photographs of three forest plots: *ay12*, *ay14*, and *ay15*.

Uncastillo

The Uncastillo sector is positioned in the northwest of Aragon, nestled in the foothills of the Pre-Pyrenees, yet still within the bounds of the Ebro Valley. It encompasses a total of 11 forest plots, with the majority having a 15-m circular radius, except for one of 5-m due to terrain constraints (plot *un14*) (Figure 2.4).

With an altitudinal range spanning from 500 to 800 m a.s.l., the terrain is generally rugged. Land uses are dedicated primarily to agriculture and forestry. Prevailing vegetation type is *Pinus halepensis* Mill., *Juniperus oxycedrus* L., and *Pinus nigra* L. The area is sparsely populated, with the nearest towns being Castiliscar and Uncastillo. This sector was affected by a large forest fire in 1994, which burned a total of 8,000 hectares. Consequently, some forest plots still consist of young growth, with extremely dense tree populations, while others, where regeneration has been less successful, are dominated by low to high shrublands.

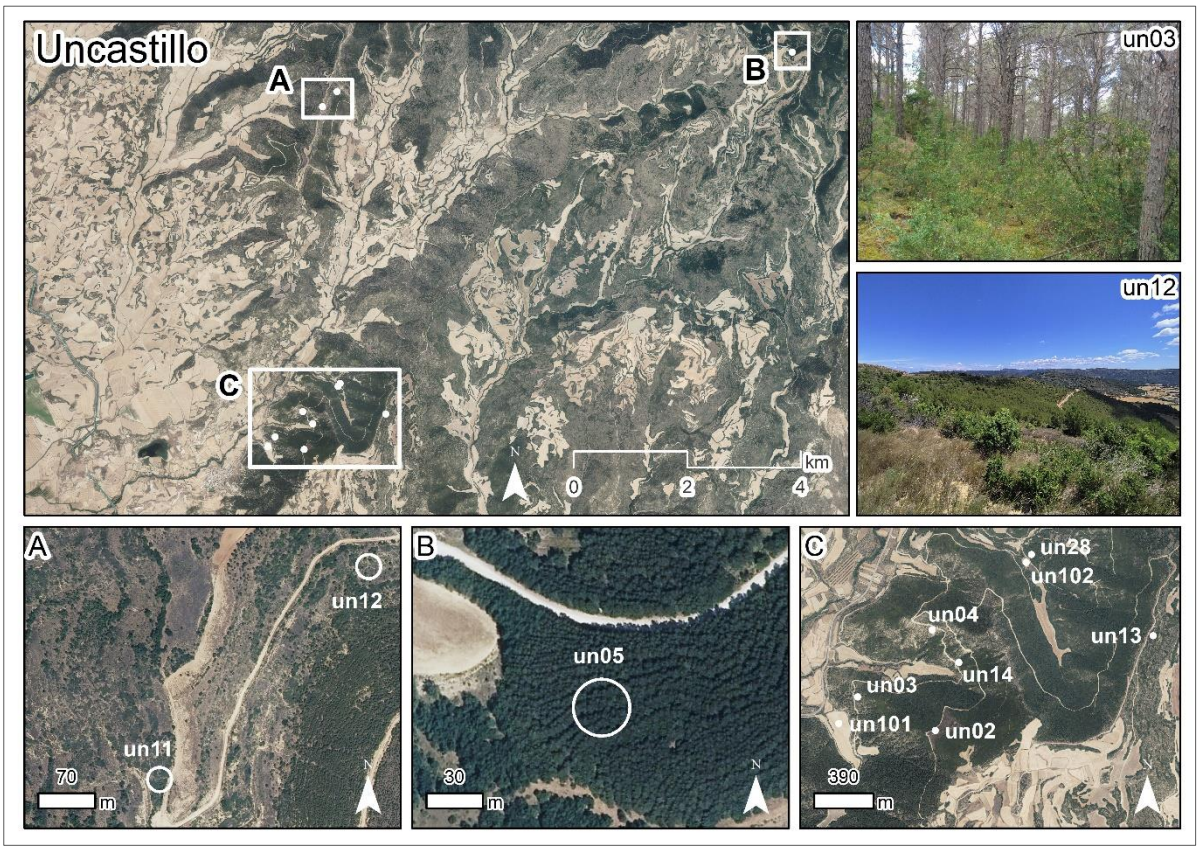

Figure 2.4. Location of the 11 forest plots (white dots) of the Uncastillo sector distributed in the three study areas and photographs of two forest plots: *un03* and *un12*.

Villarluengo

The Villarluengo sector is situated in the southeast of Aragon, in the Iberian Range. It comprises 16 forest plots of 15-m circular radius (Figure 2.5). Six of these plots are located in the province of Castellón, within Valencian Community, but very close to Aragon. This area is characterized by rugged topography, with elevations ranging from 540 to 1,500 m a.s.l. The current relief is a result of differential erosion processes acting on various lithologies, primarily karst formations, alongside tertiary and quaternary sandstone and

clays. Predominant land uses include forests of *Pinus halepensis* Mill. and *Pinus nigra* L., agriculture, and livestock farming. With very low population density, the principal inhabited areas include the small towns of Castellote, Tronchón, Bordón, and Olocau del Rey. This sector was severely affected by a massive forest fire in 1994, consuming 29,000 hectares. As a consequence, coupled with the high average altitude of this sector, some forested areas are characterized by shrubs and low trees.

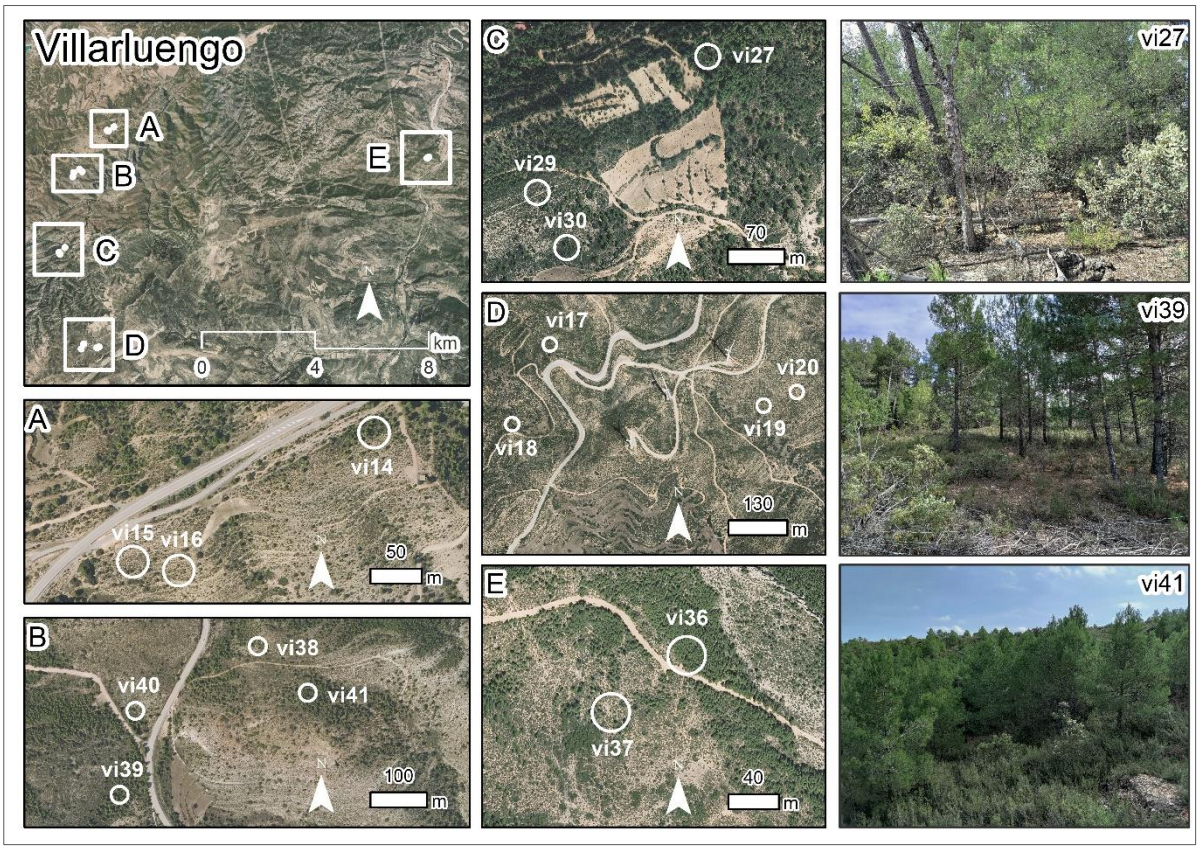

Figure 2.5. Location of the 16 forest plots (white dots) of the Villarluengo sector distributed in the five study areas and photographs of three forest plots: *vi27*, *vi39*, and *vi41*.

Zuera

The Zuera sector lies on the center of the Ebro Valley, characterized by significant daily and annual thermal contrasts and scarce rainfall. It comprises a total of 9 forest plots, most of 15-m circular radius, with one plot being of 10-m circular radius due to terrain limitations (plot *zu38*) (Figure 2.6). Additionally, the sector contains 59,554 footprints of approximately 25-m diameter from GEDI SLS system intersecting the area (as of February 2022). Most of this sector falls within the Military Training Center "*San Gregorio*", under the jurisdiction of the Ministry of Defense of Spain. The prevailing vegetation consists of grassland, along with low and medium shrubs. Out of the military area, the north

and northeast of the sector is designated as a Site of Community Importance and Special Protection Area (*ZEPA "Montes de Zuera, Castejón de Valdejasa y El Castellar"*) within the European register of protected areas of the Natura 2000 network. The topography ranges from 300 to 750 m a.s.l., featuring flat lands in the south and rugged terrain in the northern part, aligning with the Zuera Mountains. Beyond the CENAD boundaries, the predominant land use is forest dominated by *Pinus halepensis* Mill. and high shrubs, with little areas dedicated to agriculture and minimal human settlements. This sector has been the subject of several significant forest fires, occurring in 1995 (3,800 hectares burned), 2008 (2,500 hectares burned), and 2009 (7,000 hectares burned).

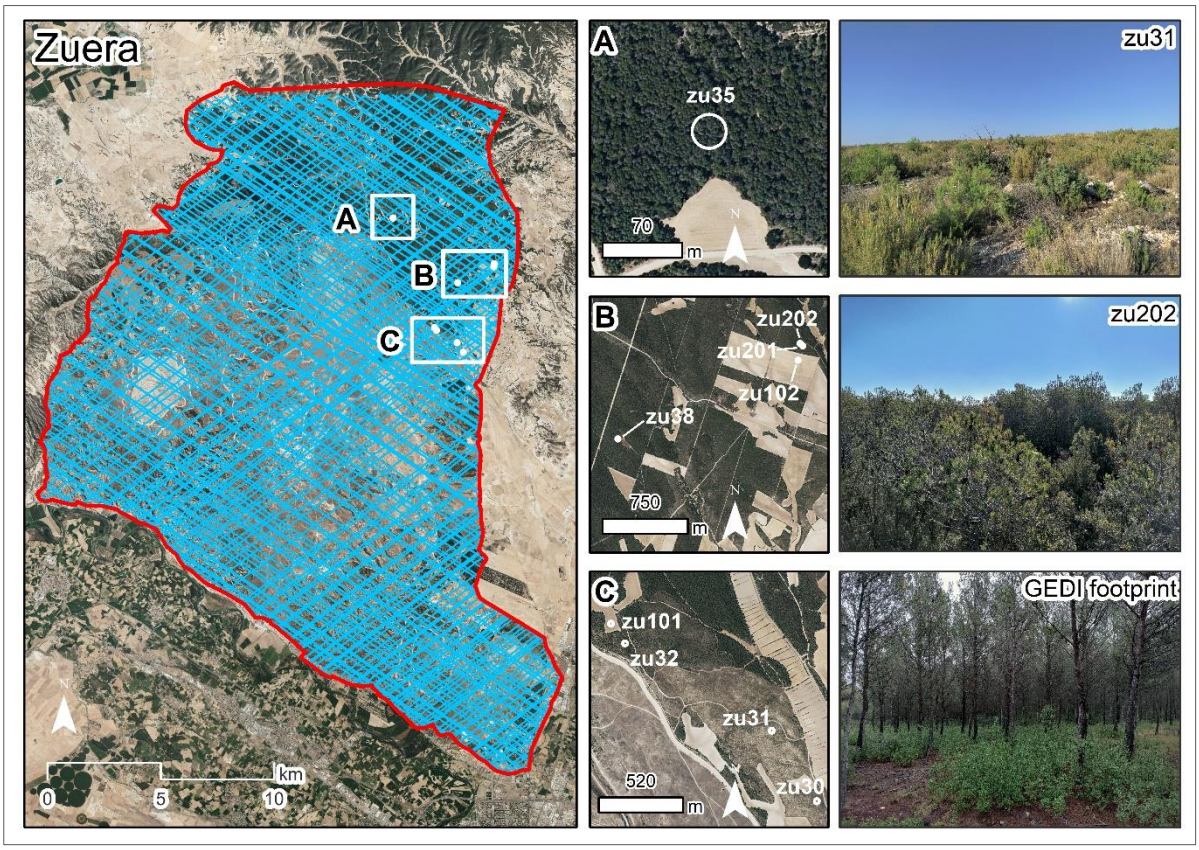

Figure 2.6. Location of the 9 forest plots (white dots) of the Zuera sector distributed in the three study areas, limits of the sector (red line), GEDI footprints intersected (blue dots), and photographs of plots *zu31*, *zu202*, and of a GEDI footprint.

2.2. THE PROMETHEUS FUEL CLASSIFICATION

The Prometheus fuel classification system (Prometheus, 1999) was developed in the 1990s by European scientists. It simplifies and adapts de NFFL classification to Mediterranean conditions (Arroyo *et al*., 2008), considering the height and density of vegetation as the primary factors influencing fire propagation. It

comprises seven fuel types, divided into three main fire carriers: grass, shrubs, and trees (Figure 2.7).

- Fuel type 1: grass and herbaceous fuels.
- Fuel type 2: low shrub fuels (up to 0.60 m).
- Fuel type 3: medium shrub fuels (up to 2 m).
- Fuel type 4: high shrub fuels (up to 4 m).
- Fuel type 5: tree fuels without understory.
- Fuel type 6: tree fuels with understory but no continuity to canopy.
- Fuel type 7: tree fuels with full continuity between understory and canopy.

In addition to these fuel type characteristics, shrub types must contain more than 60% shrubs cover and may include trees, but not exceeding 50% cover. Likewise, fuel type 5 must have less than 30% shrub vegetation cover, in contrast to types 6 of 7. For fuel type 6, the average distance between the undergrowth and the canopy must be approximately 0.50 m.

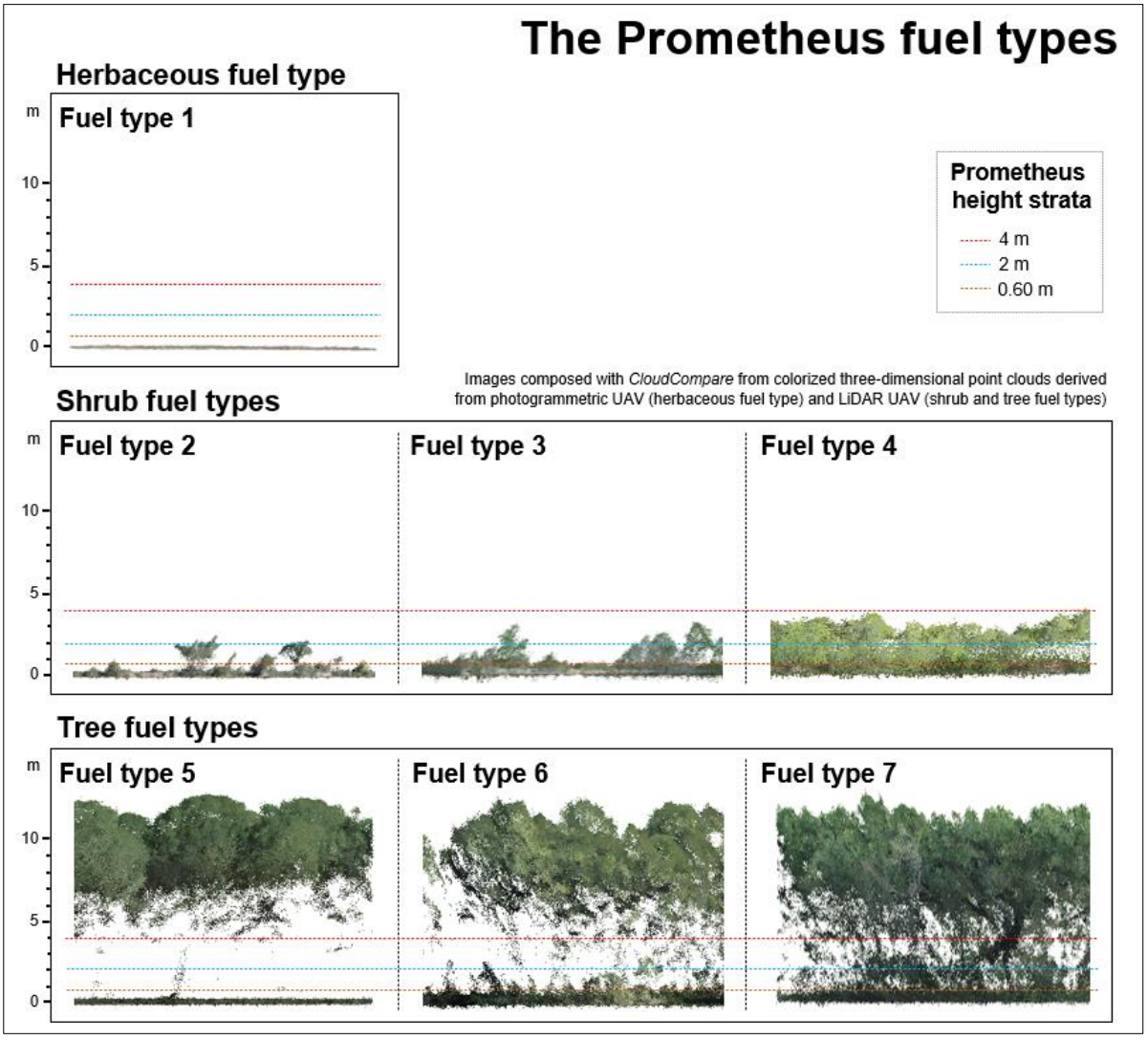

Figure 2.7. Graphic diagram of the seven fuel types of the Prometheus classification.

This PhD Thesis has relied on the Prometheus fuel types as it is adapted to the fuels found in Mediterranean environments (Arroyo *et al*., 2008). Numerous studies have employed the Prometheus classification to identify fuels in Mediterranean forests using a wide range of techniques (e.g., Riaño *et al*., 2002; Arroyo *et al*., 2006; Lasaponara *et al*., 2006; Mitri *et al*., 2011; Domingo *et al*., 2020; García-Cimarras *et al*., 2021). In order to identify the fuel types, in Chapters 3, 4, and 6 machine learning-based classification models were employed, while in Chapter 5 fuel volume was quantified at very high spatial resolution. In all cases, it was necessary to build a ground-truth based on the predominant fuel type observed in each forest plot to assess the accuracy of the remote sensing system in classifying the fuel types. The ground-truth was established using two methods: direct observation in the field for Chapters 4, 5, and 6, and fuel type maps derived from previous studies for Chapter 3. For field observations, a *Leica VIVA*® GS15 CS10 GNSS real-time kinematic Global Positioning System with sub-meter accuracy was used to establish the central point of each forest plot. This allowed defining the plot boundaries and conducting the visual analysis. On the other hand, the fuel type maps were used to construct the ground-truth for the GEDI footprints, considering the large number of footprints within the study area and the observed uncertainty in their geolocation (Shannon *et al*., 2023; Tang *et al*., 2023). Thereby, two classification models of Prometheus fuel types conducted in the same study area by Montealegre *et al*. (2015) and Revilla *et al*. (2021) were utilized. The first study mapped the classification results, while for the second, the map had to be derived from the outcomes of the classification model. Given the inherent uncertainty of both classification models, only the fuel types that were spatially coincident in both studies were used. Further details on the generation of this ground-truth can be found in Chapter 3.

2.3. REMOTE SENSING MAIN SOURCES

The evaluation of the main remote sensing systems was performed using three primary platforms: satellites, unmanned aerial vehicles (UAVs) and ground-based platforms. The GEDI SLS system was assessed in Chapter 3 both independently and in combination with Landsat-8 OLI optical imagery. Two types of UAVs were evaluated: in Chapter 4 a fixed-wing optical UAV (*eBee Classic* of SenseFly), equipped with two sensors (*SONY-WX* RGB camera and *Parrot Sequoia* multispectral sensor); and in Chapter 6 a quadcopter UAV (*DJI Matrice 300 RTK*), equipped with LiDAR sensor (*DJI Zenmuse L1*). Finally, in Chapters 5 and 6 the ground-based platform was a *GeoSLAM ZEB-Horizon*

HMLS system was assessed. The main characteristics of these instruments are outlined in the following sub-sections.

2.3.1. The Global Ecosystem Dynamics Investigation

GEDI is a SLS system developed by the University of Maryland (USA) in collaboration with NASA. The primary goal of GEDI is to advance the ability to characterize the effects of changing climate and land use on ecosystems (Dubayah *et al*., 2020). GEDI is attached to the Japanese Experiment Module-Exposed Facility (JEM-EF) on board the International Space Station (ISS). Launched in December 2018, the system commenced operations in April 2019 and continued until March 2023, when it was temporarily deactivated for recommissioning during 2024. GEDI's measurements are made between latitudes 51.6ºN and 51.6ºS and the instrument can be rotated on the JEM-EF by up to 6º (~40 km) on both sides of the ISS ground track to sample the Earth's surface as completely as possible and to avoid gaps due to clouds (Figure 2.8).

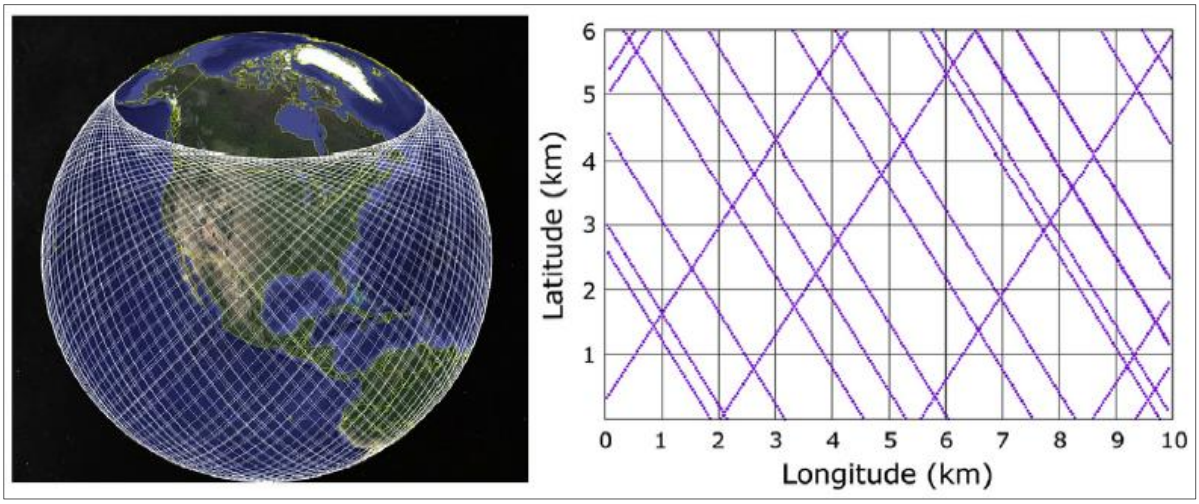

Figure 2.8. GEDI orbital tracks (left). Lines representing one track (right). Figure reproduced from Dubayah *et al*. (2020).

GEDI utilizes a full-waveform LiDAR system to quantify the vertical structure of vegetation by capturing the amount of laser energy backscattered by objects at different height intervals (i.e., tree canopies, plant stems, branches, or leaves) and by the surface. From these waveforms, several structural metrics of vegetation can be derived, such as forest canopy height, canopy vertical structure, and surface elevation (Drake *et al*., 2002; Tang *et al*., 2012; Dubayah *et al*., 2020). The system comprises three lasers emitting at 242 Hz in the near infrared (1064 nm), producing footprint transects of ~25 m diameter (Figure 2.9). Two lasers operate at full power (*power beams*), each one emitting two signals, while the remaining laser operates at half power (*coverage beam*),

emitting four signals. Therefore, there are a total of 8 signals collecting data simultaneously in the same transect, each signal being separated by ~600 m across the flight track direction within a ~4.2 km swath (Dubayah *et al.*, 2020). For each transect, the centroids of each footprint are separated by 60 m along track direction.

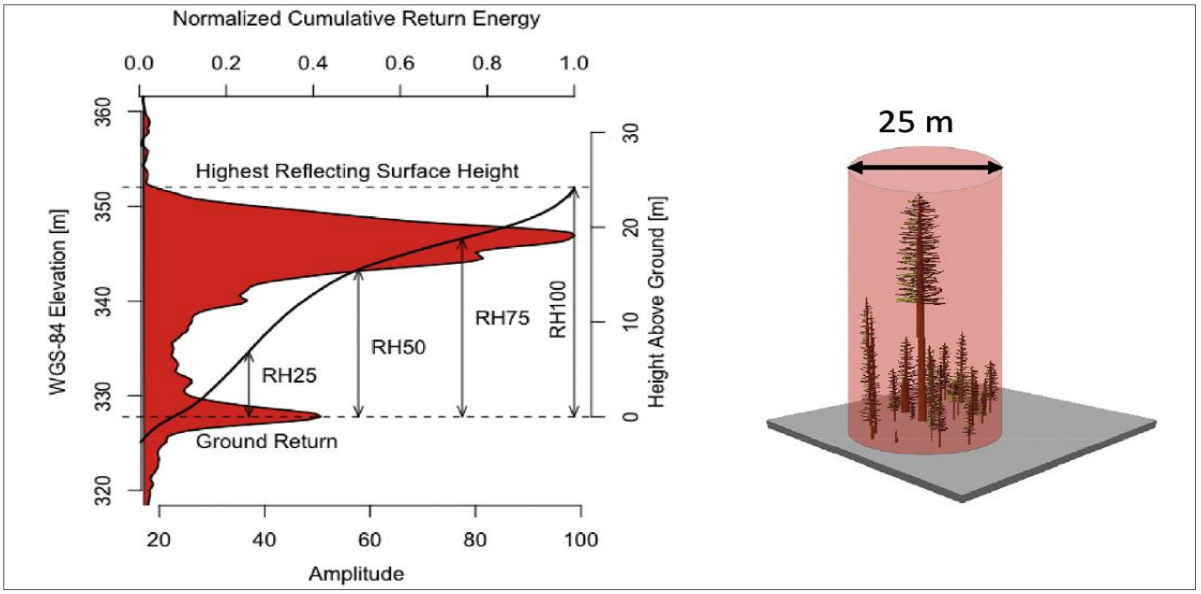

Figure 2.9. Graphical scheme of a typical waveform and footprint of the GEDI system. Figure reproduced from Dubayah *et al.* (2020).

Two version of GEDI data have been released to date; the second and final version until date was released in February 2022. Version 2 contains improvements in the LiDAR waveform processing algorithms and in the geolocation of the footprints. In version 1, a systematic spatial uncertainty of ~20 m was observed in 50% of the footprints (Shannon *et al.*, 2023), while in version 2 the error was reduced to ~10 m in 80% of the footprints (Tang *et al.*, 2023).

Different processing levels of GEDI data have been progressively published during the development of the mission. The Level-1A product (L1A: *TX/RX Transmitted/Received Waveform Fitted Parameters*) stands as the most basic level, containing the original raw waveforms and being the only data level not publicly available. The Level-1B product (L1B: *Geolocated Waveforms Data*) comprises all corrected and geolocated receive waveforms relative to the Earth's ellipsoid and provides the basis for the higher Level 2 products. In addition, this product allows users to apply their own waveform interpretation algorithms (Hofton and Blair, 2019). The Level-2 products have been processed using six different algorithm setting groups resulting from different processing of the L1B-derived corrected waveforms and noise thresholds (Hofton and Blair, 2019). However, it is recommended to use the default algorithm as it has been

designed to work in most cases (Roy *et al*., 2021). The Level-2A product (L2A: *Elevation and Height Metrics Data*) provides footprint-level L1B-derived data on terrain elevation, canopy top height, and relative vegetation height metrics divided in 100 height intervals or percentiles. Terrain elevation is obtained from the elevation of the center of the lowest detected mode of the receive waveforms (Hofton and Blair, 2019). Canopy top height and relative vegetation height metrics are computed by linear interpolation of the L1B geolocation data and then subtracting the heights from the terrain elevation, while relative height metrics are based on the receive waveforms cumulative products (Hofton and Blair, 2019). The Level-2B product (L2B: *Canopy Cover and Vertical Profile Metrics Data*) includes four canopy profile metrics: The *Plant Area Index* (PAI), the *Plant Area Volume Density* profile (PAVD), the *Foliage Height Diversity* index (FHD), and the *Total Canopy Cover* (TCC). PAI is a closely related concept of the *Leaf Area Index* (LAI) but incorporates all vegetation structural elements, such as branches or trunks, in addition to leaves (Tang and Armston, 2019). For the PAI formula (Eq. 2.1; Tang and Armston, 2019; Lin *et al*., 2023), *Pgap(θ)* represents the probability of the land surface being directly visible from the satellite platform in nadiral angle of incidence. PAVD is a function of plant area per unit volume obtained by GEDI, used to quantify the vertical structure of forests (Xi *et al*., 2022). FHD (Eq. 2.2; Tang and Armston, 2019) refers to the Shannon-Wiener diversity index (H'), measuring the complexity of canopy structure (Tang and Armston, 2019). Higher FHD values often results in more complex structure (James and Wamer, 1982; Bergen *et al*., 2009), which can be an accurate indicator of habitat quality for wildlife (MacArthur and MacArthur, 1961). Lastly, TCC (Eq. 2.3; Li *et al*., 2024) describes the percentage of the ground covered by all canopy structural elements (Tang and Armston, 2019; Lin *et al*., 2023).

$$PAI = \frac{-1\,[\ln(Pgap(\theta)) - \ln(Pgap(\theta))]}{G(\theta) \times \Omega(\theta)} \quad (2.1)$$

$$FHD = -\sum_i N_i \times \log(N_i) \quad (2.2)$$

$$TCC = \frac{R_v}{R_v + (\gamma_v / \gamma_g \times R_g)} \quad (2.3)$$

Where *PAI* is the Plant Area Index, *FHD* is the Foliage Height Diversity, *TCC* is the Total Canopy Cover, *Pgap* is the directional gap probability, θ is the nadir view angle, *G(θ)* is the spherical leaf angle distribution, $\Omega(\theta)$ is the random spatial distribution of canopy elements, N_i is the proportion of vertical LAI profile that lies in the i^{th} of the chosen horizontal layers, R_v and R_g are the pulse return energy of vegetation canopy and ground of a GEDI footprint, respectively, with a height threshold of 4 m, and γ_v/γ_g is the backscattering coefficient set as 1.5 over the globe (Tang and Armston, 2019).

The Level-3 product (L3: *Gridded Canopy Height Metrics and Variability Data*) is the next processing level of GEDI data. This product is spatialized to 1 km^2 grid based on the L2 product metrics, including terrain elevation, vegetation height, canopy cover, LAI, and vertical vegetation profiles, along with their associated uncertainties (Dubayah *et al*., 2020). Lastly, the highest processing level of GEDI data are Level-4A (L4A: *Footprint Above Ground Biomass Estimates*) and Level-4B (L4B: *Gridded Above Ground Biomass Estimates*) products. They represent the output of models derived from the L2 data products to estimate mean *Above Ground Biomass Density* (AGBD) (Dubayah *et al*., 2020) using calibration equations (Kellner *et al*., 2022). AGBD data are provided either at footprint level (L4A) and gridded in cells of 1 km^2 (L4B). The prediction of AGBD requires field estimates of aboveground biomass from allometric models in a given area (e.g., in forest plots). From remotely sensed data, empirical relationship to AGBD can be established (Drake *et al*., 2002; Lefsky *et al*., 2002), either with optical imagery (Foody *et al*., 2003), SAR (Saatchi *et al*., 2011), ALS (Næsset *et al*., 2013; Duncanson *et al*., 2015), or SLS systems (Lefsky *et al*., 2005). In this way, the prediction of the AGBD for GEDI was developed using 8,587 simulated GEDI waveforms associated with field estimates of AGBD in 21 countries (Kellner *et al*., 2022). The algorithm uses L2A-derived relative height metrics and 13 linear models to predict AGBD in 32 combinations of plant functioning types (Kellner *et al*., 2022).

Finally, it should be noted that GEDI footprints contain a series of metadata that indicate additional attributes of the recorded data, allowing users to discard footprints with unwanted attributes and high uncertainty. This is very useful as spaceborne LiDAR system waveforms are frequently impacted by cosmic, solar and atmospheric noise, disrupting the quality of the laser signal. The metadata that integrates several individual quality assessment parameters is "*quality_flag*" (Hofton and Blair, 2019), providing users a preliminary quality assessment of each GEDI footprint. In addition, the "*degrade_flag*" metadata indicates degraded state of pointing and/or positioning information, i.e., a high uncertainty in the footprint geolocation. According to Beck *et al*. (2021), the "*beam*" metadata identifies the signal recording the data, allowing to know whether it comes from lasers operating at full power (*power beams*) or at half power (*coverage beams*). In the case of the latter, they are not expected to penetrate dense forest, so in these cases it is recommended to filter they out and to use only the full power beams. The "*solar_elevation*" metadata indicates whether the data was recorded at day or night. It is recommended to filter the data recorded during day due to the negative impact of solar noise in the GEDI waveforms. Finally, the "*sensitivity*" metadata allow users to select the best data by using a

conservative threshold of 0.9 over land areas, and higher in dense forest conditions, otherwise the signal may not have the sufficient energy to penetrate through vegetation to the ground (Hofton and Blair, 2019). In this PhD Thesis, several quality filters were applied based on these metadata to work with footprints of lower uncertainty. Furthermore, an additional filter was generated due to the high uncertainty in the geolocation of the footprints, even in version 2 (Tang *et al*., 2023). This filter involved disregarding footprints with high land cover variability to ensure the homogeneity of the ground-truth within each footprint. A more detailed description of this process is provided in Chapter 3.

2.3.2. Optical unmanned aerial vehicle

The optical UAV assessed in the thesis was a fixed-wing UAV *eBee Classic*, developed by SenseFly SA (Cheseaux-sur-Laussane, Switzerland), a company of AgEagle Aerial Systems Inc. (Wichita, KS, USA). The complete system comprises the UAV itself, the *eMotion* v.3.5.0 software for flight preparation and post-processing management, a 2.4 GHz ground USB modem for radio data link between the UAV and *eMotion*, and two optical sensors (Figure 2.10).

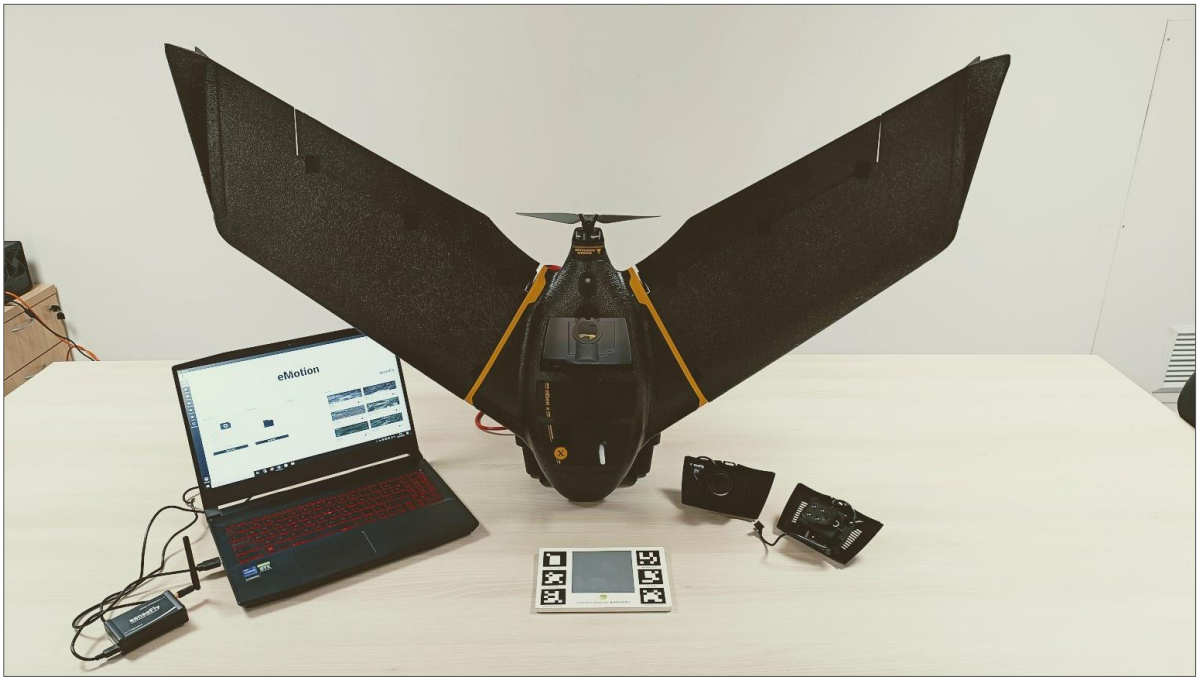

Figure 2.10. The *eBee Classic* full system: UAV unit (center), *eMotion* software and ground USB modem (left), *Airinov* reference target (center), and the two optical sensors (right).

The *eBee Classic* has a weight of 0.41 kg without camera and battery and a nominal take-off weight of 0.69 kg. The material is composed by expanded polypropylene foam, carbon structure and composite parts. The battery is a 3-cell Lithium-Polymer (LiPo) of 0.14 kg which enables a nominal average flight

time of about 35-40 minutes with standard camera. Propulsion is provided by electric brushless motor with nominal static thrust of 0.63 kgf and the nominal cruise speed is between 40-90 km/h. The UAV's wind resistance is up to 45 km/h and the maximum single flight coverage is 12 km^2. The absolute horizontal and vertical accuracy using only the UAV's GNSS signal is between 1 to 5 m and 2 to 5 m, respectively. The UAV consists of two main parts: the central body and a pair of detachable wings. The central body serves as the core of the UAV, housing all the electronic components. Internal components include the electric motor and the flight controller board, which incorporates the IMU system, barometer, geolocation system, and radio receiver. External components comprise the front propeller, antenna, pitot probe, LED status indicator, camera and battery compartments, ground sensor, and servo-connectors. The propeller generates thrust during flight. The antenna enables communication between the *eBee Classic* and the *eMotion* software via the ground USB modem. The pitot probe detects airspeed, wind and altitude. The status LED provides current status information of the UAV using different color indicators: blue during the initialization process, green when ready to fly, and red if preflight checks fail. The camera compartment accommodates the camera or sensor for data capture during flight. The battery compartment allows the insertion of one LiPo battery unit. The ground sensor consists of an optical sensor that detects the UAV's proximity to the ground. The pair of wings is connected to the central body through the union of its ailerons with the servo-connectors and two wing struts and clips to hold it in place. The ailerons also serve to control the *eBee Classic* during flight. Wings also include winglets, which add aerodynamic stability while it is in flight.

Two optical sensors, one RGB and one multispectral, were used to capture the data with the *eBee Classic* (Figure 2.10). The *SONY-WX* is an RGB camera of 18.2 MP resolution, which allows acquiring images in the visible spectrum. This enables the generation of two different products of very high resolution: aerial RGB orthophotographs and photogrammetric point clouds, the latter through the SFM photogrammetric technique. The *Parrot Sequoia* sensor is a multispectral camera, capable of capturing images at 1.2 MP in four different spectral bands: green (550 nm ±40 nm), red (660 nm ±40 nm), red edge (735 nm ±10 nm), and near infrared (790 nm ±40 nm). The camera includes an *Airinov* auxiliary reference target of known reflectance to calibrate each spectral band to the prevailing light conditions before each flight. To do this, four photos must be taken, one for each spectral band, pointing at the reference target, which must be free of any shadow. In addition, attached on the upper part of the camera is a sunshine sensor, used to calibrate the images during flight depending on the

incident light conditions of the moment. This allows comparing images at different times, as it eliminates the effect of light variations during image acquisition. Similar to the *SONY-WX* camera, the *Parrot Sequoia* allows generating two different products with lower resolution than RGB images: aerial orthophotographs in the four spectral bands and photogrammetric point clouds. Thus, this sensor enables the acquisition of multispectral images, which bands can be combined to produce multispectral vegetation indices. These indices provide additional insights into the condition of vegetation, such as vegetation health and biomass, chlorophyll content, photosynthetic activity, or moisture content, complementing the information provided by the three-dimensional point clouds.

2.3.3. LiDAR unmanned aerial vehicle

The UAV-LiDAR system consisted of a quadcopter UAV *DJI Matrice 300 RTK* and a *DJI Zenmuse L1* LiDAR sensor, both developed by Da Jiang Innovations (DJI), a commercial firm of Shenzhen DJI Sciences and Technologies (Shenzhen, China). The complete system comprises the UAV and the LiDAR sensor themselves and the *DJI Smart Controller Enterprise* controller, which includes the proprietary *DJI Pilot 2* software for automated flight mission preparation and UAV control management during flight (Figure 2.11).

Figure 2.11. The UAV-LiDAR full system: *DJI Matrice 300 RTK* UAV unit (center), controller (left), and *DJI Zenmuse L1* LiDAR sensor (right).

The *DJI Matrice 300 RTK* has a weight of 3.60 kg without camera and batteries and a nominal take-off of 9 kg. It consists of a single chassis formed by the central body, four frame arms, and two pairs of detachable landing gears. As in the case of the *eBee Classic*, the central body houses the UAV's main electronic components. The internal components include the IMU system, barometer, geolocation and geosensing systems, and radio receiver, and RTK (*Real Time Kinematic*) system. The external components consist of a first-person view RGB camera, infrared detection systems, auxiliary vision systems, two battery compartments, an air filter, lights, beacons, and a stabilizer connector where the sensor is attached. At the extremes of the four frame arms are located the propellers, motors, light indicators of the UAV status, transmission antennas and the RTK system. The mechanical power is generated by two LiPo batteries working together, each weighing approximately 1.35 kg. Propulsion is provided by four propellers positioned on each of the UAV's frame arms. Maximum speeds reach 21.6 km/h (6 m/s) during ascent, 25.2 km/h (7 m/s) during descent, and 82.8 km/h (23 m/s) horizontally. The UAV can withstand maximum wind speeds of up to 54 km/h. Under standard conditions, it can fly for approximately 45 minutes.

The *DJI Zenmuse L1* sensor integrates a LiDAR LIVOX™ module, an IMU system, and an RGB camera on a 3-axis stabilizer that is connected to the UAV through the stabilizer connector and allows the sensor to be pointed both in nadiral and frontal 360º view. The sensor has a weight of 930 g (±10 g) and includes various external components, such as visual positioning sensor, memory card slot, and pan, tilt and rotation motors. It operates in the near infrared wavelength (905 nm) with a maximum scanning frequency up to 240,000 points/s and laser divergence of 0.03º horizontally and 0.28º vertically. It can capture up to three returns on a single laser point.

The RTK module integrated in the UAV is a positioning augmentation system based on GNSS reference ground stations, enabling planimetric accuracies of up to 0.30 m. It establishes connection via the Internet between the GNSS system and a network of nearby geodetic reference stations, which have precise coordinates of their location based on geodetic techniques. In Aragon, there are two network available for free public access: the permanent GNSS station network of the Spanish National Geographic Institute and the active geodesy network of the Spatial Knowledge Infrastructure of Aragon. GNSS satellites are also estimating the location of the reference stations, allowing to compare it with the real location and thus to calculate the mean error of the satellite position estimation, which is transmitted back to the GNSS systems. Consequently, the error in the position estimation is minimized and sub-meter accuracies can be

achieved for the location of the forest plots without the need to use ground control points (GCPs) for indirect georeferencing of the data.

2.3.4. Handheld mobile laser scanner system

The HMLS system utilized was a *GeoSLAM ZEB-Horizon*, developed by GeoSLAM Ltd. (Ruddington, UK), a firm integrated in FARO® Technologies Inc. (Lake Mary, FL, USA). The full system comprises the HMLS unit itself, the *ZEB-Horizon* real-time datalogger, and the proprietary *GeoSLAM Connect* v.2.3.0 software (Figure 2.12).

Figure 2.12. The *GeoSLAM ZEB-Horizon* full system, including HMLS unit (above-right) and ZEB-Horizon real-time datalogger (below-left).

The HMLS unit and the real-time datalogger work together as the latter provides power to the HMLS and serves as the storage location of the recorded data. The HMLS unit is equipped with a LiDAR sensor that collects data in the near infrared wavelength (903 nm) mounted on a 360º rotating motor. The scanning rate of the LiDAR is 300,000 points/s, with a maximum range of 100 m. The system relies on an IMU unit for georeferencing the data in local coordinates. This demands the use of GCPs for the transformation of local coordinates to a coordinate reference system. The HMLS unit employs SLAM technology for simultaneous 3D localization and mapping, integrating data from the LiDAR and IMU to generate the three-dimensional point cloud. Power from the datalogger

to the HMLS unit is supplied through a connecting cable. However, for data collection and storage, communication between the HMLS unit and the datalogger is done via network connection using a device such as a laptop, tablet, or cell phone. The connection can be either wired or wireless via Wi-Fi. To do this, the datalogger acts as an access point with a predetermined IP address that can be accessed from any of the aforementioned devices. This enables real-time data collection and storage, and additionally allows users to visualize the captured data in real time. The collected data can then be transferred from the datalogger to an external device for further post-processing using a USB storage device. The data collection process must be in loop closure format, that is, the start and end of the scan must coincide at the same point. In addition, manufacturer recommend a walking speed relatively slow in order to capture the environment in detail. The proprietary *GeoSLAM Connect* v.2.3.0 software (FARO® Technologies Inc., Lake Mary, FL, USA) facilitates preliminary processing of the captured data. Its primary function is to convert the raw data into standardized files (i.e., in *las* format) for further processing with other typical LiDAR point cloud processing tools. Additionally, the software supports georeferencing of the data by transforming the recorded local coordinates into a coordinate reference system.

2.4. REMOTE SENSING ANCILLARY DATA

The evaluation of the GEDI SLS system and the optical UAV was supported by ancillary data from passive and active sensors, respectively. For GEDI, its integration capability with Landsat-8 OLI optical images to improve the identification of fuel types was verified, building upon successful outcomes reported in prior studies related to different forest attributes analyses (e.g., Saarela *et al*., 2018; Potapov *et al*., 2021; Francini *et al*., 2022; Shendryk, 2022). For its part, point clouds from the optical UAV were combined with publicly available ALS-LiDAR data from the Spanish PNOA (*National Plan for Aerial Orthophotography*) project. This approach was chosen due to observed limitations in the ability of photogrammetric point clouds to generate accurate DEMs (Wallace *et al*., 2016; White *et al*., 2016; Guerra-Hernández *et al*., 2018; Salach *et al*., 2018; Cao *et al*., 2019; Lamping *et al*., 2021) and thus to convert absolute point cloud height (in m a.s.l.) to relative heights above ground (in m a.g.l.).

The Landsat-8 system captures systematic images of Earth's land cover. It is part of NASA's Landsat program which has monitored Earth's surface continuously since the launch of the first Landsat satellite (*Earth Resources Technology*

Satellite, ERTS-1) in 1972. Landsat-8 was launched into orbit in 2013 and includes two instruments: the multispectral sensor OLI (*Operational Land Imager*) and the thermal sensor TIRS (*Thermal Infrared Sensor*). The system orbits sun-synchronously in a polar direction at an altitude of 705 km and a period of revolution of 99 minutes (i.e., ~14.5 orbits/day). The orbital configuration ensures systematic data collection from the same point of the Earth's surface in scene sizes of 185 km cross-track by 180-km along-track. There are different processing levels for Landsat images. The highest level is the *Precision and Terrain Correction* (L1TP) product, which uses GCPs for geodetic and radiometric correction and DEMs from different sources (e.g., WorldView, CDEM, or NASADEM, among others) for topographic displacement correction. The *Systematic Terrain Correction* (L1GT) product has a lower level of processing and provides systematic, radiometric, and geometric accuracy along with DEMs for topographic displacement corrections. Lastly, the *Systematic Correction* (L1GS) product is created when the location accuracy is insufficient to apply terrain corrections, being the product with the lowest level of processing. The OLI images are acquired across several bands of the electromagnetic spectrum (Table 2.1). The combination of the different spectral bands enabled the generation of a set of multispectral vegetation indices used for integration with GEDI data using the L1TP product.

Table 2.1. Landsat-8 OLI spectral bands. Spatial resolution for all bands is 30 m except band 8 "Panchromatic" which is 15 m.

Name	**Wavelengths (µm)**	**Description**
Band 1	0.435 – 0.451	Coastal/Aerosol
Band 2	0.452 – 0.512	Blue
Band 3	0.533 – 0.590	Green
Band 4	0.636 – 0.673	Red
Band 5	0.851 – 0.879	Near-infrared (NIR)
Band 6	1.566 – 1.651	Short-wave-infrared-1 (SWIR-1)
Band 7	2.107 – 2.294	Short-wave-infrared-2 (SWIR-2)
Band 8	0.503 – 0.676	Panchromatic
Band 9	1.363 – 1.384	Cirrus

The PNOA project, developed by the National Geographic Institute of Spain, is a national initiative aimed at acquiring high-resolution orthophotographs, generating high-resolution DEMs, and capturing discrete-return ALS-LiDAR

data across the entire territory of Spain. PNOA was established in the framework of the INSPIRE Directive (Directive 2007/2/CE: *Infrastructure for Spatial Information in Europe*). The first national ALS-LiDAR coverage was carried out between 2008 and 2015 with an average density of 0.5 points/m^2. Despite the low point density, several studies demonstrated the usefulness of these data for various forestry applications. These include modeling canopy fuel variables (González-Ferreiro *et al*., 2014), mapping forest structural types (Ruiz *et al*., 2016); estimating biomass losses and carbon emissions in Aleppo pine forests (Domingo *et al*., 2017), and assessing carbon emissions in the event of fire in Mediterranean pine forests (Montealegre *et al*., 2017). The LiDAR-PNOA data are provided in 2x2 km tiles in both standardized *laz*/*las* formats with basic preprocessing, including geometric quality control of the point cloud and flights, transformation of ellipsoidal heights to orthometric heights, automatic classification of the point cloud, and other processes to facilitate visualization and interpretation of the point clouds. The horizontal and vertical accuracy after the preprocessing is <30 cm (1 sigma) and <20 cm (1 sigma), respectively, although higher errors may occur in dense vegetation and steep slope areas. The integration of PNOA data with the point clouds obtained from the optical UAV corresponds to the second national ALS-LiDAR coverage, conducted between 2015 and 2023 with an average density of 1 point/m^2. From these data, DEMs were generated at three different spatial resolutions (0.50 m, 1 m, and 2 m) to convert the absolute heights of the photogrammetric point cloud to relative heights above the ground. Using different spatial resolutions of the DEM allowed for evaluating the effect of resolution on the accuracy of generating structural variables and, consequently, identifying fuel types.

2.5. POINT CLOUD PROCESSING

The processing of point clouds from both discrete-return LiDAR systems and photogrammetric processes for forestry applications follows a typical workflow to ensure the quality of the obtained data. As shown in Figure 2.13, these steps include: i) removing outliers; ii) filtering points corresponding to the ground, iii) generating DEMs from points classified as ground, iv) converting absolute heights to heights relative to the ground, and v) generating metrics and variables that can be related to the structure, texture, or volume of forest vegetation, among others. This set of variables will ultimately serve as input to identify fuel types.

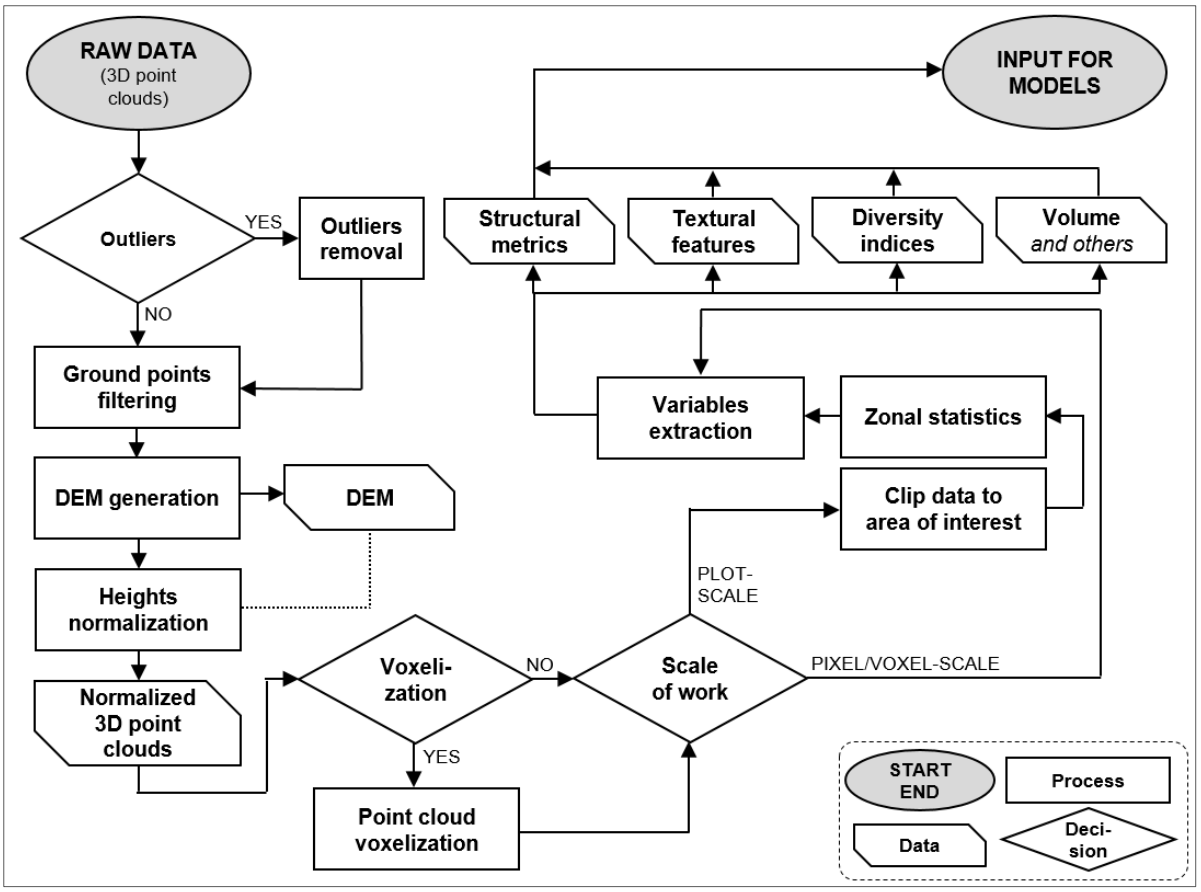

Figure 2.13. Typical workflow for the processing of three-dimensional point clouds obtained from remote sensing techniques to derive vegetation-related variables.

Likewise, there are a wide range of tools for processing LiDAR and photogrammetric point clouds. In this thesis, the R environment (R Core Studio, 2022) facilitated spatial analysis and processing of three-dimensional remote sensing data through functions embedded in specialized packages or libraries, such as *lidR* (Roussel and Auty, 2022) and *VoxR* (Lecigne *et al*., 2018). In addition, the *FUSION/LDV* v.4.21 software (McGaughey, 2021), developed by the Pacific Northwest Research Station of the USDA Forest Service, was mainly used to extract the metrics from both LiDAR and photogrammetric processed point clouds. These two tools are able to operate at any step of the point cloud processing workflow, while other tools are specialized in specific steps of the workflow. The *MCC-LiDAR* v.2.1 tool (Evans and Hudak, 2007) is especially designed to classify ground points using the *Multiscale Curvature Classification* (MCC: Evans and Hudak, 2007) algorithm. Nevertheless, MCC is also available in the *lidR* package for R. Finally, it should be noted that while LiDAR systems directly provide three-dimensional point clouds, generating photogrammetric point clouds requires an additional first step: the conversion of two-dimensional images with a high degree of overlap into three-dimensional point clouds. This is typically achieved through the SFM algorithm, implemented in several

photogrammetric programs. In this thesis, the proprietary software *PIX4Dmapper* v.4.5.6 (PIX4D SA, Prilly, Switzerland) was used for this purpose, given the successful results provided in previous forest-related studies (e.g., Guerra-Hernández *et al*., 2017; Malambo *et al*., 2018; Cao *et al*., 2019).

The first step in processing three-dimensional point clouds is to remove potential outliers, i.e., artifacts mainly caused by sensor errors, issues with the emitted and returned laser pulse, or interactions with unwanted elements such as suspended atmospheric particles, birds, or insects. These factors can result in abnormally high elevation measurements compared to the rest of the point cloud heights. In addition, points with negative height values may occur due to photon scattering within a returned pulse. This scattering increases the return time of the emitted laser pulse to the sensor, inflating the perceived distance traveled and causing a measurement error where the surface is recorded lower than the surrounding measurements (Evans and Hudak, 2007). Therefore, the first step involves identifying and removing out outliers. There are several techniques implemented in the processing programs for this purpose, such as the "filter noise" function in *lidR*, the "lasnoise" tool in *LasTools* (rapidlasso, GmbH), or the SOR (*Statistical Outliers Removal*) filter available in *VoxR* or *CloudCompare*. All these techniques enable to filter out points labeled as outlier or when a point's average distance from its nearest neighbors is significantly greater than the average distance among neighboring points, allowing the workflow to continue from a clean and error-free point cloud.

Identifying ground points is a crucial step in the point cloud processing workflow because it allows for the creation of DEMs, which are essential for subsequent height normalization and accurate extraction of height metrics. According to Roberts *et al*. (2019), there are five major categories of ground point filter algorithms: slope-based, mathematical-morphology-based, surface-based, segmentation-based, and deep-learning-based. All algorithms offer accurate results in non-complex areas. However, rough terrain, steep slopes, and complex forest stands present more of a challenge, as points can be more easily confused with the lower parts of vegetation and vice versa (Sithole and Vosselman, 2004). Following the categories and descriptions given by Roberts *et al*. (2019), slope-based algorithms, such as the *Modified Slope-Based Filter* (MSBF: Vosselman, 2000) and those developed by Sithole and Vosselman (2001) or Wang and Tseng (2010), assume that variations in terrain slope will be gradual based on local neighborhood calculations, while changes between ground and other elements (e.g., vegetation) will be comparatively larger. Mathematical-morphology-based algorithms like the *Progressive Morphology Filter* (PMF: Zhang *et al*., 2003) or the *Simple Morphological Filter* (SMRF: Pingel *et al*., 2013) classify ground

points based on height differences with local minima and maxima. These algorithms are sometimes combined with other filtering techniques, such as slope-based methods (Roberts *et al.*, 2019). Surface-based algorithms are subdivided into three types: interpolation-based, TIN-based, and active shape models. Interpolation-based algorithms, which include the Kraus and Pfeifer (Kraus and Pfeifer, 1998), the MCC (Evans and Hudak, 2007), and the *Multiresolution Hierarchical Classification* (MHC: Chen *et al.*, 2013) algorithms, iteratively densify ground points to gradually generate a surface representing the terrain. TIN-based (or *Triangulated-Irregular-Network*-based) algorithms classify ground points based on user-set slope and distance thresholds, such as the Axelsson algorithm (Axelsson, 2000). The *Cloth Simulation Filter* (CSF: Zhang *et al.*, 2016) is an active shape model algorithm that uses a membrane that floats to the surface of the point clouds and attaches points representing the ground based on user-defined cloth rigidness and resolution parameters. Segmentation-based algorithms cluster points based on a minimum elevation threshold within the neighborhood of points. Examples include the algorithms developed by Filin and Pfeifer (2006) or the *Segmentation-Based Filter* (SBF: Lin and Zhang, 2014). Finally, novel deep-learning-based algorithms utilize neural networks to filter out ground points. Examples of these methods include VoxNet (Maturana and Scherer, 2015), PointNet (Qi *et al.*, 2017a), PointNet++ (Qi *et al.*, 2017b) or PointCNN (Li *et al.*, 2018), among others.

Once the points corresponding to the ground have been filtered, DEMs are generated. For this, three main interpolation techniques are typically used: The *Inverse Distance Weighting* (IDW), the *Triangulated Irregular Network* (TIN), and kriging-based methods. IDW assigns weights to nearby points based on their distance to the interpolated location. TIN creates DEMs by connecting the ground points into a network of triangles, ensuring that each triangle is as close as possible to the original points. Kriging are spatial inference methods that use statistical techniques to estimate values at unknown locations based on the values of nearby points. Each interpolation technique has its own set of advantages and disadvantages. TIN interpolation is known for being fast and generating accurate DEMs (Guo *et al.*, 2010; Montealegre *et al.*, 2015; Adedapo and Zurqani, 2024). However, it may struggle with accuracy at the edges of the dataset where there are fewer points to triangulate. IDW tends to produce fewer errors at the edges, but it can be computationally more intensive and time-consuming than TIN. Kriging is the slowest and the most computationally demanding of the three interpolation methods, thus it is recommended for small areas where high accuracy is the primary consideration (Guo *et al.*, 2010). In this PhD Thesis,

DEMs were generated using the TIN interpolation method because it provides accurate models. Additionally, since the DEMs were created for the entire study areas recorded with the UAVs and HMLS systems, there were no issues with edge artifacts, as DEMs were subsequently clipped to the boundaries of the forest plots.

2.6. INDEPENDENT VARIABLES EXTRACTION

2.6.1. Point cloud-derived variables

The main purpose of the generation of DEMs in forestry is the normalization of vegetation heights, that is, the conversion of point clouds absolute heights (in m a.s.l.) to relative heights based on the terrain (i.e., on the generated DEMs). This facilitates the estimation of different parameters related to forest structure (e.g., shrub and tree height, fuel density across different height strata, canopy height and volume), vegetation canopy texture (e.g., canopy roughness, dissimilarity or variability), forest diversity indices, and fuel volume. The descriptor variables for these parameters can be generated at a pixel scale, with a specific spatial resolution, or at a zonal scale, such as forest plots, as in the case of the present thesis. In addition, the variables can be derived directly from the normalized point cloud (Chapters 4 and 6) or from its voxelization (Chapters 5 and 6), which involves transforming the point clouds into a set of three-dimensional voxels with a specified spatial resolution. Variables related to forest structure are typically derived from a set of structural metrics associated with the distribution of heights of vegetation, the variability of heights of vegetation, and the canopy cover density. Tables 2.2, 2.3 and 2.4 list and describe the structural metrics generated in the present PhD Thesis from the processed three-dimensional UAV point clouds, both photogrammetric (Chapter 4) and LiDAR (Chapter 6), using the *FUSION/LDV* software (McGaughey, 2021).

Table 2.2. List and description of the structural metrics related to the distribution of heights of vegetation generated for Chapters 4 and 6 using *FUSION/LDV*. x_i is the height value of the return, N is the total number of observations, r_i is the return, and p is the pulse. Adapted from Domingo (2019). Part 1 of 3.

Metric	Abbreviation	Description
Minimum elevation	Elev.mininum	x_i minimum.

Table 2.2. List and description of the structural metrics related to the distribution of heights of vegetation generated for Chapters 4 and 6 using *FUSION/LDV*. x_i is the height value of the return, N is the total number of observations, r_i is the return, and p is the pulse. Adapted from Domingo (2019). Part 2 of 3.

Metric	**Abbreviation**	**Description**
Mean elevation	Elev.mean	x_i mean elevation. $\mu_{x_i} = \frac{\sum_{i=}^{N} x_i}{N}$
Mode elevation	Elev.mode	x_i value more frequent in the plot.
Maximum elevation	Elev.maximum	x_i maximum.
Elevation quadratic mean	Elev.SQRT.mean.SQ	Generalized mean for the 2nd power. $M_2 = \left(\frac{1}{N}\sum_{i=1}^{n} x_i^2\right)^{\frac{1}{2}}$
Elevation cubic mean	Elev.CURT.mean.CUBE	Generalized mean for the 3rd power. $M_3 = \left(\frac{1}{N}\sum_{i=1}^{n} x_i^3\right)^{\frac{1}{3}}$
Percentiles of the heights 1, 5, 10, 20, 25, 30, 40, 50, 60, 70, 75, 80, 90, 95, and 99	Elev.P01, Elev.P05, Elev.P10, Elev.P20, Elev.P25, Elev.P30, Elev.P40, Elev.P50, Elev.P60, Elev.P70, Elev.P75, Elev.P80, Elev.P90, Elev.P95, Elev.P99.	Percentiles values are computed using the following method (McGaughey, 2021). $(N-1)P = I + f \left\{ \begin{matrix} I \text{ is the integer part of } (N-1)P \\ f \text{ is the fractional part of } (N-1)P \end{matrix} \right\}$ where N is the number of observation and P is the percentile value divided by 100. $if\ f = 0\ then\ Percentile\ value = x_{i+1}$ $if\ f > 0\ then\ Percentile\ value = x_{i+1} + f(x_{i+2} - x_{i+1})$ where x_i is the observation value considering that observations are ranked in ascending order.

Table 2.2. List and description of the structural metrics related to the distribution of heights of vegetation generated for Chapters 4 and 6 using *FUSION/LDV*. x_i is the height value of the return, N is the total number of observations, r_i is the return, and p is the pulse. Adapted from Domingo (2019). Part 3 of 3.

Metric	Abbreviation	Description
L-moments (λ_1 to λ_4)	Elev.L1, Elev.L2, Elev.L3, Elev.L4.	Product moments describe the characteristics of a distribution, being the most common moments the 1st (λ_1: mean), 2nd (λ_2: variance), 3rd (λ_3: skewness), and 4th (λ_4: kurtosis) (McGaughey, 2021). $\lambda_1 = \frac{1}{{}^nC_1}\sum_{i=1}^{N} X_{(i)}$ $\lambda_2 = \frac{1}{2}\times\frac{1}{{}^nC_2}\sum_{i=1}^{N}({}^{i-1}C_1 - {}^{n-1}C_1)x_{(i)}$ $\lambda_3 = \frac{1}{3}\times\frac{1}{{}^nC_3}\sum_{i=1}^{N}({}^{i-1}C_2 - 2^{i-1}C_1\,{}^{n-1}C_1 + {}^{n-1}C_2)x_{(i)}$ $\lambda_4 = \frac{1}{4}\times\frac{1}{{}^nC_4}\sum_{i=1}^{N}({}^{i-1}C_3 - 3^{i-1}C_2\,{}^{n-1}C_1 + 3^{i-1}C_1\,{}^{n-1}C_2 - {}^{n-1}C_3)x_{(i)}$ where $x_{(i)}$ $i=1, 2, ..., n$, are sample values ranked in ascending order and: ${}^mC_k = \left(\frac{m}{k}\right) = \frac{m!}{k!\ (m-k!)}$ is the number of combinations of any k items from m items and is equal to zero when $k > m$.

Table 2.3. List and description of the structural metrics related to the variability of vegetation generated for Chapters 4 and 6 using *FUSION/LDV*. x_i is the height value of the return, N is the total number of observations, r_i is the return, and p is the pulse. Adapted from Domingo (2019). Part 1 of 2.

Metric	Abbreviation	Description
Standard deviation	Elev.stddev.	Standard deviation of point height distribution. $\sigma = \sqrt{\frac{\sum_{i=1}^{N}(x_i - \mu)^2}{N}}$
Variance	Elev.variance	Variance of point height distribution. $\sigma^2 = \frac{\sum_{i=1}^{N}(x_i - \mu)^2}{N}$

Table 2.3. List and description of the structural metrics related to the variability of vegetation generated for Chapters 4 and 6 using *FUSION/LDV*. x_i is the height value of the return, N is the total number of observations, r_i is the return, and p is the pulse. Adapted from Domingo (2019). Part 2 of 2.

Metric	Abbreviation	Description
Coefficient of variation	Elev.CV	Coefficient of variation of point height distribution. $CV = \frac{\sigma}{\mu} \times 100$
Skewness	Elev.skewness	Skewness of point height distribution. $skewness = \frac{\sum_{i=1}^{N}(Y_i - \overline{Y})^3}{(N-1)s^3}$
Kurtosis	Elev.kurtosis	Kurtosis of point height distribution. $kurtosis = \frac{\sum_{i=1}^{N}(Y_i - \overline{Y})^4}{(N-1)s^4}$
Interquartile distance	Elev.IQ	Interquartile distance of point height distribution. $IQ = P_{75}(x) - P_{25}(x)$
Average Absolute Deviation	Elev.AAD	Average Absolute Deviation of point height distribution. It is a summary statistic of variability. $AAD = \frac{\sum_{i=1}^{N}(Y_i - \overline{Y})}{N}$
L-moments ratios corresponding to coefficient of variation ($\tau 2$), skewness ($\tau 3$), and kurtosis ($\tau 4$)	Elev.L.CV, Elev.L.skewness, Elev.L.kurtosis.	A more robust set of statistics presented by Hosking (1990), based on the method of L-moments. L-moments ratios provide statistics that are comparable to variance, skewness, and kurtosis (McGaughey, 2021). $\tau_2 = \frac{\lambda_2}{\lambda_1} \quad 0 < \tau_2 < 1$ $\tau_3 = \frac{\lambda_3}{\lambda_2} \quad -1 < \tau_3 < 1$ $\tau_4 = \frac{\lambda_4}{\lambda_2} \quad \frac{1}{4}(5\tau_{3^2} - 1) \leq \tau_4 < 1$

Table 2.4. List and description of the structural metrics related to the density of canopy cover generated for Chapters 4 and 6 using *FUSION/LDV*. x_i is the height value of the return, N is the total number of observations, r_i is the return, and p is the pulse. Adapted from Domingo (2019).

Metric	Abbreviation	Description
Percentage of first returns above a height-break, above the mean, or the mode	Percentage.first.returns. above.*height-break* Percentage.first.returns. above.mean Percentage.first.returns. above.mode	$PR_{first} = \frac{\sum_{i=1}^{N} r_{i\ first\ returns} > heightbreak}{\sum_{i=1}^{N} r_{i\ first\ returns}} \times 100$
Percentage of all returns above a height-break, above the mean, or the mode	Percentage.all.returns. above.*height-break* Percentage.all.returns. above.mean Percentage.all.returns. above.mode	$PR_{all} = \frac{\sum_{i=1}^{N} r_i > heightbreak}{N} \times 100$
Canopy relief ratio	Canopy.relief.ratio	Describes the degree to which canopy surfaces are in the upper or in the lower portions of the height range (Torresan *et al*., 2016). $CRR = \frac{\mu - x_{i\ minimum}}{x_{i\ maximum} - x_{i\ minimum}}$
All returns above a height-break, above the mean, or the mode × 100	All.returns.above.*height-break*..Total.all.first. returns..100 All.returns.above.mean.. Total.all.first.returns.. 100 All.returns.above.mode.. Total.all.first.returns.. 100	$AR_{all} = \frac{\sum_{i=1}^{N} r_{i\ all\ returns} > heightbreak}{\sum_{i=1}^{N} r_{i\ all\ returns}} \times 100$
Number of all returns within a given height-strata	All.returns.above.*height-break* Elev.strata.*height-strata*.total.return.count	$NR = \sum_{i=1}^{N} height_{x_u} \geq r_i > height_{x_l}$ where x_u is the upper height strata and x_l is the lower height strata.
Proportion of returns within a given height-strata	Percentage.returns. above..*height.break* Elev.strata..*height-strata*..return.proportion	$PR = \frac{\sum_{i=1}^{N} height_{x_u} \geq r_i > height_{x_l}}{N} \times 100$ where x_u is the upper height strata and x_l is the lower height strata.

In addition to structural metrics, three-dimensional point clouds enable the generation of variables related to vegetation textural characteristics. Texture captures several components of vegetation heterogeneity (Farwell *et al*., 2021) which may be important for explaining fuels variability and density. Textural analysis through remote sensing involves measuring the heterogeneity in pixel values within a given area (Zhou *et al*., 2017). In this thesis, texture variables were generated for Chapter 4 and defined as the heterogeneity in height values of the aerial parts of vegetation (i.e., tree canopy, and top of shrub and grasses) within the study forest plots. To achieve this, Canopy Height Models (CHMs) were first generated from the returns of the photogrammetric point clouds. Textural indices were then derived directly from the generated CHMs. Several methods exist to calculate vegetation texture using remote sensing techniques (Kupidura, 2019). For instance, Laplacian filters can detect rapid changes in image pixels. While their primary use is in edge detection, they are also effective in identifying textural changes in images (e.g., Ahearn, 1988; Faber and Förstner, 1999). Another method involves granulometric techniques introduced by Haas *et al*. (1967). Here, local granularity must be calculated at the pixel scale (Dougherty *et al*., 1992; Vincent, 1996) to generate a series of images that detect textural changes in the pixels (Kupidura, 2019). Nevertheless, for this PhD Thesis, the GLCM (*Gray Level Co-Occurrence Matrix*) method was employed. This approach, developed by Haralick *et al*. (1973) based on an original work by Julesz (1962), analyses image texture by quantifying the spatial distribution of pixels in a gray level co-occurrence matrix, establishing relationships between pixels of similar values. Haralick *et al*. (1973) proposed a set of textural features derived from the matrix, which quantify various textural properties of the images. The features generated for this PhD Thesis were: contrast, dissimilarity, entropy, homogeneity, mean, second moment, and variance (Table 2.5).

Table 2.5. Textural features from GLCM method generated for Chapter 4. *i* and *j* are the gray levels, *P(i,j)* is the value in the GLCM at position *(i,j)*, representing the frequency of occurrence of the pair of gray levels *i* and *j* in the specified spatial relationship. Part 1 of 2.

Feature	Description	Equation
Contrast	Measures the intensity of local differences in the image. It is high when there is a large difference in intensities between adjacent pixels.	$GLCM_c = \sum_{(i,j)} (i-j)^2 \times P(i,j)$
Dissimilarity	Sum of the weighted absolute differences between the pixel values. High dissimilarity values indicate greater differences between the neighboring pixels.	$GLCM_d = \sum_{(i,j)} \lvert i-j \rvert \times P(i,j)$

Table 2.5. Textural features from GLCM method generated for Chapter 4. *i* and *j* are the gray levels, *P(i,j)* is the value in the GLCM at position *(i,j)*, representing the frequency of occurrence of the pair of gray levels *i* and *j* in the specified spatial relationship. Part 2 of 2.

Feature	Description	Equation
Entropy	Measures the randomness in the texture of the image. It is high when the GLCM elements are uniformly distributed.	$GLCM_e = \sum_{(i,j)} P(i,j) \log P(i,j)$
Homogeneity	Measures the proximity of the distribution of elements in the GLCM to the diagonal of the matrix.	$GLCM_h = \sum_{(i,j)} \frac{P(i,j)}{1 + (i-j)^2}$
Mean	Measures the average of the summed values of the indices.	$GLCM_m = \sum_{k=2}^{2(N-1)} k \times P_{x+y}(k)$ where k is the sum of i and j indices (i.e., $k = i + j$), and $P_{x+y}(k)$ is the joint probability that the pairs of gray levels i and j add up to k.
Second moment	Also known as "energy", it indicates the order of the texture, being high when image is texturally uniform.	$GLCM_{sm} = \sum_{(i,j)} P(i,j)^2$
Variance	Measures the variability of the GLCM distribution.	$GLCM_v = \sum_{(i,j)} (i - \mu)^2 \times P(i,j)$

Furthermore, for Chapter 6, forest diversity indices were generated from the three-dimensional point clouds. These indices estimate the structural richness and composition of vegetation in a forest stand. Some common diversity indices used in forestry include the Shannon-Wiener Index (H'), Simpson's Index (D), and Pielou's Index (J'), among others. In this PhD Thesis, three indices related to the horizontal and vertical structure of vegetation were generated: the LHDI (*LiDAR Height Diversity Index*), the LHEI (*LiDAR Height Evenness Index*), and the Rumple Index. The LHDI (Equation 2.4), which is similar to FHD (*Foliage Height Diversity* index) used in the GEDI SLS system, measures the horizontal structural diversity of a forest stand. It is an adaptation of the H' index and provides information on canopy complexity and vegetation diversity at the horizontal level. Higher LHDI values suggest greater variability in the structural diversity of the forest. The LHEI (Equation 2.5) estimates the evenness of vegetation distribution at the horizontal level. It is an adaptation of the J' eveness index, first introduced by Listopad *et al*. (2015). Higher LHEI values indicate

greater evenness and homogeneity in forest structure. The Rumple Index (Equation 2.6) quantifies the roughness or structural complexity of the forest canopy. High Rumple Index values suggest complex canopy with many variations in height and density, thus indicating significant structural heterogeneity. These indices were computed for each height stratum of the Prometheus fuel classification (i.e., 0.60, 2, and 4 m).

$$LHDI = -\sum[(P_h) \times \ln(P_h)] \quad (2.4)$$

$$LHEI = \frac{LHDI}{\ln(P_h)} \quad (2.5)$$

$$Rumple\ index = \frac{3D\ canopy\ surface\ area}{ground\ area} \quad (2.6)$$

where P is the proportion of returns at the defined Prometheus model intervals (h).

Structural metrics, textural variables, and forest diversity indices are typically derived directly from the point cloud. However, managing the entire point cloud in very high-resolution LiDAR datasets, such as those from ground-based laser systems, can be challenging in terms of time and computational resources. In such scenarios, alternative techniques such as voxelization are employed, which consist of the conversion of the point clouds into three-dimensional voxels (Figure 2.14). A voxel, short for "volumetric pixel", represents a point in space and serves as the fundamental unit of a three-dimensional image, analogous to a pixel in a two-dimensional image. Voxelization algorithms typically involve an iterative process that organizes points into a regular three-dimensional grid of voxels of a given resolution (Fernández-Sarría *et al*., 2013). Each point in the three-dimensional point cloud is assigned to a voxel based on its coordinates, determining which voxel encompasses each point. Once voxels are generated, the simplified dataset enables several forest analyses, such as quantification of fuel volume (e.g., Barton *et al*., 2020; Eusuf *et al*., 2020), estimation of vertical fuel layers (Arkin *et al*., 2021), detection of individual tree stems (Hershey *et al*., 2022), wildfire modeling (Marcozzi *et al*., 2023), and description of complex forest structure (Whelan *et al*., 2023). In this PhD Thesis, a voxelization process was applied to the ground-based laser scanner system point cloud to estimate fuel volume at a very high spatial resolution (5 cm^3) within each of the Prometheus model height strata 0.60, 2, and 4 m). The voxelization enabled the evaluation of the HMLS system's capability to define and assign Prometheus fuel types in structurally complex forest stands (Chapter 5) and to improve the identification of understory fuels, thereby improving the classification of the Prometheus fuel types (Chapter 6).

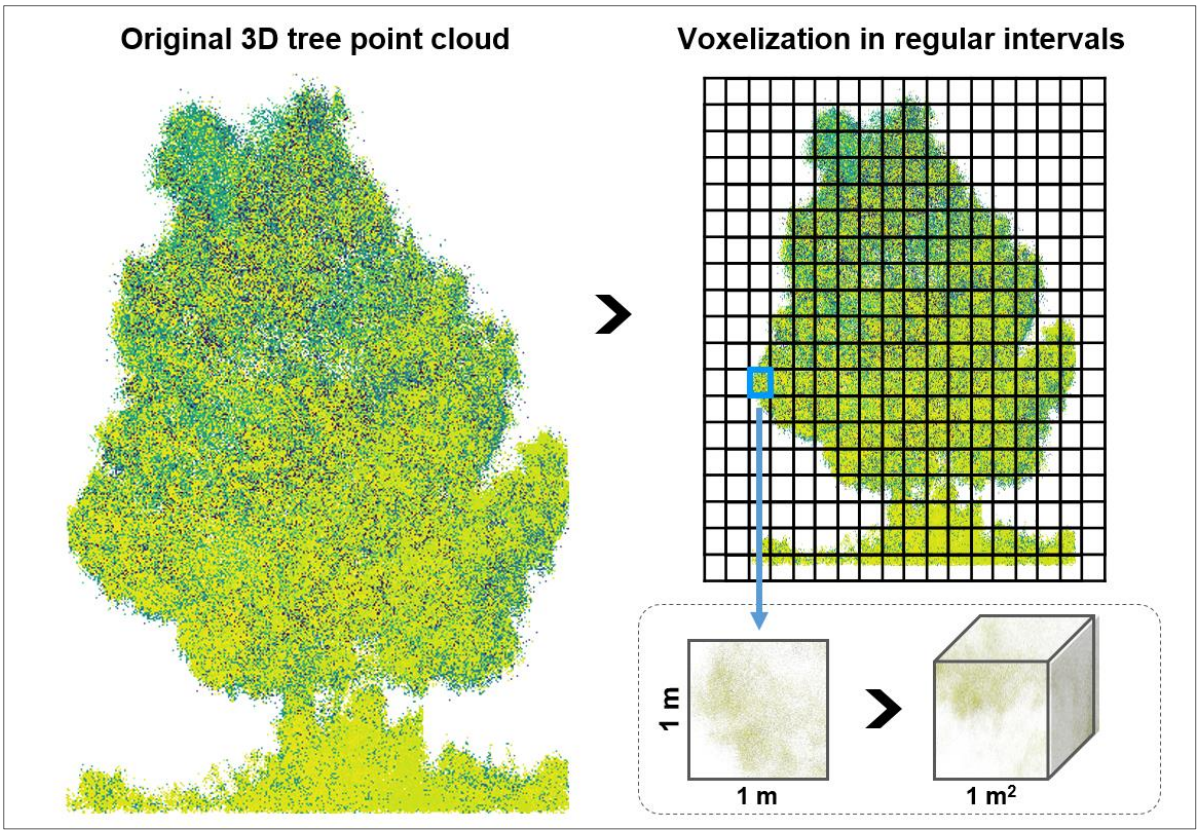

Figure 2.14. Example of the voxelization process of a three-dimensional point cloud generated for Chapters 5 and 6.

2.6.2. Multispectral-derived variables

Multispectral images acquired from Landsat-8 OLI satellite and the optical UAV were processed to derive a set of spectral indices. Through the combination of the different bands of the images, these indices provide valuable information on vegetation health and productivity. In this PhD Thesis, a total of 9 different vegetation indices and 3 additional indices derived from the Tasseled Cap transformation were generated as independent variables for Chapters 3 and 4, alongside variables derived from the three-dimensional point clouds, considering the specific spectral bands that each of the two systems is capable of recording.

The vegetation indices considered in this thesis, along with the formulas used to derive them, are presented in Equations 2.7 to 2.15. The *Normalized Difference Vegetation Index* (NDVI, Equation 2.7) is one of the most widely utilized indices in forestry and remote sensing. Originally proposed by Rouse *et al.* (1974), the NDVI measures vegetation greenness and density by calculating the normalized difference between the red and near infrared bands, which are highly sensitive to physiological changes in vegetation and exhibit contrasting responses. The *Soil Adjusted Vegetation Index* (SAVI, Equation 2.8), proposed by Huete (1988),

serves an alternative to NDVI by addressing the influence of ground reflectance. To achieve this correction, a constant factor (*L*) is introduced, which dampens the ground's effect. The value of *L* ranges from 0 to 1, representing areas of high and low vegetation density, respectively. The *Enhanced Vegetation Index* (EVI, Equation 2.9) was developed by Liu and Huete (1995) as a further refinement of NDVI. EVI incorporates additional corrections to account for the influence of atmospheric aerosols (factors C_1 and C_2) using the red and blue bands, and canopy background noise (factor *K*). The *Advanced Vegetation Index* (AVI, Equation 2.10), introduced by Roy *et al*. (1996), is more sensitive to vegetation quantity and offers more accurate estimates of canopy density. The *Green Normalized Difference Vegetation Index* (GNDVI, Equation 2.11), proposed by Gitelson *et al*. (1996), differs from NDVI by using the green band instead of the red band, enabling the estimation on photosynthetic activity and vegetation moisture content. The *Normalized Difference Moisture Index* (NDMI, Equation 2.12), developed by Gao *et al*. (1996), utilizes the near infrared and shortwave infrared bands to assess vegetation water stress. The *Normalized Difference Water Index* (NDWI, Equation 2.13), developed by McFeeters (1996), employs the same bands as GNDVI but with the operators arranged in reverse order as a different way to estimate vegetation moisture content. The *Normalized Difference Red Edge Index* (NDRE, Equation 2.14), proposed by Barnes *et al*. (2000), serves as another alternative to NDVI by using the red-edge band instead of the red band, which provides higher sensitivity to vegetation condition and a more contrasted response with the near infrared band. Consequently, NDRE offers better estimates of plant water stress and is less prone to saturation issues in dense vegetation areas. The *Green Chlorophyll Index* (GCI, Equation 2.15), proposed by Gitelson *et al*. (2003), estimates chlorophyll content in vegetation by using the near infrared and green bands.

Finally, using the Tasseled Cap transformation (Kauth and Thomas, 1976) on the original image bands, three new bands were derived: band 1, or *Brightness* (Equation 2.16), which estimates the total reflectivity of the image and is associated with variations in ground reflectance; band 2, or *Greeness* (Equation 2.17), which estimates the vigor of the vegetation; and band 3, or *Wetness* (Equation 2.18), which is related to the water content of the vegetation.

$$NDVI = \frac{NIR - R}{NIR + R} \tag{2.7}$$

$$SAVI = \frac{(1 + L) \times (NIR - R)}{NIR + R + L} \tag{2.8}$$

$$EVI = Gf \times \frac{NIR - R}{(NIR + C_1 \times R - C_2 \times B) + K} \tag{2.9}$$

$$AVI = [NIR \times (255 - R) \times (NIR - R)]^{1/3} \quad (2.10)$$

$$GNDVI = \frac{NIR - G}{NIR + G} \quad (2.11)$$

$$NDMI = \frac{NIR - SWIR1}{NIR + SWIR1} \quad (2.12)$$

$$NDWI = \frac{G - NIR}{G + NIR} \quad (2.13)$$

$$NDRE = \frac{NIR - RedEdge}{NIR + RedEdge} \quad (2.14)$$

$$GCI = \left(\frac{NIR}{G}\right) - 1 \quad (2.15)$$

$$Brightness = 0.3029 \times B + 0.2786 \times G + 0.4733 \times R + 0.5599 \times NIR + 0.508 \times SWIR1 + 0.1872 \times SWIR2 \quad (2.16)$$

$$Greenness = -0.2941 \times B - 0.243 \times G - 0.5424 \times R + 0.7276 \times NIR + 0.0713 \times SWIR1 - 0.1608 \times SWIR2 \quad (2.17)$$

$$Wetness = 0.1511 \times B + 0.1973 \times G + 0.3283 \times R + 0.3407 \times NIR - 0.7117 \times SWIR1 - 0.4559 \times SWIR2 \quad (2.18)$$

where *NIR* is the near infrared band, *R* is the red band, *Gf* is a gain factor, C_1 and C_2 are coefficients of the aerosol resistance, *B* is the blue band, *K* is the canopy background adjustment, *G* is the green band, *RedEdge* is the red-edge band, *SWIR1* is the shortwave infrared band 1, and *SWIR2* is the shortwave infrared band 2.

2.7. FUEL TYPE IDENTIFICATION AND CLASSIFICATION

Descriptor variables of vegetation structure, texture, and volume derived from the point clouds, together with the spectral indices from Landsat-8 OLI and the optical UAV, served as the primary inputs for identifying the Prometheus fuel types using each of the assessed systems. For this purpose, machine learning-based supervised classification models were applied in Chapters 3, 4, and 6, while a quantitative estimation of fuel volume was utilized in Chapter 5.

Machine learning models require a prior selection of variables to identify those that best predict the reality being modeled, following the principles of the *Law of Parsimony*. Some of the numerous variable selection techniques used in forestry studies include LASSO (Kantola *et al*., 2010; Domingo *et al*., 2019a),

stepwise (García-Gutiérrez *et al*., 2013; Jarron *et al*., 2020), principal components analysis (Fayad *et al*., 2014; Silva *et al*., 2016), VSURF (Rodríguez-Puerta *et al*., 2020), and Boruta (Blackburn *et al*., 2021; Donager *et al*., 2021a). In this PhD Thesis, variable selection was performed using the non-parametric Spearman's rank correlation coefficient (Spearman, 1904), Kruskal-Wallis H test (Kruskal and Wallis, 1952) and Dunn's test for multiple comparisons (Dunn, 1964). Spearman and Kruskal-Wallis tests were used for the initial selection of GEDI variables and Landsat-8 OLI vegetation indices (Chapter 3). Spearman's rank correlation coefficient provided the direction and strength of the relationships between predictor variables and ground-truth. This selection method has been widely used in forestry studies (e.g., Zellweger *et al*., 2013; Adhikari *et al*., 2020; Domingo *et al*., 2020; Revilla *et al*., 2021) and it is considered a good tool to establish relationship between LiDAR and ground-truth data (Kristensen *et al*., 2015). On the other hand, Kruskal-Wallis tested for significant differences in the predictor variables for the different categories of the ground-truth. The null hypothesis states that the variables come from identical populations, while the alternative hypothesis assumes that at least one group comes from a different population than the others. This means that alternative hypothesis is satisfied when the variables are able to differentiate between the fuel types that constitute the ground-truth, although the test does not specify which fuel types are distinct. For this reason, Dunn's test was used as the third selection method for Chapter 3 and, given the good results provided, the unique method in Chapters 4 and 6. Dunn's test is similar to Kruskal-Wallis test but possesses the capability to identify the fuel types that exhibit significant differences. In essence, Dunn's test specifies which pairs of the Prometheus fuel types (i.e., FT2-FT3, FT2-FT4, etc.) are distinguished by the predictor variables. It is a semi-automatic selection method, as the user ultimately decides which variables to introduce into the classification models based on the results provided by the test. A variable may be selected if it has a high potential to distinguish between a large number of pairs of fuel types. However, a variable may also be selected if it can distinguish between a few pairs or even a single pair of fuel types that no other variable can differentiate. Thus, users may consider variables for classification models not only for the quantity of fuel type pairs they can differentiate but also for the quality of the distinction.

Classification models based on machine learning enable the identification of categories or groups (e.g., the fuel types) from a set of input variables. Their use in forestry studies is well established, including *Gradient Nearest Neighbor* (GNN) imputation (Pierce *et al*., 2009), *Classification and Regression Tree* (CART) (Pierce *et al*., 2009; Chirici *et al*., 2013), *Support Vector Machine*

(SVM) (García *et al*., 2011; Alonso-Benito *et al*., 2012; Domingo *et al*., 2020), *Stochastic Gradient Boosting* (SGB) models (Chirici *et al*., 2013), and *Random Forest* (RF) (Hudak *et al*., 2016; Domingo *et al*., 2020). In this PhD Thesis, the non-parametric classification models RF and SVM with linear and radial kernel were used to identify the Prometheus fuel types. RF involves constructing multiples decision trees, each of which splits the data into smaller and homogeneous subsets. Through bagging, multiple data samples are generated, and each decision tree is trained on a different sample. The final classification is determined by aggregating the predictions of all the trees and selecting the most frequent class. SVM works by identifying a hyperplane that best separates the different classes in a two-dimensional, three-dimensional, or higher-dimensional space. The margins represent the distance between the hyperplane and the nearest data points (i.e., support vectors) of each class. The objective of SVM algorithms is to maximize these margins to achieve the best separation between classes. The support vectors that are closest to the hyperplane are crucial because they define the optimal hyperplane and its margins. SVM can employ different kernel functions to transform the original data into a higher-dimensional space to find the hyperplanes that separate the classes most effectively. Linear kernels SVM use the original input data space, while radial kernels SVM transform the data into a higher-dimensional space to better identify the separating hyperplanes. In both cases, it is necessary to adjust the "cost" parameter, which penalizes classification errors while maximizing margins. A higher "cost" value minimizes classification errors at the expense of smaller margins, and vice versa. The RF and SVM models were assessed using "overall accuracy" (OA) and Cohen's kappa (κ) coefficients, along with confusion matrices. OA and κ coefficients offer a comprehensive assessment of model performance. OA measures the proportion of accurate predictions made by the model out of all predictions. In turn, κ complements OA by correcting for the rate of agreement that could be due to chance. Confusion matrices describe the models' performance by indicating the accuracy and misclassification rates for each class. Errors can occur in two ways: commission errors, where the model incorrectly predicts a category, and omission errors, where the model fails to predict a category correctly. The combination of both information enables the calculation of the F-score (F) metric, used in Chapter 6, which facilitates the evaluation of error for each class and the analysis of confusion among the different classes within the model.

Additionally, in Chapter 6, the results of the classification models were used to predict and map the Prometheus fuel types across the UAV flight areas, extending beyond the surveyed plots. Both RF and SVM models can function

for classification and regression, enabling the spatial extension of results to larger areas. In this way, it is intended to demonstrate the capability of these tools not only to identify fuel types but also to predict them at larger spatial scales. Thus, the generation of fuel type maps can be highly valuable for wildfire management.

Finally, in Chapter 5, the fuel types were identified using quantitative data directly related to the vertical distribution of the fuel, rather than machine learning classification models. For this purpose, the voxels of 5 cm^3 resulting from the voxelization process of the very high-density point cloud were used. The availability of such detailed information for each height stratum allowed the generation of fuel volume distributions in order to detect the typical distribution of each Prometheus fuel type, thus enabling a more accurate assignment of each plot's fuel type. This approach aims to improve the definition of fuel types in structurally complex forest plots, where field observation of fuels can be challenging due to the lack of homogeneous plots with respect to their dominant fuel type, and the presence of mixed fuels, particularly in Mediterranean environments. In addition, variables related to fuel volume in each Prometheus height strata (0.60, 2, and 4 m) were generated from the voxels and combined with the structural variables generated from the data recorded by the UAV-LiDAR in Chapter 6, with the aim of determining if integrating data from both systems improves the identification of fuel types, especially those related to the understory.

2.8. COMPARATIVE ANALYSIS OF REMOTE SENSING SYSTEMS

The results obtained from the classification (Chapters 3, 4, and 6) and definition (Chapter 5) of the Prometheus fuel types provided a foundation for evaluating the capabilities and limitations of the systems analyzed in this PhD Thesis for effective forest fuel management. In addition, other contemporary systems of significant interest have been considered. These include the ICESat-2/ATLAS SLS system, commercial and non-commercial ALS systems, and TLS systems. ICESat-2/ATLAS represents an emerging three-dimensional remote sensing technology, contemporaneous with the other SLS system analyzed (GEDI), with the capability to analyze forest ecosystems, although its initial focus was on ice masses. ALS systems represent a widely used data source for forest fuel estimation. During the course of this thesis, non-commercial ALS data have been examined indirectly through a minor contribution to the work of Domingo *et al*. (2020) and have been utilized as auxiliary data to normalize the heights of the photogrammetric point cloud generated by the optical UAV. TLS systems are

highly regarded as valuable tools for estimating forest fuels, as they enable the collection of data with exceptionally high spatial resolution. This capability provides critical insights into understory and ground fuels. Additionally, TLS allow for direct comparisons with the HMLS system analyzed in this thesis.

To minimize potential bias between the systems evaluated in the core of the PhD Thesis and those that have not been directly assessed, a literature review was conducted to better understand the capabilities of these systems for improved forest fuel estimation. A total of 167 scientific articles were consulted in journal indexed in the *Scopus*, *Web Of Science*, and *FECYT* databases. In addition, 9 web portals of the non-commercial ALS data providers with national coverage were checked with the support of the report published by Kakoulaki *et al*. (2021). The following number of articles were consulted for each system: 32 for GEDI, 27 for ICESat-2/ATLAS, 43 for ALS systems, 31 for optical UAVs, 32 for UAV-LiDAR systems, 11 for HMLS systems, and 47 for TLS systems. The review covers research published since 2006, but 73% of the focus is on articles published during the thesis development period (2020-2024) with 95% of the sources coming from the last 10 years (2015-2024). It is important to note that some reviewed works utilize several of these systems simultaneously, so the total number of articles does not match the sum for each individual system.

The comparative analysis was conducted focusing on three main components: intrinsic characteristics, data processing and analysis capabilities, and accuracy in estimating fuel types for each system. Each component was divided into five different functionalities, which were scored on a scale of 0 to 3, where 0 indicated a non-existent functionality, and 1, 2, and 3 represented low, medium, and high capacity, respectively, for each evaluated system. In this manner, a total score was obtained for each component, and the sum of these scores provided an overall score, which served to semi-quantitatively evaluate the capabilities of each system.

To evaluate the intrinsic characteristics of each system, the following functionalities were considered: (i) sampling density (i.e., points, pulses, or footprints), which determines the spatial resolution of the data, and consequently, the precision and accuracy of the information obtained; (ii) temporal resolution, which reflects the system's ability to acquire data at different time intervals; (iii) low economic cost to user, indicating the initial financial investment required to operate the system; (iv) spatial coverage, representing the area that the system can record; and (v) accuracy of planimetric and altimetric location, which refers to the mean geolocation error in data acquisition.

The data processing and analysis capabilities of each system was evaluated based on the following functionalities: (i) computational requirements, determined by the size of the data obtained; (ii) processing accessibility, referring to the availability of tools for data processing, as well as whether these tools are proprietary or open-source; (iii) the intensity of field work required to accurately obtain the data; (iv) pre-processing requirements, representing the system's compatibility with the typical workflow of three-dimensional point cloud processing (see Figure 2.13), and (v) the accuracy in generating independent predictor variables for estimating fuel types.

Finally, the functionalities evaluated to determine the accuracy in estimating fuel types were as follows: (i) the accuracy in the classification and/or definition of fuels, based on the results of the classification models and fuel vertical volume distributions; (ii) the capability for multisensor integration, specifically the merging of three-dimensional point clouds with optical sensors and other systems; (iii) the ability to integrate multiplatform laser or photogrammetric systems; (iv) the effective working scale of the results obtained, ensuring their applicability to forest fuel management; and (v) the capacity for spatializing the results to generate forest fuels maps, while considering the effective scale required for forest management.

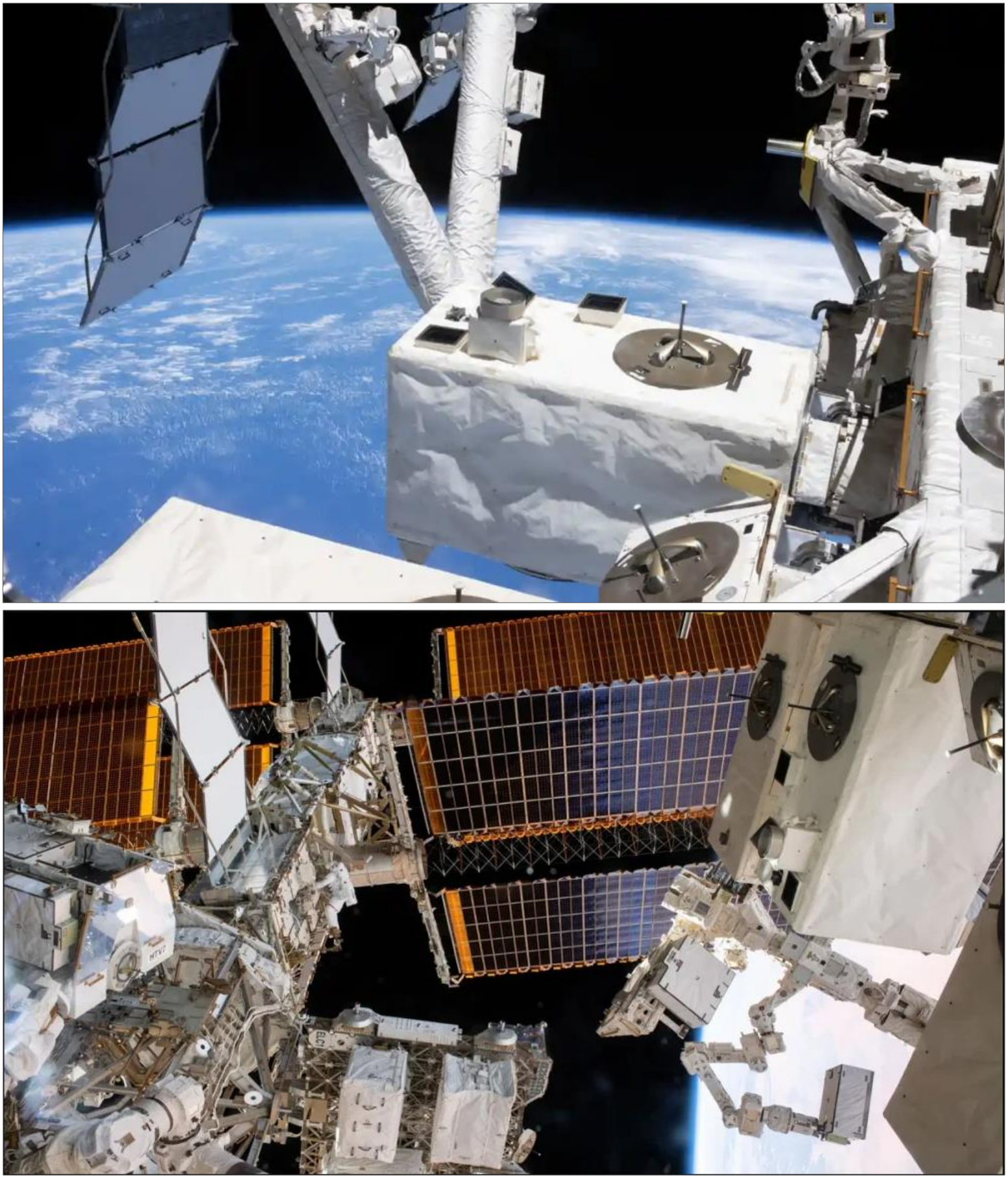

The GEDI system on the ISS. Photographs by NASA (https://gedi.umd.edu/gallery/).

CHAPTER 3

THE GLOBAL ECOSYSTEM DYNAMICS INVESTIGATION SYSTEM FOR FOREST FUEL ESTIMATION

This chapter corresponds to:

Hoffrén, R., Lamelas, M.T., de la Riva, J., Domingo, D., Montealegre, A.L., García-Martín, A., and Revilla, S., 2023. Assessing GEDI-NASA system for forest fuels classification using machine learning techniques. *International Journal of Applied Earth Observation and Geoinformation* 116, 103175.

https://doi.org/10.1016/j.jag.2022.103175

Assessing GEDI-NASA system for forest fuels classification using machine learning techniques

Raúl Hoffrén[1,2,*], María Teresa Lamelas[2,3], Juan de la Riva[1,2], Darío Domingo[2,4], Antonio Luis Montealegre[2,3], Alberto García-Martín[2,3], Sergio Revilla[5].

[1] Department of Geography and Land Management, University of Zaragoza, Calle Pedro Cerbuna 12, 50009, Zaragoza, Spain.
[2] Geoforest Group, University Institute for Research in Environmental Sciences of Aragón (IUCA), University of Zaragoza, Spain.
[3] Centro Universitario de la Defensa, Academia General Militar, Ctra. Huesca s/n, 50090, Zaragoza, Spain.
[4] EiFAB-iuFOR, University of Valladolid, Campus Duques de Soria, 42004, Soria, Spain.
[5] Instituto Geográfico de Aragón, Paseo María Agustín 36, Ed. Pignatelli, 50071, Zaragoza, Spain.
[*] Corresponding author, email: rhoffren@unizar.es.

ABSTRACT

Identification of forest fuels is a key step for forest fire prevention since they provide valuable information of fire behavior. This study assesses NASA's Global Ecosystem Dynamics Investigation (GEDI) system to classify fuel types in Mediterranean environments according to the Prometheus model in a forested area of NE Spain. We used 59,554 GEDI footprints and extracted variables related to height metrics, canopy profile metrics, and aboveground biomass density estimates from products L2A, L2B, and L4A, respectively. Four quality filters were applied to discard high uncertainty data, reducing the initial footprints to 9,703. Spectral indices from Landsat-8 OLI scenes were created to test the effect of their integration with GEDI variables on fuel types estimation. Ground-truth data were comprised of Prometheus fuel types estimated in two previous studies. Only the types that matched in each GEDI footprint in both studies were used, resulting in a final sample of 1,112 footprints. Spearman's correlation coefficient, Kruskal-Wallis and Dunn's tests determined the variables to be included in the classification models: the relative height at the 85th percentile, the Plant Area Index, and the Aboveground Biomass Density from GEDI, and the brightness from Landsat-8 OLI. Best performances were achieved with *Random Forest* (RF) and *Support Vector Machine* with radial kernel (SVM-R), which were lower including only GEDI variables (accuracies: RF and SVM-R = 61.54%) than integrating the brightness from Landsat-8 OLI (accuracies: RF = 83.71%, SVM-R = 81.90%). These results allow validating GEDI for fuel type classification of Prometheus model, constituting a promising information for forest management over large areas.

1. INTRODUCTION

One of the most common worldwide disturbances of forests are wildfires. In particular, Mediterranean ecosystems are recurrently affected by forest fires, averaging 45,000 events yearly (Oliveira *et al*., 2012), which produce negative environmental effects, such as soil erosion, biodiversity loss, or greenhouse effect increase. Thus, it is essential to understand fire behavior to help forest managers prevent forest fires and evaluate fire risk over population. In this sense, forest fuels provide valuable information on fire spread and intensity, as they determine the fire regime (Flannigan *et al*., 2000). In addition, forest fuels represent all the organic matter available for combustion in a forest fire and are the only driver that can be quantified to assess fire risk (Ferraz *et al*., 2016). In general, forest fuels are classified into different fuel types based mainly on the height and density of vegetation, presenting similar fire behavior (Huesca *et al*., 2019). Several fuel type classifications have been developed in last decades, most of them in USA and Canada, such as the Rothermel fire-spread model (Rothermel, 1972) or the Northern Forest Fire Laboratory (NFFL) model (Albini, 1976). The Prometheus model (Prometheus, 1999) adapts the NFFL fuel types to Mediterranean environments (Riaño *et al*., 2002), considering vegetation height and density as the main fire spreaders and comprising seven categories: one for grassland (FT1), three for shrublands (FT2, FT3, FT4), and three for woodlands (FT5, FT6, FT7) (Table 1).

Table 1. Prometheus fuel types classification.

Fuel type	**Main fire carrier**	**Cover**	**Shrub mean height**	**Vertical difference between shrubs and trees**
FT1	Grass	> 60% grass		
FT2	Shrubs	> 60% grass and < 50% trees (> 4 m)	0.30 – 0.60 m	
FT3			0.60 – 2.00 m	
FT4			2.00 – 4.00 m	
FT5	Trees	< 30% shrub and > 50% trees (> 4 m)		
FT6		> 30% shrub and > 50% trees (> 4 m)		> 0.50 m
FT7				< 0.50 m

Remote sensing, specifically LiDAR (*Light Detection and Ranging*) technology, is particularly useful for classifying forest fuels, as they are capable of modelling forest features such as vegetation height, crown density, or biomass volume (Revilla *et al*., 2021). Furthermore, integration of LiDAR data with multispectral imagery can provide an improvement in forest fuel model classification (e.g., García *et al*., 2011; Marino *et al*., 2016; Domingo *et al*., 2020). Several studies have used spaceborne LiDAR sensors for forest fuel estimation. For instance, the NASA's *Geoscience Laser Altimeter System* (GLAS) was used to estimate fire fuel models (e.g., Ashworth *et al*., 2010), canopy fuel properties for crown fire behavior (e.g., García *et al*., 2012), and canopy structure and fuel data (e.g., Peterson *et al*., 2013). The NASA's *Advanced Topographic Laser Altimeter System* (ATLAS) instrument, launched in 2018, can also be used for vegetation characterization (Narine *et al*., 2020), although few studies have been conducted to date (e.g., Narine *et al*., 2019; Lin *et al*., 2020; Jiang *et al*., 2021) and none of them on the estimation of forest fuels. However, it should be noted that both GLAS and ATLAS systems were not initially optimized for vegetation and forest structure characterization (Potapov *et al*., 2021; Leite *et al*., 2022). The NASA's *Global Ecosystem Dynamics Investigation* (GEDI), launched in late 2018, is the first spaceborne full-waveform LiDAR system capable of measuring forest vertical structure (Lang *et al*., 2021; Silva *et al*., 2021). GEDI differentiates from others spaceborne LiDAR systems in its penetration capability in dense vegetation (Leite *et al*., 2022), reported in up to ~99% canopy cover (Hancock *et al*., 2019; Duncanson *et al*., 2020). GEDI system has been used in recent studies to estimate forest attributes (e.g., Fayad *et al*., 2021b; Potapov *et al*., 2021; Rishmawi *et al*., 2021), biomass (e.g., Duncanson *et al*., 2020; Puletti *et al*., 2020; Silva *et al*., 2021), vegetation height growth dynamics (Guerra-Hernández and Pascual, 2021), and its accuracy for canopy height and above-ground biomass estimates have been assessed (e.g., Dorado-Roda *et al*., 2021; Fayad *et al*., 2021a; Lang *et al*., 2021). However, until now, research concerning forest fuels using GEDI have only been conducted by Leite *et al*. (2022), who specifically focused on fuel loads in a Brazilian savanna region. Thus, the capability of GEDI for the estimation of fuel types has not yet been evaluated, even though it could help to improve their identification and classification. Data collected by GEDI provide valuable large-scale information that can be used freely and efficiently by users, instead of costly regional and/or national initiatives. It could also support other remote sensing data sources which have proven to be efficient for forest fuels modelling, such as multispectral imagery, airborne laser scanner (ALS) systems, unmanned aerial vehicles, or other current and future satellite LIDAR systems.

In this context, the overall goal of our study is to assess the capability of GEDI to estimate Prometheus fuel types in a Mediterranean forest environment by means of machine learning classification techniques. Our main hypothesis is that GEDI is able to estimate Prometheus fuel types, constituting a valuable information for forest fire prevention at large spatial scales in Mediterranean ecosystems, especially in areas where there is a lack of other LiDAR data to work with. To this end, in order to overcome the high uncertainty in location and poor signal quality of some footprints of GEDI data (Dubayah *et al.*, 2020a), we especially focus on the filtering process of the data to obtain a highest accurate sample to work with. In addition, we test the effect of integrating spectral indices from Landsat-8 Operational Land Imager (OLI) multispectral imagery into the GEDI data to improve the classification of forest fuels.

2. MATERIALS AND METHODS

To reach the objectives we have developed a methodology for the selection of the highest quality GEDI footprints and their integration with multispectral imagery from Landsat-8 OLI. Then, we have assigned the ground-truth to each footprint, consisting in Prometheus fuel types mapped in two previous studies. After that, we have selected the most relevant GEDI variables, which have been finally introduced in the classification models using machine learning techniques. Figure 1 synthetizes in a scheme the methodological steps developed in this study.

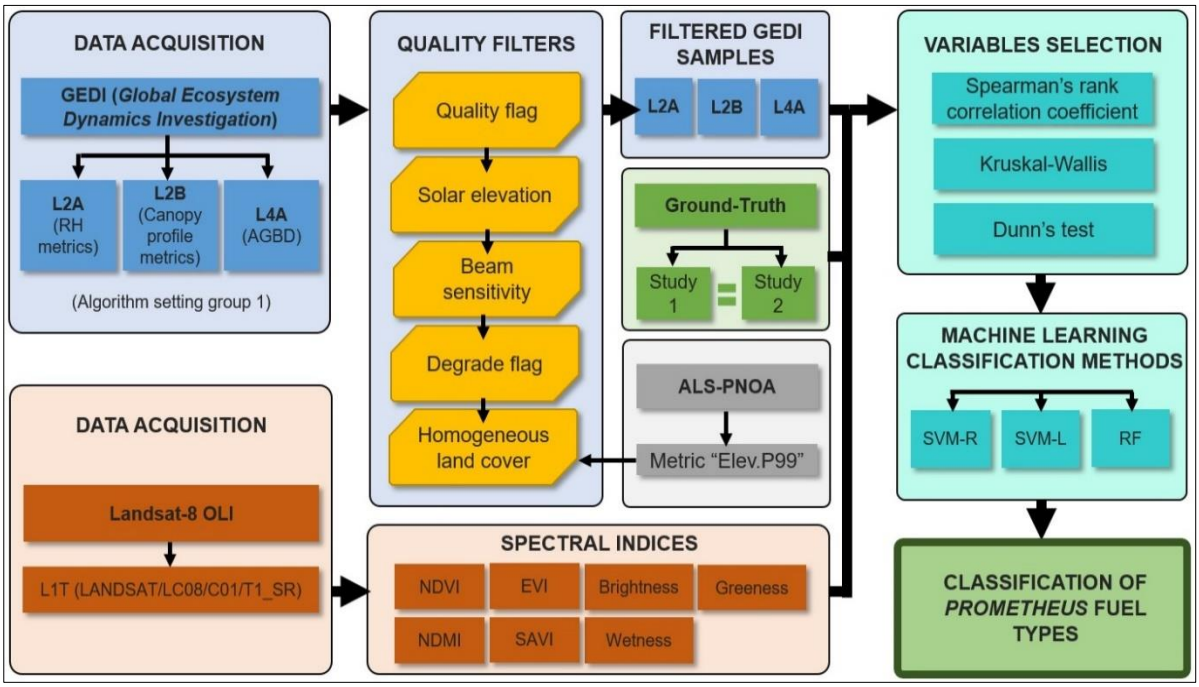

Figure 1. Synthetic scheme of the methodology followed in this study.

2.1. Study area

The study was carried out in the central sector of the Ebro Valley, located in the Autonomous Community of Aragon in the northeast of Spain (41◦51′ N, 0◦56′ W) (Figure 2). The climate of the area is semi-arid, with low and irregular annual precipitations, averaging 350 mm yearly. The annual temperature is ~14ºC, with high daily and interseasonal temperature gradient. The study area is mostly placed inside the Military Training Center "*San Gregorio*", owned by the Ministry of Defense of Spain. The main land covers include grassland, shrublands, and natural forest of Aleppo pine (*Pinus halepensis* Mill.) with understory dominated by kermes oaks (*Quercus coccifera*), cade junipers (*Juniperus oxycedrus*), thymes (*Thymus vulgaris*), and rosemary (*Rosmarinus officinalis*) (Montealegre *et al*., 2016).

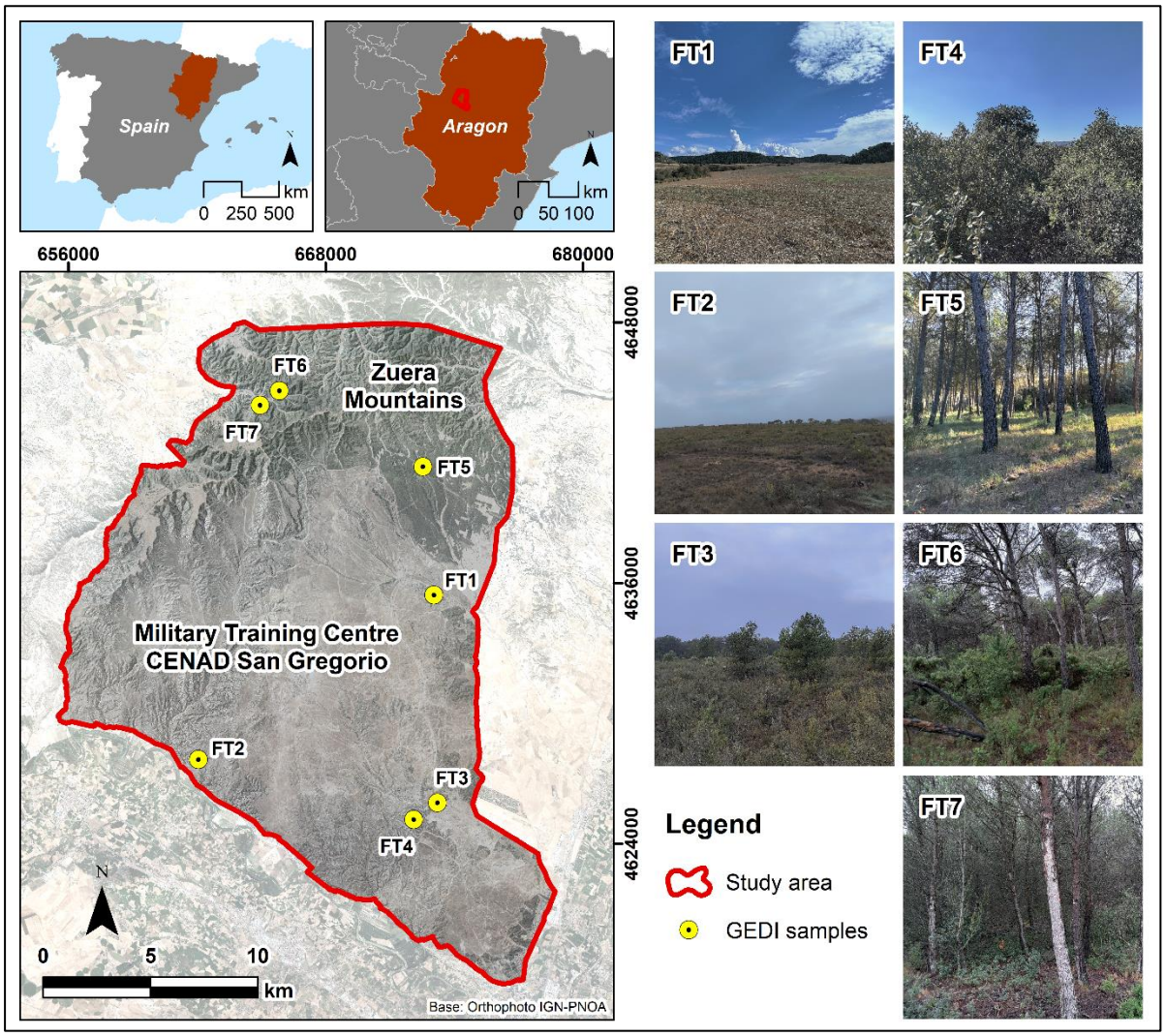

Figure 2. Study area on the central sector of the Ebro Valley, in Aragon (NE Spain), and examples of each Prometheus fuel type within a selection of GEDI footprints.

2.2. GEDI data processing

GEDI began collecting data worldwide in April 2019 between the 51.6ºN and 51.6ºS latitudes (Dubayah *et al*., 2020b). The instrument, onboard the International Space Station, is equipped with 3 lasers operating in the near infrared region (1064 nm). One of the lasers is split into two coverage beams while the other two are full-power beams. The 4 beams are dithered across track to produce a total of 8 beam ground transects of footprints of 25 m diameter, separated 60 m and 600 m along-track and cross-track, respectively. To perform this study, we have used information stored in footprint data sets with three processing levels: *Level 2A Elevation and Height Metrics Data, Version 2* (L2A) (Dubayah *et al*., 2021a), *Level 2B Canopy Cover and Vertical Profile Metrics Data, Version 2* (L2B) (Dubayah *et al*., 2021b), and *Level 4A Aboveground Biomass Density, Version 2.1* (L4A) (Dubayah *et al*., 2022), which also provide a set of quality flags that allow filtering footprints with high geolocation uncertainty, poor signal quality, and shots affected by atmospheric noise and cloud cover (Dubayah *et al*., 2020a). The L2A product includes relative height metrics in 100 height intervals or percentiles (RH0, RH1… RH100). The L2B product contains canopy profile metrics: the total *Plant Area Index* (PAI), the vertical *Plant Area Volume Density* profile (PAVD), the *Foliage Height Diversity* index (FHD), and the *Total Canopy Cover* (TCC). The L4A product stores estimations of above-ground biomass density (AGBD) derived from the L2A data. The L2A and L2B products have been processed from the Level 1B Geolocated Waveform Data, Version 2 (L1B) (Dubayah *et al*., 2021c) corrected waveforms using six different algorithm setting groups as a result of different processing of the L1B waveforms and noise thresholds. Therefore, for each product there are six different data versions. Nevertheless, this study focuses on the first algorithm setting group, which works properly in the majority of cases (Dubayah *et al*., 2020a) as it uses conservative thresholds for the waveform signal (Roy *et al*., 2021). A total of 59,554 footprints stored in 45 orbit tracks registered between April 2019 and December 2021 in our study area were used. To download and process all GEDI data the 4.0.3 version of R environment (R Core Team, 2020) and the 'rGEDI' package (Silva *et al*., 2020) were used, while the L4A data were downloaded using NASA-Earth Data platform (https://search.earthdata.nasa.gov/, last accessed 28 Mar 2022). GEDI footprints within our study area were delineated by obtaining their centroid from the geolocated XY data of the L2A product. Since RH variables consists of 100 height percentiles, we arbitrary reduced its initial number by selecting only RH variables every 5 percentiles from RH0 to RH95 along with RH98, RH99, and

RH100, in order to reduce time costs in processing in the following stages of the study.

Waveforms from a spaceborne LiDAR system are recurrently affected by cosmic/solar noise, the Earth's atmosphere, and cloud cover, which disturb the quality of the laser signal all the way from the sensor to the ground, affecting derived estimations such as height metrics and biomass estimations. In order to gather a sample with the highest quality, four filters were applied to GEDI data. First, footprints with the 'quality flag' attribute classified as 0 were discarded, meaning that laser shot does not meet the minimum quality requirements based on energy and amplitude (Dubayah *et al*., 2021c), and that the beam sensitivity has insufficient power to penetrate to the ground (Hofton and Blair, 2019). Second, observations acquired at day time were rejected to avoid negative impact of solar noise on GEDI waveforms (Potapov *et al*., 2021). Third, following Roy *et al*. (2021), samples with potential degraded geolocation were rejected based on the 'degrade flag' attribute. Finally, due to the geolocation uncertainty of GEDI data, in order to ensure the homogeneity in fuel type of GEDI footprints, shots with high land cover heterogeneity were disregarded using ALS information. For this, we used the 99th percentile of the canopy height as reference metric ("*Elev.P99*"), as one of the main bases of Prometheus fuel types is the height of vegetation. "*Elev.P99*" was derived from public ALS data from the Spanish National Plan for Aerial Orthophotography (PNOA), captured between 15 October and 16 November 2016. To create "*Elev. P99*" we removed noise and overlapping returns. Then, following Montealegre *et al*. (2015a, 2015b), ground points were classified using the MCC 2.1 command-line tool (Evans and Hudak, 2007) and interpolated using a TIN interpolation method (Renslow, 2013) to generate a Digital Elevation Model (DEM) of 1 m spatial resolution. We normalized return heights by subtracting DEM heights using FUSION/LDV 4.21 open-source software (McGaughey, 2021) and extracted the "*Elev. P99*" metric, which was then rasterized at 10 m spatial resolution. We established this pixel size in order to gather a sufficient number of returns from the low-density ALS-PNOA point-cloud (Gelabert *et al*., 2020). Then, the spatialized "*Elev.P99*" metric was extracted to each GEDI footprint by applying a buffer to avoid geolocation error in GEDI data. We used a circular buffer of 30 m radius, as for release versions 2 and 2.1 it is reported a geolocation error of about 10.2 m (Dubayah *et al*., 2021c). In this way, we ensure that we cover all the spatial uncertainty in the footprints, since the geolocation error can occur in any direction, thus extending the uncertainty to>20 m, considering the 10 m spatial resolution of the spatialized "*Elev.P99*" metric. Finally, we filtered out footprints with high heterogeneity at the 99th percentile (i.e., significant

differences in "*Elev.P99*" pixel values), which indicates that the footprint does not have homogeneous land cover. For this purpose, we defined as a threshold the standard deviation greater than the 8th decile. Therefore, footprints with a standard deviation of "*Elev.P99*" pixel values higher than the defined threshold were labeled as heterogeneous in land cover and thus discarded. These filtering processes reduced the number of footprints to 9,703, a 16% of the initial sample (Table 2), as observed in Figure 3.

Table 2. Sequentially reduction of the number of GEDI footprints and percentage of remaining footprints by filter applied.

	Number of footprints	**Percentage of remaining footprints**
Initial footprints	59,554	100%
Filter 1: Quality Flag	–37,532	37%
Filter 2: Day time observations	–9.240	22%
Filter 3: Degraded geolocation	–96	21%
Filter 4: High land cover heterogeneity	–2,983	16%
Footprints remaining	9,703	16%

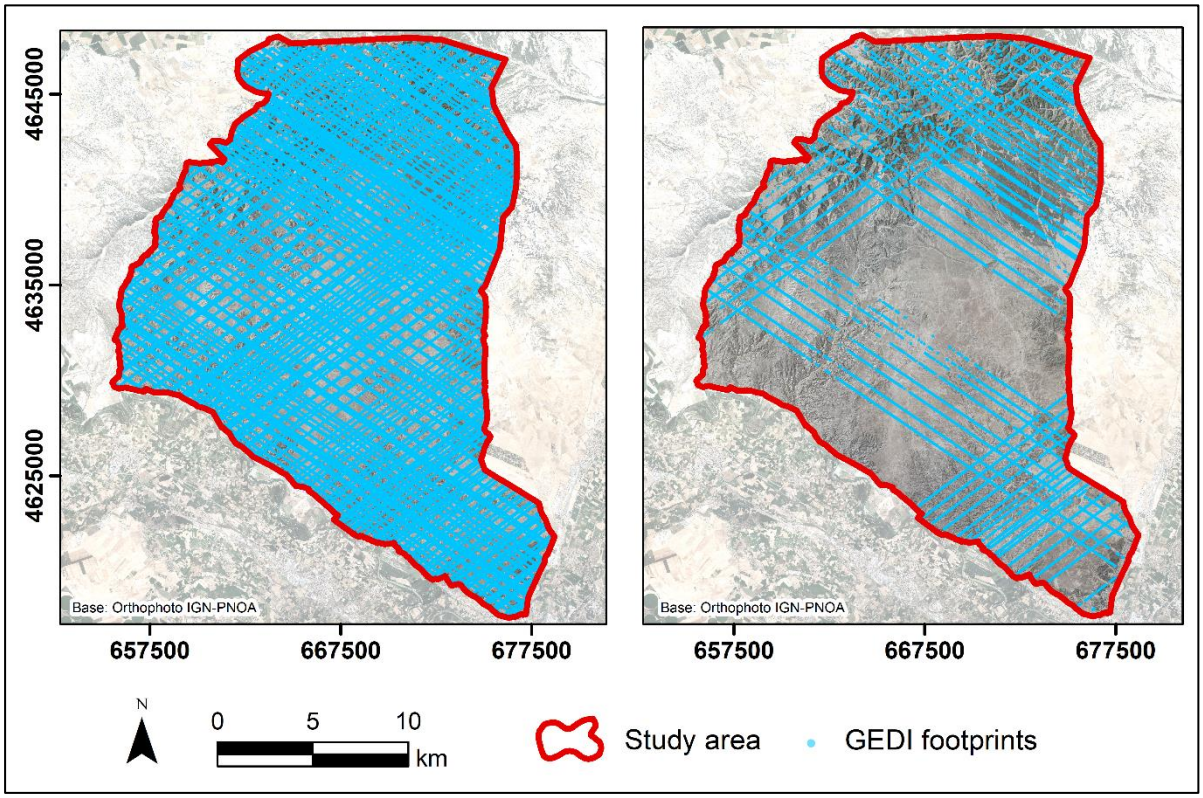

Figure 3. Spatial location of the initial GEDI footprints (left) and the remaining GEDI footprints (right) after filtering.

2.3. Landsat-8 OLI data and spectral indices

Landsat-8 OLI images were used to produce seven spectral indices. The OLI instrument began collecting data in April 2013 in the visible and infrared spectral regions, and includes a panchromatic band. In this study, we used the visible and near infrared bands of 30 m spatial resolution from the terrain-corrected scenes (L1T: "LANDSAT/LC08/C01/T1_SR"). Monthly images from June, July, and August 2019, 2020, and 2021 with less cloud cover than 10% were selected for the study area and processed through *Google Earth Engine* (GEE) (Gorelick *et al*., 2017). The seven spectral indices produced were: The *Normalized Difference Vegetation Index* (NDVI) (Eq. 1; Rouse *et al*., 1974), the *Normalized Difference Moisture Index* (NDMI) (Eq. 2; Masek *et al*., 2006), the *Enhanced Vegetation Index* (EVI) (Eq. 3; Liu and Huete, 1995), the *Soil Adjusted Vegetation Index* (SAVI) (Eq. 4; Huete, 1988), brightness, greenness, and wetness of the Tasseled Cap transformation (Eqs. 5–7; Kauth and Thomas, 1976). The GEE code developed for this study was a modification of the original by Decuyper *et al*. (2022).

$$NDVI = \frac{NIR - R}{NIR + R} \quad (1)$$

$$NDMI = \frac{NIR - SWIR1}{NIR + SWIR1} \quad (2)$$

$$EVI = 2.5 \times \frac{NIR - R}{(NIR + 6 \times R - 7.5 \times B) + 1} \quad (3)$$

$$SAVI = \frac{NIR - R}{(NIR + R + 0.5)} \times (1 + 0.5) \quad (4)$$

$$Brightness = 0.3029 \times B + 0.2786 \times G + 0.4733 \times R + 0.5599 \times NIR + 0.508 \times SWIR1 + 0.1872 \times SWIR2 \quad (5)$$

$$Greenness = -0.2941 \times B - 0.243 \times G - 0.5424 \times R + 0.7276 \times NIR + 0.0713 \times SWIR1 - 0.1608 \times SWIR2 \quad (6)$$

$$Wetness = 0.1511 \times B + 0.1973 \times G + 0.3283 \times R + 0.3407 \times NIR - 0.7117 \times SWIR1 - 0.4559 \times SWIR2 \quad (7)$$

where *NDVI* is the Normalized Difference Vegetation Index, *NDMI* is the Normalized Difference Moisture Index, *EVI* is the Enhanced Vegetation Index, *SAVI* is the Soil Adjusted Vegetation Index, *SWIR1* is the shortwave infrared band 6, *NIR* is the near infrared band, *R* is the red band, *G* is the green band, and *B* is the blue band.

From the initial 9 images of each spectral index, we calculated their maximum value to create a single composite image that better capture the vegetative period

variability. Finally, from each composite image we calculated the mean value of all pixels within each GEDI footprints for each index, applying a circular buffer of 30 m radius to avoid GEDI geolocation uncertainty (Dubayah *et al*., 2021c).

2.4. Forest fuels ground-truth data

In order to assess GEDI for forest fuels modeling, the ground-truth data was obtained from two previous studies conducted in the same area to estimate and map Prometheus fuel types. The first was developed by Montealegre *et al*. (2015c) (thereafter, study 1), and the second was conducted by Revilla *et al*. (2021) (thereafter, study 2). Study 1 combined ALS-LiDAR data from PNOA and optical imagery from SPOT-5 satellite, acquired in 2011 and 2010, respectively, for spatializing the fuel types using *Maximum Likelihood* supervised classification method, obtaining an overall accuracy of 72.7%. Study 2 assessed the suitability of the *Discrete Anisotropic Radiative Transfer* model DART (Gastellu-Etchegorry *et al*., 2016) to simulate low-density ALS-PNOA measurements and identify the fuel types. They selected the most highly correlated structural variables between the simulated and real ALS-PNOA data from 2016 using Spearman's rank correlation coefficient to classify the fuel types through *Support Vector Machine*, reaching overall accuracies of 91% and 86% using the simulated and real variables, respectively. To make this information more robust, as both data came from classification models with different global accuracies with uncertainties, it was decided to double-check both mappings, so that only footprints with the same fuel type in both studies were kept, being the ones that finally became part of the ground-truth. This caused an absence of fuel type FT6 and a very small sample size of FT5. It is important to highlight that the presence of these two fuel types was initially low, as some sectors of the study area were affected by forest fires in 1995 and 2008. In this sense, according to Domingo *et al*. (2020), these burned areas have a high density of shrubs that continue up to the tree strata (i.e., FT7). Furthermore, Gelabert *et al*. (2020) reported that differences in forest structure can be present in Aleppo pine stands after 21 years of a forest fire in Mediterranean environments. Forest fuel estimations for study 1 were acquired in a raster file format, 10 m spatial resolution. For study 2, it was required to spatialize the model at 25 m grid resolution considering the size of the field plots of this study and GEDI footprint size. We extracted the mode of the pixel values (i.e., the fuel types) contained in each selected GEDI footprint using the same circular buffers as in previous steps. Furthermore, due to the smaller pixel size of study 1 compared to the GEDI footprint size, in order to ensure that the fuel type within each footprint was homogeneous, we only considered footprints with a fuel type

mode exceeding a majority of 65%. As a result, two Prometheus classes –one from study 1 and other from study 2– were assigned to each GEDI footprint. Finally, we did the selection of footprints with matching fuel types from both studies, resulting in a final sample of 1,112 footprints.

2.5. Classification of Prometheus fuel types and model validation

A primary selection of GEDI and Landsat-8 OLI variables for classification of Prometheus fuel types was performed using three approaches for non-parametric data. The Spearman's rank correlation coefficient, considered a good tool to determine relationship between LiDAR and ground-truth data (Kristensen *et al*., 2015), determined the direction and strength of the relationship between Prometheus fuel types and GEDI and Landsat-8 OLI data. The Kruskal-Wallis and the Dunn's tests determined if there were significant differences of each selected variable between the Prometheus fuel types. After comparing results from the three selection methods, the only one variable from L4A product was selected for input into the classification models along with one very significant variable from each of the products L2A and L2B, and the most significant variable from the multispectral indices. We only introduced one variable per GEDI product and multispectral indices in order to build parsimonious models and to avoid collinearity problems. Then, two classification methods were tested to classify Prometheus fuel types: *Random Forest* (RF), calculated using the R "randomForest" (Liaw and Wiener, 2002) and 'caret' (Kuhn, 2008) packages, and *Support Vector Machine* (SVM), computed with both radial (SVM-R) and linear (SVM-L) kernels using the R package "e1071" (Meyer *et al*., 2020). After testing different combinations of parameters, RF models were parametrized with 500 trees and 2 metrics in each node, while SVM models were SVM-R and SVM-L, respectively. All explanatory variables were normalized before introducing them in the models. Two classifications were performed: the first one including exclusively GEDI most suitable variables, and the second one integrating variables from first classification with the most relevant spectral index from Landsat-8 OLI. To validate the models, the dataset was split into training and test sets (80% and 20% of the cases, respectively), resulting in a relatively balanced distribution of each fuel type (Table 3). The overall accuracy and Cohen's kappa coefficients were used to assess and determine the best classification models in general terms, and the confusion matrices allowed us to assess the prediction accuracies of the different fuel types, considering the user's and producer's accuracies in classification, determined by the commission and omission errors, respectively (Pontius *et al*., 2008).

Table 3. Number of training and test GEDI footprints and percentage (in brackets) of total GEDI footprints per Prometheus fuel type assigned for the classification models.

Dataset	FT1	FT2	FT3	FT4	FT5	FT7	Total
Training	211	177	173	150	11	169	891
	(78%)	(81%)	(82%)	(83%)	(85%)	(78%)	(80%)
Test	61	42	38	30	2	48	221
	(22%)	(19%)	(18%)	(17%)	(15%)	(22%)	(20%)
Total	272	219	211	180	13	217	1,112

3. RESULTS

3.1. Fuel type classification using GEDI variables

The variables selected by the Spearman correlation coefficients and the Kruskal-Wallis and the Dunn's tests to be introduced in the models were the relative height at the 85th percentile (RH85) and the PAI from the L2A and L2B products, respectively, along with the AGBD from the L4A product. Complete results of the variables selection are shown in the Appendix (Tables A.1, A.2, and A.3). The best performances were obtained with RF and SVM-R, both reaching an overall accuracy of 61.54%, with a kappa coefficient of 0.51. The lowest performance was obtained with SVM-L, with an overall accuracy of 57.46% and a kappa coefficient of 0.45. Confusion matrices for the three classification methods showed an important confusion in shrub fuel types (FT2, FT3, and FT4) (Table 4). FT2 reached the lowest accuracy in shrub types, since many of them were misclassified in FT1. There was also a significant error in FT4, with most of cases being categorized in shrub types FT2 and FT3, but also in tree type FT7. Furthermore, the few samples of FT5 were inaccurately classified in FT7. On the contrary, there was better success on classification of FT1 and FT7. Complete results of the confusion matrices can be seen in Tables A.4, A.5, and A.6 of the Appendix.

Table 4. Comparison between Producer's accuracies and User's accuracies of Prometheus fuel types classification methods for the selected GEDI variables (RH85 + PAI + AGBD).

Fuel types	Producer's accuracy			User's accuracy		
	SVM-R	SVM-L	RF	SVM-R	SVM-L	RF
FT1	93.44%	93.44%	83.61%	74.03%	73.08%	77.27%
FT2	23.81%	26.19%	30.95%	35.71%	26.83%	41.94%
FT3	52.63%	21.05%	47.67%	46.51%	50.00%	42.86%
FT4	26.67%	33.33%	43.33%	50.00%	41.67%	46.43%
FT5	0.00%	0.00%	0.00%	0.00%	0.00%	0.00%
FT7	85.42%	85.42%	85.42%	71.93%	66.13%	75.93%

3.2. Fuel type classification using GEDI and Landsat-8 OLI variables

The brightness of Tasseled Cap transformation was the most suitable variable of the Landsat-8 OLI spectral indices for differentiating between Prometheus fuel types according to the Spearman correlation coefficients and the Kruskal-Wallis and the Dunn's tests (Tables A.1, A.2, and A.3). It was therefore selected for input into the classification models along with the three most explanatory GEDI variables. The integration of the brightness with RH85, PAI, and the AGBD substantially improved the performance of the classification models, achieving an increase of 30% of average accuracy using the combination of both data sources. Figure 4 presents the distribution of the values of these four explanatory variables for the different Prometheus fuel types. It can be observed how the brightness is crucial to distinguish between fuel types FT1, FT2, and FT3, and between FT5 and FT7. The best performance was achieved with RF, reaching an overall accuracy of 83.71%, with a kappa coefficient of 0.79. SVM models had slightly lower performances than RF, with an overall accuracy of 81.90% and a kappa coefficient of 0.77 in the SVM-R model, and an overall accuracy of 81% and a kappa coefficient of 0.76 in the SVM-L model.

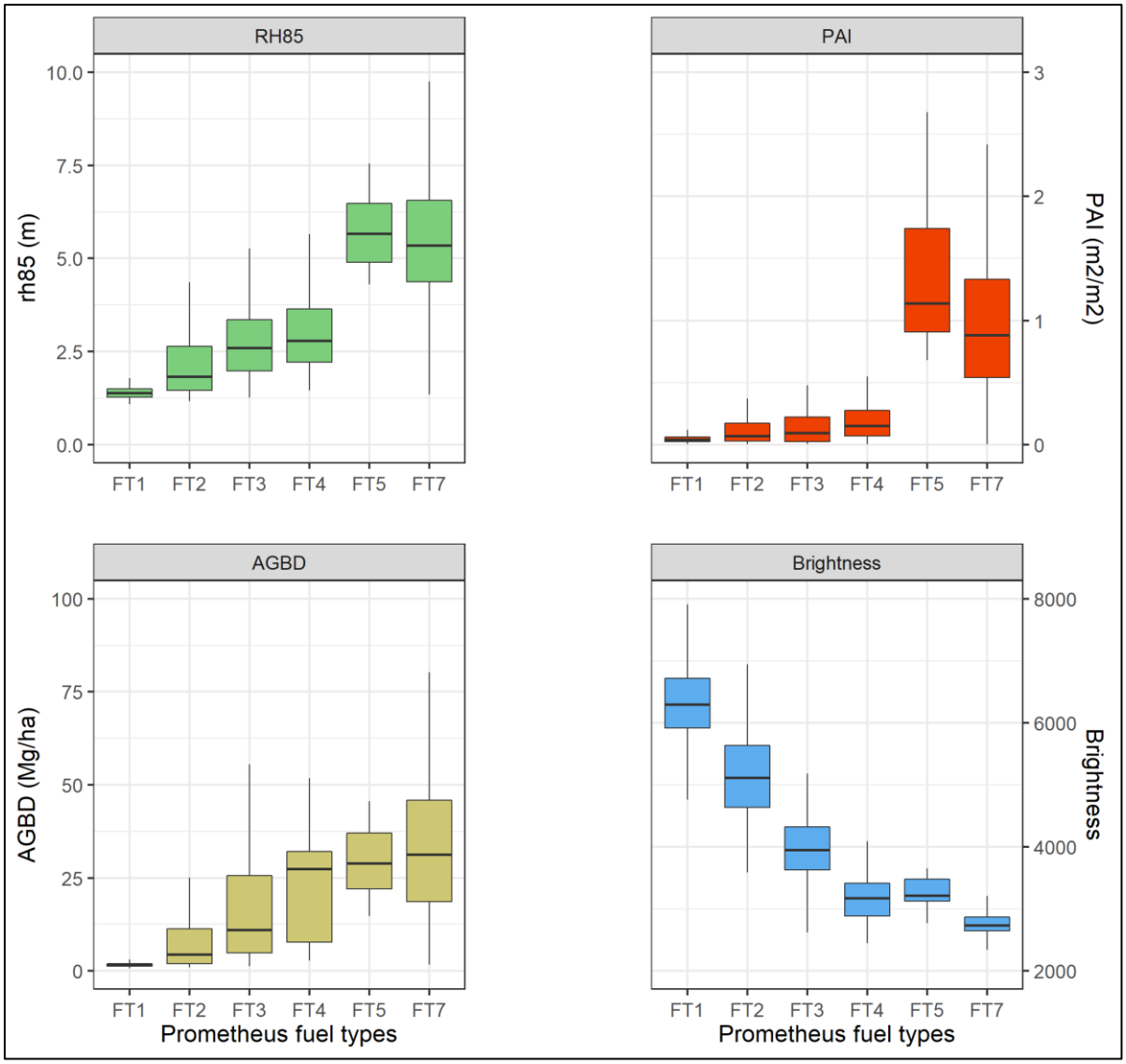

Figure 4. Distribution values of the selected GEDI and Landsat-8 OLI variables for the Prometheus fuel types classification.

The integration of brightness produced less confusion in all fuel types, especially in the shrub fuels (FT2, FT3, and FT4) which had the highest confusion rates when only GEDI variables were introduced into the classification models. An improvement in omission error of 36.68% was achieved, always exceeding the 50% of hits in each fuel type (Table 5). FT2 was now the shrub type with the highest hit rates, whereas FT4 had the highest confusion. Few FT2 samples were incorrectly classified in FT1, while in FT3 confusion was found between FT2 and FT4, and some FT4 samples were misclassified in FT7. Nonetheless, integration of the brightness did not allow to correctly categorize the scarce samples of FT5, which were classified into FT7. The hit rates for the FT1 and FT7 fuel types improved by an average of 9% and 2%, respectively, with respect to the models using only GEDI variables, highlighting the very high hit rate in FT1, which reached a 100% hit rate with both SVM classification methods.

Finally, hit rates by fuel type were more balanced when classifying with RF than with SVM models. Complete results of the confusion matrices can be seen in Tables A.7, A.8, and A.9 of the Appendix.

Table 5. Comparison between Producer's accuracies and User's accuracies of Prometheus fuel types classification methods for the selected GEDI and Landsat-8 OLI variables (RH85 + PAI + AGBD + Brightness).

Fuel types	Producer's accuracy			User's accuracy		
	SVM-R	SVM-L	RF	SVM-R	SVM-L	RF
FT1	100.00%	100.00%	96.72%	89.71%	88.41%	92.19%
FT2	78.57%	69.05%	85.71%	89.79%	87.88%	81.82%
FT3	71.05%	73.68%	71.05%	72.97%	70.00%	79.41%
FT4	60.00%	63.33%	63.33%	62.07%	53.33%	70.37%
FT5	0.00%	0.00%	0.00%	0.00%	0.00%	0.00%
FT7	87.50%	87.50%	91.67%	85.71%	85.71%	86.27%

4. DISCUSSION

This study reveals that GEDI provides useful information for classifying Prometheus fuel types using derived variables from the L2A, L2B, and L4A footprint data sets products. However, high rates of confusion were reported in shrub fuel types when only GEDI variables were included in the models, hinting certain limitations of the sensor that has been minimized by integrating multispectral data, in particular the brightness index from Landsat-8 OLI images, improving the overall accuracy of the models, as well as reducing the confusion between fuel types. Nevertheless, it should be considered the uncertainty of our ground-truth data, which was the result of classification models of Prometheus fuel types in two previous studies in the same area, influencing in the classification accuracy of our results.

A first and essential step was to filter the high uncertainty GEDI data to select the highest quality sample. We used the "quality flag" attribute combined with other quality filters satisfactory used in previous GEDI-related studies, such as the removal of samples with degraded geolocation (e.g., Di Tommaso *et al.*, 2021), acquired during the day time (e. g., Fayad *et al.*, 2021a; Potapov *et al.*, 2021), or with high land cover heterogeneity (e.g., Dorado-Roda *et al.*, 2021). Many previous studies have also worked with only full-power laser beams (e.g., Potapov *et al.*, 2021; Rishmawi *et al.*, 2021), as coverage beams are

underpowered and could produce inaccurate estimations. In this way, Duncanson *et al*. (2020) found higher RMSE values for coverage laser beams than full-power laser beams for biomass estimations using simulated GEDI data. However, we did not notice any improvement on our classification models by working only with full-power laser beams, so we used all laser beams in order to not reduce our sample size too much. In fact, the filtering process led to work with 16% of the initial footprints, similar to Lang *et al*. (2021) and Rishmawi et al. (2021), who retained ~28% and ~11% of the GEDI initial footprints in their filtering process, respectively.

The comparison between the three classification methods showed that RF and SVM-R had the highest performances for modeling Prometheus fuel types. RF has been used in several previous GEDI-related works (e.g., Di Tommaso *et al*., 2021; Fayad *et al*., 2021b; Rishmawi *et al*., 2021; Leite *et al*., 2022; Liang *et al*., 2023) but, to the best of our knowledge, none have used SVM yet, which has proven to be an efficient classification method in several previous studies using ALS-LiDAR data (e.g., García *et al*., 2011; Jakubowksi *et al*., 2013; Domingo *et al*., 2020). The overall accuracies of RF and SVM-R models using only GEDI variables were slightly better to the ones obtained by Domingo *et al*. (2020), who achieved overall accuracies of 57% with SVM-R and 54% with RF using only ALS-LiDAR variables. In this sense, the lower accuracy obtained by Domingo *et al*. (2020) could be due to the higher size of the study area that comprised a higher heterogeneity and complexity of the Mediterranean forests dominated by three species of pines, oaks, and Portuguese oaks. The inclusion of the brightness from Landsat-8 OLI imagery with the GEDI variables resulted in a substantial improvement in the classification models. Other authors had already noticed the good agreement between GEDI and multispectral imagery. For instance, Potapov *et al*. (2021) estimated global forest canopy height using both GEDI and Landsat data. Rishmawi *et al*. (2021) extrapolated GEDI measurements at 1 km spatial resolution, by including the Visible Infrared Imaging Radiometer Suite instrument. Francini *et al*. (2022) analyzed multi-temporal Landsat imagery to monitor forest disturbances in Italy and observed that GEDI provided complementary information by being able to capture forest biomass changes due to that disturbances. Similarly, Liang *et al*. (2023) combined forest structural metrics from GEDI with Landsat spectral indices to quantify biomass losses over a 10- years period in Mozambique. Since this is the first study applied to classify forest fuels integrating GEDI with multispectral imagery, we cannot compare with similar previous studies, but our results confirm that it seems appropriate to integrate GEDI with multispectral sensors to obtain more robust results.

The classification of each fuel type showed the greatest confusion within the shrub fuel types (FT2, FT3, and FT4), being higher when the brightness was not integrated in the models. When exclusively using GEDI variables, RF had less confusion in shrub types with respect to SVM-R, which was quite high in FT2 in the latter. Confusion was also observed between FT4 and FT7, which is usual due to the vertical continuity of the strata in both types, making difficult to differentiate them, even in the field itself. In contrast, the error in FT1 and FT7, the best performing fuel types, was somewhat higher in RF than in SVM-R but both always showed high hit rates. Confusion between fuel types was substantially reduced when including the brightness, especially in the shrub fuel types, thus meaning that the combination of structure with spectral response of vegetation highlights forest attributes and allows better differentiation between Prometheus fuel types. When combining GEDI and Landsat, no omission errors were found in FT1 with both SVM models, and very few with RF. On the other hand, FT4 and FT7 were slightly better classified with RF. In addition, lower omission errors were found in FT2 when classifying with RF, although commission error were lower in SVM-R. The uncertainty associated with our ground-truth, which may have been propagated to our results leading to misclassifications of fuel types, must also be taken into account. In this way, study 1 found important confusions between FT2-FT3 and FT5-FT6, while in study 2 confusions were mainly located between FT5-FT6- FT7 and FT1-FT3. This could explain the confusion of the shrub strata and the complete misclassifications in FT5 in our case, since in both studies the confusion was significant. However, it is important to bear in mind that the number of initial samples of FT5 in our study was extremely low. In this sense, previous studies have also reported high confusion rates in shrub fuels using both discrete-return and full-waveform LiDAR sensors, and also in grassland fuel types, although this is not our case. For instance, Marino *et al*. (2016) noticed more error in fuel cover and height in mixed grassland and shrublands fuels using ALS data. Similarly, Domingo *et al*. (2020) obtained generally more confusion in the Prometheus shrub fuel types. Moreover, previous GEDI-related studies have found lower performances in herbaceous and shrublands fuels (e.g., Leite *et al*., 2022), as well as lower correlation coefficients in sparse forest types with predominance of shrub and herbaceous vegetation (e.g., Dorado-Roda *et al*., 2021). At this respect, Schneider *et al*. (2020) warned that worst model performances in lower strata may be due to the mixing of ground energy with energy returned from the understory. Leite *et al*. (2022) also suggest that spaceborne LiDAR signal may interact with lower strata less strongly than with tree strata. Regarding confusion in tree fuel types, the incorrect categorization of

the few FT5 samples in FT7 are in accordance with other studies, such as Domingo *et al*. (2020) and Huesca *et al*. (2019). However, the absence of FT6 and the scarcity of FT5 samples does not allow us to conclude significant results between these fuel types. In this context, future studies should include significant sample sizes of FT5 and FT6 to test GEDI's performance in classifying Prometheus trees fuel types.

The present study has shown the usefulness of GEDI data and its combination with spectral indices to classify Prometheus fuel types in a Mediterranean forest environment dominated by Aleppo pine. Since GEDI is still a novel source of information, further research on the use of this system to estimate forest fuels is needed in order to increase the knowledge on its capabilities and limitations. Based on the successful results obtained by integrating GEDI with Landsat-8 OLI data, it may be of interest to explore the combination of GEDI variables with other remote sensing datasets, such as the NASA's ATLAS system, regional or national LiDAR surveys, SAR sensors or another multispectral data, which would be of great value to predict fire behavior in large areas in order to mitigate the negative effects of forest fires over environment.

5. CONCLUSIONS

This study has provided an initial evaluation of GEDI's ability to estimate Prometheus fuel types in Mediterranean forest environments using the GEDI footprint-level products L2A, L2B, and L4A of release version 2. In addition, we have assessed the effect of integrating Landsat- 8 OLI spectral indices with GEDI variables for the improvement of classification models. A quality filtering process was applied to the GEDI data, and the Spearman's correlation coefficient and the Kruskal-Wallis and Dunn's tests were chosen to select the relevant variables for forest fuels modelling: RH85, PAI, and AGBD from GEDI, and the brightness from Landsat-8 OLI. RF and SVM with radial kernel were the best classification methods, showing a significantly better model performance integrating the brightness with the three GEDI variables. Overall, the classification of fuel types was less accurate for shrub fuels, with much confusion between these types of fuels when only GEDI variables were introduced in the models and being lower integrating multispectral information. Given the results obtained in this study, it has been proven that GEDI footprint-level variables are useful for forest fuels modeling in forested areas where there is no availability of other LiDAR data, or for estimating forest fuels at a large spatial extent.

REFERENCES

Albini, F., 1976. Estimating wildfire behavior and effects. USDA Forest Service, Intermountain Forest and Range Experiment Station, General Technical Report INT- 30, 92 pp.

Ashworth, A., Evans, D.L., Cookie, W.H., Londo, A., Collins, C., and Neuenschwander, A., 2010. Predicting southeastern forest canopy heights and fire fuel models using GLAS data. *Photogramm. Eng. Remote Sens.* 76 (8), 915–922. https://doi.org/10.14358/PERS.76.8.915.

Decuyper, M., Chávez, R.O., Lohbeck, M., Lastra, J.A., Tsendbazar, N., Hackländer, J., Herold, M., and Vågen, T.G., 2022. Continuous monitoring of forest change dynamics with satellite time series. *Remote Sens. Environ.* 269, 112829 https://doi.org/10.1016/J.RSE.2021.112829.

Di Tommaso, S., Wang, S., and Lobell, D.B., 2021. Combining GEDI and Sentinel-2 for wall- to-wall mapping of tall and short crops. *Environ. Res. Lett.* 16 (12) https://doi.org/10.1088/1748-9326/ac358c.

Domingo, D., de la Riva, J., Lamelas, M.T., García-Martín, A., Ibarra, P., Echeverría, M., and Hoffrén, R., 2020. Fuel type classification using airborne laser scanning and Sentinel- 2 data in Mediterranean forest affected by wildfires. *Remote Sens.* 12 (21), 1–22. https://doi.org/10.3390/rs12213660.

Dorado-Roda, I., Pascual, A., Godinho, S., Silva, C.A., Botequim, B., Rodríguez-Gonzálvez, P., González-Ferreiro, E., and Guerra-Hernández, J., 2021. Assessing the accuracy of GEDI data for canopy height and aboveground biomass estimates in Mediterranean forests. *Remote Sens.* 13 (12), 2279. https://doi.org/10.3390/rs13122279.

Dubayah, R., Blair, J.B., Goetz, S., Fatoyinbo, L., Hansen, M., Healey, S., Hofton, M., Hurtt, G., Kellner, J., Luthcke, S., Armston, J., Tang, H., Duncanson, L., Hancock, S., Jantz, P., Marselis, S., Patterson, P.L., Qi, W., and Silva, C.A., 2020. The Global Ecosystem Dynamics Investigation: High-resolution laser ranging of the Earth's forests and topography. *Science of Remote Sens.* 1, 100002 https://doi.org/10.1016/j.srs.2020.100002.

Dubayah R., Hofton, M., Blair, J.B., Armston, J., Tang, H., and Luthcke, S., 2020a. GEDI L2A Elevation and Height Metrics Data Global Footprint Level V001. NASA EOSDIS Land Processes DAAC.

Dubayah, R., Hofton, M., Blair, J., Armston, J., Tang, H., and Luthcke, S., 2021a. GEDI L2A Elevation and Height Metrics Data Global Footprint Level V002. NASA EOSDIS Land Processes DAAC. Accessed 2022-12-08 from https://doi.org/10.5067/GEDI/GEDI02_A.002.

Dubayah, R., Tang, H., Armston, J., Luthcke, S., Hofton, M., and Blair, J., 2021b. GEDI L2B Canopy Cover and Vertical Profile Metrics Data Global Footprint Level V002 [Data set]. NASA EOSDIS Land Processes DAAC. Accessed 2022-12-08 from https://doi.org/10.5067/GEDI/GEDI02_B.002.

Dubayah, R., Luthcke, S., Blair, J., Hofton, M., Armston, J., and Tang, H., 2021c. GEDI L1B Geolocated Waveform Data Global Footprint Level V002 [Data set]. NASA EOSDIS Land Processes DAAC. Accessed 2022-12-08 from https://doi.org/10.5067/GEDI/GEDI01_B.002.

Dubayah, R., Armston, J., Kellner, J.R., Duncanson, L., Healey, S.P., Patterson, P.L., Hancock, S., Tang, H., Bruening, J., Hofton, M.A., Blair, J.B., and Luthcke, S.B., 2022. GEDI L4A Footprint Level Aboveground Biomass Density, Version 2.1. ORNL DAAC, Oak Ridge, Tennessee, USA. https://doi.org/10.3334/ORNLDAAC/2056.

Duncanson, L., Neuenschwander, A., Hancock, S., Thomas, N., Fatoyinbo, T., Simard, M., Silva, C.A., Armston, J., Luthcke, S.B., Hofton, M., Kellner, J.R., and Dubayah, R., 2020. Biomass estimation from simulated GEDI, ICESat-2 and NISAR across environmental gradients in Sonoma County. California. *Remote Sens. Environ.* 242 https://doi.org/10.1016/j.rse.2020.111779.

Evans, J.S. and Hudak, A.T., 2007. A multiscale curvature algorithm for classifying discrete return LiDAR in forested environments. *IEEE Trans. Geosci. Remote Sens.* 45 (4), 1029–1038. https://doi.org/10.1109/TGRS.2006.890412.

Fayad, I., Baghdadi, N., and Riedi, J., 2021a. Quality assessment of acquired GEDI waveforms: Case study over France. Tunisia and French Guiana. *Remote Sens.* 13, 3144. https://doi.org/10.3390/rs13163144.

Fayad, I., Ienco, D., Baghdadi, N., Gaetano, R., Alvares, C.A., Stape, J.L., Ferraço Scolforo, H., and le Maire, G., 2021b. A CNN-based approach for the estimation of canopy heights and wood volume from GEDI waveforms. *Remote Sens. Environ.* 265 https://doi.org/10.1016/j.rse.2021.112652.

Ferraz, A., Saatchi, S., Mallet, C., and Meyer, V., 2016. Lidar detection of individual tree size in tropical forests. *Remote Sens. Environ.* 183, 318–333. https://doi.org/10.1016/J.RSE.2016.05.028.

Flannigan, M.D., Stocks, B.J., and Wotton, B.M., 2000. Climate change and forest fires. *Sci. Total Environ.* 262, 221–229. https://doi.org/10.1016/S0048-9697(00)00524-6.

Francini, S., D'Amico, G., Vangi, E., Borghi, C., and Chirici, G., 2022. Integrating GEDI and Landsat: Spaceborne LiDAR and four decades of forest disturbances and biomass changes in Italy. *Sensors* 22, 2015. https://doi.org/10.3390/s22052015.

García, M., Riaño, D., Chuvieco, E., Salas, J., and Danson, F.M., 2011. Multispectral and LiDAR data fusion for fuel type mapping using Support Vector Machine and decision rules. *Remote Sens. Environ.* 115 (6), 1369–1379. https://doi.org/10.1016/j.rse.2011.01.017.

García, M., Popescu, S., Riaño, D., Zhao, K., Neuenschwander, A., Agca, M., and Chuvieco, E., 2012. Characterization of canopy fuels using ICESat/GLAS data. *Remote Sens. Environ.* 123, 81–89. https://doi.org/10.1016/j.rse.2012.03.018.

Gastellu-Etchegorry, J.P., Yin, T., Laurent, N., Grau, E., Rubio, J., Cook, B.D., Morton, D. C., and Sun, G., 2016. Simulation of satellite, airborne and terrestrial LiDAR with DART (I): Waveform simulation with quasi-Monte Carlo ray tracing. *Remote Sens. Environ.* 184, 418–435. https://doi.org/10.1016/j.rse.2016.07.010.

Gelabert, P.J., Montealegre, A.L., Lamelas, M.T., and Domingo, D., 2020. Forest structural diversity characterization in Mediterranean landscapes affected by fires using Airborne Laser Scanning data. *GIScience Remote Sens.* 57 (4), 497–509. https://doi.org/10.1080/15481603.2020.1738060.

Gorelick, N., Hancher, M., Dixon, M., Ilyushchenko, S., Thau, D., and Moore, R., 2017. Google Earth Engine: Planetary-scale geospatial analysis for everyone. *Remote Sens. Environ.* 202, 18–27. https://doi.org/10.1016/J.RSE.2017.06.031.

Guerra-Hernández, J. and Pascual, A., 2021. Using GEDI LiDAR data and Airborne Laser Scanning to assess height growth dynamics in fast-growing species: a showcase in Spain. *For. Ecosyst.* 8 (14) https://doi.org/10.1186/s40663-021-00291-2.

Hancock, S., Armston, J., Hofton, M., Sun, X., Tang, H., Duncanson, L.I., Kellner, J.R., and Dubayah, R., 2019. The GEDI Simulator: A large-footprint waveform LiDAR simulator for calibration and validation of spaceborne missions. *Earth Space Sci.* 6, 294–310. https://doi.org/10.1029/2018EA000506.

Hofton, M., Blair, J.B., Story, S., and Yi, D., 2019. Algorithm Theoretical Basis Document (ATBD) for GEDI transmit and receive waveform processing for L1 and L2 products. Goddard Space Flight Centre.

Huesca, M., Riaño, D., and Ustin, S.L., 2019. Spectral mapping methods applied to LiDAR data: Application to fuel type mapping. *Int. J. Appl. Earth Obs. Geoinf.* 74, 159–168. https://doi.org/10.1016/j.jag.2018.08.020.

Huete, A.R., 1988. A Soil-Adjusted Vegetation Index (SAVI). *Remote Sens. Environ.* 25, 295–309. https://doi.org/10.1016/0034-4257(88)90106-X.

Jakubowksi, M.K., Guo, Q., Collins, B., Stepehns, S., and Kelly, M., 2013. Predicting surface fuel models and fuel metrics using LiDAR and CIR imagery in a dense, mountainous forest. *Photogramm. Eng. Remote Sens.* 79 (1), 37–49. https://doi.org/10.14358/PERS.79.1.37.

Jiang, F., Zhao, F., Ma, K., Li, D., and Sun, H., 2021. Mapping the forest canopy height in northern China by synergizing ICESat-2 with Sentinel-2 using a stacking algorithm. *Remote Sens.* 13 (8), 1535. https://doi.org/10.3390/rs13081535.

Kauth, R.J. and Thomas, G.S., 1976. The Tasseled Cap—A Graphic Description of the Spectral-Temporal Development of Agricultural Crops as Seen by Landsat. *Proceedings, Symposium on Machine Processing of Remotely Sensed Data*, Purdue University, West Lafayette, IN, 29 June-1 July 1976, 41–51.

Kristensen, T., Næsset, E., Ohlson, M., Bolstad, P.V., and Kolka, R., 2015. Mapping above- and below-ground carbon pools in boreal forests: The case for airborne LiDAR. *PLOS ONE* 10, e0138450.

Kuhn, M., 2008. Building Predictive Models in R Using the caret Package. *Journal of Statistical Software* 28 (5), 1–26. https://doi.org/10.18637/jss.v028.i05.

Lang, N., Kalischek, N., Armston, J., Schindler, K., Dubayah, R., and Wegner, J.D., 2021. Global canopy height regression and uncertainty estimation from GEDI LiDAR waveforms with deep ensembles. *Remote Sens. Environ.* 268, 112760 https://doi.org/10.1016/j.rse.2021.112760.

Leite, R.V., Silva, C.A., Broadbent, E.N., do Amaral, C.H., Liesenberg, V., de Almeida, D. R.A., Mohan, M., Godinho, S., Cardil, A., Hamamura, C., de Faria, B.L., Brancalion, P.H.S., Hirsch, A., Marcatti, G.E., Dalla Corte, A.P., Zambrano, A.M.A., da Costa, M.B.T., Matricardi, E.A.T., da Silva, A.L., *et al*., 2022. Large scale multi-layer fuel load characterization in tropical savanna using GEDI spaceborne LiDAR data. *Remote Sens. Environ.* 268, 112764 https://doi.org/10.1016/j.rse.2021.112764.

Liang, M., Duncanson, L., Silva, J.A., and Sedano, F., 2023. Quantifying aboveground biomass dynamics from charcoal degradation in Mozambique using GEDI Lidar and Landsat. *Rem. Sens. Environ.* 284, 113367 https://doi.org/10.1016/j.rse.2022.113367.

Liaw, A. and Wiener, M., 2002. Classification and Regression by randomForest. R News 2 (3), 18–22.

Lin, X., Xu, M., Cao, C., Dang, Y., Bashir, B., Xie, B., and Huang, Z., 2020. Estimates of forest canopy height using a combination of icesat-2/atlas data and stereo- photogrammetry. *Remote Sens.* 12 (21), 1–21. https://doi.org/10.3390/rs12213649.

Liu, H.Q. and Huete, A.R., 1995. A feedback based modification of the NDVI to minimize canopy background and atmospheric noise. *IEEE Trans. Geosci. Remote Sens.* 33, 457–465. https://doi.org/10.1109/TGRS.1995.8746027.

Marino, E., Ranz, P., Tomé, J.L., Noriega, M.A., Esteban, J., and Madrigal, J., 2016. Generation of high-resolution fuel model maps from discrete airborne laser scanner and Landsat-8 OLI: A low-cost and highly updated methodology for large areas. *Remote Sens. Environ.* 187, 267–280. https://doi.org/10.1016/j.rse.2016.10.020.

Masek, J.G., Vermote, E.F., Saleous, N.E., Wolfe, R., Hall, F.G., Huemmrich, K.F., Gao, F., Kutler, J., and Lim, T.-K., 2006. A Landsat surface reflectance dataset for North America, 1990–2000. *IEEE Geosci. Remote Sens. Lett.* 3 (1), 68–72. https://doi.org/10.1109/LGRS.2005.857030.

McGaughey, R.J., 2009. FUSION/LDV: Software for LIDAR Data Analysis and Visualization V.4.21. USDA Forest Service. Washington DC, USA.

Meyer, D., Dimitriadou, E., Hornik, K., Weingessel, A., and Leisch, F., 2020. e1071: Misc Function of the Department of Statistics, Probability Theory Group (Formerly: E1071). TU Wien. R package version 1.7–11. Available at: https://cran.r-project.org/web/packages/e1071 (accessed 20 Jun 2022).

Montealegre, A.L., Lamelas, M.T., and de la Riva, J., 2015b. Interpolation routines assessment in ALS-derived Digital Elevation Models development for forestry applications. *Rem. Sens.* 7(7), 8631-8654, https://doi.org.10.3390/rs70708631.

Montealegre, A.L., Lamelas, M.T., García-Martín, A., de la Riva, J., and Escribano, F., 2015c. Cartografía de modelos de combustible mediante combinación de imágenes LiDAR, SAR y ópticas en el Centro de Adiestramiento "San Gregorio". In Montealegre, A.L., Lamelas, M.T., de la Riva, J. Aplicaciones forestales de los datos LiDAR-PNOA en ambiente mediterráneo: su filtrado e interpolación y el modelado de parámetros estructurales con apoyo de trabajo de campo. PhD Thesis. https://zaguan.unizar.es/record/61353.

Montealegre, A.L., Lamelas, M.T., and de la Riva, J., 2015a. A comparison of open-source LiDAR filtering algorithms in a Mediterranean forest environment. *IEEE J. Sel. Top. Appl. Earth Obs. Remote Sens.* 8 (8), 4072–4085. https://doi.org/10.1109/JSTARS.2015.2436974.

Montealegre, A.L., Lamelas, M.T., de la Riva, J., García-Martín, A., and Escribano, F., 2016. Use of low points density ALS data to estimate stand-level structural variables in Mediterranean Aleppo pine forest. *Forestry* 89 (4), 373–382. https://doi.org/10.1093/forestry/cpw008.

Narine, L.L., Popescu, S.C., and Malambo, L., 2019. Synergy of ICESat-2 and Landsat for mapping forest aboveground biomass with deep learning. *Remote Sens.* 11 (12), 1503. https://doi.org/10.3390/rs11121503.

Narine, L.L., Popescu, S.C., and Malambo, L., 2020. Using ICESat-2 to estimate and map forest aboveground biomass: A first example. *Remote Sens.* 12 (11), 1824. https://doi.org/10.3390/rs12111824.

Oliveira, S., Oehler, F., San Miguel-Ayanz, J., Camia, A., and Pereira, J.M.C., 2012. Modeling spatial patterns of fire occurrence in Mediterranean Europe using Multiple Regression and Random Forest. *For. Ecol. Manag.* 275, 117–129. https://doi.org/10.1016/j.foreco.2012.03.003.

Peterson, B., Nelson, K., and Wylie, B., 2013. Towards Integration of GLAS into a National Fuel Mapping Program. *Photogramm. Eng. Remote Sens.* 2 (9), 175–183. https://doi.org/10.14358/PERS.79.2.175.

Pontius, R.G., Boersma, W., Castella, J.C., Clarke, K., de Nijs, T., Dietzel, C., Duan, Z., Fotsing, E., Goldstein, N., Kok, K., Koomen, E., Lippitt, C.D., McConnell, W., Sood, A. M., Pijanowski, B., Pithadia, S., Sweeney, S., Trung, T.N., Veldkamp, A.T., and Verburg, P.H., 2008. Comparing the input, output, and validation maps for several models of land change. *Ann. Reg. Sci.* 42, 11–37. https://doi.org/10.1007/s00168-007-0138-2.

Potapov, P., Li, X., Hernández-Serna, A., Tyukavina, A., Hansen, M.C., Kommareddy, A., Pickens, A., Turubanova, S., Tang, H., Silva, C.A., Armston, J., Dubayah, R., Blair, J. B., and Hofton, M., 2021. Mapping global forest canopy height through integration of GEDI and Landsat data. *Remote Sens. Environ.* 253, 112165 https://doi.org/10.1016/j.rse.2020.112165.

Prometheus, 1999. Management techniques for optimization of suppression and minimization of wildfires effects. System Validation. European Commission, DG XII, ENVIR & CLIMATE, Contract Number ENV4-CT98-0716. European Commission, Luxembourg.

Puletti, N., Grotti, M., Ferrara, C., and Chianucci, F., 2020. Lidar-based estimates of aboveground biomass through ground, aerial, and satellite observation: a case study in a Mediterranean forest. *J. Appl. Remote Sens.* 14 (4), 4501. https://doi.org/10.1117/1.jrs.14.044501.

R Core Team, 2020. R: A language and environment for statistical computing. R Foundation for Statistical Computing. Vienna, Austria. Available at: https://www.R-project.org/ (accessed 20 Jun 2022).

Renslow, M., 2013. Manual of Airborne Topographic Lidar. ASPRS, Bethesda, MD.

Revilla, S., Lamelas, M.T., Domingo, D., de la Riva, J., Montorio, R., Montealegre, A.L., and García-Martín, A., 2021. Assessing the potential of the DART model to discrete return LiDAR simulation—Application to fuel type mapping. *Remote Sens.* 13 (3), 1–21. https://doi.org/10.3390/rs13030342.

Riaño, D., Chuvieco, E., Salas, J., Palacios-Orueta, A., and Bastarrica, A., 2002. Generation of fuel type maps from Landsat TM images and ancillary data in Mediterranean ecosystems. *Can. J. For. Res.* 32, 1301–1315. https://doi.org/10.1139/x02-052.

Rishmawi, K., Huang, C., and Zhan, X., 2021. Monitoring key forest structure attributes across the conterminous United States by integrating GEDI LiDAR measurements and VIIRS data. *Remote Sens.* 13 (3), 1–23. https://doi.org/10.3390/RS13030442.

Rothermel, C., 1972. A mathematical model for predicting fire spread in wildland fuels. Research Papers, INT-115. Ogden, UT: U.S. Department of Agriculture, Intermountain Forest and Range Experiment Station. 40 p.

Rouse, J.W., Haas, R.H., Schell, J.A., and Deering, D.W., 1974. Monitoring Vegetation Systems in the Great Plains with ERTS. Third ERTS-1 Symposium NASA, NASA SP- 351, Washington DC, 309–317.

Roy, D.P., Kashongwe, H.B., and Armston, J., 2021. The impact of geolocation uncertainty on GEDI tropical forest canopy height estimation and change monitoring. *Science of Remote Sens.* 4, 100024. https://doi.org/10.1016/J.SRS.2021.100024.

Schneider, F.D., Ferraz, A., Hancock, S., Duncanson, L.I., Dubayah, R.O., Pavlick, R.P., and Schimel, D.S., 2020. Towards mapping the diversity of canopy structure from space with GEDI. *Environ. Res. Lett.* 15 (11), 5006. https://doi.org/10.1088/1748-9326/ab9e99.

Silva, C.A., Duncanson, L., Hancock, S., Neuenschwander, A., Thomas, N., Hofton, M., Fatoyinbo, L., Simard, M., Marshak, C.Z., Armston, J., Lutchke, S., and Dubayah, R., 2021. Fusing simulated GEDI, ICESat-2 and NISAR data for regional aboveground biomass mapping. *Remote Sens. Environ.* 253, 112234. https://doi.org/10.1016/j.rse.2020.112234.

Silva, C.A., Hamamura, C., Valbuena, R., Hancock, S., Cardil, A., Broadbent, E.N., Almeida, D.R.A., Silva Junior C.H.L., and Klauberg, C., 2020. rGEDI: NASA's Global Ecosystem Dynamics Investigation (GEDI) data visualization and processing. version 0.1.8, Available at: https://github.com/carlos-alberto-silva/rGEDI (accessed 20 Jun 2022).

APPENDIX

Table A.1. Results from Spearman's correlation coefficient (ρ***)*** of the most significant GEDI and Landsat-8 OLI variables.

Variable	Source	ρ
Brightness	Landsat-8 OLI	-0.924
Wetness	Landsat-8 OLI	0.874
EVI	Landsat-8 OLI	0.854
NDMI	Landsat-8 OLI	0.845
NDVI	Landsat-8 OLI	0.833
SAVI	Landsat-8 OLI	0.833
RH85	GEDI L2A	0.796
RH90	GEDI L2A	0.796
RH80	GEDI L2A	0.791
RH95	GEDI L2A	0.786
RH75	GEDI L2A	0.781
AGBD	GEDI L4A	0.777
RH70	GEDI L2A	0.770
RH98	GEDI L2A	0.770
RH99	GEDI L2A	0.756
RH65	GEDI L2A	0.747
RH100	GEDI L2A	0.725
RH60	GEDI L2A	0.705
RH55	GEDI L2A	0.636
PAI	GEDI L2B	0.621
Greenness	Landsat-8 OLI	0.607
TCC	GEDI L2B	0.607
PAVD	GEDI L2B	0.597
FHD	GEDI L2B	0.567
RH50	GEDI L2A	0.551
RH45	GEDI L2A	0.467
RH40	GEDI L2A	0.380
RH35	GEDI L2A	0.287
RH30	GEDI L2A	0.200
RH0	GEDI L2A	-0.191
RH5	GEDI L2A	-0.170
RH25	GEDI L2A	0.126
RH10	GEDI L2A	-0.095
RH20	GEDI L2A	0.061
RH15	GEDI L2A	-0.022

Table A.2. Results from Kruskal-Wallis test (H) of the most significant GEDI and Landsat-8 OLI variables to distinguish Prometheus fuel types. All variables were statistically significant (p-value < 0.05).

Variable	Source	H chi-square coefficient
Brightness	Landsat-8 OLI	952.65
Wetness	Landsat-8 OLI	888.75
NDMI	Landsat-8 OLI	862.27
EVI	Landsat-8 OLI	856.08
NDVI	Landsat-8 OLI	837.18
SAVI	Landsat-8 OLI	837.13
Greenness	Landsat-8 OLI	733.49
RH90	GEDI L2A	722.93
RH85	GEDI L2A	721.79
RH80	GEDI L2A	711.49
RH95	GEDI L2A	707.78
RH75	GEDI L2A	694.07
AGBD	GEDI L4A	685.20
RH98	GEDI L2A	678.81
RH70	GEDI L2A	673.08
RH99	GEDI L2A	655.96
RH65	GEDI L2A	633.43
RH100	GEDI L2A	601.94
RH60	GEDI L2A	569.73
RH55	GEDI L2A	484.24
PAI	GEDI L2B	472.72
TCC	GEDI L2B	457.69
PAVD	GEDI L2B	446.34
RH50	GEDI L2A	406.36
FHD	GEDI L2B	363.86
RH45	GEDI L2A	361.41
RH40	GEDI L2A	341.41
RH35	GEDI L2A	336.29
RH30	GEDI L2A	327.98
RH25	GEDI L2A	316.68
RH20	GEDI L2A	313.88
RH15	GEDI L2A	298.94
RH10	GEDI L2A	290.62
RH5	GEDI L2A	282.01
RH0	GEDI L2A	167.47

Table A.3. Results from Dunn's test of the most significant GEDI and Landsat-8 OLI variables to distinguish Prometheus fuel types.

Number of significant pairs	Variable(s)
14	RH60
13	RH50, RH55, RH65, RH70, RH75, RH80, RH85, RH90, PAI, PAVD, TCC
12	RH5, RH10, RH15, RH20, RH25, RH30, RH95, RH98, RH99, AGBD, Brightness
11	RH100, FHD, EVI, NDMI, NDVI, SAVI, Wetness
10	RH35, RH45, Greenness
9	RH40

Table A.4. Confusion matrix of the SVM-R model (overall accuracy = 61.54%; kappa: 0.51) for the selected GEDI variables (RH85 + PAI + AGBD).

Fuel types	FT1	FT2	FT3	FT4	FT5	FT7	Prod.'s accuracy
FT1	**57**	20	0	0	0	0	74.03%
FT2	4	**10**	6	4	0	4	35.71%
FT3	0	8	**20**	14	0	1	46.51%
FT4	0	0	6	**8**	0	2	50.00%
FT5	0	0	0	0	**0**	0	0.00%
FT7	0	4	6	4	2	**41**	71.93%
User's accuracy	93.44%	23.81%	52.63%	26.67%	0.00%	85.42%	

Table A.5. Confusion matrix of the SVM-L model (overall accuracy = 57.46%; kappa = 0.45) for the selected GEDI variables (RH85 + PAI + AGBD).

Fuel types	FT1	FT2	FT3	FT4	FT5	FT7	Prod.'s accuracy
FT1	**57**	21	0	0	0	0	73.08%
FT2	4	**11**	13	11	0	2	26.83%
FT3	0	3	**8**	4	0	1	50.00%
FT4	0	2	8	**10**	0	4	41.67%
FT5	0	0	0	0	**0**	0	0.00%
FT7	0	5	9	5	2	**41**	66.13%
User's accuracy	93.44%	26.19%	21.05%	33.33%	0.00%	85.42%	

Table A.6. Confusion matrix of the RF model (overall accuracy = 61.54%; kappa = 0.51) for the selected GEDI variables (RH85 + PAI + AGBD).

Fuel types	FT1	FT2	FT3	FT4	FT5	FT7	Prod.'s accuracy
FT1	**51**	14	1	0	0	0	77.27%
FT2	6	**13**	6	4	0	2	41.94%
FT3	4	8	**18**	9	0	3	42.86%
FT4	0	4	9	**13**	0	2	46.43%
FT5	0	0	0	0	**0**	0	0.00%
FT7	0	3	4	4	2	**41**	75.93%
User's accuracy	83.61%	30.95%	47.67%	43.33%	0.00%	85.42%	

Table A.7. Confusion matrix of the SVM-R model (overall accuracy = 81.90%; kappa = 0.77) for the selected GEDI and Landsat-8 OLI variables (RH85 + PAI + AGBD + Brightness).

Fuel types	FT1	FT2	FT3	FT4	FT5	FT7	Prod.'s accuracy
FT1	**61**	7	0	0	0	0	89.71%
FT2	0	**33**	4	0	0	0	89.79%
FT3	0	2	**27**	7	0	1	72.97%
FT4	0	0	5	**18**	1	5	62.07%
FT5	0	0	0	0	**0**	0	0.00%
FT7	0	0	2	4	1	**42**	85.71%
User's accuracy	100.0%	78.57%	71.05%	60.00%	0.00%	87.50%	

Table A.8. Confusion matrix of the SVM-L model (overall accuracy = 81.00%; kappa = 0.76) for the selected GEDI and Landsat-8 OLI variables (RH85 + PAI + AGBD + Brightness).

Fuel types	FT1	FT2	FT3	FT4	FT5	FT7	Prod.'s accuracy
FT1	**61**	8	0	0	0	0	88.41%
FT2	0	**29**	4	0	0	0	87.88%
FT3	0	5	**28**	6	0	1	70.00%
FT4	0	0	5	**19**	1	5	63.33%
FT5	0	0	0	0	**0**	0	0.00%
FT7	0	0	1	5	1	**42**	85.71%
User's accuracy	100.0%	69.05%	73.68%	63.33%	0.00%	87.50%	

Table A.9. Confusion matrix of the RF model (overall accuracy = 83.71%; kappa = 0.79) for the selected GEDI and Landsat-8 OLI variables (RH85 + PAI + AGBD + Brightness).

Fuel types	FT1	FT2	FT3	FT4	FT5	FT7	Prod.'s accuracy
FT1	**59**	5	0	0	0	0	92.19%
FT2	2	**36**	5	0	0	1	81.82%
FT3	0	1	**27**	6	0	0	79.41%
FT4	0	0	5	**19**	0	3	70.37%
FT5	0	0	0	1	**0**	0	0.00%
FT7	0	0	1	4	2	**44**	86.27%
User's accuracy	96.72%	85.71%	71.05%	63.33%	0.00%	91.67%	

The *eBee Classic* UAV system. Photograph by Raúl Hoffrén.

CHAPTER 4

PHOTOGRAMMETRIC POINT CLOUDS AND MULTISPECTRAL INDICES FROM AN OPTICAL UAV FOR FOREST FUEL ESTIMATION

This chapter corresponds to:

Hoffrén, R., Lamelas, M.T., and de la Riva, J., 2023. UAV-derived photogrammetric point clouds and multispectral indices for fuel estimation in Mediterranean forests. *Remote Sensing Applications: Society and Environment* 31, 100997.

https://doi.org/10.1016/j.rsase.2023.100997

UAV-derived photogrammetric point clouds and multispectral indices for fuel estimation in Mediterranean forests

Raúl Hoffrén[1,2,*], María Teresa Lamelas[2,3], Juan de la Riva[1,2].

[1] Department of Geography and Land Management, University of Zaragoza, Calle Pedro Cerbuna 12, 50009, Zaragoza, Spain.
[2] Geoforest Group, University Institute for Research in Environmental Sciences of Aragón (IUCA), University of Zaragoza, Spain.
[3] Centro Universitario de la Defensa, Academia General Militar, Ctra. Huesca s/n, 50090, Zaragoza, Spain.
[*] Corresponding author, email: rhoffren@unizar.es.

ABSTRACT

Sensors attached to unmanned aerial vehicles (UAVs) allow estimating a large number of forest attributes related to forest fuels. This study assesses photogrammetric point clouds and multispectral indices obtained from a fixed-wing UAV for the classification of Prometheus fuel types in 82 forest plots in Aragon (NE Spain). Images captured by an RGB camera and a multispectral sensor allowed generating high density photogrammetric point clouds (RGB: 3,000 points/m^2; multispectral: 85 points/m^2), which were normalized using alternatively a Digital Elevation Model (DEM) of 0.50, 1, and 2 m resolution. A set of structural and textural variables were derived from the normalized point cloud heights, and for the latter, the gray-level co-occurrence matrix (GLCM) approach was used. Multispectral images were also used to create seven spectral vegetation indices. The most relevant structural, textural, and spectral variables to introduce into the fuel types classification models were selected using Dunn's test, which included: the vegetation height at the 50th percentile, the coefficient of variation of the heights, the percentage of returns above 4 m, the mean textural dissimilarity, and the mean of the Green Chlorophyll Index. Three different data samples were introduced in the models: i) the relevant structural and textural variables from the RGB camera (RGB data sample); ii) the relevant structural, textural, and spectral variables from the multispectral sensor (MS data sample); and iii) the relevant structural and textural variables from the RGB camera plus the relevant spectral variable from the multispectral sensor (integrated data sample). After comparing three machine learning classification techniques (*Random Forest*, and linear and radial *Support Vector Machine*), the best results were obtained with *Random Forest* with k-fold cross-validation (k-10) and the integrated data sample with normalized point clouds at 0.50 m DEM resolution (overall accuracy = 71%). The variables successfully identified the Prometheus main fire carriers (i.e., shrubs or trees) and confusions were mainly located within the fuel types of the same dominant stratum, especially in fuel types FT3 and FT6. These results demonstrate the ability of UAV imagery to classify forest fuels in Mediterranean environments when RGB and multispectral data are combined.

1. INTRODUCTION

Forest fires are a recurrent disturbance of Mediterranean ecosystems (Oliveira *et al*., 2012). Moreover, their exposure to fire may grow in the future due to the increase of wildfires globally (Venäläinen *et al*., 2020; Varol *et al*., 2021), making these ecosystems even more vulnerable. Therefore, it is essential to understand fire behavior in a forest stand in order to mitigate the detrimental effects of wildfires on the environment. Forest fuels allow estimating and quantifying fire spread over vegetation to assess fire risk and develop mitigation plans (Ferraz *et al*., 2016). They consist of all living or dead organic matter available for combustion in a wildfire. They are usually grouped by fuel types associated with vegetation classes that exhibit similar fire behavior. Several fuel types classifications have been developed to identify forest fuels in heterogeneous environments (e.g., Rothermel, 1972; Albini, 1976), but one specifically to Mediterranean ecosystems: The Prometheus fuel model (Prometheus, 1999), which considers vegetation height, density, and vertical continuity as the main fire spreaders and comprises seven fuel types (FT) for three main fire carriers: FT1 for grasslands; FT2, FT3, and FT4 for shrublands; and FT5, FT6, and FT7 for tree canopies. Shrub fuel types are determined by areas with more than 60% shrub cover at different mean heights, which are 0.30–0.60 m for FT2, 0.60–2 m for FT3, and 2–4 m for FT4. In terms of tree canopy types, these areas are characterized by tree cover greater than 50% at more than 4 m, with no associated understory for FT5, with a vertical difference between understory and canopies greater than 0.5 m for FT6, and with complete vertical continuity of fuels for FT7.

In last decades, remote sensing has shown great potential for estimating forest attributes and identifying forest fuels. Specifically, Airborne Laser Scanners (ALS) have been widely used because of their ability to penetrate the canopy cover and provide accurate details of forest structure, allowing for a comprehensive assessment of forest fuels. Several studies have also shown that the integration of ALS with multispectral imagery improves the identification of fuel types (e.g., Marino *et al*., 2016; Domingo *et al*., 2020). Nevertheless, few studies have used sensors on unmanned aerial vehicles (UAVs) to identify forest fuels (e.g., Shin *et al*., 2018; Fernández-Álvarez *et al*., 2019; Hillman *et al*., 2021), despite their ability to collect vegetation spectral response from multispectral sensors with unprecedented spatial resolution, and to estimate vegetation structure and textural features from three-dimensional point clouds. The latter can be derived directly from active sensors, such as LiDAR, or

indirectly from optical images, such as RGB or multispectral sensors, through *Structure from Motion* algorithm, which is based on traditional photogrammetry (Messinger *et al*., 2016) using a collection of overlapping images taken from different viewpoints (Puliti *et al*., 2015). Although photogrammetric point clouds cannot penetrate the canopy, they can be an affordable option for estimating forest attributes over much more expensive LiDAR systems. For instance, photogrammetric point clouds were used by Fritz *et al*. (2013) to map tree stem in open stands, by Shin *et al*. (2018) to estimate fuels and forest canopy structure in a ponderosa pine stand, and by Carbonell-Rivera *et al*. (2022) to classify Mediterranean shrub species.

In this context, the main objective of this study is to assess the suitability of UAV-derived photogrammetric point clouds and multispectral indices for the identification of fuel types based on the Prometheus model in Mediterranean forest plots, as well as for their classification using machine learning techniques. We hypothesize that optical UAVs can be a cost-effective alternative to less affordable active sensors (such as ALS and LiDAR UAVs), as they are capable of estimating a wide range of forest attributes, including structural, textural and spectral features of vegetation using a single instrument, whereas with active sensors spectral information is lost. This capability ultimately allows the identification of forest fuels at an unprecedented detail, representing a very valuable and accessible tool to prevent and mitigate forest fires at local and regional scales in Mediterranean ecosystems.

2. MATERIALS AND METHODS

2.1. Study area

UAV flights were performed in 82 forest plots of 15 m of circular radius distributed in 5 sectors of the Aragon region (NE Spain) (Figure 1), located nearby Almudévar (12 plots), Ayerbe (36 plots), Uncastillo (11 plots), Villarluengo (15 plots), and Zuera (8 plots) The average annual temperature of the entire region is 12.3ºC. All the sectors have a Mediterranean climate, but there are differences between them. The Almudévar, Ayerbe and Zuera sectors are located in the center of the Ebro Valley, characterized by very hot summers and cold winters, high daily temperature gradients, and low rainfall localized mainly in the equinoctial seasons (Almudévar: ~350 mm/year; Ayerbe: ~700 mm/year; Zuera: ~250 mm/year). The Uncastillo sector is located at the interface between the Ebro Valley and the foothills of the Pre-Pyrenean mountain range, which results in lower daily and annual thermal gradients than in the center of

the valley, although still high, and mean annual rainfall of ~700 mm/year. The Villarluengo sector is placed in the Iberian mountain range, whit less hot summers and colder winters than in the other sectors due to its higher altitude, and a mean annual rainfall of ~600 mm/year. Convective storms can be frequent in late spring and summer in all sectors, but are especially important in the Villarluengo sector, where they are often accompanied by lightning that threaten the possibility of wildfires. The Prometheus fuel types for each plot were estimated in-situ in previous field work (see Montealegre *et al*., 2016 and Domingo *et al*., 2020), but they were validated in each flight campaign, constituting the ground-truth for the classification models (Table 1). Plots were selected using a stratified random sampling in order to ensure a wide range of different environments (i.e., slope, exposure, vegetation cover, etc.) and, thus, fuel types. The center of the plots was located using a *Leica VIVA*® GS15 CS10 GNSS real-time kinematic Global Positioning System with sub-meter accuracy. Plots were mainly dominated by grassland, shrublands, and forest of Aleppo pine (*Pinus halepensis* Mill.) and bog pine (*Pinus nigra* Mill.) with understory of oaks (*Quercus ilex* subsp. *rotundifolia*, *Quercus coccifera*, *Quercus faginea*), junipers (*Juniperus oxycedrus*), boxwood (*Buxus sempervirens*), rosemary (*Rosmarinus officinalis*), and thymes (*Thymus vulgaris*).

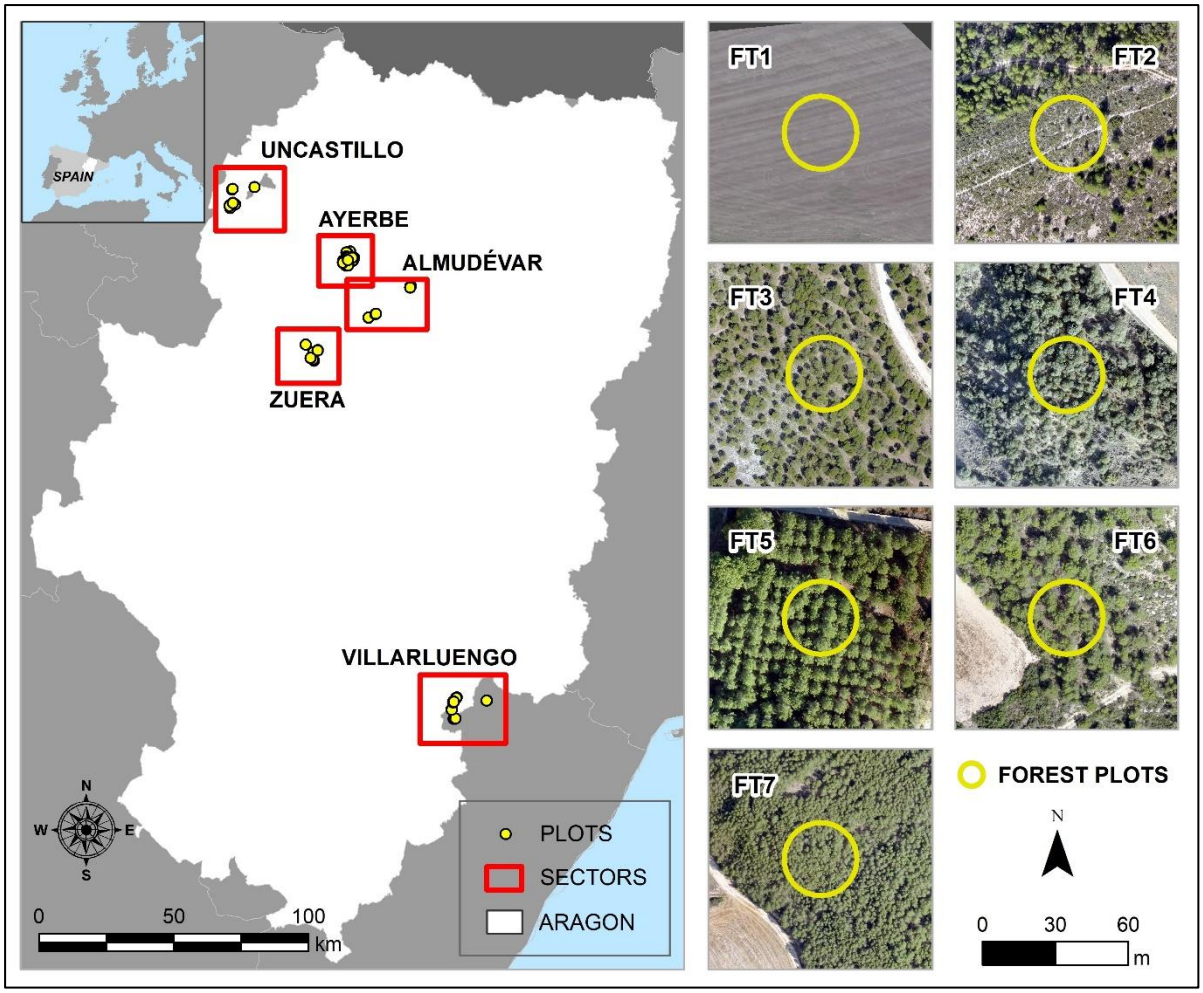

Figure 1. Study area and examples of seven circular plots, one for each Prometheus fuel type.

Table 1. Summary of the forest plots and their associated Prometheus fuel types.

	FT1	FT2	FT3	FT4	FT5	FT6	FT7
Number of plots	10	11	8	7	10	13	23

2.2. UAV data acquisition and processing

A fixed-wing UAV (*eBee Classic* of SenseFly) equipped with two optical sensors (RGB and multispectral) was used in this study (Figure 2). The RGB camera was a *SONY WX* camera of 18.2 MP resolution and the multispectral sensor (MS) was a *Parrot Sequoia* of 1.2 MP single band resolution with a sunshine sensor and capable of recording surface reflectance in the green (550 nm ± 40 nm), red (660 nm ± 40 nm), red-edge (735 nm ± 10 nm), and near infrared (790 nm ± 40 nm) spectral bands. A total of 49 flight campaigns were conducted between June and October 2021 over 82 plots, resulting in 12,007 individual images processed. Each campaign included two flights, one for each

sensor attached to the UAV, making a total of 98 flights. All of them were automated using *eMotion* v.3.5.0 software, with specified parameters including a serpentine mapping, a flight altitude of 116.5 m from the ground, an angle of incidence of 90º, and an overlap between photographs of 90%-80% (cross- and along-track, respectively). Radiometric calibration was performed on the multispectral sensor to adjust it to the prevailing light conditions. For this, we followed the manufacturer-recommended method, combining the use of a reference panel and the sunshine sensor for calibrating the images. According to Poncet *et al*. (2019), this procedure can be comparable to empirical calibration methods. Thus, we took four pictures of an *Airinov* calibration reference panel of known reflectance with the *Parrot Sequoia* camera prior to the start of each flight, while the sunshine sensor captured the current light conditions during the flights. The spatial resolutions of the RGB and multispectral images were 4 cm/px and 12 cm/px, respectively. Finally, in each flight area, at least four ground control points (GCPs) were measured with the *Leica VIVA*® GS15 CS10 GNSS. This allowed georeferencing the UAV images at centimetric scale to the ETRS89 – UTM zone 30N reference system, while the vertical coordinates were converted from WGS84 ellipsoidal heights to the EGM-96 geoidal heights model.

Figure 2. Above: (**a**) Main materials used in the study: SenseFly *eBee Classic* UAV unit with *SONY WX* camera and *Parrot Sequoia* multispectral sensor. Below: Examples of the same single image captured by the UAV in different spectral bands: (**b**) RGB; (**c**) Green band; (**d**) Red band; (**e**) Red-edge band; and (**f**) Near infrared band.

The data collected were processed using PIX4Dmapper v.4.5.6 software to obtain structural metrics, textural features, and spectral vegetation indices (Figure 3). Multispectral images, captured with the Parrot Sequoia camera, were automatically calibrated by the PIX4Dmapper software during data processing (Poncet *et al*., 2019). Structural data were obtained from photogrammetric point clouds using *Structure from Motion* and stereo-matching algorithms included in PIX4Dmapper. These algorithms enabled image alignment and multi-view stereo reconstruction by detecting and matching image feature points in the acquired highly overlapping images (Domingo *et al*., 2019). Two photogrammetric point cloud datasets were generated, one for each sensor, with a higher average density in the RGB point clouds (3,000 points/m^2) than in the multispectral point clouds (85 points/m^2). The "lidR" package (Roussel *et al*., 2020) for R environment v.4.2.0 (R Core Team, 2022) was used to clip both point cloud datasets in each forest plot and normalize their absolute heights. Normalization was performed using alternatively Digital Elevation Models (DEMs) with spatial resolutions of 0.50, 1, and 2 m, to examine the effect of DEM resolution on the accuracy of estimated heights and classification of forest fuels. DEMs were obtained from public ALS data from the PNOA project (*Spanish National Aerial Orthophotography Plan*). Noise and overlapping returns were removed, and ground points were classified following Montealegre *et al*. (2016) using the MCC-LiDAR v.2.1 command line tool (Evans and Hudak, 2007). The ground points were then interpolated using a TIN-to-Raster method (Renslow, 2013) to create the final DEMs. From the normalized UAV point clouds, a set of structural and textural variables was generated. Forest structural metrics were extracted at plot scale using FUSION/LDV v.4.21 software (McGaughey, 2021). They were related to height distribution (i.e., the minimum, mean and maximum elevation, and different height percentiles: P01, P05, P10.... P99), height variability (i.e., the coefficient of variation, kurtosis, skewness, standard deviation, and variance of the heights), and canopy cover density (i.e., statistics of the returns at different height strata: 0.60, 2 and 4 m). Textural features were calculated from the gray-level co-occurrence matrix (GLCM) (Haralick *et al*., 1973), using the "glcm" package for R environment (Zvoleff, 2020). GLCM were applied to previously created Canopy Height Models (CHM) in each plot using the *rasterize_canopy* function of the "lidR" package. Different window sizes were tested (3x3, 5x5, 7x7, and 9x9), with the 3x3 window providing the best results. Then, the mean values of four different offsets (0º, 45º, 90º, 135º) were analyzed and seven textural features were extracted at the three spatial resolutions of the DEM (contrast, dissimilarity, entropy, homogeneity, mean, second moment, and variance). Finally, four zonal

statistics were calculated for each plot-scale metric (minimum, maximum, mean, and median).

In addition, seven spectral vegetation indices were calculated from reflectance data of multispectral images: the *Advanced Vegetation Index* (AVI) (Equation 1; Roy *et al*., 1996), the *Green Chlorophyll Index* (GCI) (Equation 2; Gitelson *et al*., 2003), the *Green Normalized Difference Vegetation Index* (GNDVI) (Equation 3; Gitelson *et al*., 1996), the *Normalized Difference Red Edge Index* (NDRE) (Equation 4; Barnes *et al*., 2000), the *Normalized Difference Vegetation Index* (NDVI) (Equation 5; Rouse *et al*., 1974), the *Normalized Difference Water Index* (NDWI) (Equation 6; Gao, 1996), and the *Soil Adjusted Vegetation Index* (SAVI) (Equation 7; Huete *et al*., 1988). For each of the seven indices, the same four zonal statistics at plot scale as in the textural metrics were calculated.

$$AVI = [NIR \times (255 - R) \times (NIR - R)]^{1/3} \quad (1)$$

$$GCI = \left(\frac{NIR}{G}\right) - 1 \quad (2)$$

$$GNDVI = \frac{NIR - G}{NIR + G} \quad (3)$$

$$NDRE = \frac{NIR - RedEdge}{NIR + RedEdge} \quad (4)$$

$$NDVI = \frac{NIR - R}{NIR + R} \quad (5)$$

$$NDWI = \frac{G - NIR}{G + NIR} \quad (6)$$

$$SAVI = \frac{(1+L) \times (NIR - R)}{NIR + R + L} \quad (L = 0.5) \quad (7)$$

where *NIR* is near infrared band, *R* is red band, *G* is green band, *RedEdge* is red-edge band.

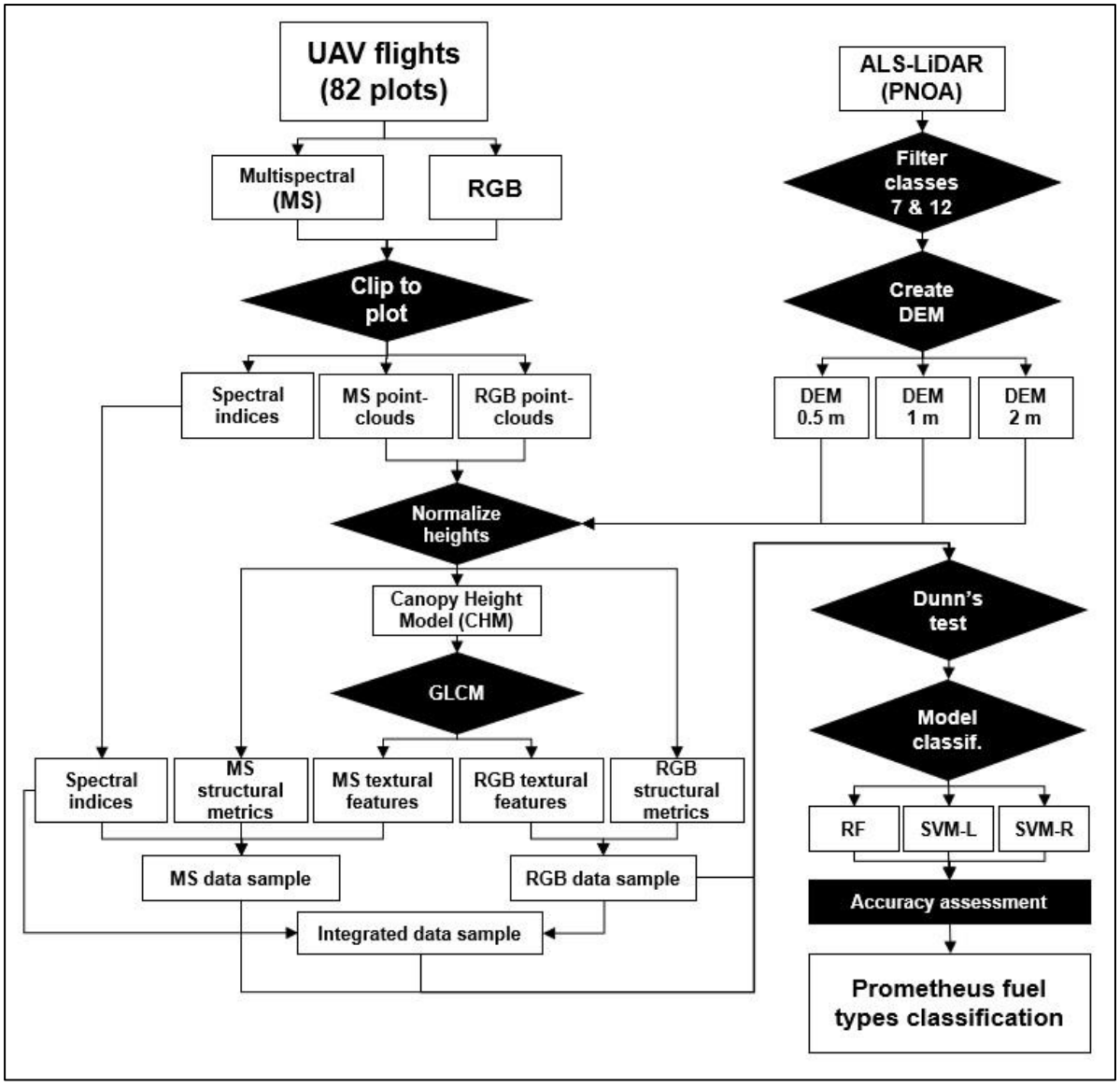

Figure 3. Methodological scheme of the study.

2.3. Prometheus fuel types classification and model validation

A total of 138 variables were generated for input into the classification models, which included 82 structural metrics, 28 textural features, and 28 spectral indices. The post hoc non-parametric Dunn's test of multiple comparison was used to select the most relevant variables. This method is similar to Kruskal-Wallis test but with the ability to determine the groups that are statistically different for the classification of forest attributes on machine learning models (García-Galar *et al*., 2023). From each of the three groups of variables, including the three subgroups of structural metrics, we finally selected those with a high ability to differentiate between the pairs for input into the classification models.

Three different data samples were tested: the relevant structural and textural variables from the RGB sensor (RGB data sample), the relevant structural,

textural, and spectral variables from the multispectral sensor (MS data sample), and the relevant structural and textural variables from the RGB sensor combined with the relevant spectral variable from the multispectral sensor (integrated data sample). For each of these three data samples, the three normalized point cloud datasets from the different DEM resolutions were tested, totalizing 9 data samples to introduce into the classification models. Three non-parametric predictive models were then tested through the "caret" package (Kuhn, 2008) for R environment: *Random Forest* (RF) and *Support Vector Machine* with both linear (SVM-L) and radial (SVM-R) kernels. RF classifiers were parametrized by applying between 2 to 10 decision trees at each node and SVM models were fitted by applying a cost parameter within the interval 1-1,000. Models were validated using the k-fold cross-validation method, recommended for small datasets (Anderson *et al*., 2005), testing in groups of 5 and 10 observations, and 10, 50, and 100 repeats in each case. Finally, the most accurate data sample, model, and validation method was assessed based on the overall accuracy (OA) coefficient and the producer's and user's accuracies of the confusion matrices, which are determined by the commission and omission errors, respectively (Pontius *et al*., 2008).

3. RESULTS

3.1. Most significant variables for the classification models

Dunn's test revealed the variables with the highest distinguishability among the 21 pairs of Prometheus fuel types. In general, Prometheus main fire carriers were well differentiated, while more difficulties were observed in fuels of the same dominant stratum. As shown in Figure 4, a maximum of 109 variables were able to differentiate between the FT1-FT7, which was the peer group with the highest distinguishing ability. High differentiation abilities were also found between FT2-FT5 (84 variables), FT1-FT6 (83 variables), FT1-FT5 (80 variables), FT3-FT5 (66 variables), FT2-FT7 (69 variables), and FT2-FT6 (60 variables). The ability to differentiate between grassland and shrub fuel types was somewhat lower (FT1-FT2: 40 variables; FT1-FT3: 29 variables; FT1-FT4: 35 variables). As for differentiation within tree fuel types, 39 variables differentiated between FT5-FT7, 9 variables between FT5-FT6, and only 2 variables between FT6-FT7. Finally, only 3 variables differentiated between FT2-FT4 shrub fuel types, and none of them distinguished between FT2-FT3 and FT3-FT4.

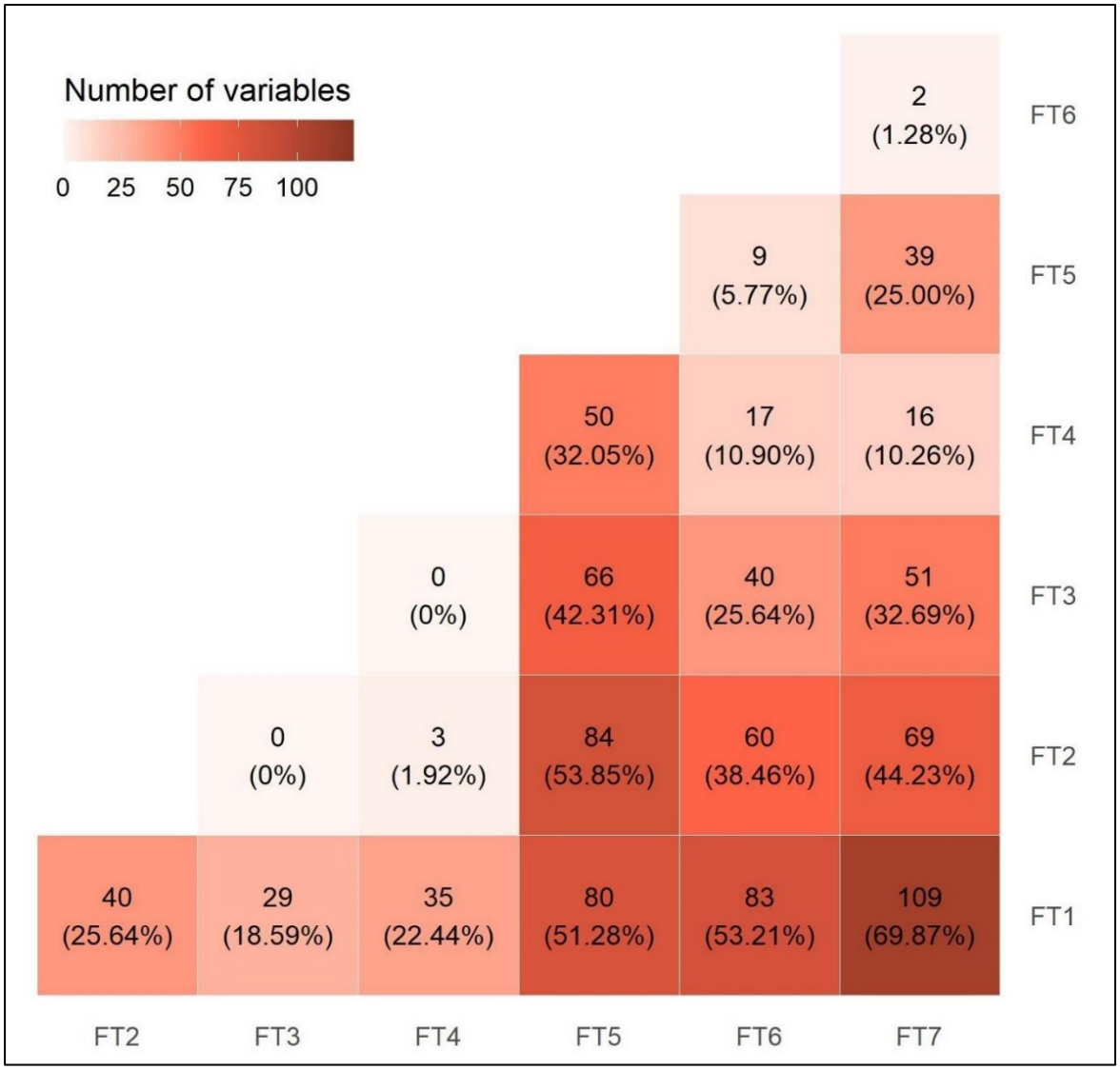

Figure 4. Number of variables and percentage with respect to the total of variables able to differentiate the 21 pairs of Prometheus fuel types according to Dunn's test.

Out of the three sub-groups of structural metrics, 9 variables related to vegetation height distribution were able to differentiate up to 11 pairs of fuel types, the coefficient of variation from the height variability subgroup distinguished 9 pairs, and 6 variables related to the canopy cover density were able to discern up to 12 pairs. In addition, 6 variables from the textural features statistics were able to distinguish up to 7 pairs, and 12 variables from the spectral indices statistics distinguished a maximum of 7 pairs. All relevant variables are shown in Table 2 and full results are described in Table A.1 of the Appendix.

Table 2. Relevant variables for their high ability to distinguish between pairs of Prometheus fuel types according to Dunn's test.

Groups of variables	Variables	Maximum number of pairs able to differentiate
Height distribution	Elev. maximum, Elev. P50–Elev. P99	11
Height variability	Elev. CV	9
Canopy cover density	Elev. strata > 4 m: max, mean, median, mode, return proportion; Percentage of returns > 4 m	12
Textural features	GLCM dissimilarity: mean; GLCM mean: max, median, min; GLCM variance: max, min	7
Spectral indices	GCI: max, mean, median; GNDVI: max, median; NDRE: max; NDVI: max, mean, median; NDWI: median, mean; SAVI: max	7

Based on the results obtained and in order to generate parsimonious models after testing different combinations, the variables selected from each group for inclusion in the classification models were the vegetation height at the 50th percentile, the coefficient of variation of the heights, the percentage of returns above 4 m, the mean dissimilarity, and the mean of the Green Chlorophyll Index (Table 3).

Table 3. Final variables introduced in the classification models.

Groups of variables	Variable	Description
Height distribution	Elev. P50	Vegetation height at the 50th percentile
Height variability	Elev. CV	Coefficient of variation of the heights
Canopy cover density	Percentage of returns > 4 m	Percentage of returns above 4 meters
Textural features	GLCM dissimilarity mean	Mean dissimilarity
Spectral indices	GCI mean	Mean of the Green Chlorophyll Index

3.2. Performance of Prometheus fuel types classification

The best performing models were obtained systematically using the integrated data sample and the RF classification method (Table 4). Overall, best k-fold cross validation method was obtained with 10 observations and 10 repeats in each case. The SVM-L and SVM-R models had significantly lower accuracies in all cases (see Tables A.2 and A.3 of the Appendix). The best classification of the Prometheus fuel types was reached with the point cloud normalized to the DEM of 0.50 m resolution, yielding an OA of 71%. When the MS data sample was introduced, the best OA was 7.58% lower than the integrated data sample (OA=66%) using the same DEM resolution to normalize the point cloud. The best OA of the RGB data sample was 10.94% and 3.13% lower than the integrated and MS data samples, respectively (OA=64%), in this case with the point cloud normalized to the DEM of 1 m resolution, although the classification with the 0.50 m DEM had very similar accuracies (OA=63%) (Table 4.4).

Table 4. Summary of overall accuracies of Prometheus fuel types classification for the nine RF model data samples with k-10 cross validation and 10 repeats in each case.

DEM resolution	**0.50 m**			**1 m**			**2 m**		
Data sample	RGB	MS	Integ.	RGB	MS	Integ.	RGB	MS	Integ.
Overall accuracy	63%	66%	71%	64%	61%	70%	59%	62%	65%

The confusion matrix of the best model shows the classification accuracy of each of the 7 Prometheus fuel types (Table 5). FT1 had the best hit rate, with a 98% of producer's accuracy and 83% of user's accuracy. FT2 and FT7 were the types with the best hit rate among the shrub and tree types, respectively, followed by FT4 and FT5. On the other hand, the highest confusion rates were found in FT3 and FT6. In general, confusions occurred between fuel types of the same main fire carrier, with some exceptions. For instance, a high percentage of FT3 plots were misclassified as FT2 and some as FT4, although commission errors due to incorrect classification in grasslands (FT1) were also found. Regarding confusion in FT6, many plots were misclassified as FT7 and, to a lesser extent, FT5, with no errors outside of tree fuel types. The main confusion between fuel types of different strata occurred between FT4 and FT7 (dense shrub and tree fuel types, respectively), and there were a few omission errors in FT1 due to misclassifications in FT3 and FT4. Regarding confusion matrices of the best MS

and RGB data samples (Tables A.4 and A.5 of the Appendix), more confusion rates were observed in all fuel types, but still, very few errors were found between the different strata.

Table 5. Confusion matrix of the best model (RF, integrated data sample, and point-cloud normalized at 0.50 m DEM resolution) for Prometheus fuel types classification.

Fuel types	FT1	FT2	FT3	FT4	FT5	FT6	FT7	Prod.'s acc.
FT1	**98**	0	10	10	0	0	0	83%
FT2	2	**90**	37	0	0	0	0	70%
FT3	0	16	**31**	10	0	0	0	54%
FT4	0	4	2	**47**	0	0	9	76%
FT5	0	0	0	0	**73**	29	10	65%
FT6	0	0	0	0	17	**54**	29	54%
FT7	0	0	0	3	10	37	**192**	79%
User's acc.	98%	82%	39%	67%	73%	45%	80%	

The percentage of hits and misclassification errors in the fuel types can be explained by observing the distribution values of the five variables of the classification models, as shown in Figure 5. Both the three shrub and the three tree fuel types present similar patterns that, in general, make their correct differentiation difficult. The values of FT1 (grassland fuel type) are quite different from the rest, which explains the high percentages of success obtained in their classification. The values of the shrub and tree fuel types are very different from each other, although they present a similar distribution in the GCI spectral index. Thus, confusions within types of the same stratum are to be expected, since their distribution values are similar, especially between FT2-FT3 in the three structural variables. In the tree types, the FT5 and FT7 values of the structural and spectral variables are distributed differently, while FT6 values overlap with those of FT5 and FT7, which explains the greater confusion in this type compared to the other two.

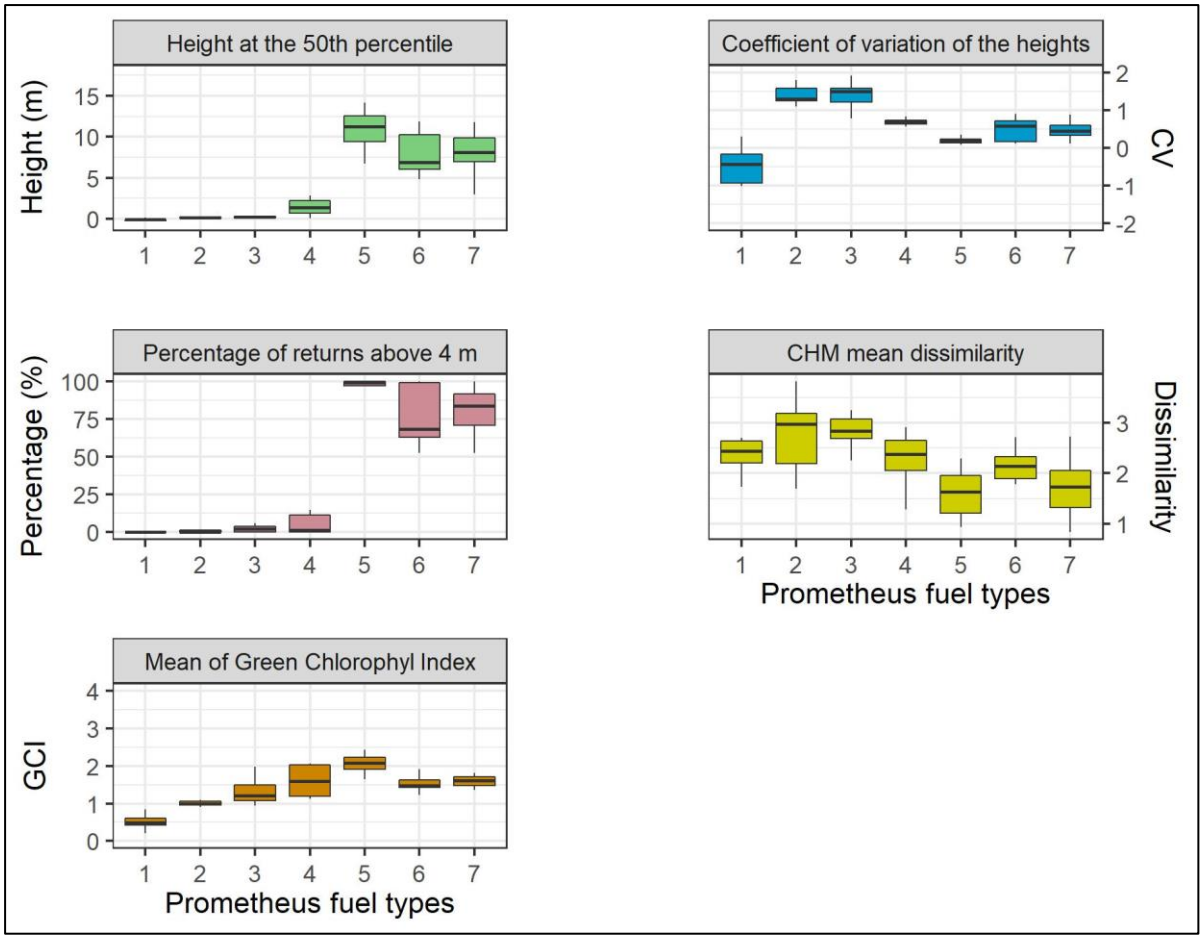

Figure 5. Distribution values of the five UAV variables introduced into the classification models for the identification of the Prometheus fuel types.

4. DISCUSSION

UAV-derived photogrammetric point clouds and multispectral indices allowed classifying fuel types in the Prometheus scale with good levels of accuracy, with most of the confusions found in types belonging to the same dominant stratum. Our results suggest that the combined use of RGB and multispectral data is the best option to classify fuel types. Furthermore, better classifications were observed when using the point cloud normalized to the DEM of 0.50 m resolution and when classifying with RF, which proved to be substantially better than SVM-L and SVM-R. The main fire carriers were well distinguished, and confusions were observed mainly within the three shrub and tree fuel types, especially in the shrub strata.

The integrated data sample obtained the best results in the classification models, reaching accuracies similar to those of Marino *et al*. (2016), who used ALS-LiDAR, Landsat-8 OLI multispectral imagery, and decision-based algorithms to classify specific Canary Island fuel types (OA=70%). Domingo *et al*. (2020)

obtained lower accuracies when classifying Prometheus fuel types in Mediterranean forest stands using low-density ALS-LiDAR and Sentinel-2 imagery by means of machine learning. However, they got better accuracies with SVM-R (OA=59%) than RF (OA=56%). We assume that the better performance of the integrated data sample was due to the higher average of the point clouds from RGB images compared to the point clouds of the multispectral images, which allowed for more normalized point heights and consequently more accurate structural and textural variables. Kandare *et al*. (2016) also found higher accuracy in individual tree crowns delineation with higher ALS point cloud density, and Ruiz *et al*. (2014) achieved better correlation values in forest attributes prediction with high LiDAR data density. In addition, Domingo *et al*. (2019) obtained better accuracies when using UAV photogrammetric point clouds derived from RGB cameras than from multispectral sensors. Our integrated data sample used both RGB and multispectral data, which could imply a higher time cost in data acquisition when these sensors cannot collect information simultaneously, requiring two flights of the UAV, as in our case. Accuracies for the MS data sample were lower than for the integrated data sample due to the lower density of the point cloud, and confusions between fuel types were higher in all cases. Here, the OA was higher when the 0.5 m resolution DEM was used to normalize the point clouds, underscoring the importance of using fine-scale DEMs for this purpose, as noted by other authors (e.g., Shin *et al*., 2018; Cao *et al*., 2019).

The confusion matrices indicated the presence of significant misclassification error rates between fuel types belonging to the same main fire carrier (i.e., within the three shrub fuel types and the three tree fuel types). According to the results of the Dunn's test, only 3 variables were able to distinguish between FT2-FT4 and none were able to distinguish between the others two pairs of shrub fuel types. There were also few variables capable of distinguishing between the tree types. These confounds were to be expected, as there are no absolutely unequivocal plots in terms of fuel type, even though we worked on plots as homogeneous as possible for each type in order to avoid confusion. However, this may also indicate a limitation of optical UAVs to differentiate between similar fuel types, given the inability of photogrammetric point clouds to penetrate the canopy. Therefore, medium to high confusion among shrub fuels can be expected when using optical UAVs, especially in the closest types (FT2-FT3 and FT3-FT4), since they present few differences in terms of height criteria and similar features. The same is true for the confusion observed between tree types. In contrast, no significant problems were observed between the fuel types of different main fire carriers, except for FT4-FT7, which has also been noted

using ALS-LiDAR data (Domingo *et al*., 2020). This confusion is due to the high density of understory and canopy and the vertical continuity of the fuel in both types. The low capability of optical UAVs to collect fuel information in medium and low strata could be overcome by using LiDAR UAVs (e.g., Dalla Corte *et al*., 2020; Neuville *et al*., 2021), although their economic costs are considerably high. However, previous work related to forest structure estimation and mapping have obtained successful results using photogrammetric point clouds (e.g., Shin *et al*., 2018; Carbonell-Rivera *et al*., 2022). Additionally, Wallace *et al*. (2016) and Cao *et al*. (2019) shown that UAV-derived photogrammetric point clouds can be useful and effective substitutes for UAV-LiDAR point clouds for estimating structural attributes of forests. Based on the results obtained in this study, optical UAVs can be considered as suitable alternatives to ALS-LIDAR systems, especially ALS flights of systematic coverage for large extensions carried out by public or private initiatives, whose point density is usually low. In this sense, the higher point density that can be obtained with optical UAVs compared to these low-density ALS flights may allow a better characterization of vegetation structure and forest fuels at local or regional scales. In addition, UAV data can be obtained on demand, allowing for greater temporal flexibility. Photogrammetric point clouds can also be integrated with ALS data to reduce misclassification errors in fuel types and improve their classification (e.g., Guerra-Hernández *et al*., 2018; Yoshii *et al*., 2022). Another option to improve the classification could be to fuse canopy information from photogrammetric point clouds with understory data collected from terrestrial or mobile laser scanners (e.g., Brede *et al*., 2022; Panagiotidis *et al*., 2022).

Regarding the multispectral indices, the *Parrot Sequoia* camera has proven to be able to capture the state of the vegetation (i.e., healthy or diseased). Previous studies have reported good overall performance for this camera. For instance, Fawcett *et al*. (2020) compared vegetation indices generated by *Parrot Sequoia* camera, *HyPlant* airborne imaging spectrometer and Sentinel-2 imagery, showing overall good agreement, although some bias was noticed in the *Parrot Sequoia* camera for high and low reflective surface. Lu *et al*. (2020) demonstrated that the *Parrot Sequoia* offered similar performance to the *DJI Phantom 4* multispectral camera, despite having different spectral response functions, and that both accurately estimated NDVI when compared to spectroradiometer recordings. However, Pérez-Cardiel *et al*. (2022) found that the *Parrot Sequoia* had some underestimates in the red edge band and small overestimates in the NIR band when compared to spectroradiometer records and Sentinel-2 images. Additionally, Stow *et al*. (2019) observed slightly lower reflectance in the NIR band of the *Parrot Sequoia* around solar noon and noted

the contrast between the shadowed and illuminated areas in all spectral bands. Therefore, some uncertainty must be assumed in the data recorded by our multispectral sensor.

5. CONCLUSIONS

The identification of forest fuels is an important step for the prevention and mitigation of wildfires, as it allows forest managers to understand the behavior and intensity of fire in a forest stand. This study used imagery from a fixed-wing UAV to derive a set of structural, textural, and spectral variables, which have been capable of classifying the Prometheus fuel models in Mediterranean forest environments with good levels of agreement. However, more research is needed to understand the capabilities and limitations of these promising instruments. The results obtained allow validating optical UAVs as affordable tools to identify and monitor forest fuels at a local and regional scale and contribute to the successful prevention of forest fires in Mediterranean ecosystems.

REFERENCES

Albini, F., 1976. Estimating wildfire behavior and effects. In: USDA Forest Service, Intermountain Forest and Range Experiment Station, General Technical Report INT, 30, p. 92.

Anderson, H.E., McGaughey, R.J., and Reutebuch, S.E., 2005. Estimating forest canopy fuel parameters using LiDAR data. *Remote Sens. Environ.* 94 (4), 441–449. https://doi.org/10.1016/j.rse.2004.10.013.

Barnes, E.M., Clarke, T.R., and Richards, S.E., 2000. Coincident detection of crop water stress, nitrogen status and canopy density using ground-based multispectral data. In *Proceedings of the 5th International Conference on Precision Agriculture and Other Resource Managements*, July 16–19, 2000, Bloomington, MN, USA.

Brede, B., Terryn, L., Barbier, N., Bartholomeus, H.M., Bartolo, R., Calders, K., Derroire, G., Moorthy, S.M.K., Lau, A., Levick, S.R., Raumonen, P., Verbeeck, H., Wang, D., Whiteside, T., van der Zee, J., and Herold, M., 2022. Non-destructive estimation of individual tree biomass: allometric models, terrestrial and UAV laser scanning. *Remote Sens. Environ.* 280, 113180. https://doi.org/10.1016/j.rse.2022.113180.

Cao, L., Liu, H., Fu, X., Zhang, Z., Shen, X., and Ruan, H., 2019. Comparison of UAV LiDAR and Digital Aerial Photogrammetry point clouds for estimating forest structural attributes in subtropical planted forests. *Forests* 10 (2), 145. https://doi.org/10.3390/f10020145.

Carbonell-Rivera, J.P., Torralba, J., Estornell, J., Ruiz, L.A., and Crespo-Peremarch, P., 2022. Classification of Mediterranean shrub species from UAV point clouds. *Rem. Sens.* 14, 199. https://doi.org/10.3390/rs14010199.

Dalla Corte, A.P., Rex, F.E., Alves de Almeida, D.R., Sanquetta, C.R., Silva, C.A., Moura, M.M., Wilkinson, B., Almeyda Zambrano, A.M., da Cunha Neto, E.M., Veras, H.F.P., de Moraes, A., Klauberg, C., Mohan, M., Cardil, A., and Broadbent, E.N., 2020. Measuring individual tree diameter and height using GatorEye high-density UAV-LiDAR in an integrated crop-livestock-forest system. *Rem. Sens.* 12 (5), 863. https://doi.org/10.3390/rs12050863.

Domingo, D., Orka, H.Ø., Næsset, E., Kachamba, D., and Gobakken, T., 2019. Effects of UAV image resolution, camera type, and image overlap on accuracy of biomass predictions in a tropical woodland. *Rem. Sens.* 11, 948. https://doi.org/10.3390/rs11080948.

Domingo, D., de la Riva, J., Lamelas, M.T., García-Martín, A., Ibarra, P., Echeverría, M., and Hoffrén, R., 2020. Fuel type classification using airborne laser scanning and sentinel 2 data in Mediterranean forest affected by wildfires. *Rem. Sens.* 12 (21), 1–22. https://doi.org/10.3390/rs12213660.

Evans, J.S. and Hudak, A.T., 2007. A multiscale curvature algorithm for classifying discrete return LiDAR in forested environments. IEEE Trans. Geosci. *Rem. Sens.* 45 (4), 1029–1038. https://doi.org/10.1109/TGRS.2006.890412.

Fawcett, D., Panigada, C., Tagliabue, G., Boschetti, M., Celesti, M., Evdokimov, A., Biriukova, K., Colombo, R., Miglietta, F., Rascher, U., and Anderson, K., 2020. Multi-scale evaluation of drone-based multispectral surface reflectance and vegetation indices in operational conditions. *Rem. Sens.* 12 (3), 514. https://doi.org/10.3390/ rs12030514.

Fernández-Álvarez, M., Armesto, J., and Picos, J., 2019. LiDAR-based wildfire prevention in WUI: the automatic detection, measurement and evaluation of forest fuels. *Forests* 10, 148. https://doi.org/10.3390/f10020148.

Ferraz, A., Saatchi, S., Mallet, C., and Meyer, V., 2016. Lidar detection of individual tree size in tropical forests. *Remote Sens. Environ.* 183, 318–333. https://doi.org/10.1016/J.RSE.2016.05.028.

Fritz, A., Kattenborn, T., and Koch, B., 2013. UAV-based photogrammetric point clouds – tree stem mapping in open stands in comparison to terrestrial laser scanner point clouds. *ISPRS Int. Arch. Photogram. Rem. Sens. Spatial Inf. Sci.* XL-1/W2, 141–146. https://doi.org/10.5194/isprsarchives-XL-1-W2-141-2013.

García-Galar, A., Lamelas, M.T., and Domingo, D., 2023. Assessment of oak groves conservation statuses in Natura 200 sacs with single photon LiDAR and Sentinel-2 data. *Rem. Sens.* 15, 710. https://doi.org/10.3390/rs15030710.

Gao, B.C., 1996. NDWI – a Normalized Difference Water Index for remote sensing of vegetation liquid water from space. *Remote Sens. Environ.* 58 (3), 257–266. https://doi.org/10.1016/S0034-4257(96)00067-3.

Gitelson, A.A., Gritz, Y., and Merzlyak, M.N., 2003. Relationships between leaf chlorophyll content and spectral reflectance and algorithms for non-destructive chlorophyll assessment in higher plant leaves. *J. Plant Physiol.* 160, 271–282. https://doi.org/10.1078/0176-1617-00887.

Gitelson, A.A., Kaufman, Y.J., and Merzlyak, M.N., 1996. Use of a green channel in remote sensing of global vegetation from EOS-MODIS. *Remote Sens. Environ.* 58, 289–298. https://doi.org/10.1016/S0034-4257(96)00072-7.

Guerra-Hernández, J., Cosenza, D.N., Rodriguez, L.C.E., Silva, M., Tomé, M., Díaz-Varela, R.A., and González-Ferreiro, E., 2018. Comparison of ALS- and UAV(SfM)-derived high-density point clouds for individual tree detection in Eucalyptus plantations. *Int. J. Rem. Sens.* 39 (15–16), 5211–5235. https://doi.org/10.1080/01431161.2018.1486519.

Haralick, R.M., Shanmugam, K., and Dinstein, I., 1973. Textural features for image classification. *IEEE Trans. Syst. Man Cybern. Syst.* 3 (6), 610–621. https://doi.org/10.1109/TSMC.1973.4309314.

Hillman, S., Wallace, L., Lucieer, A., Reinke, K., Turner, D., and Jones, S., 2021. A comparison of terrestrial and UAS sensors for measuring fuel hazard in a dry sclerophyll forest. *Int. J. Appl. Earth Obs. Geoinf.* 95, 102261. https://doi.org/10.1016/j.jag.2020.102261.

Huete, A.R., 1988. A soil-adjusted vegetation index (SAVI). *Remote Sens. Environ.* 25, 295–309. https://doi.org/10.1016/0034-4257(88)90106-X.

Kandare, K., Orka, H.Ø., Cheung-Wai Chan, J., and Dalponte, M., 2016. Effects of forest structure an airborne laser scanning point cloud density on 3D delineation of individual tree crowns. *Eur. J. Remote Sens.* 49, 337–359. https://doi.org/10.5721/EuJRS20164919.

Kuhn, M., 2008. Building predictive models in R using the caret package. *J. Stat. Software* 28 (5), 1–26. https://doi.org/10.18637/jss.v028.i05.

Lu, H., Fan, T., Ghimire, P., and Deng, L., 2020. Experimental evaluation and consistency comparison of UAV multispectral minisensors. *Rem. Sens.* 12 (16), 2542. https://doi.org/10.3390/rs12162542.

Marino, E., Ranz, P., Tomé, J.L., Noriega, M.Á., Esteban, J., and Madrigal, J., 2016. Generation of high-resolution fuel model maps from discrete airborne laser scanner and Landsat-8 OLI: a low-cost and highly updated methodology for large areas. *Remote Sens. Environ.* 187, 267–280. https://doi.org/10.1016/j.rse.2016.10.020.

McGaughey, R.J., 2021. FUSION/LDV: Software for LIDAR Data Analysis and Visualization V.4.21. USDA Forest Service, Washington DC, USA.

Messinger, M., Asner, G., and Silman, M., 2016. Rapid assessments of Amazon forest structure and biomass using small unmanned aerial systems. *Rem. Sens.* 8, 615. https://doi.org/10.3390/rs8080615.

Montealegre, A.L., Lamelas, M.T., de la Riva, J., García-Martín, A., and Escribano, F., 2016. Use of low point density ALS data to estimate stand-level structural variables in Mediterranean Aleppo pine forest. *Forestry* 89, 373–382. https://doi.org/10.1093/forestry/cpw008.

Neuville, R., Bates, J.S., and Jonard, F., 2021. Estimating forest structure from UAV-mounted LiDAR point cloud using machine learning. *Rem. Sens.* 13 (3), 352. https://doi.org/10.3390/rs13030352.

Oliveira, S., Oehler, F., San Miguel-Ayanz, J., Camia, A., and Pereira, J.M.C., 2012. Modeling spatial patterns of fire occurrence in mediterranean Europe using multiple regression and random forest. *For. Ecol. Manag.* 275, 117–129. https://doi.org/10.1016/j.foreco.2012.03.003.

Panagiotidis, D., Abdollahnejad, A., and Slavík, M., 2022. 3D point cloud fusion from UAV and TLS to assess temperate managed forest structures. *Int. J. Appl. Earth Obs. Geoinf.* 112, 102917. https://doi.org/10.1016/j.jag.2022.102917.

Pérez-Cardiel, E., de la Riva, J., Rodrigues, M., Domingo, D., and Casterad, M.A., 2022. Evaluación de la consistencia de los datos obtenidos desde UAV por el sensor Sequoia para su aplicación en agricultura. In Ruiz, L.A., Estornell, J., González-Audícana, M., Álvarez-Mozos, J. (Eds.), *Teledetección para una agricultura sostenible en la era del Big Data.* XIX Congreso de la Asociación Española de Teledetección. Pamplona. eISBN: 978-84-9769-383-7.

Poncet, A.M., Knappenberger, T., Brodbeck, C., Fogle, Jr, M., Shaw, J.N., and Ortiz, B.V., 2019. Multispectral UAS data accuracy for different radiometric calibration methods. *Rem. Sens.* 11 (16), 1917. https://doi.org/10.3390/rs11161917.

Pontius, R.G., Boersma, W., Castella, J.C., Clarke, K., de Nijs, T., Dietzel, C., Duan, Z., Fotsing, E., Goldstein, N., Kok, K., Koomen, E., Lippitt, C.D., McConnell, W., Sood, A.M., Pijanowski, B., Pithadia, S., Sweeney, S., Trung, T.N., Veldkamp, A.T., and Verburg, P.H., 2008. Comparing the input, output, and validation maps for several models of land change. *Ann. Reg. Sci.* 42, 11–37. https://doi.org/10.1007/s00168-007-0138-2.

Prometheus, 1999. Management Techniques for Optimization of Suppression and Minimization of Wildfires Effects. System Validation. European Commission, DG XII, ENVIR & CLIMATE. European Commission, Luxembourg. Contract Number ENV4–CT98–0716.

Puliti, S., Olerka, H., Gobakken, T., and Næsset, E., 2015. Inventory of small forest areas using an unmanned aerial system. *Rem. Sens.* 7, 9632–9654. https://doi.org/ 10.3390/rs70809632.

R Core Team, 2022. R: A Language and Environment for Statistical Computing. R Foundation for Statistical Computing, Vienna, Austria. URL. https://www.R-project.org/.

Renslow, M., 2013. Manual of Airborne Topographic Lidar. ASPRS, Bethesda, MD. ISBN: 978-1570830976.

Rothermel, C., 1972. A Mathematical Model for Predicting Fire Spread in Wildland Fuels. Research Papers, INT-115. U.S. Department of Agriculture, Intermountain Forest and Range Experiment Station, Ogden, UT, p. 40.

Rouse, J.W., Haas, R.H., Schell, J.A., and Deering, D.W., 1974. Monitoring Vegetation Systems in the Great Plains with ERTS. *Third ERTS-1 Symposium NASA*, NASA SP- 351, Washington DC, pp. 309–317.

Roussel, J.R., Auty, D., Coops, N.C., Tompalski, P., Goodbody, T.R.H., Sánchez-Meador, A., Bourdon, J.F., de Boissieu, F., and Achim, A., 2020. lidR: An R package for analysis of Airborne Laser Scanning (ALS) data. *Remote Sens. Environ.* 251, 112061. https://doi.org/10.1016/j.rse.2020.112061.

Roy, P.S., Sharma, K.P., and Jain, A., 1996. Stratification of density in dry deciduous forest using satellite remote sensing digital data – an approach based on spectral indices. *J. Biosci.* 21 (5), 723–734. https://doi.org/10.1007/BF02703148.

Ruiz, L.A., Hermosilla, T., Mauro, F., and Godino, M., 2014. Analysis of the influence of plot size and LiDAR density on forest structure attribute estimates. *Forests* 5 (5), 936–951. https://doi.org/10.3390/f5050936.

Shin, P., Sankey, T., Moore, M.M., and Thode, A.E., 2018. Evaluating unmanned aerial vehicle images for estimating forest canopy fuels in a Ponderosa pine stand. *Rem. Sens.* 10, 1266. https://doi.org/10.3390/rs10081266.

Stow, D., Nichol, C.J., Wade, T., Assmann, J.J., Simpson, G., and Helfter, C., 2019. Illumination geometry and flying height influence surface reflectance and NDVI derived from multispectral UAS imagery. *Drones* 3 (3), 55. https://doi.org/10.3390/drones3030055.

Varol, T., Canturk, U., Cetin, M., Ozel, H.B., and Sevil, H., 2021. Impacts of climate scenarios on European ash tree (Fraxinus excelsior L.) in Turkey. *For. Ecol. Manag.* 491, 119199. https://doi.org/10.1016/j.foreco.2021.119199.

Venäläinen, A., Lehtonen, I., Laapas, M., Ruosteenoja, K., Tikkanen, O.L., Viiri, H., Ikonen, V.P., and Peltola, H., 2020. Climate change induces multiple risks to boreal forests and forestry in Finland: a literature review. *Global Change Biol.* 26 (8), 4178–4196. https://doi.org/10.1111/gcb.15183.

Wallace, L., Lucieer, A., Malenovský, Z., Turner, D., and Vopěnka, P., 2016. Assessment of forest structure using two UAV techniques: a comparison of Airborne Laser Scanning and Structure from Motion (SfM) point clouds. *Forests* 7 (3), 62. https://doi.org/10.3390/f7030062.

Yoshii, T., Matsumura, N., and Lin, C., 2022. Integrating UAV-SfM and airborne lidar point cloud to plantation forest feature extraction. *Rem. Sens.* 14 (7), 1713. https://doi.org/10.3390/rs14071713.

Zvoleff, A., 2020. glcm: calculate textures from grey-level co-occurrence matrices (GLCMs). R package version 1.6.5. https://CRAN.R-project.org/package=glcm.

APPENDIX

Table A.1. Number of Prometheus fuel type pairs differentiated by each variable according to Dunn's test, by sensor and by resolution of the DEM used to normalize the point-cloud heights. (Part 1 of 6).

Variables	RGB camera			Multispectral sensor		
	DEM 0.50 M	DEM 1 M	DEM 2 M	DEM 0.50 M	DEM 1 M	DEM 2 M
Elev.maximum	10	10	10	11	11	11
Elev.mean	10	10	10	10	10	10
Elev.minimum	0	0	0	4	2	3
Elev.P01	3	3	4	4	4	4
Elev.P05	5	5	6	6	6	8
Elev.P10	7	7	8	8	8	10
Elev.P20	9	9	10	10	10	10
Elev.P25	9	9	10	10	10	10
Elev.P30	9	9	10	10	10	10
Elev.P40	10	10	10	10	10	10
Elev.P50	10	10	10	11	11	11
Elev.P60	10	10	10	11	11	11
Elev.P70	10	10	10	11	11	11
Elev.P75	10	10	10	11	11	11
Elev.P80	10	10	10	11	11	11
Elev.P90	10	10	10	11	11	11
Elev.P95	10	10	10	11	11	11
Elev.P99	10	10	11	11	11	11
Elev.CV	8	9	8	6	5	6
Elev.kurtosis	3	3	3	2	2	1
Elev.skewness	8	8	8	7	7	7

Table A.1. Number of Prometheus fuel type pairs differentiated by each variable according to Dunn's test, by sensor and by resolution of the DEM used to normalize the point-cloud heights. (Part 2 of 6).

Variables	RGB camera			Multispectral sensor		
	DEM 0.50 M	DEM 1 M	DEM 2 M	DEM 0.50 M	DEM 1 M	DEM 2 M
Elev.stddev	8	7	7	5	5	5
Elev.variance	8	7	7	5	5	5
Elev.strata..0.00.to.0.60..CV	0	0	0	4	3	2
Elev.strata..0.00.to.0.60..kurtosis	0	1	1	3	3	2
Elev.strata..0.00.to.0.60..max	8	8	7	6	3	5
Elev.strata..0.00.to.0.60..mean	2	2	3	2	2	2
Elev.strata..0.00.to.0.60..median	2	2	3	2	2	2
Elev.strata..0.00.to.0.60..min	0	0	0	1	2	0
Elev.strata..0.00.to.0.60..mode	1	0	1	2	2	2
Elev.strata..0.00.to.0.60..return. proportion	8	8	8	5	5	5
Elev.strata..0.00.to.0.60..skewness	0	0	1	4	4	2
Elev.strata..0.00.to.0.60..stddev	2	2	2	4	3	1
Elev.strata..0.00.to.0.60..total. return.count	8	8	8	7	7	6
Elev.strata..0.60.to.2.00..CV	5	5	3	3	2	2
Elev.strata..0.60.to.2.00..kurtosis	4	4	3	4	4	4
Elev.strata..0.60.to.2.00..max	6	8	8	6	5	6
Elev.strata..0.60.to.2.00..mean	5	5	5	5	4	5
Elev.strata..0.60.to.2.00..median	6	6	6	4	4	4
Elev.strata..0.60.to.2.00..min	6	6	1	1	0	0
Elev.strata..0.60.to.2.00..mode	4	4	3	3	3	3
Elev.strata..0.60.to.2.00..return. proportion	7	7	7	6	6	7
Elev.strata..0.60.to.2.00..skewness	4	3	4	3	3	2
Elev.strata..0.60.to.2.00..stddev	5	5	5	4	4	3
Elev.strata..0.60.to.2.00..total. return.count	8	8	7	6	6	7
Elev.strata..2.00.to.4.00..CV	4	4	4	2	2	2
Elev.strata..2.00.to.4.00..kurtosis	6	5	4	3	3	3
Elev.strata..2.00.to.4.00..max	5	6	4	4	2	4

Table A.1. Number of Prometheus fuel type pairs differentiated by each variable according to Dunn's test, by sensor and by resolution of the DEM used to normalize the point-cloud heights. (Part 3 of 6).

Variables	RGB camera			Multispectral sensor		
	DEM 0.50 M	DEM 1 M	DEM 2 M	DEM 0.50 M	DEM 1 M	DEM 2 M
Elev.strata..2.00.to.4.00..mean	2	2	3	2	2	2
Elev.strata..2.00.to.4.00..median	2	2	3	2	2	2
Elev.strata..2.00.to.4.00..min	2	3	3	2	2	3
Elev.strata..2.00.to.4.00..mode	2	3	3	2	2	2
Elev.strata..2.00.to.4.00..return. proportion	6	6	6	3	3	3
Elev.strata..2.00.to.4.00..skewness	6	6	4	4	4	4
Elev.strata..2.00.to.4.00..stddev	4	4	4	2	2	2
Elev.strata..2.00.to.4.00..total. return.count	6	6	6	4	4	4
Elev.strata..above.4.00..CV	7	7	7	7	7	6
Elev.strata..above.4.00..kurtosis	3	3	3	4	4	4
Elev.strata..above.4.00..max	12	12	12	12	12	12
Elev.strata..above.4.00..mean	11	11	12	11	11	11
Elev.strata..above.4.00..median	12	12	12	12	12	12
Elev.strata..above.4.00..min	4	5	5	6	4	5
Elev.strata..above.4.00..mode	12	12	12	11	11	12
Elev.strata..above.4.00..return. proportion	12	12	12	12	12	12
Elev.strata..above.4.00..skewness	5	5	5	5	5	5
Elev.strata..above.4.00..stddev	9	10	9	10	10	10
Elev.strata..above.4.00..total. return.count	11	11	11	11	11	10
Elev.strata..below.0.00..CV	3	3	2	5	4	2
Elev.strata..below.0.00..kurtosis	1	1	0	2	2	3
Elev.strata..below.0.00..max	3	4	0	6	4	4
Elev.strata..below.0.00..mean	2	2	0	3	2	1
Elev.strata..below.0.00..median	7	6	4	1	1	3

Table A.1. Number of Prometheus fuel type pairs differentiated by each variable according to Dunn's test, by sensor and by resolution of the DEM used to normalize the point-cloud heights. (Part 4 of 6).

Variables	RGB camera			Multispectral sensor		
	DEM 0.50 M	DEM 1 M	DEM 2 M	DEM 0.50 M	DEM 1 M	DEM 2 M
Elev.strata..below.0.00..min	2	2	2	2	2	2
Elev.strata..below.0.00..mode	5	3	2	1	3	3
Elev.strata..below.0.00..return.proportion	7	6	5	5	5	5
Elev.strata..below.0.00..skewness	2	2	0	3	3	1
Elev.strata..below.0.00..stddev	1	1	0	1	1	0
Elev.strata..below.0.00..total.return.count	7	7	5	6	6	4
Percentage.all.returns.above.4.00	12	12	12	12	12	12
Percentage.all.returns.above.mean	8	8	8	5	6	5
Percentage.all.returns.above.mode	1	1	1	2	1	3
Total.all.returns	6	6	6	9	9	9
GLCM_contrast_max	0	2	4	2	4	3
GLCM_contrast_mean	6	4	5	4	5	4
GLCM_contrast_median	4	4	3	2	3	1
GLCM_contrast_min	5	2	0	2	3	1
GLCM_dissimilarity_max	1	4	4	4	5	3
GLCM_dissimilarity_mean	7	6	4	3	5	2
GLCM_dissimilarity_median	3	3	2	2	3	1
GLCM_dissimilarity_min	5	2	0	2	3	1
GLCM_entropy_max	5	2	0	2	2	1
GLCM_entropy_mean	3	1	0	2	3	0
GLCM_entropy_median	3	1	0	1	2	0
GLCM_entropy_min	5	2	0	2	2	1
GLCM_homogeneity_max	5	2	0	2	3	0
GLCM_homogeneity_mean	3	1	0	2	4	0

Table A.1. Number of Prometheus fuel type pairs differentiated by each variable according to Dunn's test, by sensor and by resolution of the DEM used to normalize the point-cloud heights. (Part 5 of 6).

Variables	RGB camera			Multispectral sensor		
	DEM 0.50 M	DEM 1 M	DEM 2 M	DEM 0.50 M	DEM 1 M	DEM 2 M
GLCM_homogeneity_median	3	1	0	2	4	0
GLCM_homogeneity_min	6	5	0	6	5	1
GLCM_mean_max	6	5	5	7	7	3
GLCM_mean_mean	6	6	4	6	3	2
GLCM_mean_median	7	6	4	6	3	3
GLCM_mean_min	3	5	5	7	6	3
GLCM_second_max	5	2	0	3	2	1
GLCM_second_mean	4	1	0	2	3	0
GLCM_second_median	3	1	0	1	2	0
GLCM_second_min	4	1	0	2	3	0
GLCM_variance_max	7	0	4	8	6	1
GLCM_variance_mean	6	6	4	6	3	2
GLCM_variance_min	4	6	5	7	6	3
AVI_max	4	4	4	4	4	4
AVI_mean	4	4	4	4	4	4
AVI_median	1	1	1	1	1	1
AVI_min	1	1	1	1	1	1
GCI_max	7	7	7	7	7	7
GCI_mean	7	7	7	7	7	7
GCI_median	7	7	7	7	7	7
GCI_min	4	4	4	4	4	4
GNDVI_max	7	7	7	7	7	7
GNDVI_mean	6	6	6	6	6	6

Table A.1. Number of Prometheus fuel type pairs differentiated by each variable according to Dunn's test, by sensor and by resolution of the DEM used to normalize the point-cloud heights. (Part 6 of 6).

Variables	RGB camera			Multispectral sensor		
	DEM 0.50 M	DEM 1 M	DEM 2 M	DEM 0.50 M	DEM 1 M	DEM 2 M
GNDVI_median	7	7	7	7	7	7
GNDVI_min	4	4	4	4	4	4
NDRE_max	7	7	7	7	7	7
NDRE_mean	6	6	6	6	6	6
NDRE_median	5	5	5	5	5	5
NDRE_min	0	0	0	0	0	0
NDVI_max	7	7	7	7	7	7
NDVI_mean	7	7	7	7	7	7
NDVI_median	7	7	7	7	7	7
NDVI_min	9	9	9	9	9	9
NDWI_max	4	4	4	4	4	4
NDWI_mean	6	6	6	6	6	6
NDWI_median	7	7	7	7	7	7
NDWI_min	7	7	7	7	7	7
SAVI_max	7	7	7	7	7	7
SAVI_mean	6	6	6	6	6	6
SAVI_median	6	6	6	6	6	6
SAVI_min	0	0	0	0	0	0

Table A.2. Summary of overall accuracies of Prometheus fuel types classification for the nine SVM-L model data samples with k-10 cross validation and 10 repeats in each case.

DEM resolution	**0.50 m**			**1 m**			**2 m**		
Data sample	RGB	MS	Integ.	RGB	MS	Integ.	RGB	MS	Integ.
Overall accuracy	59%	55%	59%	57%	54%	58%	58%	57%	57%

Table A.3. Summary of overall accuracies of Prometheus fuel types classification for the nine SVM-R model data samples with k-10 cross validation and 10 repeats in each case.

DEM resolution	**0.50 m**			**1 m**			**2 m**		
Data sample	RGB	MS	Integ.	RGB	MS	Integ.	RGB	MS	Integ.
Overall accuracy	61%	53%	61%	53%	49%	57%	58%	54%	63%

Table A.4. Confusion matrix of the best MS data sample model (RF, point cloud normalized at 0.50 m DEM resolution) for Prometheus fuel types classification.

Fuel types	**FT1**	**FT2**	**FT3**	**FT4**	**FT5**	**FT6**	**FT7**	**Prod.'s acc.**
FT1	**70**	0	0	10	0	0	0	88%
FT2	1	**80**	39	11	0	0	0	61%
FT3	0	26	**21**	2	0	0	0	43%
FT4	0	4	20	**46**	0	0	9	58%
FT5	0	0	0	1	**61**	30	19	55%
FT6	0	0	0	0	27	**64**	27	54%
FT7	9	0	0	0	12	26	**185**	80%
User's acc.	88%	73%	26%	66%	61%	53%	77%	

Table A.5. Confusion matrix of the best RGB data sample model (RF, point cloud normalized at 1 m DEM resolution) for Prometheus fuel types classification.

Fuel types	**FT1**	**FT2**	**FT3**	**FT4**	**FT5**	**FT6**	**FT7**	**Prod.'s acc.**
FT1	**90**	0	10	0	0	0	0	90%
FT2	7	**83**	55	0	0	0	0	57%
FT3	3	17	**15**	10	0	0	0	33%
FT4	0	10	0	**60**	0	0	0	86%
FT5	0	0	0	0	**49**	34	39	40%
FT6	0	0	0	0	21	**55**	29	52%
FT7	0	0	0	0	30	31	**172**	74%
User's acc.	90%	75%	19%	86%	49%	45%	72%	

The *GeoSLAM ZEB-Horizon* HMLS system. Photograph by Juan de la Riva.

CHAPTER 5

HANDHELD MOBILE LASER SCANNER SYSTEM FOR FOREST FUEL DEFINITION

This chapter corresponds to:

Hoffrén, R., Lamelas, M.T., and de la Riva, J., 2024. Evaluation of handheld mobile laser scanner systems for the definition of fuel types in structurally complex Mediterranean forest stands. *Fire* 7 (2), 59.

https://doi.org/10.3390/fire7020059

Evaluation of handheld mobile laser scanner systems for the definition of fuel types in structurally complex Mediterranean forest stands

Raúl Hoffrén[1,2], María Teresa Lamelas[2,3], Juan de la Riva[1,2,*].

[1] Department of Geography and Land Management, University of Zaragoza, Calle Pedro Cerbuna 12, 50009, Zaragoza, Spain.
[2] Geoforest Group, University Institute for Research in Environmental Sciences of Aragón (IUCA), University of Zaragoza, Spain.
[3] Centro Universitario de la Defensa, Academia General Militar, Ctra. Huesca s/n, 50090, Zaragoza, Spain.
[*] Corresponding author, email: delariva@unizar.es.

ABSTRACT

The exposure of Mediterranean forests to large wildfires requires mechanisms to prevent and mitigate their negative effects on the territory and ecosystems. Fuel models synthesize the complexity and heterogeneity of forest fuels and allow for the understanding and modeling of fire behavior. However, it is sometimes challenging to define the fuel type in a structurally heterogeneous forest stand due to the mixture of characteristics from the different types and limitations of qualitative field observations and passive and active airborne remote sensing. This can impact the performance of classification models that rely on the *in situ* identification of fuel types as the ground-truth, which can lead to a mistaken prediction of fuel types over larger areas in fire prediction models. In this study, a handheld mobile laser scanner (HMLS) system was used to assess its capability to define Prometheus fuel types in 43 forest plots in Aragon (NE Spain). The HMLS system captured the vertical and horizontal distribution of fuel at an extremely high resolution to derive high-density three-dimensional point clouds (average: 63,148 points/m^2), which were discretized into voxels of 0.05 m^3. The total number of voxels in each 5 cm height stratum was calculated to quantify the fuel volume in each stratum, providing the vertical distribution of fuels (m^3/m^2) for each plot at a centimetric scale. Additionally, the fuel volume was computed for each Prometheus height stratum (0.60, 2, and 4 m) in each plot. The Prometheus fuel types were satisfactorily identified in each plot and were compared with the fuel types estimated in the field. This led to the modification of the ground-truth in 10 out of the 43 plots, resulting in errors being found in the field estimation between types FT2–FT3, FT5–FT6, and FT6–FT7. These results demonstrate the ability of the HMLS systems to capture fuel heterogeneity at centimetric scales for the definition of fuel types in the field in Mediterranean forests, making them powerful tools for fuel mapping, fire modeling, and ultimately for improving wildfire prevention and forest management.

1. INTRODUCTION

Wildfires are natural disasters that commonly affect forests (Bowman *et al*., 2009; Pausas and Keeley, 2009). Mediterranean environments are particularly vulnerable to wildfires, primarily due to the climatic conditions and the structural complexity of Mediterranean forest ecosystems (Nocentini and Coll, 2013). Furthermore, these areas may be more exposed to fire in the future due to climate change (Varela *et al*., 2019; Ruffault *et al*., 2020; Jones *et al*., 2022; Rovithakis *et al*., 2022), recent socio-economic processes such as the abandonment of fields (Koutsias *et al*., 2013; Moreno *et al*., 2014; Ascoli *et al*., 2021), and the increase in buildings in the wildland–urban interface and in rural areas adjacent to forest stands (Chas-Amil *et al*., 2013; Ganteaume *et al*., 2021; Godoy *et al*., 2022). Improvements in wildland fire management can help reduce the number of wildfires (Turco *et al*., 2014) and bolster their resilience to current and future impacts. A pivotal step in wildfire prevention is understanding forest fuels, as they offer insights into potential fire behavior in case of a hypothetical fire.

Forest fuels comprise all living or dead matter available in the forest for combustion. They are one of the three components of the so-called 'fire triangle', together with a heat source and oxygen. However, fuel is the only one that can be managed, so its characterization is fundamental to predict fire behavior and establish management plans to assess the risk of fire (Ferraz *et al*., 2016). Different fuel models have been developed to synthesize fuel types according to their height and density (Huesca *et al*., 2019). These parametrized models will ultimately serve as inputs for fire behavior and spread models over larger areas. There are different fuel-type classifications, such as the Rothermel fire spread model (Rothermel, 1972), the Northern Forest Fire Laboratory (NFFL) model (Albini, 1976), and the Prometheus model (Prometheus, 1999). The latter is based on the NFFL model and adapted to Mediterranean ecosystems. It comprises seven fuel types: one grassland type (FT1), three shrub types (FT2, FT3, and FT4), and three tree types (FT5, FT6, and FT7). The precise characterization of each fuel type is essential to understand how fire will behave with vegetation. For this, it is necessary to obtain very detailed information about the structure of the fuels. However, the identification of fuel types in the field can be a difficult task, especially in Mediterranean forests, due to the coexistence of different understory species and the heterogeneous spatial distribution of vegetation. Knowing the fuel type in a forest plot is relevant when this information acts as the ground-truth of classification models to accurately predict fire behavior over larger forest areas (Arroyo *et al*., 2008). In this regard,

previous studies have noticed common classification discrepancies between the field data (i.e., the fuel type acting as the dependent variable) and the results of predictive models, for instance, between the shrub and tree fuel types (Arroyo *et al*., 2006; Domingo *et al*., 2020; Hoffrén *et al*., 2023a), but more commonly between the types of the same dominant stratum, such as between shrub types (Lasaponara *et al*., 2005; Huesca *et al*., 2019) and between tree types (García *et al*., 2011; Revilla *et al*., 2021; Hoffrén *et al*., 2023b). In a previous work carried out by Hoffrén *et al*. (2023b), in the same study area, predictive classification models based on machine learning techniques were performed to classify Prometheus fuel types using the data obtained from a photogrammetric unmanned aerial vehicle. The results from the classification models showed that the main discrepancies were between similar fuel types (e.g., FT2–FT3, FT3–FT4, and FT6–FT7), which may share the same structural features. One of the conclusions drawn in that study was that some confusion could have occurred due to the structural heterogeneity and complexity of the forest plots, which may have made it difficult to identify the ground-truth (i.e., the dominant fuel type) of the plots. In this regard, misclassifications can occur because forest plots are typically not homogeneous in terms of the fuel type but can exhibit mixed characteristics of several types (Hoffrén *et al*., 2023b), leading to confusion when estimating the ground-truth in situ. Ground-based LiDAR (*Light Detection and Ranging*) systems can provide a solution to this problem, as they are able to capture detailed structural forest information (Burt *et al*., 2013; Liang *et al*., 2016; Olofsson and Holmgren, 2016; Ritter *et al*., 2017; Åkerblom *et al*., 2021) and thus help to better define the fuel types in forest plots with high structural complexity.

There are two main ground-based LiDAR systems used in forestry: stationary terrestrial laser scanners (TLS) and mobile terrestrial laser scanners (MLS). TLS have been used for the identification of forest fuels for more than a decade, as well as large-scale fuel-type maps (Rowell and Seielstad, 2012), the classification of forest fuels to assess wildfire hazards (Chen *et al*., 2016), and the prediction of surface fuels and vegetation biomass and consumption before and after a prescribed burning (Loudermilk *et al*., 2023). They have also been used to assess the accuracy of TLS data in estimating forest phenology and shrub height and density and their comparison with field reference data (Maxwell *et al*., 2023); however, the static nature of TLS can lead to occlusion problems that can be especially significant in structurally complex forests, such as Mediterranean forests. This may result in under-predicted structural values (Donager *et al*., 2021), undetected trees (Yrttimaa *et al*., 2020), or less accurately derived digital elevation models (Crespo-Peremarch, 2020). MLS are considered

efficient alternatives to TLS to mitigate occlusion problems (Bauwens *et al*., 2016; Fol *et al*., 2023). They can be mounted on different platforms, such as smartphones (Gülci *et al*., 2023), backpacks (Hyyppä *et al*., 2020a), cars (de Paula Pires *et al*., 2022), or handheld devices. Handheld mobile laser scanners (HMLS), in particular, are among the most widely used MLS in forestry (Fol *et al*., 2023). They enable rapid and accurate acquisition of forest structural data (Donager *et al*., 2021) and can detect trees accurately (Gollob *et al*., 2020a; Solares-Canal *et al*., 2023; Tupinambá-Simões *et al*., 2023) and in less time compared to TLS systems (Bauwens *et al*., 2016). They have also been successfully capable of estimating forest fuels. For instance, Forbes *et al*. (2022) found that HMLS systems can be used to estimate ladder fuels in oak woodlands to predict wildfire burn severity with good accuracy. Post (2022) also observed good performances of a HMLS system to detect post-fire disturbances from surface fuel data. Furthermore, Coskuner *et al*. (2023) obtained good results from a HMLS system to estimate fuel characteristics in Mediterranean forest stands. Therefore, and given the very high resolution of information they are capable of collecting, HMLS systems appear to be very suitable tools for capturing the structural complexity of fuels with a high level of detail for the precise definition of fuel types in the field.

In this context, the main objective of this study is to evaluate the suitability of a HMLS system for constructing an enhanced ground-truth of fuel types, which can be used subsequently to better predict forest fuels over large areas. The initial hypothesis is that HMLS systems can capture fuel heterogeneity and quantify the fuel volume at a very high resolution, allowing for the characterization of the structural complexity of vegetation with high accuracy and definition of the fuel types in forest stands with uncertain dominant types. To this end, the HMLS system will be used to quantify the fuel volume by height strata at a very high resolution in structurally heterogeneous forest stands, facilitating the identification of the Prometheus fuel type for each stand to serve as the ground-truth in other remote sensing fuel identification technique

2. MATERIALS AND METHODS

2.1. Study area

The study was conducted across 43 forest plots of a 15 m circular radius, except for one plot of a 10 m circular radius (Tables A.1 and A.2 of Appendix). These plots were selected from those previously utilized by Hoffrén *et al*. (2023b). They were distributed across 5 sectors of the Autonomous Community of

Aragón (NE Spain) as follows: Almudévar, Ayerbe, Uncastillo, Villarluengo, and Zuera (Figure 1). The prevailing climate in these sectors is Mediterranean with a continental influence, characterized by sporadic and irregularly distributed rainfall throughout the year, substantial daily and annual thermal gradients, and convective storms, which are frequent in late spring and summer. The sectors of Almudévar, Ayerbe, and Zuera are located in the Central Ebro Valley, where climatic conditions tend to be more extreme, resembling steppe-like conditions with cold winters, very hot and dry summers, low precipitation, and a high probability of drought periods. On the other hand, the Uncastillo sector, situated to the north of the Central Ebro Valley near the southern foothills of the Pre-Pyrenean range, experiences less extreme temperature gradients and higher rainfall. Finally, the Villarluengo sector, located in the Iberian range, features colder winters and milder summers compared to the other sectors due to its higher altitude (Cuadrat *et al*., 2007). All plots are characterized by typical Mediterranean vegetation well-adapted to the local climatic conditions, including shrublands and forest predominantly consisting of Aleppo pine (*Pinus halepensis* Mill.) and bog pine (*Pinus nigra* Mill.) mixed with an understory of oaks (*Quercus coccifera* L., *Quercus faginea* Lam., and *Quercus ilex* subsp. *rotundifolia* Lam.), boxwood (*Buxus sempervirens* L.), junipers (*Juniperus oxycedrus* L.), rosemary (*Rosmarinus officinalis* L.), and thymes *(Thymus vulgaris* L.). The climatic conditions, along with the characteristics of vegetation, and together with recent processes such as cropland abandonment and natural and systematic reforestation with pine species, lead to a high risk of forest fires. In fact, 3 out of the 5 sectors experienced large wildfires (>500 ha of burned area) in the last 30 years: Uncastillo and Villarluengo in 1994 and Zuera in 1995 and 2008. Although each forest plot had initially assigned a Prometheus fuel type as the ground-truth (see Hoffrén *et al*., 2023b), fuel types were reassigned during each visit, as plots could undergo changes in the dominant Prometheus type due to natural vegetation dynamics. The grassland fuel type (FT1) was not considered in this study due to its highly homogeneous and distinctive fuel structure. The center of each plot was determined using a *Leica VIVA*® GS15 CS10 GNSS real-time kinematic global positioning system with centimeter-level accuracy.

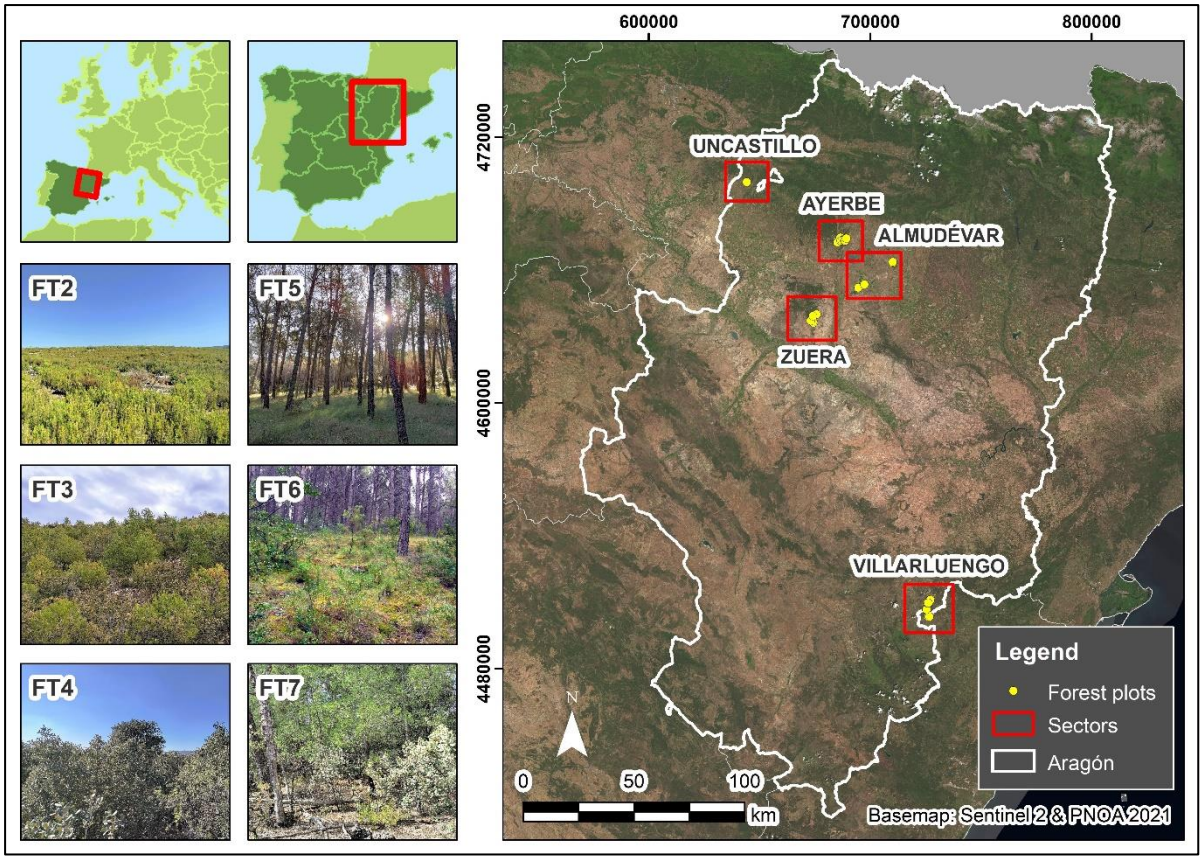

Figure 1. Study area, location of the 5 sectors and the 43 forest plots, and detailed photo of 6 plots for each Prometheus fuel type considered in the study. Coordinate reference system of the main map is EPSG: 25830 (ETRS89 – UTM zone 30N).

2.2. Data acquisition and preprocessing

HMLS data were collected at the end of May 2023 using a *GeoSLAM ZEB-Horizon* unit (GeoSLAM Ltd., Ruddington, UK) (Figure 2a), capable of scanning 300,000 points per second with a maximum scan range of 100 m and a 360° × 270° field of view. Scans were performed following methods similar to those described in Gollob *et al.* (2020a, 2020b). The scanning procedure commenced at the center of each plot, followed by an inner circular scan approximately 1 m from the plot's center and an outer circular scan at the plot's boundaries, pointing towards the center of the plot. Next, a detailed scan was performed within the plot in densely vegetated and shadowed areas to mitigate occlusion issues, concluding the scan at the starting point located at the plot's center. An example of a typical scan path on a plot can be observed in Figure 2b. The scanning time for each plot was about 10–15 minutes (longer in denser plots). The interaction of the laser system with the vegetation generated highly dense three-dimensional point clouds, with an average point density of 63,148 points/m^2 for all plots (detailed densities for each plot are presented in Tables A.1 and A.2 of the Appendix). Since the HMLS system did not incorporate an

inertial measurement unit, data were collected in local coordinates (i.e., the center of the plot had coordinates XY 0,0) and were subsequently georeferenced to a coordinate reference system. To achieve this, five ground control points (GCPs) were established in each plot before the start of the scans with the *Leica VIVA*® GS15 CS10 GNSS. One GCP was positioned at the center of the plot, and the remaining four were placed at each of the cardinal points of the plot's boundaries (Figure 2b). During the scans, the HMLS remained static and at ground level on each GCP for at least 10 seconds to record the local coordinates, which were then matched with the coordinates obtained from the GNSS at the same GCP. For data preprocessing, the proprietary software *GeoSLAM Connect* v.2.3.0 was employed. It involved the conversion of scans into LAS files and georeferencing local coordinates to a coordinate reference system (EPSG: 25830 – ETRS89 UTM zone 30N). For the latter, the *Stop and Go alignment* tool was utilized, facilitating the association of the local coordinates registered with the HMLS to the coordinates recorded with the GNSS at each GCP in the coordinate reference system. The mean georeferencing error for all plots was 0.161 m (detailed results are provided in Tables A.1 and A.2 of the Appendix).

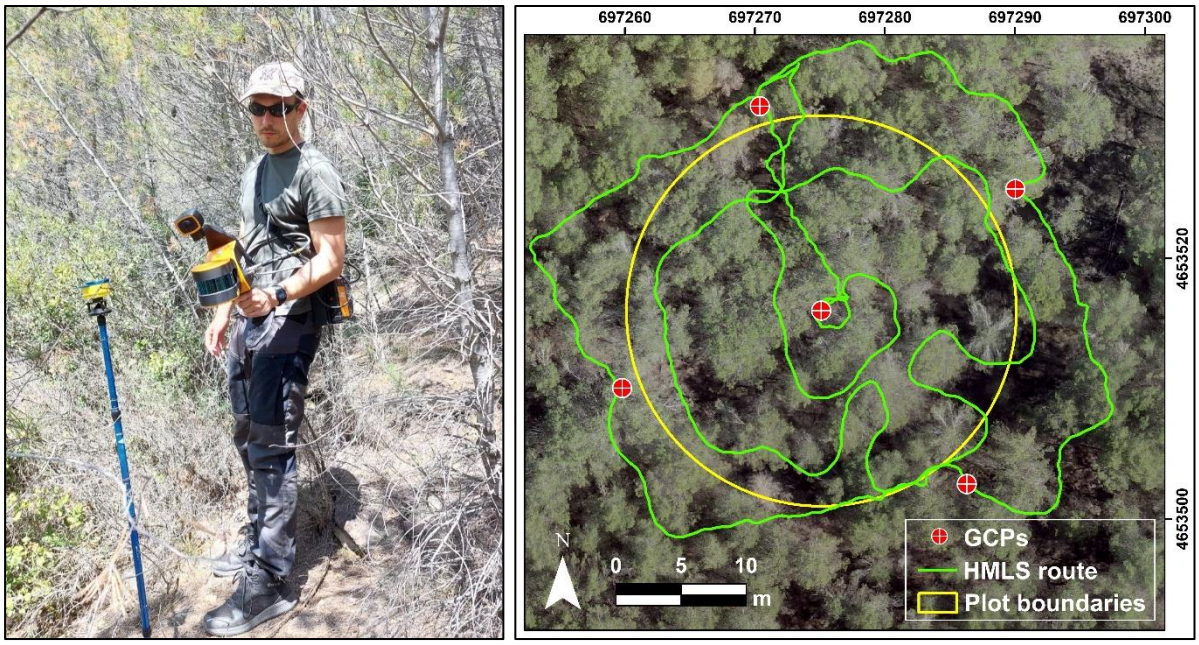

(a) (b)

Figure 2. (**a**) HMLS unit used in the study: *GeoSLAM ZEB-Horizon* (GeoSLAM Ltd., Ruddington, UK); (**b**) Example of the location of the 5 GCPs and the route followed to obtain the data in a plot.

2.3. Ground points classification

The georeferenced point clouds were classified into ground and non-ground points for the generation of Digital Elevation Models (DEMs) and height normalization. This process is a key step for ensuring that subsequent analyses are accurate, given the very high point cloud density of the HMLS data. To accomplish this, three different ground classification algorithms commonly used in forestry were tested as follows: the *lasground* algorithm of *LasTools* (Rapidlasso GmbH, Gilching, Germany), the *Multiscale Curvature Classification* (MCC) algorithm (Evans and Hudak, 2007), and the *Cloth Simulation Filter* (CSF) algorithm (Zhang *et al*., 2016). The software used for this purpose was ArcMap v.10.7.1 (ESRI, 2019) for *LasTools*, MCC-LiDAR v.2.1 (Evans and Hudak, 2007) for the MCC, and the lidR package (Roussel *et al*., 2020; Roussel and Auty, 2022) of the R environment (R Core Team, 2022) for the CSF. The classification could be applied without reducing the original point cloud densities in the cases of *LasTools* and the CSF, but with the MCC, the point clouds had to be decimated to 1,000 points/m^2 due to computational limitations. The points classified as ground by the three algorithms were used to generate DEMs with a spatial resolution of 0.20 m by the TIN-to-Raster interpolation method (Renslow, 2013) using the *rasterize terrain* function of the lidR package. Subsequently, the elevation values were extracted from the DEMs through the random sampling of 2,000 points, and they were compared with each other to compute the mean height error for each algorithm. The DEMs from the algorithm with the lowest mean error were selected to normalize the heights of the point clouds. This was achieved using the *normalize heights* function of the lidR package. Finally, normalized points with negative height values or exceeding 40 m (i.e., outliers) were removed using the *filter poi* function of lidR.

2.4. Voxelization and fuel load quantification

Estimation of the fuel load was performed by calculating the volume of the normalized point clouds. For this purpose, a voxelization process was conducted, which has been reported as a well-suited approach for estimating forest fuels (e.g., Barton *et al*., 2020; Eusuf *et al*., 2020; Rowell *et al*., 2020; Marcozzi *et al*., 2023) and allows for simplifying the huge amount of data coming from ground-based LiDAR systems (Popescu and Zhao, 2008; Kato *et al*., 2013; Lecigne *et al*., 2018; Hillman *et al*., 2021; Martínez-Rodrigo *et al*., 2022). In doing so, the effect of uneven point distributions, many of which tend to be located closer to the sensor, is normalized (Kato *et al*., 2013; Lecigne *et al*., 2018). The first step prior to the voxelization process was to consider the resolution of the voxels so

that they could accurately describe the heterogeneous structure and distribution of fuel loads without a loss of information. Considering the average point cloud densities, voxels were generated at a 5 cm grid resolution using the VoxR package for R (Lecigne *et al*., 2018; Lecigne, 2020). Before that, the points considered as noise were filtered out using the *Statistical Outliers Removal* (SOR) filter available in the VoxR package. The SOR filter considers a point to be noise if it is at a distance to its nearest neighbors greater than the mean distance of the entire point cloud plus 1.5 times the standard deviation of the other points (Lecigne, 2020). As a result of voxelization, each plot was composed of a collection of filled and empty voxels in the XYZ space (Figure 3). Filled voxels indicated the presence of at least one point of the point cloud, while empty voxels denoted an absence of points.

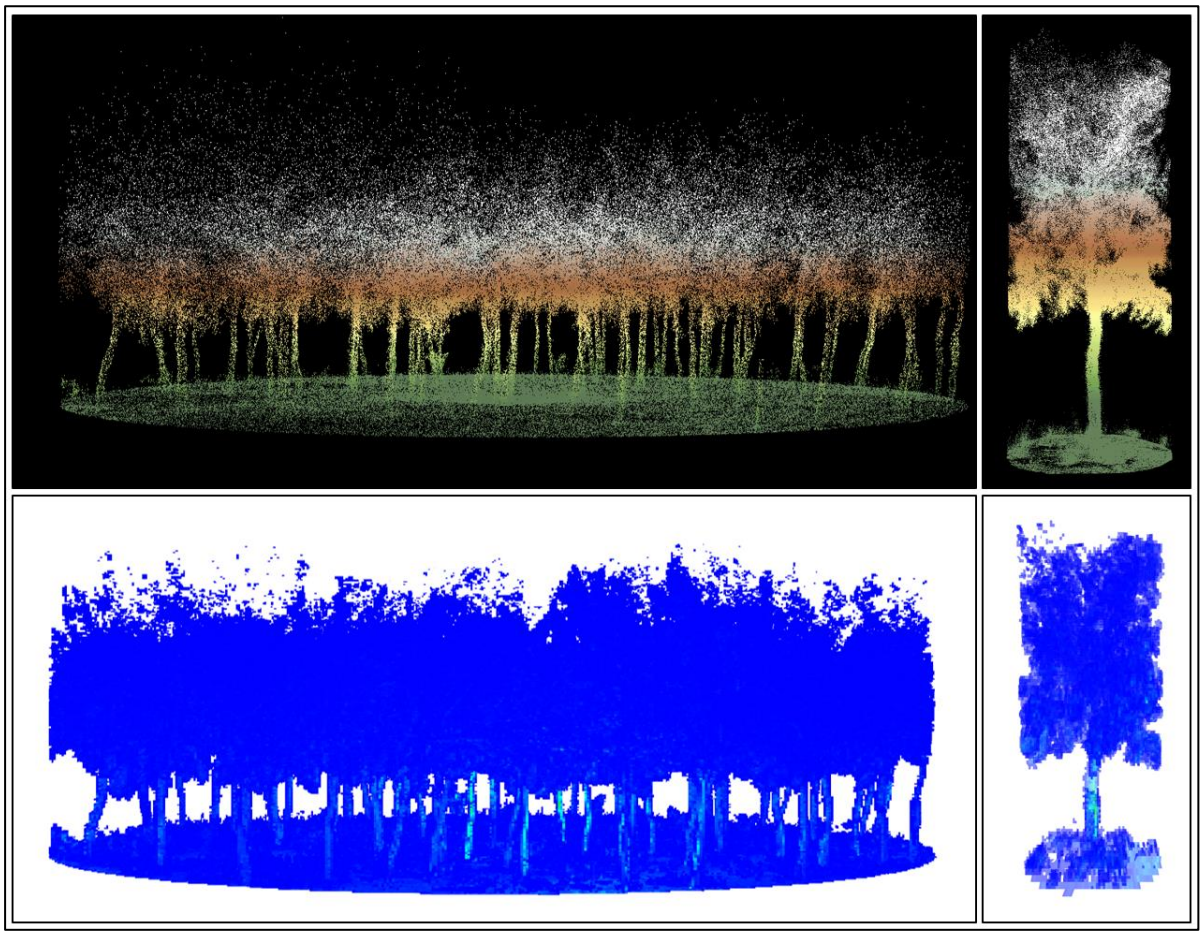

Figure 3. Results of voxelization (below) of the point cloud (above) for the entire forest plot *al02* (left) and for an individual tree within the plot (right). For a better visualization, only the filled voxels are displayed.

The total volume for each plot in each 5 cm height stratum was computed as the sum of the filled voxels in each stratum multiplied by their volume (Equation 5.1), following the methods adopted by Martínez-Rodrigo *et al*. (2022). In order

to take into account, with a cautious approach, the measurement accuracy of the instrument, which is around 1–3 cm, for subsequent analyses, the first voxelized stratum (i.e., voxels between 0 and 5 cm of height) was not considered to ensure an exclusion of returns that may belong to the ground and not to the fuel. The volume of each height stratum was calculated in absolute (m^3/m^2) and relative (% of the total) terms. Additionally, the total volume of the fuel load was calculated for each height threshold of the Prometheus model: below 0.60 m for the low shrub (*LSh*) stratum, between 0.60–2 m for the medium shrub (*MSh*) stratum, between 2–4 m for the high shrub (*HSh*) stratum, and above 4 m for the tree stratum (*Tr*), for quantifying the average fuel load for each fuel type.

$$VOL_s = \sum VOX_s \times (0.05)^3 \quad (1)$$

where *VOL* represents the total volume in absolute (m^3/m^2) and relative (% of the total) terms in the *s* height stratum, and *VOX* represents the filled voxels in the *s* height stratum.

3. RESULTS

3.1. Visual analyses of the processed point clouds

A preliminary assessment of the differentiation capability between the Prometheus fuel types was conducted through a visual analysis of the point clouds. Figure 4 illustrates the structural heterogeneity of vegetation at both the plot and transect scales by fuel type. It can be observed that the acquired and processed data successfully represent the vertical distribution of vegetation, even in the upper strata (e.g., canopies), which are further away from the ground, where data are acquired. The *LSh*, *MSh*, and *HSh* strata (i.e., shrub strata) are predominant in FT2, FT3, and FT4, respectively. In addition, some scattered larger shrubs or small trees can be found in the FT2 and FT3 plots, while FT4 exhibits a greater spatial continuity of tall shrubs. In FT5, the point cloud clearly represents the tree profile and the absence of an understory. Continuity of vegetation can be observed between the lower and upper strata for the tree fuel types, as in FT6, but to a lesser extent compared to FT7, where the fuel reaches the maximum structural volume and the highest stand compactness.

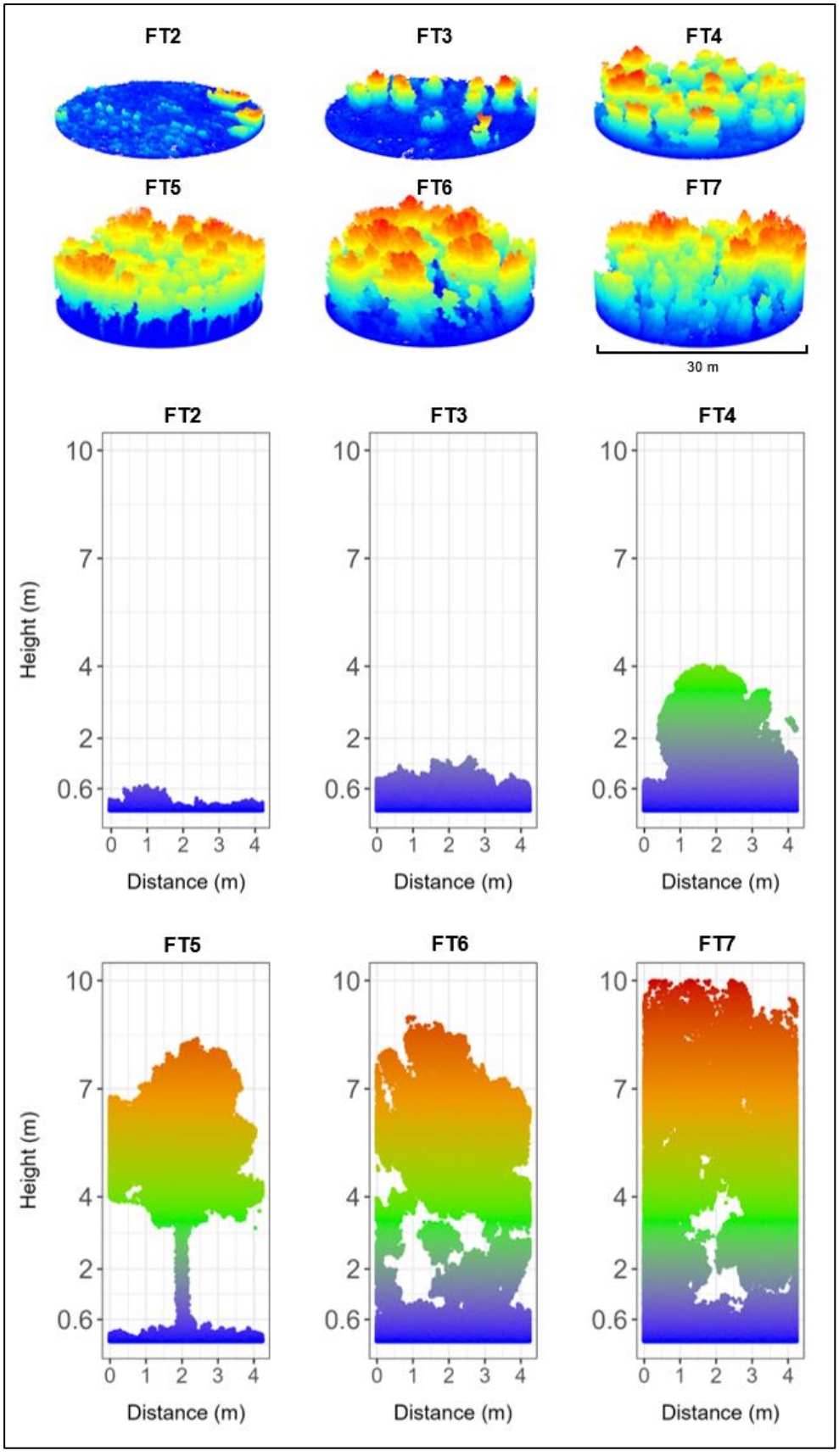

Figure 4. Spatial distribution of the HMLS point cloud by representative plots (above) and transects (below) for each Prometheus fuel type considered in the study. Colors refer to height of vegetation.

3.2. Selection of the ground points classification algorithm

Figure 5 depicts the results of the comparative analyses of the mean height error for each plot and between algorithms. The detailed results can be found in Tables A.3 and A.4 of the Appendix. There were minimal differences in the height values extracted from the MCC and CSF (mean error = 4 cm, standard deviation = 4 cm), whereas, with *LasTools*, the differences with the other two algorithms were slightly larger (*LasTools*–MCC: mean error = 19 cm, standard deviation = 28 cm; *LasTools*–CSF: mean error = 20 cm, standard deviation = 26 cm). Regarding the classification process, the MCC took considerable time to process the decimated point cloud, while *LasTools* and the CSF processed the complete point cloud in less time. Therefore, based on these results, the CSF algorithm was chosen as the most suitable for filtering and classifying the point clouds into ground and non-ground points to normalize the heights of the point clouds.

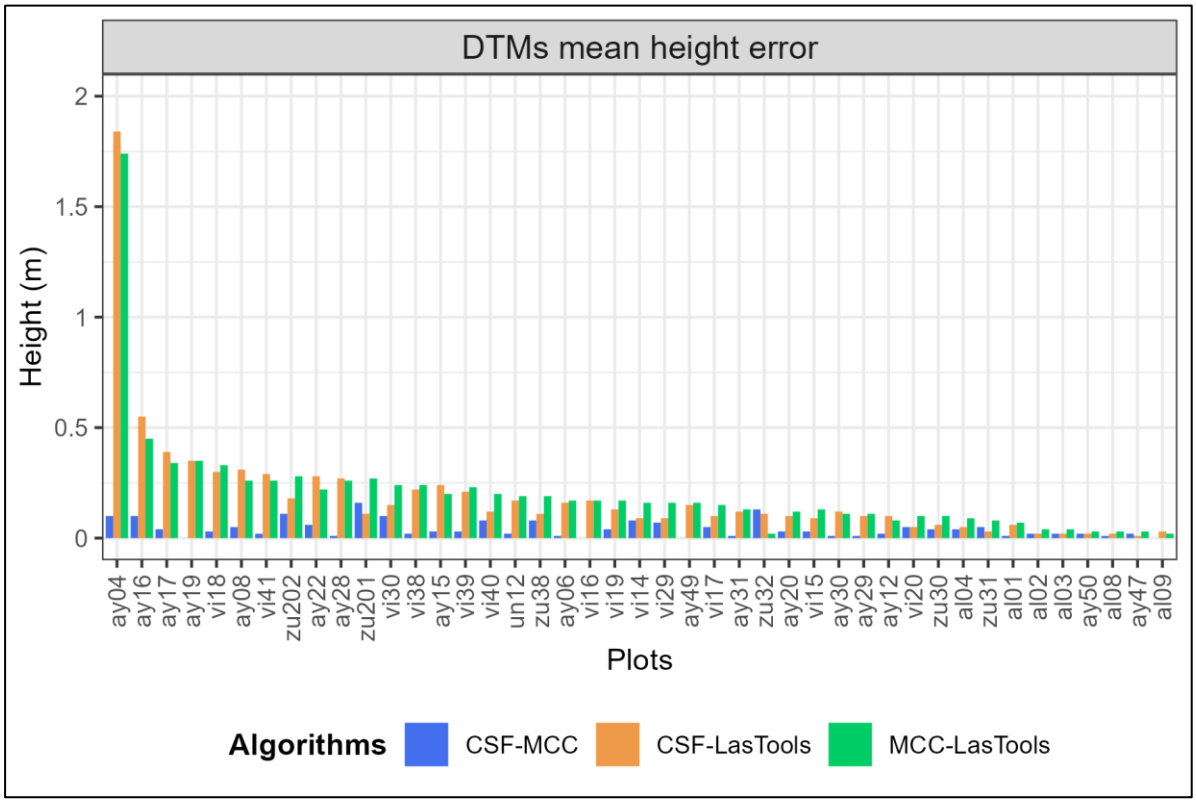

Figure 5. DEMs mean height error for each forest plot and each pair of ground point classification algorithms considered in the study.

3.3. Definition of Prometheus fuel types

The vertical distribution of the fuel volume every 5 cm enabled the definition of specific distributions of the Prometheus fuel types for each forest plot (see Figure A.1 of the Appendix), facilitating the detection of plots with inaccurately estimated fuel types in the field.

In general terms, the Prometheus shrub fuel types (FT2, FT3, and FT4) exhibit a unimodal distribution, except for some cases in FT4, with peaks in the *LSh* stratum and a gradual decrease in fuel towards the higher strata, nearly diminishing in the *MSh* stratum (Figure 6). In FT2, the fuel is primarily concentrated in the *LSh* stratum, with only a few plots showing a slight increase between 0.60 and 4 m, likely due to scattered low trees within those plots, though it does not significantly alter the overall distribution. In FT3, the decline in fuel load is less abrupt than in FT2 within the *LSh* stratum but stabilizes in the *MSh* stratum before gradually decreasing to the *Tr* stratum. The distribution of FT4 differs slightly from that of FT2 and FT3, with the peak found in both the *LSh* and *MSh* strata. Moreover, there is a higher volume of fuel in the *MSh* stratum. Some plots exhibit a bimodal distribution, with peaks in both the *LSh* and *MSh* strata. These distributions in FT4 suggest a continuity of the vertical fuel structure below 4 m, characteristic of this fuel type. Based on these findings, a total of four shrub-type plots with inaccurately estimated fuel types in the field were identified. One plot, initially classified as FT2 (*vi40*), did not align with the average distribution for this fuel type, as it exhibited a higher fuel volume in the *MSh* stratum, aligning more closely with FT3. Consequently, the ground-truth was changed to this fuel type. Additionally, three plots classified as FT3 (*vi17*, *zu30*, and *zu31*) were reclassified as FT2, as their volume distribution showed an abrupt decrease in fuel from the *MSh* stratum, better fitting with the FT2 distributions. In the case of the FT4 plots, no modifications were made.

Regarding the Prometheus tree fuel types (Figure 7), FT5 displays a distinctly bimodal distribution, with a primary peak in the *LSh* stratum and a secondary peak starting in the *HSh* stratum and continuing into the *Tr* stratum or originating directly in the *Tr* stratum, with a minimal fuel load volume in the *MSh* stratum. The distribution of FT6 exhibits a peak in the *LSh* stratum, followed by a decrease in the *MSh* stratum and a slight increase in the *HSh* stratum, culminating in a gradual decline from the *Tr* stratum. FT7 exhibits a very similar distribution to FT6, except for a more consistent volume along the *MSh* and *HSh* strata before declining from the *Tr* stratum. This indicates greater volume in the intermediate strata and consequently, more vertical continuity of the fuel load, characteristic of this type. These findings revealed misidentifications of ground-truth in six tree-type fuel plots. Two plots, initially categorized as FT6 (*ay12* and *ay49*), were reassigned to FT5 due to the distinct bimodality of their distributions and minimal volume present in the *MSh* and *HSh* strata. Another plot initially labeled as FT6 in the field (*ay31*) was corrected to FT7, as it demonstrated a consistent fuel volume between the *LSh* and *MSh* strata. Moreover, three plots originally labeled as FT7 (*ay06*, *ay19*, and *ay28*) were modified to FT6, as their

distributions indicated a decrease in volume in the *MSh* stratum, suggesting less vertical continuity of vegetation. Finally, a plot labeled as FT7 (*vi41*, corresponding to the pink line in the FT7 plots of Figure 7) displayed a distinctive signature compared to others of the same fuel type. While this plot could potentially fall between FT4 and FT7 due to its clear bimodality resembling some FT4 plots, the significant fuel load from the *Tr* stratum, persisting until approximately 8 meters, suggests excessive height for the FT4 plot. Consequently, the ground-truth was not modified, assuming it to be a FT7 plot with a low tree height.

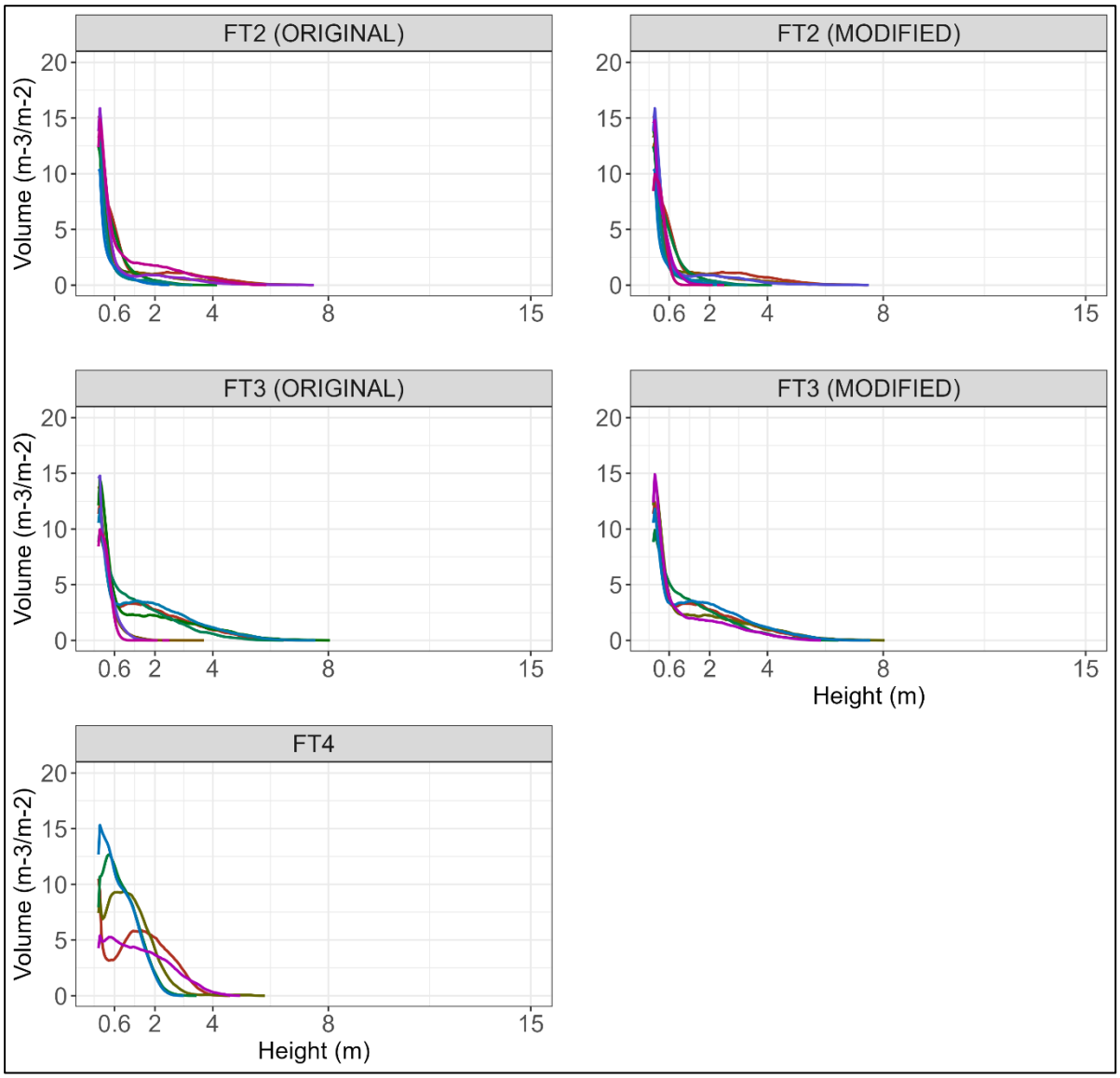

Figure 6. Vertical distribution of the volume of fuel load every 0.05 m of the Prometheus shrub fuel types. Each line represents a forest plot arranged by the fuel type estimated in the field (left) and corrected with HMLS data (right). No modifications were made in FT4 plots.

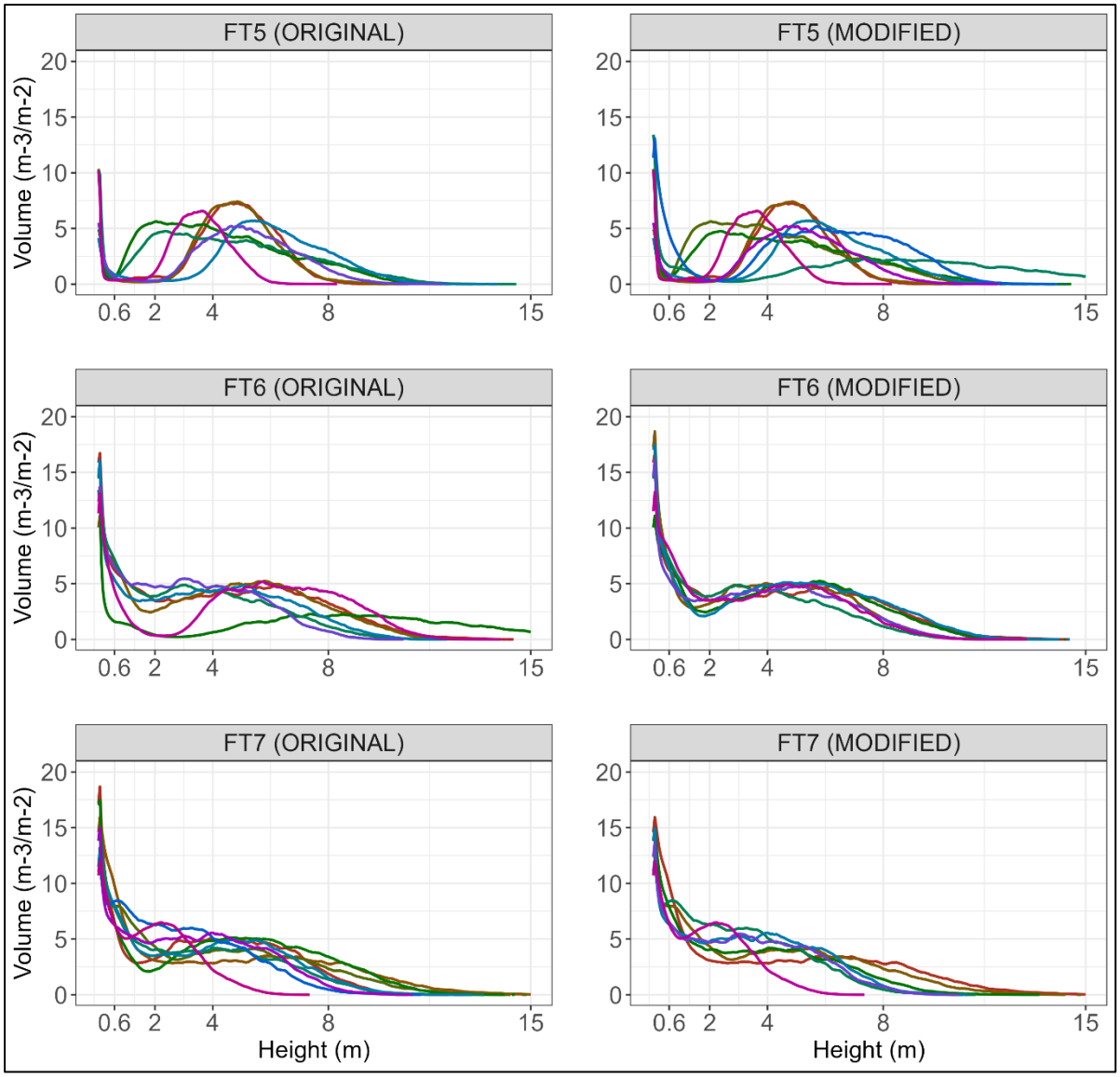

Figure 7. Vertical distribution of the volume of fuel load every 0.05 m of the Prometheus tree fuel types. Each line represents a forest plot arranged by the fuel type estimated in the field (left) and corrected with HMLS data (right).

3.4. Quantification of Prometheus fuel load

The quantification of fuel load by Prometheus height strata confirmed the corrections made to the ground-truth in the 10 forest plots. The results presented below are grouped by the fuel types modified from the HMLS data, as mentioned in the previous section. Figure 8 illustrates the fuel volume of each Prometheus shrub fuel type, revealing a generally progressive increase in the total volume from FT2 to FT4; specifically, the volume is less than 250 m^3/m^2 in FT2, slightly over 250 m^3/m^2 in FT3 (except for one plot: *vi40*), and somewhat higher than 250 m^3/m^2 in FT4. Plot *vi40* was misclassified as FT2 in the field and is the only one among FT3 that does not exceed 250 m^3/m^2 of the total volume. This suggests that this plot could be on the border between FT2 and FT3. However,

the percentage of volume contained in the *MSh* and *HSh* strata in this plot is quite high (> 20%), resembling the percentages of FT3 plots more closely. Regarding the percentage of volume in each Prometheus stratum, a clear dominance of the *LSh* stratum is observed in FT2 (> 50% of the total volume in all plots except for one), with greater parity in FT3 but with more significant proportions in the two lower strata, and a predominance of the *MSh* stratum in FT4. As expected, the percentage of the total volume in the *Tr* stratum is almost negligible in the three shrub types. Only three FT2 plots have volume in the *HSh* and *Tr* strata, which are related to the small volume increments seen in these strata in Figure 5 and explained before. There is a higher volume percentage in the *Tr* stratum in the FT3 plots, but they are still low values, while there is hardly any in FT4. Finally, it is worth noting that the volume of the plots where the ground-truth was corrected (*vi17*, *vi40*, *zu30*, and *zu31*) fits quite well within their respective new groups.

In the Prometheus tree fuel types, there is a lower volume of fuel load in FT5 (<750 m^3/m^2) due to the absence of understory and a slightly higher volume in the FT6 plots compared to FT7 (Figure 9) due to a greater volume of tree canopies in the former. In general terms, the dominant stratum in these types is the *Tr* stratum, reaching the highest percentages in the FT5 plots. The FT7 plots have greater uniformity in the volume contained in each Prometheus stratum, although some plots show similar volume percentages in the *MSh* and *HSh* strata to others identified as FT6 (e.g., *ay16* and *ay17*). This may be an indicator of the high complexity of the vertical fuel structure in both types. However, in the FT6 plots, there are no cases of a volume percentage higher than 20% in the same plot in both the *MSh* and *HSh* strata, while this is a characteristic in most FT7 plots, suggesting a greater vertical continuity of fuel between the strata in the latter. Regarding FT5, the amount of volume in the *LSh* and *MSh* strata is very low, and appreciable amounts are only found in plots *al08*, *al09*, *ay12*, and *ay49*. In the case of the former two, it is due to a higher percentage of *MSh* strata, although this percentage is not high. The latter two were labeled in the field as FT6 because they had a higher volume of fuel in the *MSh* stratum compared to the other FT5 plots. However, their volume by Prometheus height strata seems to fit better in FT5, confirming the corrections made previously. Plot *zu32* has the most distinctive volume distribution of all FT5 plots, as the dominant stratum is the *HSh* stratum, assuming that this is a FT5 plot with a low tree height. On the other hand, the volume of plot *ay31*, whose fuel type was labeled as FT6 in the field, fits quite well as FT7. Plots *ay06*, *ay19*, and *ay28*, which transitioned from FT7 to FT6, also seem to fit better with their new type. Lastly, it is confirmed that plot *vi41* is a low FT7 plot since it has very little volume in the

Tr stratum but a lot in the *HSh* stratum. Its distribution closely resembles those of FT4 plots, although with significantly more volume in the upper strata, so it might not be appropriate to be labeled as FT4.

Figure 8. Total volume (left) and percentage of the total volume (right) of fuel load for each plot by Prometheus height strata and for the Prometheus shrub fuel types. Percentage values within bar plots are represented in %. Volume < 3% is not labeled due to space constraints. The plots are arranged by the fuel types modified from the HMLS data.

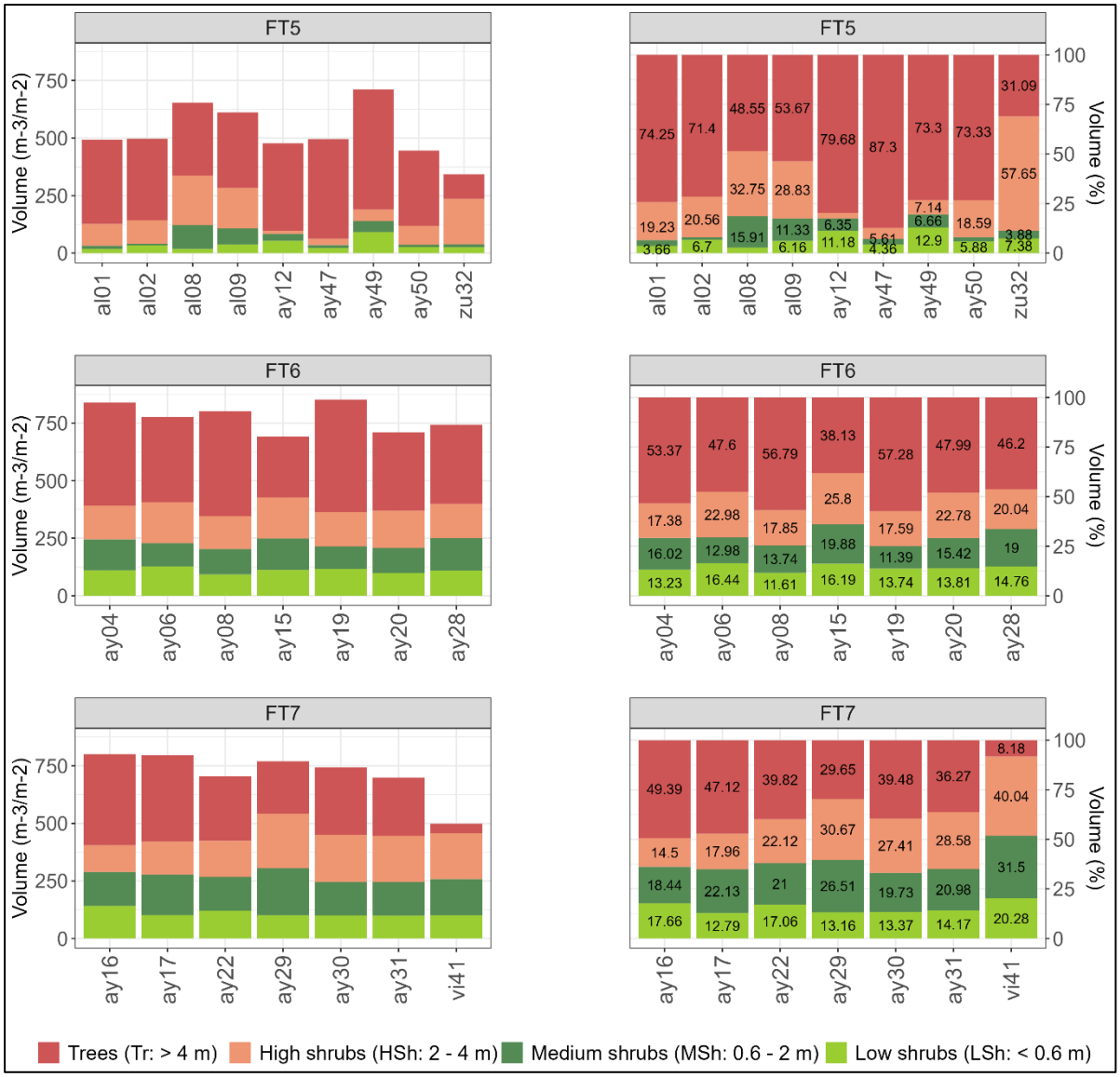

Figure 9. Total volume (left) and percentage of the total volume (right) of fuel load for each plot by Prometheus height strata and for the Prometheus tree fuel types. Percentage values within bar plots are represented in %. Volume < 3% is not labeled due to space constraints. The plots are arranged by the fuel types modified from the HMLS data.

4. DISCUSSION

In the current context of increasing exposure to wildfires, it is necessary to develop plans to mitigate their negative effects on the environment. An effective step is to correctly identify fuel types in the field to accurately model fire behavior in larger areas. However, forest stands are often structurally complex and present mixed features of several fuel types, especially in the Mediterranean region, making the in situ estimation of fuels challenging at times. This study has relied on a HMLS system to address this challenge, as its ability to obtain detailed data on forest vertical and horizontal structure allows for a more precise

characterization of vegetation and the definition of Prometheus fuel types at the plot level. Thanks to the large amount of data involved, the corrections made to incorrectly identified fuel types in the field were successful, resulting in 10 out of the 43 plots changing their assigned fuel type, which could explain some of the confusion between similar fuel types observed in Hoffrén *et al.* (2023b). Additionally, the proposed methodology, based on the use of a HMLS system, provides an efficient alternative for the estimation and correction of fuel types in the field in Mediterranean forest environments. Overall, the results show that voxelization of the very-high-density three-dimensional point clouds from the HMLS data allowed the identification of specific distributions of the vertical fuel volume for each Prometheus fuel type, while quantification of the fuel volume by Prometheus height strata validated the information provided by the distributions.

The CSF algorithm was the most suitable for the classification of the ground points. Filtering is a key process to normalize the heights and ensure the greatest accuracies in the subsequent voxelization and fuel volume estimation. This algorithm has already been used in previous studies that have employed HMLS systems (e.g., Donager *et al.*, 2021; Gollob *et al.*, 2020a), as well as TLS systems (e.g., Hillman *et al.*, 2021; Panagiotidis *et al.*, 2021) and other MLS systems (e.g., de Paula Pires *et al.*, 2022). The results of the centimetric-scale voxelization (5 cm) appear to be adequate for better identifying the vertical distribution of fuels and accurately estimating the Prometheus fuel types without loss of information on the structural complexity of the forest stands. Although the voxel size will depend on the research objectives and the quality of the data (Lecigne *et al.*, 2018), several studies using ground-based LiDAR systems have employed small-sized voxels for volume estimation with satisfactory results. For instance, when using the TLS system, Lecigne *et al.* (2018) noticed that smaller voxels were more suitable for capturing fine changes in tree features compared to larger voxel sizes, which is crucial when working in structurally complex environments such as Mediterranean forests. Yan *et al.* (2019) generated voxels of a 20 cm size for the crown volume estimation from MLS-derived point clouds. Voxel sizes of 10 cm have also been used to estimate forest fuel characteristics with a TLS system (Rowell *et al.*, 2020) and stand structural features with the HMLS system (Martínez-Rodrigo *et al.*, 2022). In this study, the volume of fuel load has been calculated directly from the voxels, but it can also be estimated indirectly. For instance, a voxel-derived index called PDI (*Plant Diversity Index*) was proposed by Puletti *et al.* (2021), which relates the number of filled voxels to the total number of voxels within the same height stratum, resulting in the satisfactory estimation of the vertical distribution of fuel volume. Despite the

small voxel size used for the voxelization and the very high density of the point clouds, the process was relatively fast and allowed for more efficient management of the vast amount of data collected with the HMLS. In this regard, voxels allow for the removal of some unwanted effects typical of ground-based LiDAR systems, such as occlusion or differences in point cloud densities, which can introduce bias in the characterization of fuel structure. This process of discretizing point clouds also helps in monitoring forest changes over different time periods (Srinivasan *et al*., 2014; McCarley *et al*., 2017; Zhao *et al*., 2018), which could be valuable for detecting progressive changes in the fuel types over time due to natural vegetation growth. In this sense, working directly with the point cloud would have been computationally more demanding, as the extraction of structural metrics to estimate the distribution and density of forest structure is typically done at the pixel or plot level. Thus, this study proposes a simpler methodology for better defining fuel types and correcting those that were incorrectly estimated in the field.

Among the various platforms of ground-based LiDAR systems, this study has utilized a HMLS in a novel application in forestry. Overall, the results of the modifications for incorrectly estimated fuel types in the field are satisfactory and underscore the value of HMLS systems for quantifying the fuel load volume and precisely defining Prometheus fuel types. However, certain limitations related to intrinsic system errors and to the estimation of fuel volume in quantitative units (m^3/m^2) must be considered. On one hand, the system itself may exhibit jitter errors that are challenging to control, necessitating the acceptance of some uncertainty in the recorded data. Additionally, the manner in which scans are conducted by the user can influence data accuracy. Therefore, methods from previous studies, such as predefined routes, sensor orientation, and designated starting and ending scanning points, were followed in order to minimize uncertainty (e.g., Bauwens *et al*., 2016; Gollob *et al*., 2020a; Gollob *et al*., 2020b; Forbes *et al*., 2022). Furthermore, the voxelization process helped to homogenize the point clouds, thus mitigating bias (Lecigne *et al*., 2018). On the other hand, estimating the fuel volume in quantitative units may not always be entirely satisfactory. For example, some FT6 and FT7 plots exhibited very similar vertical fuel distributions (Figure 9), potentially leading to confusion between the different types, even when working at centimetric scales, as in this study. Moreover, the voxels were computed for the entire point cloud without differentiation of the objects from which they were returned. They lacked information related to the presence of different vegetation parts, such as foliage, branches, trunks, or bark, which are relevant for wildfire considerations. In this context, some studies have attempted to categorize voxels according to their

class to enhance fuel quantification (e.g., Barton *et al*., 2020; Eusuf *et al*., 2020). However, this can be a complex task in forest environments of very high structural heterogeneity, where different fuel classes are intermingled. Another limitation is the inability to differentiate between live and dead fuel from the raw point cloud data. Some HMLS systems allow the collection of data in combination with RGB images, which could aid in distinguishing between both types of fuel, although the processing could be time- and resource-intensive. Nevertheless, it would enable an improved fuel characterization and more accurate fire spread modeling. Despite these limitations, the HMLS system has facilitated the identification of plots with incorrectly estimated fuel types in the field and corrected them to their closest type. Confusions observed in the vertical distributions of fuel load volume (Figures 6 to 9) align with previous studies, which also reported inaccuracies in those fuel types using other remote sensing methodological approaches (e.g., Lasaponara *et al*., 2005; Arroyo *et al*., 2006; García *et al*., 2011; Domingo *et al*., 2020). The categories that underwent changes here also presented confounding issues in Hoffrén *et al*. (2023b), where the worst classified types were FT3 and FT6. In this study, Figures 6 and 7 confirm the existence of discrepancies in these two fuel types, with three plots initially assigned as FT3 in the field through visual analysis being modified to FT2, while three other FT6 plots had their assignment adjusted from FT6 to FT5 (two plots) and to FT7 (one plot).

The main confusion between fuel types may be due to the incorrect estimation of the volume of shrub or understory, i.e., understory fuels. In shrub fuel types, it determines the maximum height, while in tree fuel types, it defines the degree of vertical continuity between the understory and the canopies. Although ground-based LiDAR systems have demonstrated greater capabilities in identifying understory fuel than other systems (Beland *et al*., 2019; Arkin *et al*., 2023), leveraging alternative remote sensing platforms could enhance the estimation of understory fuels. For instance, Hillman *et al*. (2021) observed that LiDAR sensors mounted on unmanned aerial vehicles (LiDAR UAVs) effectively estimated understory fuels in a dry sclerophyll forest, achieving accuracy comparable to the TLS systems. Conversely, Hyyppä *et al*. (2020a) demonstrated that above-canopy LiDAR UAVs struggle to identify forest understory attributes, while under-canopy LiDAR UAVs can achieve a similar performance to ground-based LiDAR systems (Hyyppä *et al*., 2020a; *Hyyppä et al*., 2020b). Therefore, LiDAR UAVs offer a viable alternative for fuel-type identification, as they can cover larger areas and provide valuable data. However, they may be subject to more restrictive regulations and operational challenges in dense and complex forests. HMLS data also offer the potential to

obtain data over extensive areas, albeit requiring more time and effort. In addition, some forest plots may be inaccessible due to their extremely high vegetation density, particularly in Mediterranean forests. Despite these challenges, HMLS systems offer advantages such as a larger scanning area than the TLS system (Bauwens *et al*., 2016), flexibility in mobility within the forest, and the ability to georeference data indirectly with GCPs or directly with an inertial measurement unit. Consequently, based on our findings, HMLS systems should be regarded as promising tools to enhance field fuel load estimations. This improvement will contribute to better forest fuel modeling, thereby aiding in the development of effective forest fire prevention and mitigation plans.

5. CONCLUSIONS

Knowing the spatial distribution of forest fuels is a crucial step to understanding fire behavior in a hypothetical wildfire. In this sense, ground-based LiDAR systems can provide very detailed information on the vertical distribution of forest fuels in exceptional detail, which can be of great interest in improving the field estimation of fuel types. The results of this study conclude that HMLS systems are capable of detecting fuel loads in centimeter-scale height strata in heterogeneous forest plots. With this information, it is possible to determine the fuel type to which the plot belongs, even when there is a mixture of characteristics of different fuel types, a situation quite common in Mediterranean forest environments. This study has focused on the Prometheus model, but the approach could be applied to other relevant fire models. Thus, a better identification of fuel types can enhance the ground-truth of classification models, enabling more accurate modeling of fire behavior in larger areas. Ultimately, this contributes to improved wildfire prevention and mitigation in the territory.

ACKNOWLEDGMENTS

The authors would like to thank Grafinta S.A. (Av. Filipinas 46, 28003 Madrid, Spain) for providing the *GeoSLAM ZEB-Horizon* HMLS unit and the *GeoSLAM Connect* v.2.3.0 software, as well as for their continuous support and guidance, especially David Cruz. The authors also thank Dr. Darío Domingo for his support in the fieldwork.

REFERENCES

Åkerblom, M. and Kaitaniemi, P., 2021. Terrestrial laser scanning: A new standard of forest measuring and modelling? *Ann. Bot.* 128 (6), 653–662, https://doi.org/10.1093/aob/mcab111.

Albini, F., 1976. Estimating wildfire behavior and effects. USDA Forest Service. Intermountain Forest and Range Experiment Station. General Technical Report, INT-30, 92 pp.

Arkin, J., Coops, N.C., Daniels, L.D., and Plowright, A., 2023. Canopy and surface fuel estimations using RPAS and ground-based point clouds. *Forestry: An International Journal of Forest Research* cpad020, https://doi.org/10.1093/forestry/cpad020.

Arroyo, L.A., Healey, S.P., Cohen, W.B., Cocero, D., and Manzanera, J.A., 2006. Using object-oriented classification and high-resolution imagery to map fuel types in a Mediterranean region. *J. Geophys. Res.* 111, G04S04, https://doi.org/10.1029/2005JG000120.

Arroyo, L.A., Pascual, C., and Manzanera, J.A., 2008. Fire models and methods to map fuel types: The role of remote sensing. *For. Ecol. Manag.* 256 (6), 1239-1252, https://doi.org/10.1016/j.foreco/2008.06.048.

Ascoli, D., Moris, J.V., Marchetti, M., and Sallustio, L., 2021. Land use change towards forests and wooded land correlates with large and frequent wildfires in Italy. *Ann. Silvic. Res.* 46 (2), 177–188, https://doi.org/10.12899/asr-2264.

Barton, J., Gorte, B., Eusuf, M.S.R.S., and Zlatanova, S., 2020. A voxel-based method to estimate near-surface and elevated fuel from dense LiDAR point cloud for hazard reduction burning. *ISPRS Ann. Photogramm. Remote Sens. Spatial Inf. Sci.*, VI-3/W1-2020, 3–10, https://isprs-annals.copernicus.org/articles/VI-3-W1-2020/3/2020/.

Bauwens, S., Bartholomeus, H., Calders, K., and Lejeune, P., 2016. Forest inventory with terrestrial LiDAR: A comparison of static and hand-held mobile laser scanning. *Forests* 7, 127, https://doi.org/10.3390/f7060127.

Beland, M., Parker, G., Sparrow, B., Harding, D., Chasmer, L., Phinn, S., Antonarakis, A., and Strahler, A., 2019. On promoting the use of LiDAR systems in forest ecosystem research. *For. Ecol. Manag.* 450, 117484, https://doi.org/10.1016/j.foreco.2019117484.

Bowman, D.M.J.S., Balch, J.K., Artaxo, P., Bond, W.J., Carlson, J.M., Cochrane, M.A., D'Antonio, C.M., Defries, R.S., Doyle, J.C., Harrison, S.P., Johnston, F.H., Keeley, J.E., Krawchuk, M.A., Kull, C.A., Marston, J.B., Moritz, M.A., Prentice, I.C., Roos, C.I., Scott, A.C., Swetnam, T.W., van der Werf, G.R., and Pyne, S.J., 2019. Fire in the Earth System. *Science* 324, 5926, https://doi.org/10.1126/science.1163886.

Burt, A., Disney, M.I., Raumonen, P., Armston, J., Calders, K., and Lewis, P. Rapid characterization of forest structure from TLS and 3D modelling. In *Proceedings of the 2013 IEEE International Geoscience and Remote Sensing Symposium – IGARSS 2013*, Melbourne, VIC, Australia, pp. 3387–3390 (26 07 2013), https://doi.org/10.1109/IGARSS.2013.6723555.

Chas-Amil, M.L., Touza, J., and García-Martínez, E., 2013. Forest fires in the wildland-urban interface. A spatial analysis of forest fragmentation and human impacts. *Appl. Geogr.* 43, 127–137, https://doi.org/10.1016/j.apgeog.2013.06.010.

Chen, Y., Zhu, X., Yebra, M., Harris, S., and Tapper, N., 2016. Strata-based forest fuel classification for wild fire hazard assessment using terrestrial LiDAR. *J. Appl. Remote Sens.* 10 (4), 046025, https://doi.org/10.1117/1.JRS.10.046025.

Coskuner, K.A., Vatandaslar, C., Ozturk, M., Harman, I., Bilgili, E., Karahalil, U., Berber, T., and Gormus, E.T., 2023. Estimating Mediterranean stand fuel characteristics using handheld mobile laser scanning technology. *Int. J. Wildland Fire* 32 (9), 1347-1363, https://doi.org/10.1071/WF23005.

Crespo-Peremarch, P., Torralba, J., Carbonell-Rivera, J.P., and Ruiz, L.A., 2020. Comparing the generation of DTM in a forest ecosystem using TLS, ALS and UAV-DAP, and different software tools. *Int. Arch. Photogramm. Remote Sens. Spatial Inf. Sci.*, XLIII-B3-2020, 575–582, https://doi.org/10.5194/isprs-archives-XLIII-B3-2020-575-2020.

Cuadrat, J.M., Saz, M.A., and Vicente, S.M., 2007. Atlas Climático de Aragón. Servicio de Información y Educación Ambiental. Dirección General de Calidad Ambiental y Cambio Climático. Departamento de Medio Ambiente, Gobierno de Aragón. Zaragoza, Spain. https://www.aragon.es/-/atlas-climatico-de-aragon.

de Paula Pires, R., Olofsson, K., Persson, H.J., Lindberg, E., and Holmgren, J., 2022. Individual tree detection and estimation of stem attributes with mobile laser scanning along boreal forests roads. *ISPRS J. Photogramm. Remote Sens.* 187, 211–224, https://doi.org/10.1016/j.isprsjprs.2022.03.004.

Domingo, D., de la Riva, J., Lamelas, M.T., García-Martín, A., Ibarra, P., Echeverría, M.T., and Hoffrén, R., 2020. Fuel type classification using airborne laser scanning and Sentinel-2 data in Mediterranean forest affected by wildfires. *Remote Sens.* 12 (21), 1-22, https://doi.org/10.3390/rs12213660.

Donager, J.J., Sánchez-Meador, A.J., and Blackburn, R.C., 2021. Adjudicating perspectives on forest structure: How do airborne, terrestrial, and mobile LiDAR-derived estimates compare? *Remote Sens.* 13, 2297, https://doi.org/10.3390/rs13122297.

Eusuf, M.S.R.S., Barton, J., Gorte, B., and Zlatanova, S., 2020. Volume estimation of fuel load for hazard reduction burning: First results to a voxel approach. *ISPRS Ann. Photogramm. Remote Sens. Spatial Inf. Sci.*, VI-3/W1-2020, 3–10, https://doi.org/10.5194/isprs-archives-XLIII-B3-2020-1199-2020.

Evans, J.S. and Hudak, A.T., 2007. A multiscale curvature algorithm for classifying discrete return LiDAR in forested environments. *IEEE Trans. Geosci. Remote Sens.* 45 (4), 1029–1038, https://doi.org/10.1109/TGRS.2006.890412.

Ferraz, A., Saatchi, S., Mallet, C., and Meyer, V., 2016. LiDAR detection of individual tree size in tropical forests. *Remote Sens. Environ.* 183, 318–333, https://doi.org/10.1016/j.rse.2016.05.028.

Fol, C.R., Kükenbrink, D., Rehush, N., Murtiyoso, A., and Griess, V.C., 2023. Evaluating state-of-the-art 3D scanning methods for stem-level biodiversity inventories in forests. *Int. J. Appl. Earth Obs. Geoinf.* 122, 103396, https://doi.org/10.1016/j.jag.2023.103396.

Forbes, B., Reilly, S., Clark, M., Ferrell, R., Kelly, A., Krause, P., Matley, C., O'Neil, M., Villasenor, M., Disney, M.I., Wilkes, P., and Bentley, L.P., 2022. Comparing remote sensing and field-based approaches to estimate ladder fuels and predict wildfire burn severity. *Front. For. Glob. Change* 5, https://doi.org/10.3389/ffgc.2022.818713.

Ganteaume, A., Barbero, R., Jappiot, M., and Maillé, E., 2021. Understanding future changes to fires in southern Europe and their impacts on the wildland-urban interface. *J. Saf. Sci. Resil.* 2 (1), 20–29, https://doi.org/10.1016/j.jnlssr.2021.01.001.

García, M., Riaño, D., Chuvieco, E., Salas, J., and Danson, F.M., 2011. Multispectral and LiDAR data fusion for fuel type mapping using Support Vector Machine and decision rules. *Remote Sens. Environ.* 115 (6), 1369-1379, https://doi.org/10.1016/j.rse.2011.01.017.

Godoy, M.M., Martinuzzi, S., Masera, P., and Defossé. G.E., 2022. Forty years of Wildland Urban Interface growth and its relation with wildfires in Central-Western Chubut, Argentina. *Front. For. Glob. Change* 5, https://doi.org/10.3389/ffgc.2022.850543.

Gollob, C., Ritter, T., and Nothdurft, A., 2020a. Comparison of 3D point clouds obtained by terrestrial laser scanning and personal laser scanning on forest inventory sample plots. *Data* 5 (4), 103, https://doi.org/10.3390/data5040103.

Gollob, C., Ritter, T., and Nothdurft, A., 2020b. Forest inventory with long range and high-speed personal laser scanning (PLS) and simultaneous localization and mapping (SLAM) technology. *Remote Sens.* 12, 1509, https://doi.org/10.3390/rs12091509.

Gülci, S., Yurtseven, H., Akay, A.O., and Akgul, M., 2023. Measuring tree diameter using a LiDAR-equipped smartphone: A comparison of smartphone- and caliper-based DBH. *Environ. Monit. Assess.* 195, 678, https://doi.org/10.1007/s10661-023-11366-8.

Hillman, S., Wallace, L., Lucieer, A., Reinke, K., Turner, D., and Jones, S., 2021. A comparison of terrestrial and UAS sensors for measuring fuel hazard in a dry sclerophyll forest. *Int. J. Appl. Earth Obs. Geoinf.* 95, 102261. https://doi.org/10.1016/j.jag.2020.102261.

Hoffrén, R., Lamelas, M.T., and de la Riva, J., 2023b. UAV-derived photogrammetric point clouds and multispectral indices for fuel estimation in Mediterranean forests. *Remote Sens. Appl.: Soc. Environ.* 31, 100997, https://doi.org/10.1016/j.rsase.2023.100997.

Hoffrén, R., Lamelas, M.T., de la Riva, J., Domingo, D., Montealegre, A.L., García-Martín, A., and Revilla, S., 2023a. Assessing GEDI-NASA system for forest fuels classification using machine learning techniques. *Int. J. Appl. Earth. Obs. Geoinf.* 116, 103175, https://doi.org/10.1016/j.jag.2022.103175.

Huesca, M., Riaño, D., and Ustin, S.L., 2019. Spectral mapping methods applied to LiDAR data. Application to fuel type mapping. *Int. J. Appl. Earth Obs. Geoinf.* 74, 159–168, https://doi.org/10.1016/j.jag.2018.08.020.

Hyyppä, E., Hyyppä, J., Hakala, T., Kukko, A., Wulder, M.A., White, J.C., Pyöräla, J., Yu, X., Wang, Y., Virtanen, J.P., Pohjavirta, O., Liang, X., Holopainen, M., and Kaartinen, H., 2020b. Under-canopy UAV laser scanning for accurate forest field measurements. *ISPRS J. Photogramm Remote Sens.* 164, 41–60, https://doi.org/10.1016/j.isprsjprs.2020.03.021.

Hyyppä, E., Yu, X., Kaartinen, H., Hakala, T., Kukko, A., Vastaranta, M., and Hyyppä, J., 2020a. Comparison of backpack, handheld, under-canopy UAV, and above-canopy UAV laser scanning for field reference data collection in boreal forests. *Remote Sens.* 12 (20), 3327, https://doi.org/10.3390/rs12203327.

Jones, M.W., Abatzoglou, J.T., Veraverbeke, S., Andela, N., Lasslop, G., Forkel, M., Smith, A.J.P., Burton, C., Betts, R.A., van der Werf, G.R., Sitch, S., Canadell, J.G., Santín, C., Kolden, C., Doerr, S.H., and Le Quéré, C., 2022. Global and regional trends and drivers of fire under climate change. *Rev. Geophys.* 60, e2020RG000726, https://doi.irg/10.1029/2020RG000726.

Kato, A., Watanabe, M., Morgenroth, J., and Gomez, C., 2013. Field tree measurement using terrestrial laser for radar remote sensing. In *Proceedings of Asia-Pacific Conference on Synthetic Aperture Radar (APSAR)*, Asia-Pacific Conference, 119–121. Tsukuba, Japan.

Koutsias, N., Martínez-Fernández, J., and Allgöwer, B., 2013. Do factors causing wildfires vary in space? Evidence from Geographically Weighted Regression. *GIScience Remote Sens.* 47 (2), 221–240, https://doi.org/10.2747/1548-1603.47.2.221.

Lasaponara, R., Lanorte, A., and Pignatti, S., 2005. Characterization and mapping of fuel types for the Mediterranean ecosystems of Pollino National Park in southern Italy by using hyperspectral MIVIS data. *Earth Interact.* 10 (13), 1–11, https://doi.org/10.1175/EI165.1.

Lecigne, B., 2020. 'VoxR': Trees geometry and morphology from unstructured TLS data. R package version 1.0.0. https://cran.r-project.org/package=VoxR.

Lecigne, B., Delagrange, S., and Messier, C., 2018. Exploring trees in three dimensions: VoxR, a novel voxel-based R package dedicated to analysing the complex arrangement of tree crowns. *Ann. Bot.* 121 (4), 589–601, https://doi.org/10.1093/aob/mcx095.

Liang, X., Kankare, V., Hyyppä, J., Wang, Y., Kukko, A., Haggrén, H., Yu, X., Kaartinen, H., Jaakkola, A., Guan, F., Holopainen, M., and Vastaranta, M., 2016. Terrestrial laser scanning in forest inventories. ISPRS J. Photogramm. *Remote Sens.* 115, 63–77, https://doi.org/10.1016/j.isprsjprs.2016.01.006.

Loudermilk, E.L., Pokwsinski, S., Hawley, C.M., Maxwell, A., Gallagher, M.R., Skowronski, N.S., Hudak, A.T., Hoffman, C., and Hiers, J.K., 2023. Terrestrial laser scan metrics predict surface vegetation biomass and consumption in a frequently burned southeastern U.S. ecosystem. *Fire* 6 (4), 151, https://doi.org/10.3390/fire6040151.

Marcozzi, A.A., Johnson, J.V., Parsons, R.A., Flanary, S.J., Seielstad, C.A., and Downs, J.Z., 2023. Application of LiDAR derived fuel cells to wildfire modeling at laboratory scale. *Fire* 6 (10), 394, https://doi.org/10.3390/fire6100394.

Martínez-Rodrigo, R., Gómez, C., Toraño-Caicoya, A., Bohnhorst, L., Uhl, E., and Águeda, B., 2022. Stand structural characteristics derived from combined TLS and Landsat data support predictions of mushroom yields in Mediterranean forest. *Remote Sens.* 14, 5025, https://doi.org/10.3390/rs14195025.

Maxwell, A.E., Gallagher, M.R., Minicuci, N., Bester, M.S., Loudermilk, E.L., Pokswinski, S.M., and Skowronski, N.S., 2023. Impact of reference data sampling density for estimating plot-level shrub heights using terrestrial laser scanning data. *Fire* 6 (3), 98, https://doi.org/10.3390/fire6030098.

McCarley, T.R., Kolden, C.A., Vaillant, N.M., Hudak, A.T., Smith, A.M.S., Wing, B.M., Kellogg, B.S., and Kreitler, J., 2017. Multi-temporal LiDAR and Landsat quantification of fire-induced changes to forest structure. *Remote Sens. Environ.* 191, 419–432, https://doi.org/10.1016/j.rse.2016.12.022.

Moreno, M.V., Conedera, M., Chuvieco, E., and Pezzatti, G.B., 2014. Fire regime changes and major driving forces in Spain from 1968 to 2010. *Environ. Sci. Policy* 37, 11–22, https://doi.org/10.1016/j.envsci.2013.08.005.

Nocentini, S. and Coll, L., 2013. Mediterranean forests: Human use and complex adaptive systems. In Managing forests as complex adaptive systems. Building resilience to the challenge of global change; Messier, C., Puettmann, K.J., Coates, K.D., Eds.; Routledge, London, UK, pp. 214–243.

Olofsson, K. and Holmgren, J., 2016. Single tree stem profile detection using terrestrial laser scanner data, flatness saliency features and curvature properties. *Forests* 7 (9), 207, https://doi.org/10.3390/f7090207.

Panagiotidis, D., Abdollahnejad, A., and Slavík, M., 2021. Assessment of stem volume on plots using terrestrial laser scanner: a precision forestry application. *Sensors* 21 (1), 301, https://doi.org/10.3390/s21010301.

Pausas, J.G. and Keeley, J.E., 2009. A burning story: The role of fire in the history of life. *Bioscience* 59 (7), 593–601, https://doi.org/10.1525/bio.2009.59.7.10.

Popescu, S.C. and Zhao, K., 2008. A voxel-based LiDAR method for estimating crown base height for deciduous and pine trees. *Remote Sens. Environ.* 112, 767-781, https://doi.org/10.1016/j.rse.2007.06.011.

Post, A.J., 2022. Using handheld mobile laser scanning to quantify fine-scale surface fuels and detect changes post-disturbance in northern California forests. Diss. Sonoma State University, https://scholarworks.calstate.edu/downloads/t435gm64s.

Prometheus, 1999. Management techniques for optimization of suppression and minimization of wildfires effects. System Validation. European Commission, DG XII, ENVIR & CLIMATE, Contract Number ENV4-CT98-0716. European Commission, Luxembourg.

Puletti, N., Galluzzi, M., Grotti, M., and Ferrara, C., 2021. Characterizing subcanopy structure of Mediterranean forests by terrestrial laser scanning data. *Remote Sens. Appl.: Soc. Environ.* 24, 100620, https://doi.org/10.1016/j.rsase.2021.100620.

R Core Team., 2022. R: A language and environment for statistical computing. R Foundation for Statistical Computing, Vienna, Austria, https://www.R-project.org.

Renslow, M., 2013. Manual of Airborne Topographic LiDAR. ASPRS, Bethesda, MD, USA. ISBN: 978-1570830976.

Revilla, S., Lamelas, M.T., Domingo, D., de la Riva, J., Montorio, R., Montealegre, A.L., and García-Martín, A., 2021. Assessing the potential of the DART model to discrete return LiDAR simulation – Application to fuel type mapping. *Remote Sens.* 13 (3), 1–21, https://doi.org/10.3390/rs13030342.

Ritter, T., Schwarz, M., Tockner, A., Leisch, F., and Nothdurft, A., 2017. Automatic mapping of forest stands based on three-dimensional point clouds derived from terrestrial laser-scanning. *Forests* 8 (8), 265, https://doi.org/10.3390/f8080265.

Rothermel, C., 1972. A mathematical model for predicting fire spread in wildland fuels. Research Papers, INT-115. Ogden, UT: U.S. Department of Agriculture, Intermountain Forest and Range Experiment Station, 40 p.

Roussel, J.R. and Auty, D., 2022. Airborne LiDAR data manipulation and visualization for forestry applications. R package version 4.0.1, https://cran.r-project.org/package=lidR.

Roussel, J.R., Auty, D., Coops, N.C., Tompalski, P., Goodbody, T.R.H., Sánchez-Meador, A., Bourdon, J.F., de Boissieu, F., and Achim, A., 2020. 'lidR': An R package for analysis of Airborne Laser Scanning (ALS) data. *Remote Sens. Environ.* 251, 112061, https://doi.org/j.rse.2020.112061.

Rovithakis, A., Grillakis, M.G., Seiradakis, K.D., Giannakopoulos, C., Karali, A., Field, R., Lazaridis, M., and Voulgarakis, A., 2022. Future climate change impact on wildfire danger over the Mediterranean: The case of Greece. *Environ. Res. Lett.* 17, 045022, https://doi.org/10.1088/1748-9326/ac5f94.

Rowell, E., Loudermilk, E.L., Hawley, C., Pokswinski, S., Seielstad, C., Queen, L., O'Brien, J.J., Hudak, A.T., Goodrick, S., and Hiers, J.K., 2020. Coupling terrestrial laser scanning with 3D fuel biomass sampling for advancing wildland fuels characterization. *For. Ecol. Manag.* 462, 117945, https://doi.org/10.1016/j.foreco.2020.117945.

Rowell, E. and Seielstad, C., 2012. Characterizing grass, litter, and shrub fuels in longleaf pine forest pre- and post-fire using terrestrial LiDAR. In *Proceedings of SilviLaser 2012*, SL2012-166 (19 09 2012).

Ruffault, J., Curt, T., Moron, V., Trigo, R.M., Mouillot, F., Koutsias, N., Pimont, F., Martin-StPaul, N., Barbero, R., Dupuy, J.L., Russo, A., and Belhadj-Khedher, C., 2020. Increased likelihood of heat-induced large wildfires in the Mediterranean Basin. *Sci. Rep.* 10, 13790, https://doi.org/10.1038/s41598-020-70069-z.

Solares-Canal, A., Alonso, L., Picos, J., and Armesto, J., 2023. Automatic tree detection and attribute characterization using portable terrestrial LiDAR. *Trees* 37, 963–979, https://doi.org/10.1007/s00468-023-02399-0.

Srinivasan, S., Popescu, S.C., Eriksson, M., Sheridan, R.D., and Ku, N.W., 2014. Multi-temporal terrestrial laser scanning for modeling tree biomass change. *For. Ecol. Manag.* 318, 304–317, https://doi.org/10.1016/j.foreco.2014.01.038.

Tupinambá-Simões, F., Pascual, A., Guerra-Hernández, J., Ordóñez, C., de Conto, T., and Bravo, F., 2023. Assessing the performance of a handheld laser scanning system for individual tree mapping – A Mixed forests showcase in Spain. *Remote Sens.* 15, 1169, https://doi.org/10.3390/rs15051169.

Turco, M., Llaset, M.C., von Hardenberg, J., and Provenzale, A., 2014. Climate change impacts on wildfires in a Mediterranean environment. *Clim. Change* 125, 369–380, https://doi.org/10.1007/s10584-014-1183-3.

Varela, V., Vlachogiannis, D., Sfetsos, A., Karozis, S., Politi, N., and Giroud, F., 2019. Projection of forest fire danger due to climate change in the French Mediterranean region. *Sustainability* 11 (16), 4284, https://doi.org/10.339/su11164284.

Yan, Z., Liu, R., Cheng, L., Zhou, X., Ruan, X., and Xiao, Y., 2019. A concave hull methodology for calculating the crown volume of individual trees based on vehicle-borne LiDAR data. *Remote Sens.* 11 (6), 623, https://doi.org/10.3390/rs11060623.

Yrttimaa, T., Saarinen, N., Kankare, V., Hynynen, J., Huuskonen, S., Holopainen, M., Hyyppä, J., and Vastaranta, M., 2020. Performance of terrestrial laser scanning to characterize managed Scots pine (Pinus sylvestris L.) stands is dependent on forest structural variation. *ISPRS J. Photogramm. Remote Sens.* 168, 277–287, https://doi.org/10.1016/j.isprsjprs.2020.08.017.

Zhang, W., Qi, J., Wan, P., Wang, H., Xie, D., Wang, X., and Yan, G., 2016. An easy-to-use airborne LiDAR data filtering method based on cloth simulation. *Remote Sens.* 8 (6), 501, https://doi.org/10.3390/rs8060501.

Zhao, K., Suárez, J.C., García, M., Hu, T., Wang, C., and Londo, A., 2018. Utility of multitemporal LiDAR for forest and carbon monitoring: Tree growth, biomass dynamics, and carbon flux. *Remote Sens. Environ.* 204, 883–897, https://doi.org/10.1016/j.rse.2017.09.007.

APPENDIX

Table A.1. Name, location, point cloud density, and mean georeferenced error of the forest plots in the Almudévar and Ayerbe sectors.

Sector	Plot ID	Plot center (ETRS89 – UTM zone 30N)		Points/ m^2	Mean georef. error
		X	Y		
Almudévar	al01	694602.478	4652067.838	71,594.08	0.396
	al02	694567.668	4652104.523	61,510.30	0.138
	al03	710134.071	4663293.626	55,084.31	0.109
	al04	710141.301	4663668.746	55,983.11	0.106
	al08	697328.819	4653490.123	91,474.10	0.146
	al09	697275.282	4653516.272	69,630.07	0.353
Ayerbe	ay04	686687.048	4674577.984	133,259.23	0.058
	ay06	688450.485	4674202.710	89,334.00	0.038
	ay08	686536.466	4674651.836	84,663.50	0.585
	ay12	685055.484	4672393.522	29,699.16	0.036
	ay15	688256,.466	4674080.083	80,750.19	0.090
	ay16	688792.329	4674281.699	115,322.61	0.100
	ay17	689248.872	4674261.269	131,697.66	0.155
	ay19	686878.800	4673256.392	119,540.63	0.682
	ay20	686703.732	4673179.904	84,514.25	0.472
	ay22	687240.410	4673227.350	77,658.80	0.360
	ay28	688371.236	4673218.006	82,040.58	0.213
	ay29	688737.669	4673129.789	85,566.76	0.162
	ay30	688775.135	4673342.463	78,094.99	0.134
	ay31	688609.831	4673178.137	78,879.46	0.155
	ay47	685130.090	4673135.506	31,830.43	0.205
	ay49	685076.359	4672599.030	52,189.36	0.121
	ay50	685122.505	4672511.905	24,966.82	0.136

Table A.2. Name, location, point cloud density, and mean georeferenced error of the forest plots in the Uncastillo, Villarluengo, and Zuera sectors.

Sector	Plot ID	Plot center (ETRS89 – UTM zone 30N)		Points/ m^2	Mean georef. error
		X	Y		
Uncastillo	un12	644240.822	4699753.646	46,152.96	0.133
Villarluengo	vi14	727270.389	4511291.669	49,447.92	0.078
	vi15	727036.262	4511166.454	35,912.14	0.122
	vi16	727080.861	4511157.835	47,463.93	0.086
	vi17	726201.413	4503645.777	26,659.39	0.096
	vi18	726118.381	4503470.237	42,036.27	0.090
	vi19	726672.818	4503511.043	17,187.46	0.080
	vi20	726746.027	4503541.186	18,689.68	0.076
	vi29	725332.834	4506874.651	31,546.16	0.036
	vi30	725369.219	4506806.618	43,004.04	0.082
	vi38	726062.493	4509797.786	50,681.73	0.119
	vi39	725818.588	4509536.031	36,774.11	0.069
	vi40	725846.450	4509684.009	32,018.89	0.099
	vi41	726150.472	4509715.661	68,006.40	0.071
Zuera	zu201	675701.773	4640029.063	49,040.58	0.063
	zu202	675677.700	4640049.351	85,760.62	0.071
	zu30	674321.251	4636134.801	47,760.41	0.123
	zu31	674042.822	4636569.962	77,218.45	0.268
	zu32	673137.179	4637107.172	23,244.28	0.141
	zu38	674071.540	4639208.676	21,633.29	0.064

Table A.3. Mean height error (in meters) between the three ground classification algorithms tested in the study for each plot in the Almudévar and Ayerbe sectors.

Sector	Plot ID	CSF-MCC	CSF-LasTools	MCC-LasTools
Almudévar	al01	0.01	0.06	0.07
	al02	0.02	0.02	0.04
	al03	0.02	0.02	0.04
	al04	0.04	0.05	0.09
	al08	0.01	0.02	0.03
	al09	0.00	0.03	0.02
Ayerbe	ay04	0.10	1.84	1.74
	ay06	0.01	0.16	0.17
	ay08	0.05	0.31	0.26
	ay12	0.02	0.10	0.08
	ay15	0.03	0.24	0.20
	ay16	0.10	0.55	0.45
	ay17	0.04	0.39	0.34
	ay19	0.00	0.35	0.35
	ay20	0.03	0.10	0.12
	ay22	0.06	0.28	0.22
	ay28	0.01	0.27	0.26
	ay29	0.01	0.10	0.11
	ay30	0.01	0.12	0.11
	ay31	0.01	0.12	0.13
	ay47	0.02	0.01	0.03
	ay49	0.00	0.15	0.16
	ay50	0.02	0.02	0.03

Table A.4. Mean height error (in meters) between the three ground classification algorithms tested in the study for each plot of Uncastillo, Villarluengo, and Zuera sectors.

Sector	Plot ID	CSF-MCC	CSF-LasTools	MCC-LasTools
Uncastillo	un12	0.02	0.17	0.19
Villarluengo	vi14	0.08	0.09	0.16
	vi15	0.03	0.09	0.13
	vi16	0.00	0.17	0.17
	vi17	0.05	0.10	0.15
	vi18	0.03	0.30	0.33
	vi19	0.04	0.13	0.17
	vi20	0.05	0.05	0.10
	vi29	0.07	0.09	0.16
	vi30	0.10	0.15	0.24
	vi38	0.02	0.22	0.24
	vi39	0.03	0.21	0.23
	vi40	0.08	0.12	0.20
	vi41	0.02	0.29	0.26
Zuera	zu201	0.16	0.11	0.27
	zu202	0.11	0.18	0.28
	zu30	0.04	0.06	0.10
	zu31	0.05	0.03	0.08
	zu32	0.13	0.11	0.02
	zu38	0.08	0.11	0.19

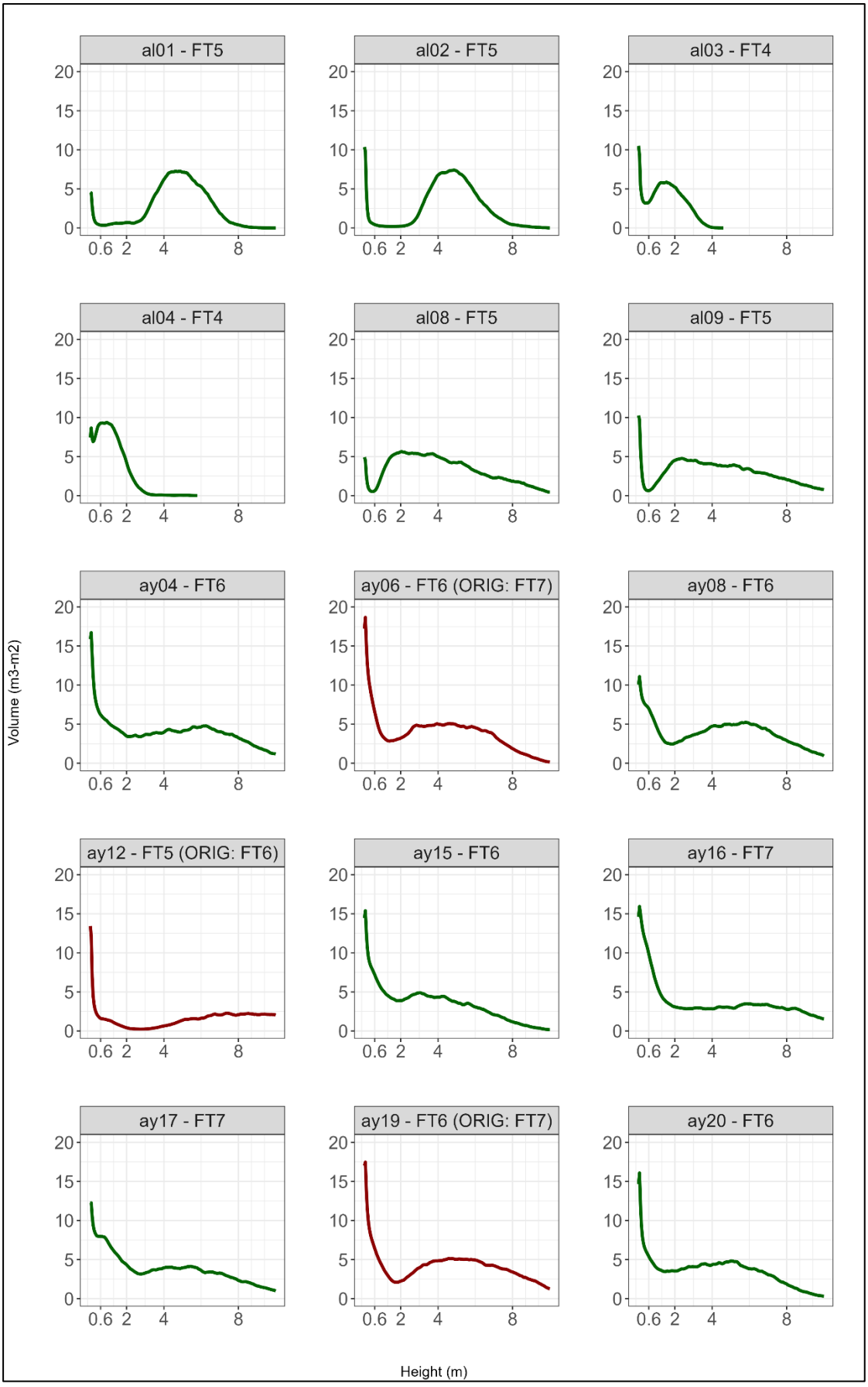

Figure A.1. Vertical distribution of the fuel volume of each forest plot every 5 cm (1/3).

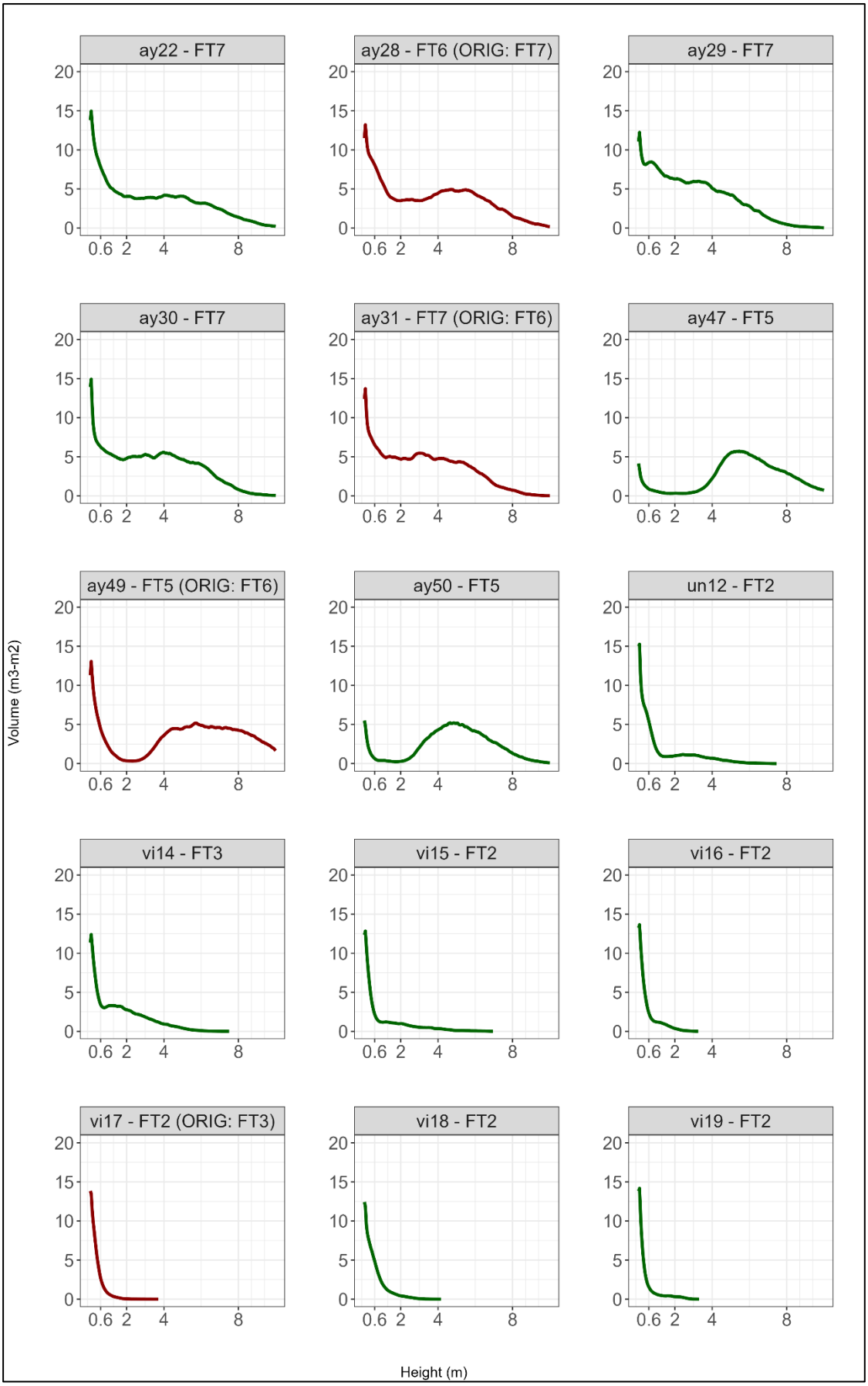

Figure A.1. Vertical distribution of the fuel volume of each forest plot every 5 cm (2/3).

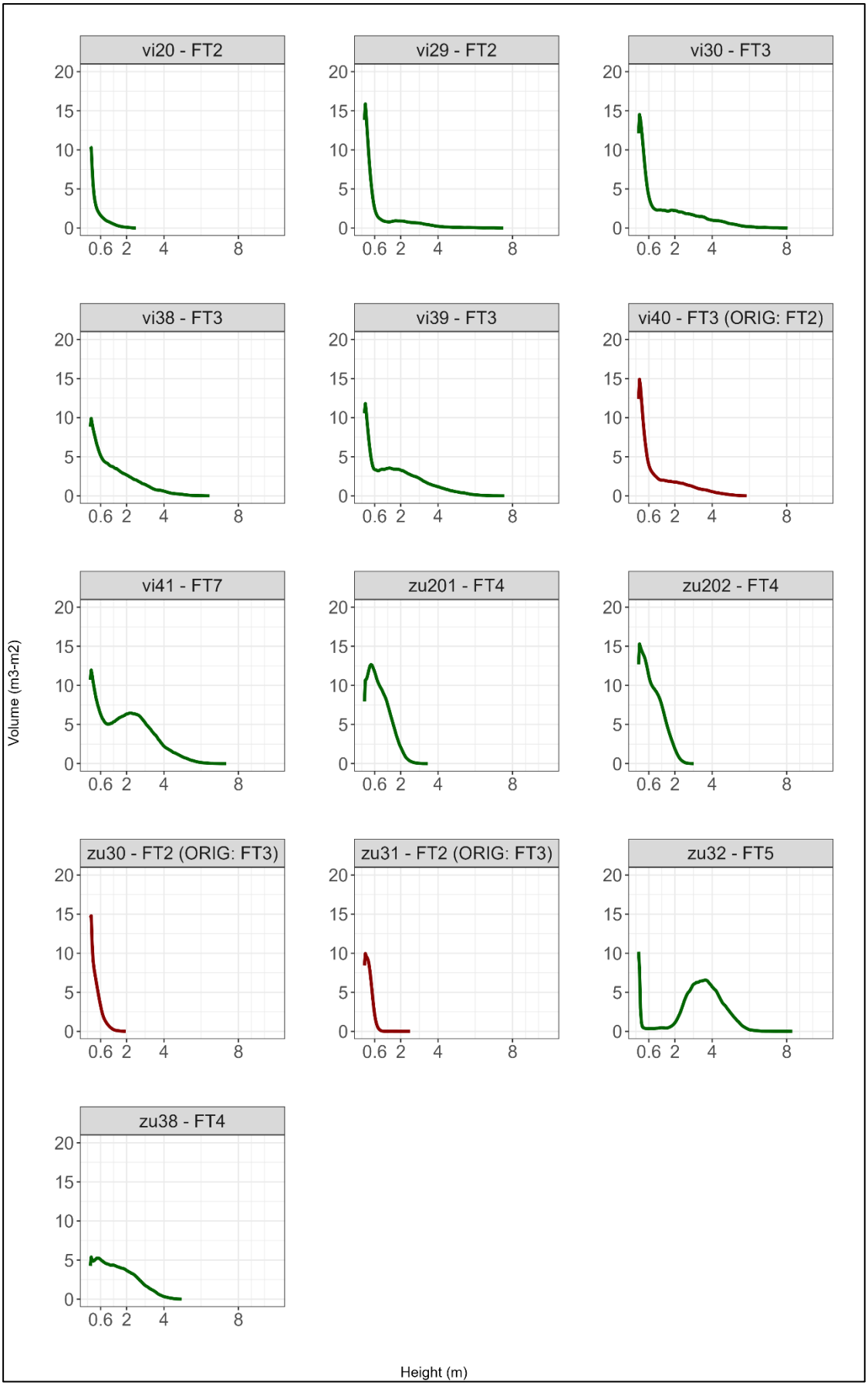

Figure A.1. Vertical distribution of the fuel volume of each forest plot every 5 cm (3/3).

The *DJI Matrice 300 RTK* UAV and the *DJI Zenmuse L1* sensor. Photograph by Raúl Hoffrén.

CHAPTER 6

UAV-LIDAR SYSTEM FOR FOREST FUEL ESTIMATION AND MAPPING, AND INTEGRATION POSSIBILITIES WITH AN HMLS SYSTEM

This chapter corresponds to:

Hoffrén, R., Lamelas, M.T., and de la Riva, J., 2024. Classification and mapping of fuels in Mediterranean forest landscapes using a UAV-LiDAR system and integration possibilities with handheld mobile laser scanner systems. *Remote Sensing* 16 (18), 3536.

https://doi.org/10.3390/rs16183536

Classification and mapping of fuels in Mediterranean forest landscapes using a UAV-LiDAR system and integration possibilities with handheld mobile laser scanner systems

Raúl Hoffrén[1,2], María Teresa Lamelas[2,3,*], Juan de la Riva[1,2].

[1] Department of Geography and Land Management, University of Zaragoza, Calle Pedro Cerbuna 12, 50009, Zaragoza, Spain.
[2] Geoforest Group, University Institute for Research in Environmental Sciences of Aragón (IUCA), University of Zaragoza, Spain.
[3] Centro Universitario de la Defensa, Academia General Militar, Ctra. Huesca s/n, 50090, Zaragoza, Spain.
[*] Corresponding author, email: tlamelas@unizar.es.

ABSTRACT

In this study, we evaluated the capability of an unmanned aerial vehicle with a LiDAR sensor (UAV-LiDAR) to classify and map fuel types based on the Prometheus classification in Mediterranean environments. UAV data were collected across 73 forest plots located in NE of Spain. Furthermore, data collected from a handheld mobile laser scanner system (HMLS) in 43 out of the 73 plots were used to assess the extent of improvement in fuel identification resulting from the fusion of UAV and HMLS data. UAV three-dimensional point clouds (average density: 452 points/m^2) allowed the generation of LiDAR metrics and indices related to vegetation structure. Additionally, voxels of 5 cm^3 derived from HMLS three-dimensional point clouds (average density: 63,148 points/m^2) facilitated the calculation of fuel volume at each Prometheus fuel type height stratum (0.60, 2, and 4 m). Two different models based on three machine learning techniques (Random Forest, Linear Support Vector Machine, and Radial Support Vector Machine) were employed to classify the fuel types: one including only UAV variables and the other incorporating HMLS volume data. The most relevant UAV variables introduced into the classification models, according to Dunn's test, were the 99th and 10th percentile of the vegetation heights, the standard deviation of the heights, the total returns above 4 m, and the LiDAR Height Diversity Index (LHDI). The best classification using only UAV data was achieved with Random Forest (overall accuracy = 81.28%), with confusion mainly found between similar shrub and tree fuel types. The integration of fuel volume from HMLS data yielded a substantial improvement, especially in Random Forest (overall accuracy = 95.05%). The mapping of the UAV model correctly estimated the fuel types in the total area of 55 plots and at least part of the area of 59 plots. These results confirm that UAV-LiDAR systems are valid and operational tools for forest fuel classification and mapping and show how fusion with HMLS data refines the identification of fuel types, contributing to more effective management of forest ecosystems.

1. INTRODUCTION

Wildfires are an inherent disturbance of forest ecosystems, yet various factors are contributing to an increase in their frequency and intensity (Pausas and Keeley, 2021; Jones *et al*., 2022; Cunningham *et al*., 2024). Some causes of this alteration are attributed to climate change (Abatzoglou *et al*., 2019; Abram *et al*., 2021), land use changes (Ascoli *et al*., 2021), reforestation policies (White and Long, 2019; Papatheodorou *et al*., 2023), and urban growth in the wildland–urban interface (Kramer *et al*., 2019). As a consequence, forests are more exposed to the negative processes of recurrent and extreme wildfires, beyond the deterioration or loss of vegetation cover by fire, such as soil degradation (Hohner *et al*., 2019) and biodiversity loss (Díaz-Delgado *et al*., 2002; Kelly *et al*., 2020; Legge *et al*., 2022), also leading to an increase in carbon emissions into the atmosphere (Ponomarev *et al*., 2021; Philips *et al*., 2022).

Mediterranean environments are particularly prone to wildfires due to the characteristics of climate and vegetation (Pausas *et al*., 2008). Moreover, the exposure of these regions to extreme wildfires is projected to increase in the future (Dupuy *et al*., 2020; Ruffault *et al*., 2020; Richards *et al*., 2023), heightening the vulnerability of these valuable ecosystems. A key mechanism for preventing and mitigating wildfires is understanding the spatial distribution of forest fuels, which constitute all living or dead matter available in forest landscapes for combustion. The characterization of fuels helps to predict fire rate of spread, fireline intensity, and propagation axes across heterogeneous forest landscapes during hypothetical fire scenarios, enabling fuel mapping across large areas (Lasaponara and Lanorte, 2006; Novo *et al*., 2020; Aragoneses and Chuvieco, 2021). Given that the structural complexity of forest fuels often makes their identification a complex task (Abdollahi and Yebra, 2023), several fuel classifications have been developed in the last decades. For Mediterranean environments, the Prometheus fuel classification (Prometheus, 1999) uses indicators/thresholds of vegetation height and percentage cover of shrubs and trees to classify fuels according to the type, height, and density of the main element of propagation (grass, shrub, or leaf litter). It comprises seven fuel types (FTs): FT1 for grass fuels; FT2, FT3, and FT4 for shrub fuels (low, medium, and high, respectively); and FT5, FT6, and FT7 for tree fuels (without understory, with non-continuous understory to canopy, and with continuous understory to canopy, respectively). Remote sensing has been extensively employed for the identification of forest fuels and, specifically, LiDAR (Light Detection and Ranging) systems, thanks to the ability of laser pulses to work their way through

the canopy and interact at different heights with the vegetation cover, enabling the representation of forests' three-dimensional structure. LiDAR sensors can be mounted on different platforms. For instance, NASA's Global Ecosystem Dynamics Investigation system onboard the International Space Station allows for characterizing fuels across vast areas (Ashworth *et al*., 2010; Leite *et al*., 2022) and can be coupled with multispectral imagery to enhance fuel classification (Hoffrén *et al*., 2023a). On the other hand, Airborne Laser Scanner (ALS) systems facilitate the identification of fuels at regional scales with high spatial resolution, integrating multispectral indices (Chirici *et al*., 2013; Domingo *et al*., 2020) and hyperspectral images (Romero-Ramírez *et al*., 2018).

In recent years, proximal remote sensing platforms, such as Unmanned Aerial Vehicles (UAVs) and ground-based laser scanner systems, have become highly promising technologies for fuel identification and classification in heterogeneous environments. One of the primary advantages of the joint use of UAVs and ground-based systems is the ability of the latter to collect data without the constraints of drone flights, as long as there is real accessibility to the forest stand and with very high spatial resolutions (Abdollahi and Yebra, 2023). UAVs have demonstrated their effectiveness even when equipped with photogrammetric sensors, such as visible or multispectral cameras, instead of LiDAR. In this respect, Shin *et al*. (2018) found that photogrammetric UAVs can efficiently estimate canopy cover and canopy height in conifer forest stands. Hoffrén *et al*. (2023b) successfully classified the Prometheus fuel types in almost the same study area as in this study by combining very high-density three-dimensional point clouds with multispectral images and textural data from a photogrammetric UAV. However, in this study, the authors noticed very discrete classification rates when classifying the Prometheus fuel types FT3 and FT6. This limitation could be attributed to the inability of photogrammetric UAVs to capture data below the upper canopy. In this regard, Hillman *et al*. (2021) demonstrated that UAVs with LiDAR sensors are better able to describe the entire vertical structure of vegetation below canopies than photogrammetric UAVs in a dry sclerophyll forest in Australia. Additionally, they noted very similar estimates of canopy and sub-canopy cover in both UAV-LiDAR and ground-based systems. Conversely, findings from Hyyppä *et al*. (2020a) suggest that ground-based systems provide better results for collecting tree-level structural data than above-canopy UAV-LiDAR systems. Consequently, the capacity of UAV-LiDAR systems to characterize fuels below canopies may be compromised by the penetration capabilities of the laser pulses into the canopy and the maximum number of returns that the sensor is able to record in a single pulse. Identifying the shrubland is very important since it is usually the place through which fires are

mainly spread. Ground-based systems can address this challenge since they operate at ground level with an extremely high-density scanning rate, enabling a more precise characterization of understory fuels. Indeed, these systems have been successfully utilized by Chen *et al*. (2016) to identify all vertical fuel layers in a forest stand and by Wilson *et al*. (2022) to evaluate the impact of fuel structure on wildfire severity. However, despite these favorable findings, data collection with ground-based systems may pose operational challenges in terms of time and cost (Hyyppä *et al*., 2020b), particularly when compared to the relatively shorter time periods required for data collection with UAVs.

In this context, considering the demonstrated efficacy of UAVs and LiDAR remote sensing in identifying forest fuels, both individually and in combination, in this study, we aim to assess the capability of a UAV-LiDAR system for the identification of the Prometheus fuel types in Mediterranean forest stands and their classification using modeling techniques based on machine learning for the subsequent fuel mapping across larger areas. In this study, we focus primarily on shrub and tree understory fuels. The initial hypothesis is that the capacity of UAV-LiDAR systems to characterize vegetation and fuel structure enables the classification of the Prometheus fuel types with high levels of accuracy. Furthermore, recognizing the uncertainty surrounding UAV-LiDAR systems' ability to identify fuels below canopies, in this study, we also utilize data collected in a previous work (Hoffrén *et al*., 2024) employing a ground-based handheld mobile laser scanning (HMLS) system. In this context, the secondary objective is to assess the extent of improvement in fuel identification resulting from the integration of UAV-collected data with HMLS data, especially shrub fuels, to better differentiate between shrub and tree understory fuel types. The hypothesis is that HMLS systems have the potential to mitigate classification errors that occur between fuel types with high structural heterogeneity, particularly in the middle and lower strata. Ultimately, in this work, we aim to underscore the utility of UAV-LiDAR systems and their potential synergy with ground-based laser scanner systems to improve forest management practices related to forest fuels and, thus, mitigate the negative impacts of wildfires on the ecosystem.

2. MATERIALS AND METHODS

2.1. Study area

The study area was located in five sectors within the Autonomous Community of Aragón (NE of Spain): Almudévar, Ayerbe, Uncastillo, Villarluengo, and

Zuera. UAV data were collected across 73 forest plots of 15 m circular radius, except for one plot of 10 m radius due to terrain constraints (a comprehensive description of the forest plots is available in Table A.1 of the Appendix). HMLS data were obtained in 43 out of the 73 forest plots in the context of a previous work (for further details, see Hoffrén *et al*., 2024). The center of each plot was determined using a Leica Viva® GS15 CS10 GNSS Real-Time Kinematic (RTK) Global Positioning System with sub-meter accuracy. To form the ground-truth for the classification models, the fuel type of each plot was estimated by visual analyses in the field and validated with the processed HMLS point cloud in the plots where HMLS data were collected (Hoffrén *et al*., 2024). The number of plots for each fuel type is shown in Table 1. Note that, in this work, FT1 (grass fuel) was not considered as the study focuses on shrubs and tree understory fuel types. Figure 1 shows six study plots in frontal view using the UAV's colored point cloud, each with a different fuel type.

Table 1. The Prometheus fuel types: general characteristics and number of forest plots for each fuel type and platform considered in this study. The difference between FT6 and FT7 is the vertical dif- ference between shrubs and trees, which is >0.5 m in FT6 and <0.5 m in FT7.

Fuel type	Cover	Shrub mean height	UAV plots	UAV and HMLS plots
FT2	> 60% grass and < 50% trees (> 4 m)	0.30 – 0.60 m	11	10
FT3		0.60 – 2.00 m	7	5
FT4		2.00 – 4.00 m	5	5
FT5	< 30% shrub and > 50% trees (4 m)		14	9
FT6	> 30% shrub and > 50% trees (> 4 m)		12	7
FT7			24	7

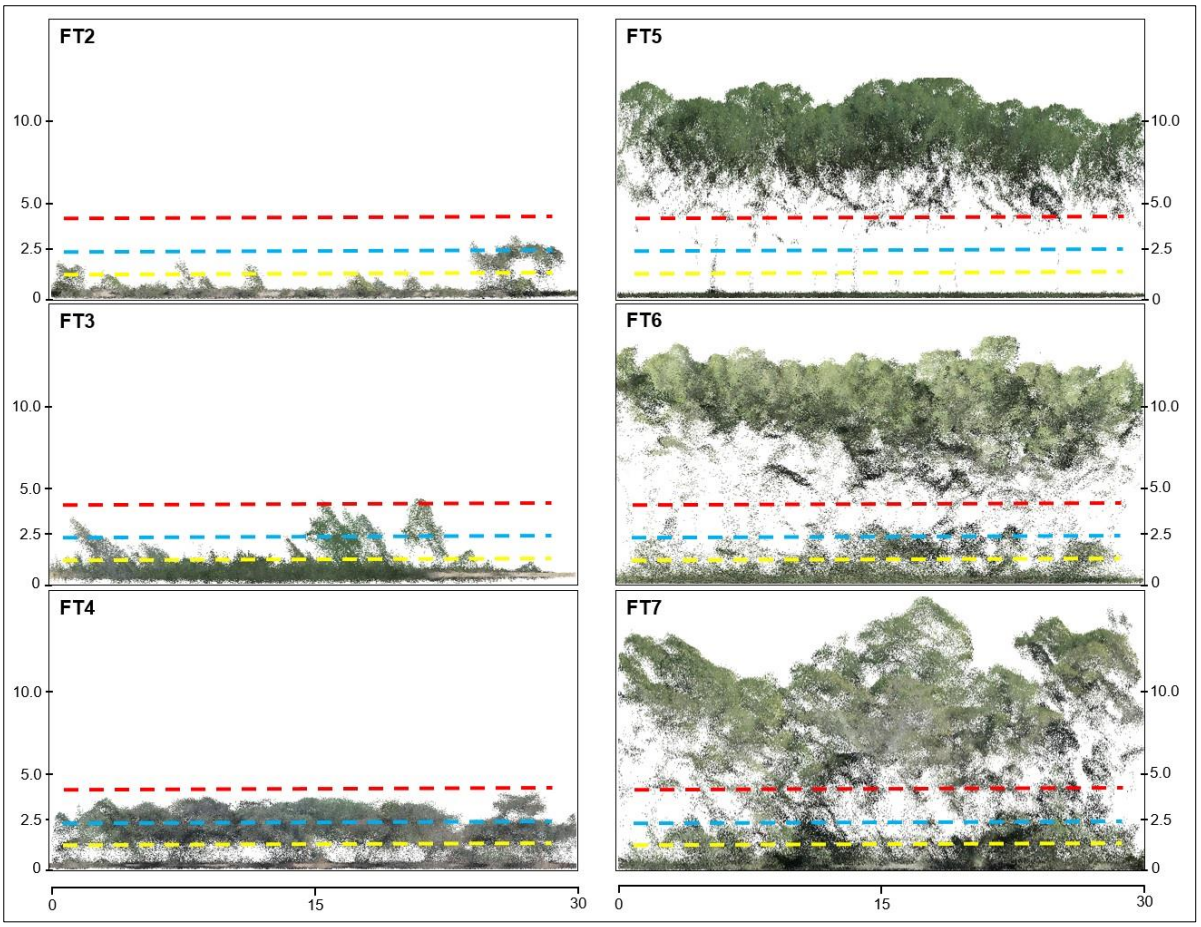

Figure 1. Graphical representation from the UAV's colored point cloud of the structural differences of the Prometheus fuel types considered in this study. Units are in meters. The yellow, blue, and red dotted lines correspond to the height thresholds of the Prometheus classification (0.60, 2, and 4 m, respectively).

All sectors experience a predominant Mediterranean climate with continental influ- ence (Figure 2). The sectors of Almudévar, Ayerbe, and Zuera are situated in the Central Ebro Valley, characterized by substantial daily and annual temperature fluctuations, featuring hot summers, cold winters, and scarce rainfall throughout the year (less than 500 mm/year). The sector of Uncastillo, located to the north of the Central Ebro Valley in the foothills of the Pre-Pyrenees, experiences less pronounced temperature variations compared to the aforementioned sectors, although they are still high, and average annual rainfall is somewhat higher (~700 mm/year). The sector of Villarluengo, placed in the southernmost part of Aragón within the Iberian mountain range, also experiences pronounced daily and annual temperature fluctuations. However, its highest mean altitude results in cooler summers than those observed in the Central Ebro Valley, albeit winters are colder. The average annual precipitation is somewhat higher (~800 mm/year), with a high possibility of winter snowfall. Convective storms are frequent in this sector, often accompanied by lighting due to its proximity to the Mediterranean Sea and the convergence of prevailing winds

(Amatulli *et al*., 2007). All forest plots are predominantly characterized by Mediterranean-type vegetation, well adapted to the climatic conditions. The most representative forest types within the plots include Aleppo pine (*Pinus halepensis* Mill.) and bog pine (*Pinus nigra* Mill.) forests, mixed with understory vegetation dominated by boxwood (*Buxus sempervirens*), junipers (*Juniperus oxycedrus*), oaks (*Quercus coccifera*, *Quercus faginea*, and *Quercus ilex* subsp. *rotundifolia*), rosemary (*Rosmarinus officinalis*), and thyme (*Thymus vulgaris*) (Loidi, 2017).

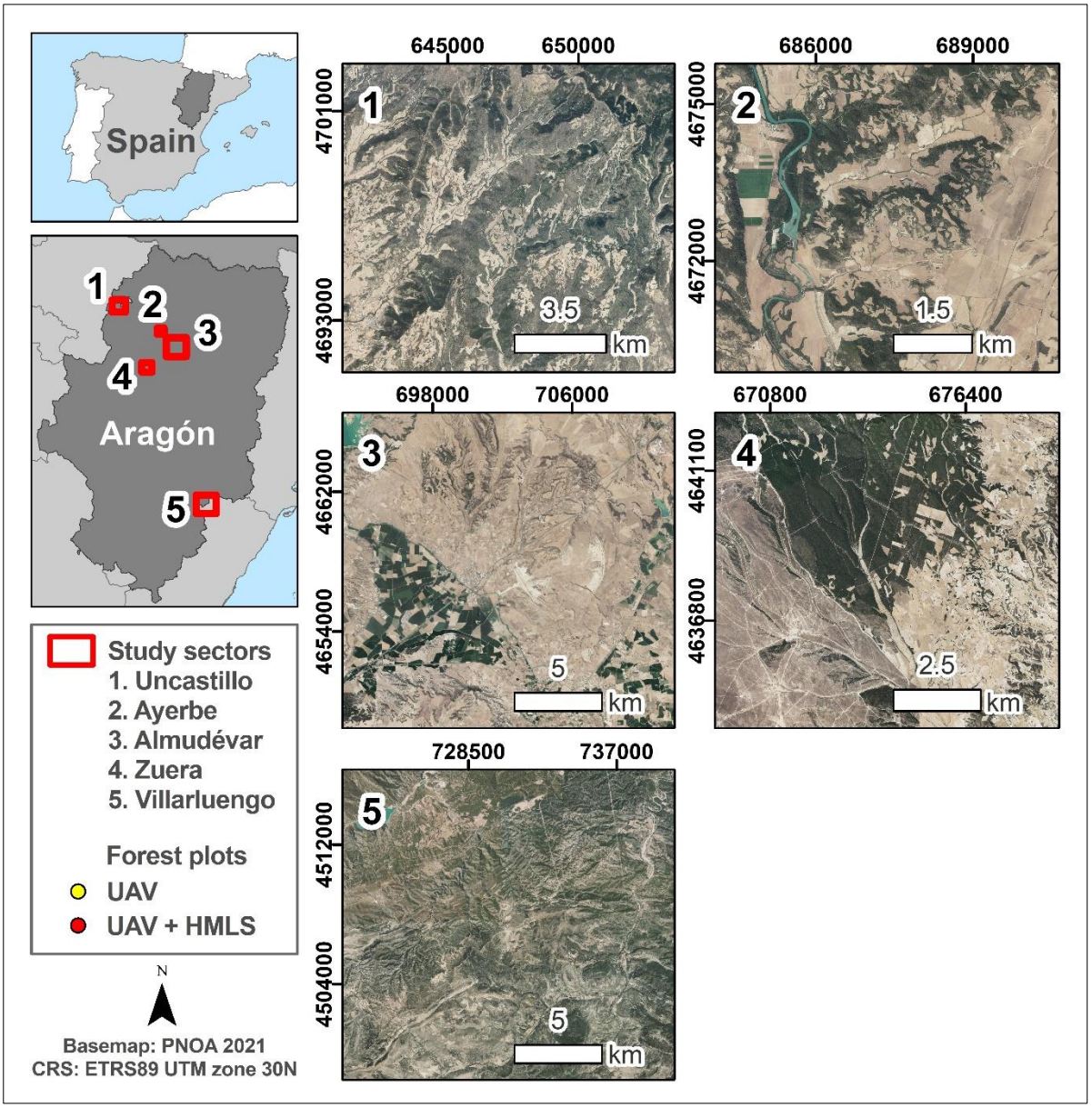

Figure 2. Spatial distribution of study sectors and forest plots where UAV and HMLS data were collected in the Autonomous Community of Aragón (NE Spain).

2.2. LiDAR data collection and processing

The primary instrument utilized to collect data in the 73 plots was a quadcopter *DJI Matrice 300 RTK* UAV unit (DJI, Shenzhen, China) equipped with a *DJI Zenmuse L1* LiDAR sensor (Figure 3a). Additionally, data were collected in 43 out of the 73 plots with a *GeoSLAM ZEB-Horizon* HMLS system (GeoSLAM, Ruddington, UK) at the end of May 2023 as part of the study developed by Hoffrén *et al*. (2024). A comprehensive description of HMLS data acquisition and processing methods can be found in Hoffrén *et al*. (2024).

UAV data were acquired in several field campaigns performed between March and May 2023. The UAV flights over the plots were automated using the *DJI Pilot 2* application. A flight altitude of 100 m above ground level was established based on 1 m resolution Digital Elevation Models (DEMs) derived from ALS-LiDAR data from the 2nd coverage of the Spanish National Orthophotography Project (PNOA, 2024: https://pnoa.ign.es/web/portal/pnoa-lidar/, accessed on 13 June 2024). A serpentine mapping pattern was utilized with an 80% overlap between scans in both cross-track and along-track directions, along with a zenith angle of incidence and a flight speed of 7 m/s. An illustrative example of the UAV flight scheme over the plots is presented in Figure 3b. The LiDAR sensor on the UAV operated at a scanning rate of 240,000 points per second, allowing for up to 3 returns in a single laser pulse. These scans facilitated the generation of very high-density three-dimensional point clouds, with an average density of 452 points/m^2 (further details are available in Table A.1 of the Appendix). The UAV was equipped with an RTK system, enabling the georeferencing of data in real-time without the necessity for ground control points in the field. The RTK system allows the UAV's global navigation system to connect via the Internet to the Geodetic Reference Stations of the Spanish National Geographic Institute and, in cases where coverage was deficient, to the UAV's RTK total station, providing differential corrections for the average positioning error of GNSS satellites and thus ensuring sub-meter accuracies.

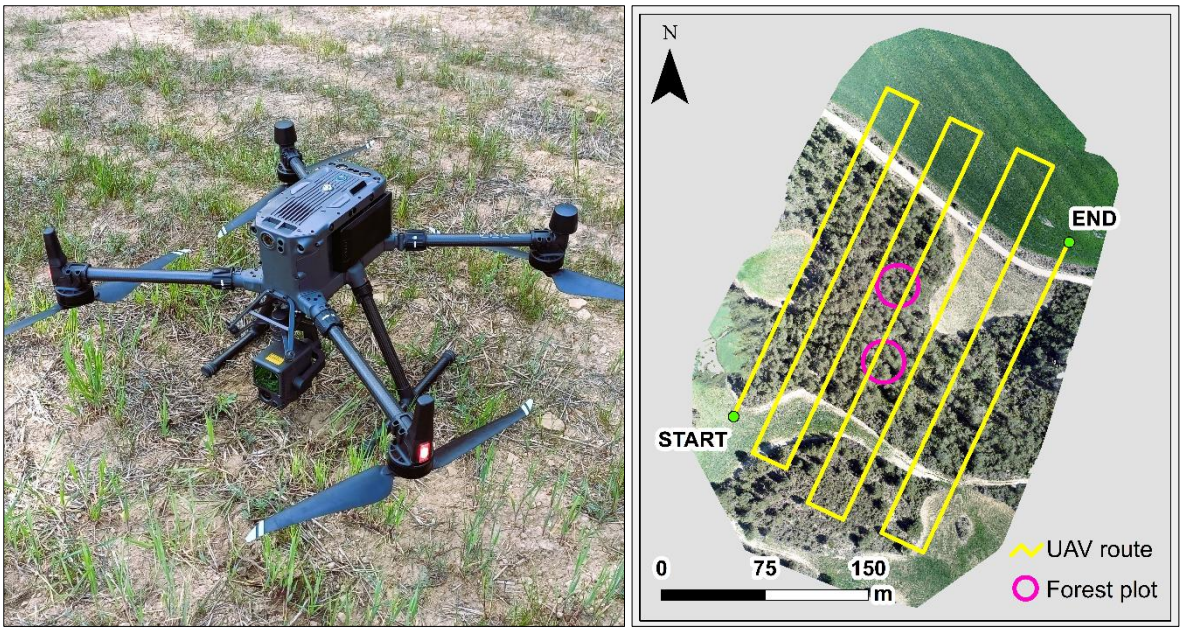

(a) (b)

Figure 3. (**a**) *DJI Matrice 300 RTK* UAV unit with *DJI Zenmuse L1* LiDAR sensor; (**b**) General flight scheme for UAV data collection on two forest plots.

The UAV scans underwent initial preprocessing using *DJI Terra* v.3.6.7 proprietary software. The data were converted into LAS files and georeferenced to the local reference system (EPSG: 25830–ETRS89/UTM zone 30N) for XY coordinates and to the EGM-96 geoidal model for Z coordinates. Subsequently, point clouds from the LAS files were categorized into ground and non-ground points. To achieve this, the Multiscale Curvature Classification algorithm was employed utilizing the *MCC-LiDAR* v.2.1 command line tool (Evans and Hudak, 2007), following the parameters established by Montealegre *et al*. (2015). Points classified as ground were utilized to create DEMs with a 0.20 m spatial resolution using the TIN-to-raster interpolation method (Renslow, 2013). To accomplish this, the *rasterize terrain* function from the "lidR" package (Roussel *et al*., 2020; Roussel and Auty, 2022) for R environment (R Core Team, 2020) was employed. The heights of the point clouds were normalized with respect to ground level using the previously created DEMs through the *normalize heights* function from the "lidR" package. Lastly, metrics related to fuel structure and diversity indices were extracted at the plot scale. To mitigate uncertainty in Z coordinates, points below 5 cm in height were excluded from subsequent analyses to prevent the inclusion of data potentially associated with the ground rather than vegetation, as a vertical accuracy of 1.5 cm + 1 ppm is reported by the UAV manufacturer (https://enterprise.dji.com/es/matrice-300/specs, last accessed on 13 June 2024). Three types of structural metrics were generated utilizing the *Cloudmetrics* function from FUSION/LDV v.4.21 software

(McGaughey, 2021): heights distribution (e.g., minimum, mean, and maximum elevation, and elevation at different height percentiles), heights variability (e.g., standard deviation, variance, skewness, kurtosis, and L-moments of heights), and canopy cover density (e.g., percentage of cover within specific height intervals of the Prometheus fuel classification: below 0.60 m, 0.60–2 m, 2–4 m, and above 4 m). In addition to structural metrics, three forest diversity indices were computed: the LiDAR Height Diversity Index (LHDI) (Equation 1), which is a modified version of the Shannon–Wiener diversity index (H'); the LiDAR Evenness Diversity Index (LHEI) (Equation 2), which adapts the Pielou's evenness index; and the rumple index, defined as the ratio between the Canopy Surface Model (CSM) and ground area (Equation 3). Both LHDI and LHEI were initially introduced by Listopad *et al.* (2015) and, for their computation, the proportion of returns within each height interval of the Prometheus fuel classification was estimated according to Domingo *et al.* (2020) using the *Cloudmetrics* function from FUSION/LDV software. For the rumple index, CSMs and ground area were calculated using the *Canopymodel* and *Surfacestats* functions from FUSION/LDV software, with a pixel resolution of 0.50 m and a 3 × 3 smoothing algorithm, accounting for the density of the UAV point cloud. Rumple index was also calculated for each height interval of the Prometheus fuel classification and additionally for the entire forest canopy structure within each plot.

$$LHDI = -\sum[(P_h) \times \ln(P_h)] \quad (1)$$

$$LHEI = \frac{LHDI}{\ln(P_h)} \quad (2)$$

$$Rumple\ index = \frac{3D\ canopy\ surface\ area}{ground\ area} \quad (3)$$

where P is the proportion of returns at the defined Prometheus classification intervals (h).

2.3. Variables selection and classification of Prometheus fuel types

The Prometheus fuel types were classified using machine learning classification algorithms. Specifically, three non-parametric classification models were evaluated: Random Forest (RF), Linear Support Vector Machine (SVM-L), and Radial Support Vector Machine (SVM-R). This will provide insight into the most suitable classification technique for the classification of the Prometheus fuel types using UAV-LiDAR in combination with HMLS systems, as to date, there is no evidence of a preponderant technique (García *et al.*, 2011; Domingo *et al.*, 2020; García-Cimarras *et al.*, 2021; Hoffrén *et al.*, 2023b).

A preliminary selection of variables was conducted to identify the most relevant ones for inclusion in the classification models. This selection process utilized the post hoc non-parametric Dunn's test for multiple comparisons (Dunn, 1964), which is similar to the Kruskal–Wallis test but provides the ability to pinpoint precisely which groups (i.e., pairs of fuel types: FT2–FT3, FT2–FT4, etc.) differ from each other (Dunn's test, $p \leq 0.05$). The principle of parsimony was also followed in the final selection of variables so that the most relevant of the four types of metrics and variables generated (i.e., height distribution, height variability, canopy cover density, and diversity indices) were included. Subsequently, the classification models were performed using the "caret" package (Kuhn, 2008) for R. Two different types of models were evaluated: a model incorporating relevant variables derived from the data collected with the UAV in the 73 forest plots and a model that encompasses the relevant UAV variables along with vegetation volume at specific height intervals of the Prometheus classification, extracted from the HMLS-derived voxels in the 43 forest plots (Hoffrén *et al*., 2024). RF models were parametrized by employing between 2 and 10 decision trees at each node. SVM-L and SVM-R models were fitted by adjusting a cost parameter within the range of 1–1000. Following the recommendation by Andersen *et al*. (2005) for small datasets, model validation was conducted using the *k-fold* cross-validation method with groups of 10 observations and 10 repeats in each instance. The overall performance of each model was evaluated using the overall accuracy (OA) coefficient. The classification accuracy of each fuel type was estimated using confusion matrices, the Producer's and User's accuracy metrics (also known as the "recall" and the "precision", respectively (Nicolau *et al*., 2023)), and the F-score (F), which combines the Producer's and User's accuracy into a single metric to assess the overall performance of the classification for each fuel type.

2.4. Spatialization mapping of the Prometheus fuel types model

The mapping of the Prometheus fuel types was performed using the most accurate model, exclusively considering the UAV data. This decision was made because UAV data were captured over larger areas both within and outside the forest plots. In contrast, HMLS data were solely recorded within the plots. Fuel mapping was carried out at a spatial resolution of 20 m, deemed suitable due to its similarity to the diameter of the forest plots under study. Furthermore, the spatialization of fuels at higher resolutions may prove impractical for the effective management of forest fuels, which require lower resolution for large-scale mapping (Abdollahi and Yebra, 2023). Similarly, fuels tend to be distributed at the scale of forest stands in their fire behavior. The mapped areas corresponded

to the designated UAV flight zones, encompassing the locations of the forest plots. To achieve this, the variables introduced into the classification models were generated at a pixel scale of 20 m resolution using the *Gridmetrics* function from FUSION/LDV software and subsequently mapped using the *CSV2Grid* function from FUSION/LDV software. Finally, the spatial model was performed using the "predict" function of the terra package (Hijmans, 2022) for R. Afterwards, for each forest plot, a comparison was made between the observed fuel type (i.e., the ground-truth) and those estimated by the model in the mappings. To accomplish this, the spatialized pixels within each plot were extracted and checked to see if the majority of those that were mapped aligned with the observed fuel type.

3. RESULTS

3.1. Classification of Prometheus fuel types using UAV data

The most relevant variables according to Dunn's test ($p \leq 0.05$) and, consequently, included in the models were the 99th ("Elev. P99") and 10th ("Elev. P10") percentile of the point cloud height distribution, the standard deviation of the heights ("Elev. stdev."), the total returns above 4 m ("All returns > 4 m"), and the LiDAR Height Diversity Index ("LHDI"). The complete results of Dunn's test are detailed in Table A.2 of the Appendix. The variable "Elev. P99" was among the group of height distribution metrics that distinguished the highest number of pairs of fuel types (up to eight), whereas the variable "Elev. P10" managed to differentiate seven pairs. The variable "Elev. stdev." was part of the second group of metrics related to height variability that distinguished the most pairs (up to seven), but it was selected due to the improvement its inclusion in the model implied. The variable "All returns > 4 m", related to the canopy cover density, also distinguished up to seven pairs of Prometheus fuel types, the maximum within this group of metrics. Fewer pairs were differentiated by the vegetation indices, with the "rumple index" distinguishing the most fuel types. However, significant collinearity was found between this variable and "Elev. stdev.", leading to the selection of the next relevant index, "LHDI".

Table 2 shows the best performance of the three classification models using the UAV data. The best classification model was RF, reaching an OA of 81.28%. SVM-L and SVM- R achieved OAs of 75.10% and 78.32%, respectively. Table 3 shows the confusion matrix of the best classification model (RF). Confusion matrices of the SVM-L and SVM-R can be found in Tables A.3 and A.5 of the Appendix, respectively. In general terms, confusions were observed to primarily

occur among similar fuel types, with minimal confusion between types of different dominant strata, i.e., between shrubs (FT2 to FT4) and trees (FT5 to FT7). The lowest hit rates were observed for FT3, which was primarily confused with FT2 and occasionally misclassified as FT5 (resulting in omission errors) and FT7 (both commission and omission errors). Additionally, there was confusion between FT6 and FT7, although hit rates for both types exceeded 70%. FT5 exhibited minor confusion with FT3 and FT7, yet its hit rates surpassed 85%. FT2 and FT4 emerged as the most accurately classified fuel types, boasting hit rates exceeding 90% and no commission errors noted for FT4. Regarding the F-score (Table 4), the highest coefficients were observed in FT4, followed by FT5, while the lowest coefficients were associated with the intermediate shrub (FT3) and tree (FT6) fuel types. Results of the F-score for SVM-L and SVM-R can be found in Tables A.4 and A.6 of the Appendix, respectively.

Table 2. Performances of the three classification models using the overall accuracy (OA) coefficient for the five selected variables of the UAV data.

Variables	Model	OA
Elev. P99, Elev. P10, Elev. stdev., All returns > 4 m, LHDI	RF	81.28%
	SVM-L	75.10%
	SVM-R	78.32%

Table 3. Confusion matrix of the best UAV classification model (RF).

Fuel types		Predicted						Prod.'s accuracy
		FT2	FT3	FT4	FT5	FT6	FT7	
Actual	FT2	**99**	20	0	0	0	0	83.19%
	FT3	10	**42**	0	10	0	8	60.00%
	FT4	1	0	**50**	0	0	0	98.04%
	FT5	0	0	0	**120**	0	10	92.31%
	FT6	0	0	0	0	**91**	31	74.59%
	FT7	0	8	0	10	29	**191**	80.25%
User's accuracy		90.00%	60.00%	100%	85.71%	75.83%	79.58%	

Table 4. F-score (F) coefficient for each fuel type of the best UAV classification model (RF).

	FT2	FT3	FT4	FT5	FT6	FT7
F	0.87	0.57	1.00	0.89	0.69	0.74

3.2. Classification of Prometheus fuel types combining UAV and HMLS data

The inclusion of the volume of vegetation from the HMLS voxelized dataset resulted in a substantial enhancement of accuracy across all three classification models (Table 5) and minimized confusion between fuel types (Table 6). Notably, the Prometheus height interval that demonstrated the most significant improvement was the volume between 0.60 and 2 m in height. Integration of this variable boosted the RF model to achieve an OA of 95.05%. Furthermore, there was a notable enhancement of the SVM-R model, achieving an OA of 86.17% and, to a lesser extent, in the SVM-L model, attaining an OA of 81.73%. While the volume at other Prometheus height intervals also contributed to model improvement, its impact was comparatively smaller (Table 5). Confusions between fuel types in the best-performing classification model (RF) were limited to FT2 and FT3 (Table 6). Similarly, the F-score was maximum in all fuel types except for FT2 and FT3 (Table 7), where confounding occurred. However, both types exhibited high performances. In the case of SVM-L and SVM-R models, confusions were observed among other fuel types, yet hit rates and the F-score remained consistently high across all types (Tables A.7 to A.10 of the Appendix, respectively).

Table 5. Performances of the three classification models for UAV data incorporating the four HMLS variables using the overall accuracy (OA) coefficient.

Variables		**RF**	**SVM-L**	**SVM-R**
UAV	**HMLS**	**OA**	**OA**	**OA**
Elev. P99, Elev. P10, Elev. stdev. All returns > 4 m, LHDI	Volume < 0.60 m	83.83%	80.65%	81.00%
	Volume 0.60 – 2 m	95.05%	81.73%	86.17%
	Volume 2 – 4 m	83.76%	79.90%	85.85%
	Volume > 4 m	82.50%	81.27%	82.15%

Table 6. Confusion matrix of the best classification model (RF) integrating UAV and HMLS data.

Fuel types		Predicted						Prod.'s accuracy
		FT2	FT3	FT4	FT5	FT6	FT7	
Actual	FT2	**90**	10	0	0	0	0	90.00%
	FT3	10	**40**	0	0	0	0	80.00%
	FT4	0	0	**50**	0	0	0	100%
	FT5	0	0	0	**90**	0	0	100%
	FT6	0	0	0	0	**70**	0	100%
	FT7	0	0	0	0	0	**70**	100%
User's accuracy		90.00%	80.00%	100%	100%	100%	100%	

Table 7. F-score (F) coefficient for each fuel type of the best classification model (RF) integrating UAV and HMLS data.

	FT2	FT3	FT4	FT5	FT6	FT7
F	0.90	0.80	1.00	1.00	1.00	1.00

3.3. Mapping of Prometheus fuel types

Figures 4 and 5 illustrate the mapping of Prometheus fuel types according to the spatialization of the best classification model of the UAV data (RF). It is important to note that, by disregarding the FT1 fuel type in this study, it is assumed that some pixels classified as FT2 may actually correspond to FT1, as well as roads or bare soil. However, for crop areas, a mask has been applied to exclude the spatialized pixels, as these areas have not been modeled. Each figure presents three different areas, each containing two plots representing the different Prometheus fuel types considered in this study. Additional mapping can be found in Figures A.1 to A.13 of the Appendix. Fuel types were accurately determined across the entire area of 55 plots (75.34% of the total plots) and in at least part of the area of 59 plots (80.82% of the total plots). Among shrub fuel type plots, FT2 was correctly classified in 8 out of 11 plots (88.89%), with 2 plots classified as FT3 and 1 as FT4. In FT3 plots, the correct fuel type was mapped in 6 out of 7 plots (85.71%), with only 1 plot misclassified as FT4. Additionally, FT4 was accurately mapped in 100% of the plots with this observed type. Regarding tree

fuel type plots, 11 out of 14 plots identified as FT5 (78.57%) were spatialized with their correct fuel type, while 3 plots were incorrectly classified as FT7. The highest error rate was observed in FT6 plots, with only 3 out of 12 plots (25%) being accurately spatialized. Furthermore, two additional plots contained some FT6 pixels, albeit not in the majority, resulting in only five plots of this type (41.67%) containing all or part of the pixels with their correct type. Misclassified FT6 plots were consistently categorized as FT7. Finally, 22 out of 24 observed FT7 plots (91.67%) were classified with their correct fuel type, with 100% of these plots containing some FT7 pixels.

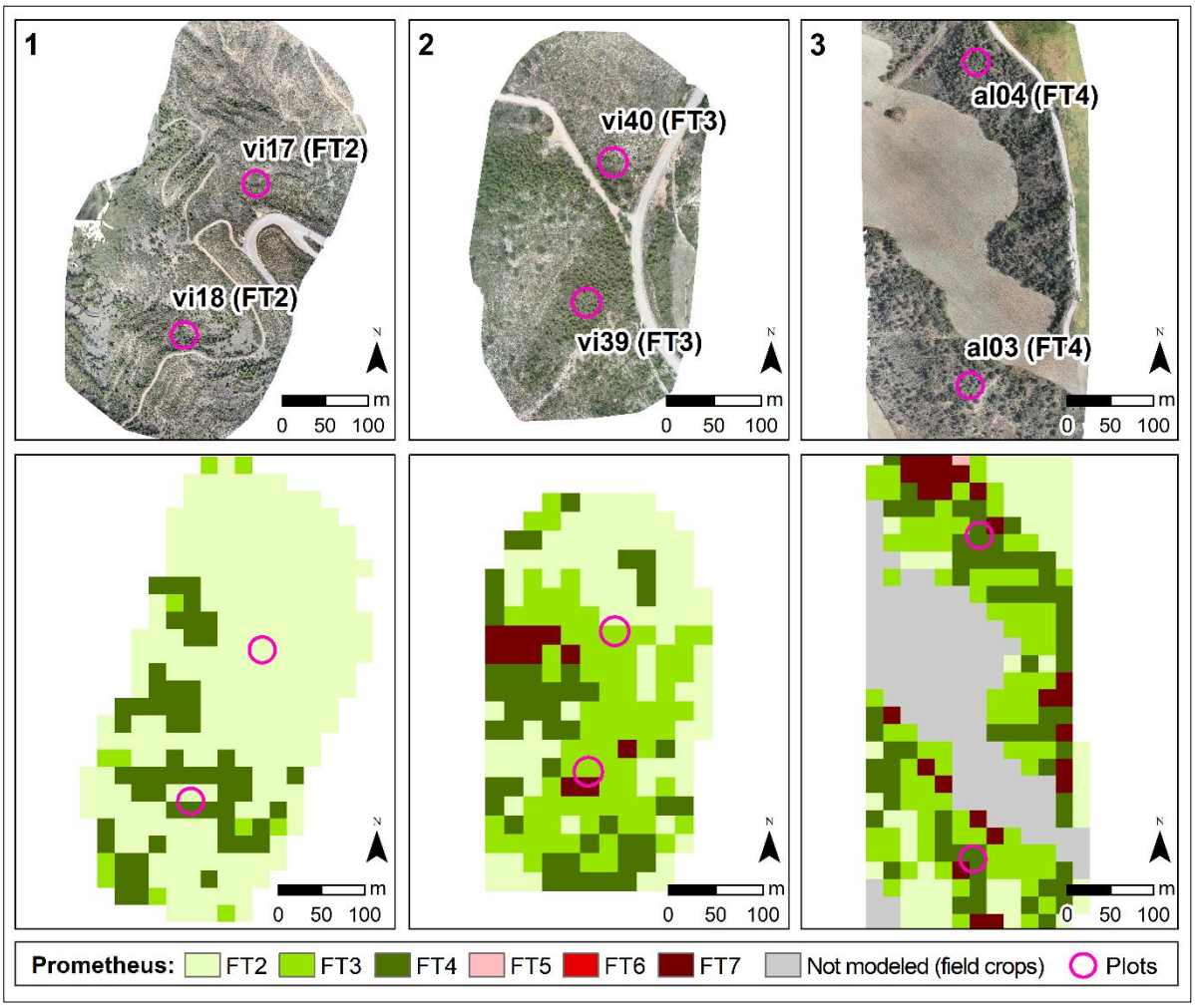

Figure 4. Mapping of Prometheus fuel types from the best classification model (RF) of the UAV data at 20 m spatial resolution. Results in areas with shrub types forest plots: (1) Plots "vi17" and "vi18": FT2; (2) Plots "vi39" and "vi40": FT3; (3) Plots "al03" and "al04": FT4.

The convergence of various fuel types depicted in the mapping enables showing the structural heterogeneity and mixture of fuels in Mediterranean forests. The observed ground-truth represents a generalization of the fuel type across the entire plot, which primarily relies on the predominant cover percentage (i.e., vegetation height and density) within the plots. However, as an example, Figure

6 illustrates the heterogeneity of three forest plots whose assigned ground-truth was FT5, showcasing the structural metrics and the diversity index that were introduced into the models. In plot "ay12", the convergence of FT5 and FT7 is observed, primarily due to variations in vegetation height at the 10th percentile and different canopy cover densities above 4 m within the plot, thus indicating a higher presence of understory in the pixels categorized as FT7. In plot "ay49", only a small sector is covered by FT7, primarily due to variations in canopy cover density above 4 m compared to the rest of the plot categorized as FT5. Lastly, in plot "ay50", variations in canopy cover density are again observed, but they do not appear to exert as much influence as seen in the previous cases since the plot exhibits FT5 in its entire area.

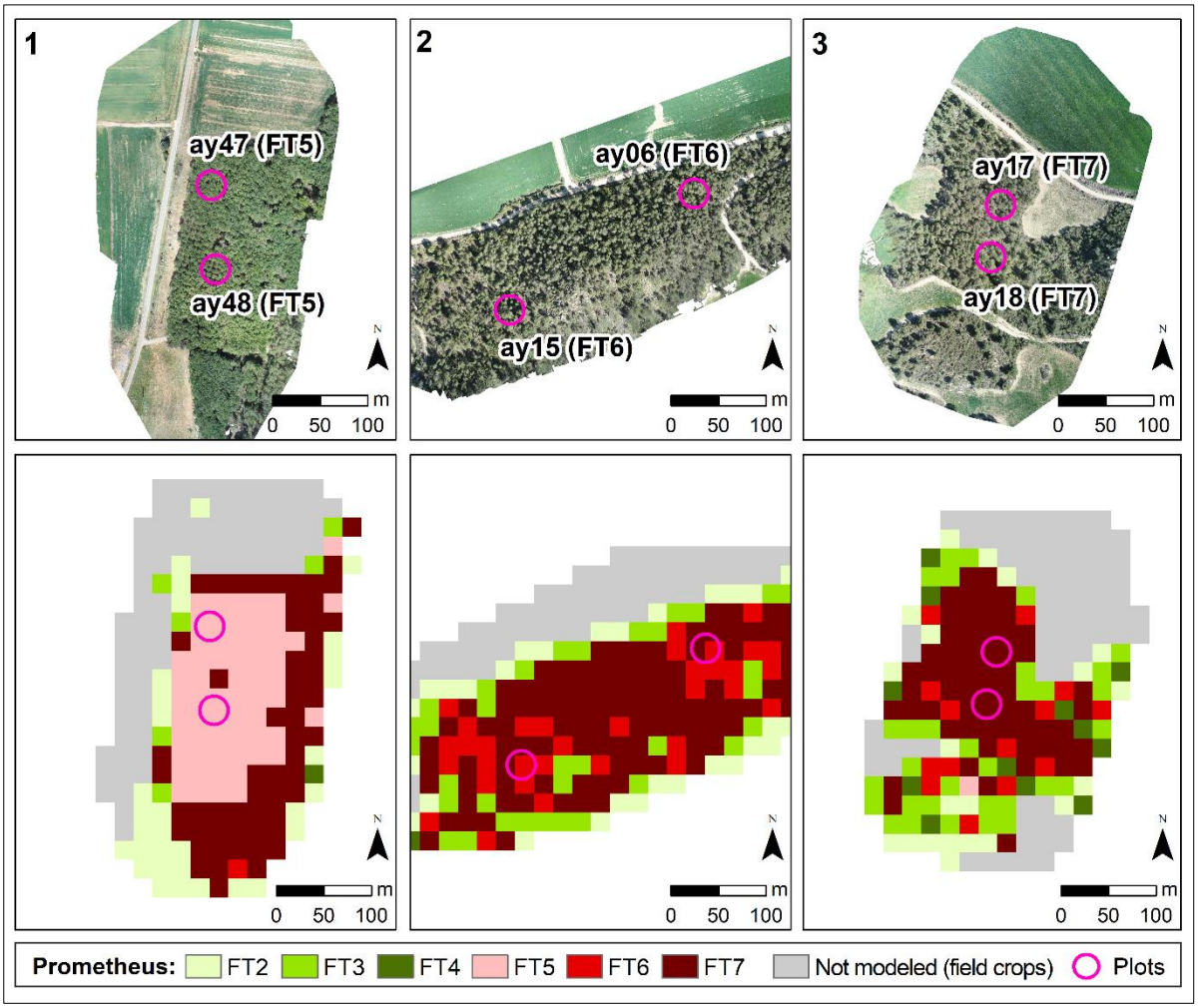

Figure 5. Mapping of Prometheus fuel types from the best classification model (RF) of the UAV data at 20 m spatial resolution. Results in areas with tree types forest plots: (1) plots "ay47" and "ay48": FT5; (2) plots "ay06" and "ay15": FT6; (3) plots "ay17" and "ay18": FT7.

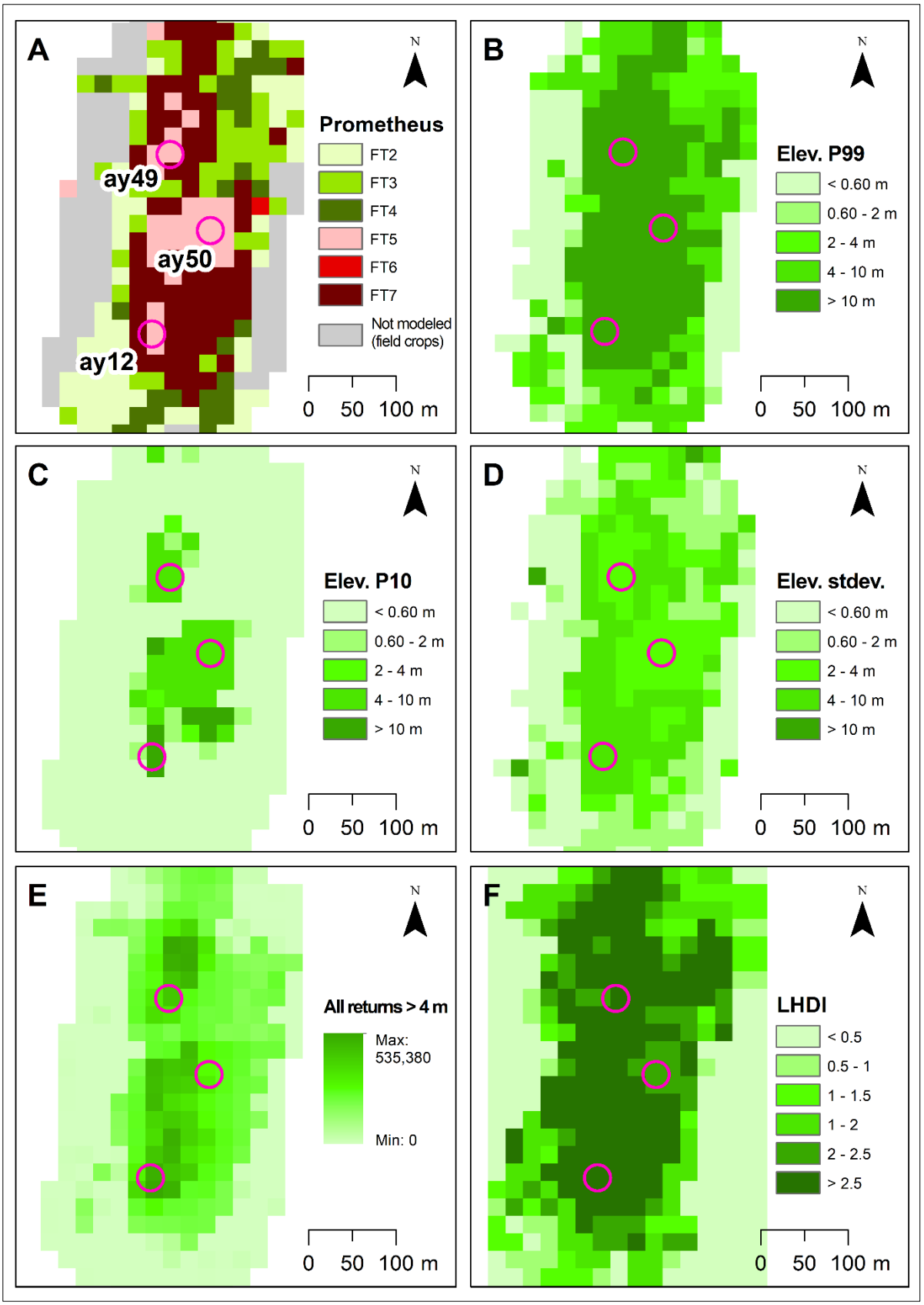

Figure 6. Spatial distribution of the Prometheus fuel types identified by the best UAV classification model (A) and the variables introduced into the models (B–F) in the UAV flight area of plots "ay12", "ay49", and "ay50" (represented as pink circles).

4. DISCUSSION

The increasing frequency and intensity of wildfires require the formulation of prevention and mitigation plans to minimize adverse impacts on the territory. Mediterranean environments rank among the most fire-prone ecosystems globally, and the looming threat of climate change may potentially cause certain regions to acquire Mediterranean characteristics in the future, thus increasing the wildfire issue (Birot, 2009). Mapping of forest fuels helps to understand fire spread and velocity within forested areas, serving as a crucial tool for effective forest management. The findings of this study underscore the efficacy of utilizing UAVs equipped with LiDAR sensors for forest fuel identification, as well as the substantial enhancement in the classification achieved through the integration of UAV and HMLS data, particularly when identifying the understory fuel between 0.60 and 2 m in height. Overall, the spatialization of Prometheus fuel types yielded satisfactory results, albeit encountering some challenges with the FT6 fuel type, thus validating the utility of UAV-LiDAR systems for fuel mapping across extensive areas.

4.1. Adequacy of the modeled variables in identifying the Prometheus fuel types

The UAV variables introduced into the classification models were selected according to the results given by Dunn's test, a method already employed in previous forest-related studies in order to determine differences between groups (e.g., Varol *et al.*, 2020; García-Galar *et al.*, 2023). The use of Dunn's test allows the variables included in the models to have a more logical explanatory meaning than that derived from the automatic selection of other procedures (e.g., *VSURF*), which tends to optimize the results by including metrics that may be similar. This may complicate the model and make the results less interpretable. Figure 7 provides insights into the consistency and discriminatory ability of the model variables in distinguishing between the different fuel types. The variable "Elev. P99", representing maximum vegetation or canopy height, effectively differentiates between shrub fuel types (FT2, FT3, FT4) and tree fuel types (FT5, FT6, FT7), thereby preventing confusion between these two groups. This is consistent with other studies that have identified canopy height as an ef-fective metric for characterizing fuels (Andersen *et al.*, 2005; Jakubowksi *et al.*, 2013). Similarly, "Elev. P10" clearly distinguishes FT5 from other types. Given that this type represents forests with minimal understory, the heights at the 10th percentile tend to be higher, aiding in correctly classifying FT6 and FT7. The effectiveness of LiDAR-derived low vegetation height metrics for characterizing

fuels has already been observed by Domingo *et al*. (2020). "Elev. stdev." reflects the variability of height distributions, facilitating differentiation between shrub and tree fuel types, although some overlap is observed, particularly in FT3 with FT5 and FT7. Concerning "All returns > 4 m", this metric is very useful for distinguishing between tree fuel types (García *et al*., 2011). It identifies the quantity of fuel above 4 m (indicative of tree fuel), yet values are distributed similarly within shrub and tree fuel types, leading here to limited discriminatory power. FT2, FT3, and FT4 exhibit minimal returns above 4 m, likely attributed to scattered small trees or tall shrubs within the plots. Conversely, FT5 demonstrates maximum fuel above 4 m, possibly due to larger trees or denser canopy cover inhibiting laser penetration to lower strata. Additionally, laser returns penetrating the crowns may have been misclassified as ground, given the sparse understory vegetation in FT5 plots. FT6 and FT7 show fewer returns above 4 m compared to FT5, suggesting smaller-sized trees or greater canopy openness facilitating laser penetration to lower strata. The variable "LHDI" serves to identify the relative abundance of fuel, regardless of vegetation height. This variable has also been effective for classifying fuel types in previous work (Revilla *et al*., 2021), as well as for characterizing forest structures (Gelabert *et al*., 2020). While "LHDI" may not distinguish between shrub and tree types, it effectively discriminates between types within a dominant stratum. "LHDI" clearly delineates FT2 from other types, which aligns logically with FT2 being a low-shrub type characterized by minimal structural diversity. Additionally, it facilitates strong differentiation among the three tree types, with low values in FT5, medium values in FT6, and high values in FT7. However, "LHDI" may not differentiate between FT3 and FT4, as these types exhibit overlapping values. Lastly, the volume between 0.60 and 2 m derived from the HMLS voxelized data demonstrates considerable variation across fuel types, particularly among tree types. As expected, values are minimal in FT2 and FT5, reflecting the low shrub type and limited understory characteristic of these types, respectively. Intermediate values are evident in FT3 and FT6, reflecting their transitional nature between low (FT2) and high (FT4) shrubs and between minimal understory (FT5) and complete vertical canopy continuity (FT7), respectively. Consequently, maximum volumes are observed in FT4 and FT7, where vertical fuel continuity is pronounced. Furthermore, minimal variability is observed in FT7 values, suggesting homogeneity in volume within this height stratum across plots.

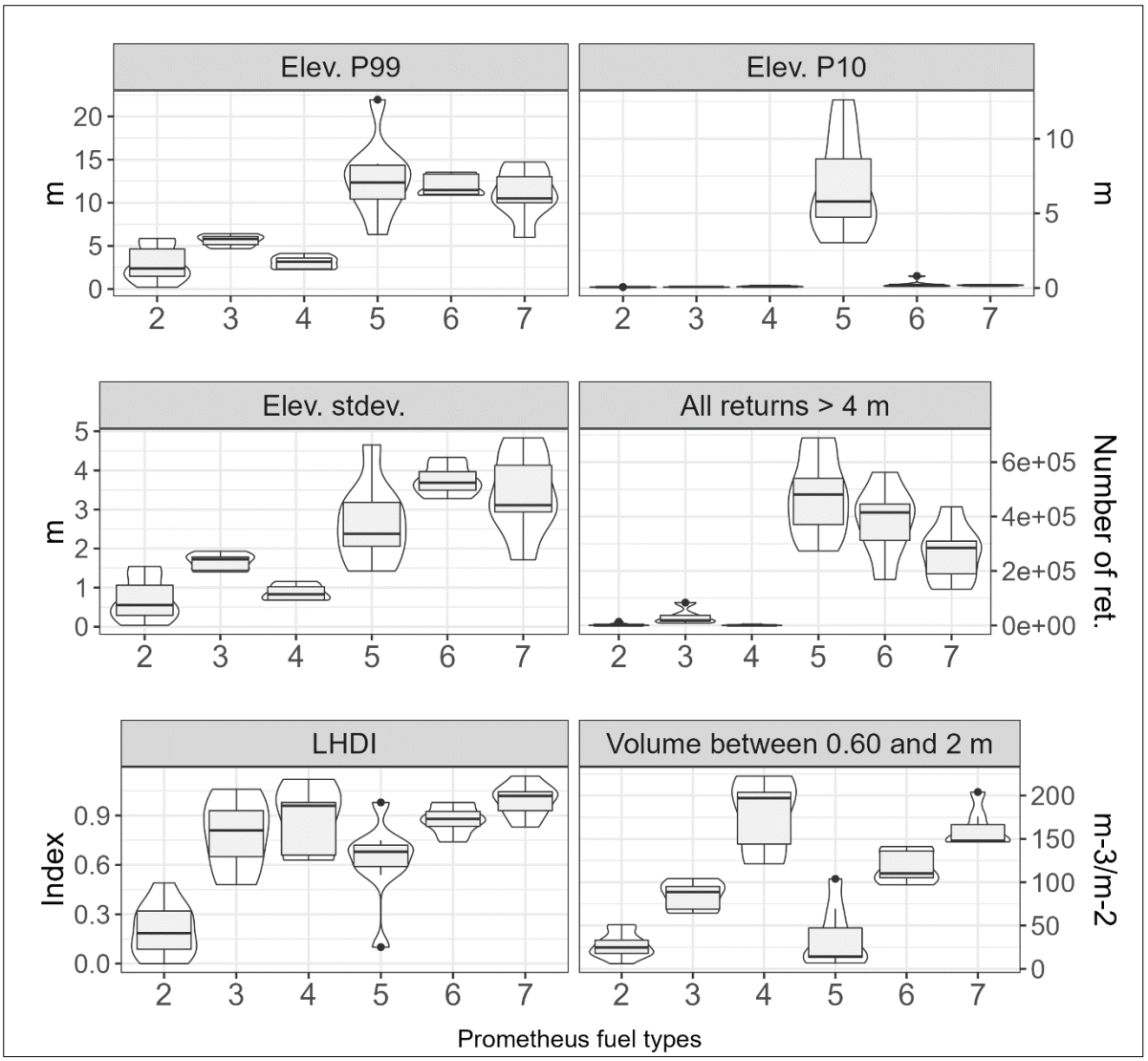

Figure 7. Distribution of values by each Prometheus fuel type for the five UAV variables and the HMLS variable introduced in the classification models.

4.2. Capabilities of UAV-LiDAR and HMLS systems to classify Prometheus fuel types

The classification of the Prometheus fuel types was conducted utilizing machine learning techniques, a methodology widely employed in previous studies with satisfac- tory outcomes (e.g., García *et al.*, 2011; Domingo *et al.*, 2020; Azim *et al.*, 2022; Hoffrén *et al.*, 2023b), although recent studies have also shown promising results in fuel classification modeling based on deep learning methods (Azim *et al.*, 2022; Labenski *et al.*, 2022; Alipour *et al.*, 2023; Carbone *et al.*, 2023). The RF model emerged as the most effective in this study, achieving the highest overall accuracy among the models tested. RF also yielded the most balanced confusion matrices, primarily demonstrating confusion between similar fuel types and minimal errors between types of different dominant strata.

The SVM-L and SVM-R models also exhibited satisfactory overall accuracies. In this sense, all the classification models improved their performance compared to those conducted by Hoffrén *et al.* (2023b) on almost the same study plots. That work offers a robust validation of the capacity of the UAV-LiDAR system employed in this study, given the similarity in the study area and the use of identical machine learning techniques, albeit Hoffrén *et al.* (2023b) used variables derived from UAV photogrammetric data. Notably, all fuel types were classified more accurately with the UAV-LiDAR system compared to the photogrammetric UAV data, with significant improvements observed, particularly in the classification of FT3, FT4, and FT6 types. These findings are consistent with those reported by Wallace *et al.* (2016), who similarly compared UAVs with LiDAR and photogrammetric sensors in dry sclerophyll eucalypt forest stands, noting that both systems could effectively describe terrain and canopy properties, although the performance of photogrammetric UAVs was compromised in densely forested areas. This aspect was also observed by Hillman *et al.* (2021) again in sclerophyll eucalypt forests, who noted underperformance in characterizing canopy and below-canopy structures. Furthermore, the results from classification models presented here improve upon fits of fuel classification models based on ALS and multispectral data reported in previous studies (e.g., Marino *et al.*, 2016; Huesca *et al.*, 2019; Domingo *et al.*, 2020), though they are somewhat lower compared to those of García *et al.* (2011), who applied decision rules to the classification outputs. Hoffrén *et al.* (2023a) achieved lower classification accuracies when using LiDAR data from NASA's Global Ecosystem Dynamics Investigation satellite system, though performances were comparable to this study when LiDAR-derived metrics were combined with multispectral imageries from Landsat-8 OLI.

The integration of UAV variables with vegetation volume data derived from HMLS-voxelized point clouds yielded a significant enhancement in the classification models. The fuel volume between 0.60 and 2 m reached the most promising results for the models, although other heights strata also contributed to improving accuracies, but to a lesser extent. This outcome aligns logically with the operational characteristics of HMLS systems, which, operating from the ground, are less susceptible to canopy bounce effects compared to UAVs. Consequently, this integration minimized confusion between similar fuel types and notably eradicated them almost entirely, with the inclusion of vegetation volume between 0.60 and 2 m. In this study, we benefited from HMLS data collected in a prior work (Hoffrén *et al.*, 2024), which aimed to characterize Prometheus fuel types using high-density voxels (5 cm^3) generated from HMLS point clouds. In that study, the analysis of the vertical distribution of fuels based

on the voxels for each observed fuel type revealed significant confusion in field identification between types FT2-FT3, FT5-FT6, and FT6-FT7, consistent with the highest error rates observed in this study (FT3) and in Hoffrén *et al*. (2023b) (FT3 and FT6). Therefore, the HMLS system effectively captured the structural heterogeneity of understory fuels—a prevalent scenario in Mediterranean forests—and minimized confusion between Prometheus fuel types by amalgamating its data with UAV-LiDAR data. This synergy between both systems has also demonstrated effectiveness in previous studies (Hillman *et al*., 2021), albeit with slightly superior estimates achieved by TLS in identifying elevated canopy cover in a dry schlerophyll forest. Furthermore, Hyyppä *et al*. (2020a) found better identification of forest understory attributes using a ground-based mobile laser scanner (MLS) and an under-canopy UAV system in a boreal forest. Additionally, the fusion of UAV and MLS data facilitated the effective quantification of post-fire tree structures in a mixed forest in Western Canada (Qi *et al*., 2022). Other authors underscore the importance of combining TLS, MLS, and UAV systems for validating spaceborne LiDAR, radar, and optical missions (Levick *et al*., 2021). Despite these promising findings, the use of ground-based LiDAR systems may not always be practical in terms of productivity, as data collection requires more time and access within the forest, which can be challenging due to terrain obstacles (e.g., steep slopes, water masses, or rocky cliffs), dense vegetation, or wildlife. In contrast, UAVs enable faster data collection over larger areas without direct penetration into forests, offering a significant advantage. Thus, in this study we cannot spatialize the UAV-HMLS model because it was impracticable to collect data in the whole UAV flight areas in terms of time, cost, and effort. In this sense, the capacity of UAVs themselves to cover greater extents and generate fuel maps presents a very valuable opportunity for effective forest management.

4.3. Fuel mapping from UAV data

The analysis of the spatialized fuel types within the forest plots yielded good overall correspondences with the ground-truth observations. In some cases, the plots exhibited a mix of several fuel types, as depicted in Figure 6—an expected scenario given the inherent heterogeneity of fuel types, particularly in Mediterranean areas, characterized by high forest structural complexity. Primary challenges arose in categorizing the FT6 fuel type, which was inaccurately spatialized in many of its corresponding plots, and furthermore, there were few such pixels spatialized in general on the maps. In all plots where FT6 was misclassified, the spatialized fuel type was FT7, which confirms the high confusion between these two fuel types already observed in many previous

studies (García *et al*., 2011; Huesca *et al*., 2019; Domingo *et al*., 2020; García-Cimarras *et al*., 2021; Hoffrén *et al*., 2023b). Discrepancies between the hit rate percentages of FT6 in the RF classification model, which were relatively high, and the resulting mapping could potentially be attributed to the tendency of RF models to overfit, a phenomenon documented in prior studies (Arellano-Pérez *et al*., 2018; Hu *et al*., 2020). Additionally, these confusions may stem from a limitation of the model variables in discerning between FT6 and FT7. Examination of the complete results of Dunn's test (Table A.2 of the Appendix) reveals that none of the variables were able to differentiate between these two types. Furthermore, Figure 7 illustrates that the distribution of values of the UAV variables in FT6 and FT7 consistently overlap, unlike other fuel types, where such overlap is absent in at least one variable. However, it is important to note the converse scenario, wherein the FT3 fuel type obtained the highest error rates in the classification model, yet all observed FT3 type plots, except one, were correctly assigned their respective fuel types in the maps. Ultimately, despite some observed limitations, the maps of fuel types have shown good performance and confirm UAV-LiDAR systems as powerful tools for better understanding the distribution of fuels across large areas.

Fuel maps are critical tools for improving decision-making and risk management of wildfires, especially in highly fire-prone regions such as Mediterranean ecosystems. These maps aid in the development of structural mitigation plans, including activities such as clearing, grazing, scrub removal, and periodic necromass cleaning over time. Furthermore, their integration with other cartographic data adds significant value to improve fire risk prevention over ecosystems and populations. In this study, the Prometheus fuel types were successfully classified and mapped across the UAV flight areas. Although it is outside the scope of our research, scaling up from our small test areas to a landscape scale, which is more effective for establishing fire management strategies, could be achieved through multi-sensor integration. The collection of highly accurate UAV data offers a method that improves both the time efficiency and accuracy of traditional forest inventory based on fieldwork while enhancing the precision of data obtained from remote sensors, such as ALS or SLS, which is critical in complex environments like Mediterranean forest landscapes. In this way, UAV data would serve as the ground-truth for subsequently spatializing the results to larger areas using sensors that cover broader spatial scales.

5. CONCLUSIONS

The identification and mapping of forest fuels play a crucial role in wildfire prevention and mitigation efforts. The integration of two remote sensing technologies, LiDAR and UAVs, known for their efficacy in estimating vegetation structural characteristics, as well as the use of machine learning-based classification algorithms, has facilitated the classification of Prometheus fuel types in Mediterranean forest stands and the generation of fuel maps with high levels of accuracy. While further research is necessary to explore the potential and limitations of these instruments, as well as their integration with other platforms and sensors (such as TLS, multispectral, or hyperspectral imaging), the findings of this study underscore the capabilities of UAV-LiDAR systems as high-valuable instruments to identify and map forest fuels and, ultimately, for improving efficient management of forest ecosystems at local and regional scales.

ACKNOWLEDGMENTS

The authors would like to thank Grafinta S.A. (Av. Filipinas 46, 28003 Madrid, Spain) for providing the *GeoSLAM ZEB-Horizon* HMLS unit and the *GeoSLAM Connect* v.2.3.0 software. The authors also thank Darío Domingo for his support in the fieldwork.

REFERENCES

Abatzoglou, J.T., Williams, A.P., and Barbero, R., 2019. Global emergence of anthropogenic climate change in fire weather indices. *Geophys. Res. Lett.* 46, 326–336, https://doi.org/10.1029/2018GL080959

Abdollahi, A. and Yebra, M., 2023. Forest fuel type classification: Review of remote sensing techniques, constraints and future trends. *J. Environ. Manag.* 342, 118315, https://doi.org/10.1016/j.jenvman.2023.118315.

Abram, N.J., Henley, B.J., Gupta, A.S., Lippmann, T.J.R., Clarke, H., Dowdy, A.J., Sharples, J.J., Nolan, R.H., Zhang, T., Wooster, M.J., *et al.*, 2021. Connections of climate change and variability to large and extreme forest fires in southeast Australia. *Commun. Earth Environ.* 2, 8, https://doi.org/10.1038/s43247-020-00065-8.

Alipour, M., La Puma, I., Picotte, J., Shamsaei, K., Rowell, E., Watts, A., Kosovic, B., Ebrahimian, H., and Tacirogl, E., 2023. A multimodal data fusion and deep learning framework for large-scale wildfire surface fuel mapping. *Fire* 6, 36, https://doi.org/10.3390/fire6020036.

Amatulli, G., Pérez-Cabello, F., and de la Riva, J., 2007. Mapping lightning/human-caused wildfires occurrence under ignition point location uncertainty. *Ecol. Modell.* 200, 321–333, https://doi.org/10.1016/j.ecolmodel.2006.08.001.

Andersen, H.E., McGaughey, R.J., and Reutebuch, S.E., 2005. Estimating forest canopy fuel parameters using LiDAR data. *Remote Sens. Environ.* 94, 441–449, https://doi.org/10.1016/j.rse.2004.10.013.

Aragoneses, E. and Chuvieco, E., 2021. Generation and mapping of fuel types for fire risk assessment. Fire 4, 59, https://doi.org/10.3390/fire4030059.

Arellano-Pérez, S., Castedo-Dorado, F., López-Sánchez, C.A., González-Ferreiro, E., Yang, Z., Díaz-Varela, R.A., Álvarez-González, J.G., Vega, J.A., and Ruiz-González, A.D., 2018. Potential of Sentinel-2 data to model surface and canopy fuel characteristics in relation to crown fire hazard. *Remote Sens.* 10, 1645, https://doi.org/10.3390/rs10101645.

Ascoli, D., Moris, J.V., Marchetti, M., and Sallustio, L., 2021. Land use change towards forests and wooded land correlates with large and frequent wildfires in Italy. *Ann. Silvic. Res.* 46, 177–188, https://doi.org/10.12899/asr-2264.

Ashworth, A., Evans, D.L., Cookie, W.H., Londo, A., Collins, C., and Neuenschwander, A., 2010. Predicting southeastern forest canopy heights and fire fuel models using GLAS data. *Photogramm. Eng. Remote Sens.* 76, 915–922, https://doi.org/10.14358/PERS.76.8.915.

Azim, M.R., Keskin, M., Do, N., and Gül, M., 2022. Automated classification of fuel types using roadside images via deep learning. *Int. J. Wildland Fire* 31, 982–987, https://doi.org/10.1071/WF21136.

Birot, Y., 2009. Living with Wildfires: What Science Can Tell Us, Discussion Paper 15, European Forest Institute: Joensuu, Finland, ISBN 987-952-5453-29-4.

Carbone, A., Spiller, D., and Laneve, G., 2023. Fuel type mapping using a CNN-based remote sensing approach: A case study in Sardinia. *Fire* 6, 395, https://doi.org/10.3390/fire6100395.

Chen, Y., Zhu, X., Yebra, M., Harris, S., and Tapper, N., 2016. Strata-based forest fuel classification for wild fire hazard assessment using terrestrial LiDAR. *J. Appl. Remote Sens.* 10, 046025, https://doi.org/10.1117/1.JRS.10.046025.

Chirici, G., Scotti, R., Montaghi, A., Barbati, A., Cartisano, R., López, G., Marchetti, M., McRoberts, R.E., Olsson, H., and Corona, P., 2013. Stochastic gradient boosting classification trees for forest fuel types mapping through airborne laser scanning and IRS LISS-III imagery. *Int. J. Appl. Earth Obs. Geoinf.* 25, 87–97, https://doi.org/10.1016/j.jag.2013.04.006.

Cunningham, C.X., Williamson, G.J., and Bowman, D.M.J.S., 2024. Increasing frequency and intensity of the most extreme wildfires on Earth. *Nat. Ecol. Evol.* 8, 1420–1425, https://doi.org/10.1038/s41559-024-02452-2.

Díaz-Delgado, R., Lloret, F., Pons, X., and Terradas, J., 2002. Satellite evidence of decreasing resilience in Mediterranean plant communities after recurrent wildfires. *Ecology* 83, 2293–2303, https://doi.org/10.1890/0012-9658(2002)083[2293:SEODRI]2.0.CO;2.

Domingo, D., de la Riva, J., Lamelas, M.T., García-Martín, A., Ibarra, P., Echeverría, M.T., and Hoffrén, R., 2020. Fuel type classification using airborne laser scanning and Sentinel-2 data in Mediterranean forest affected by wildfires. *Remote Sens.* 12, 3660, https://doi.org/10.3390/rs12213660.

Dunn, O.J., 1964. Multiple comparisons using rank sums. *Technometrics* 6, 241–252, https://doi.org/10.1080/00401706.1964.10490181.

Dupuy, J.-L., Fargeon, H., Martin-StPaul, N., Pimont, F., Ruffault, J., Guijarro, M., Hernando, C., Madrigal, J., and Fernandes, P., 2020. Climate change impact on future wildfire danger and activity in southern Europe: A review. *Ann. For. Sci.* 77, 35, https://doi.org/10.1007/s13595-020-00933-5.

Evans, J.S. and Hudak, A.T., 2007. A multiscale curvature algorithm for classifying discrete return LiDAR in forested environments. IEEE Trans. Geosci. *Remote Sens.* 45, 1029–1038, https://doi.org/10.1109/TGRS.2006.890412.

García, M., Riaño, D., Chuvieco, E., Salas, J., and Danson, F.M., 2011. Multispectral and LiDAR data fusion for fuel type mapping using Support Vector Machine and decision rules. *Remote Sens. Environ.* 115, 1369–1379, https://doi.org/10.1016/j.rse.2011.01.017.

García-Cimarras, A., Manzanera, J.A., and Valbuena, R., 2021. Analysis of Mediterranean vegetation fuel type changes using multitemporal LiDAR. *Forests* 12, 335, https://doi.org/10.3390/f12030335.

García-Galar, A., Lamelas, M.T., and Domingo, D., 2023. Assessment of oak groves conservation statuses in Natura 2000 sacs with single photon LiDAR and Sentinel-2 data. *Remote Sens.* 15, 710, https://doi.org/10.3390/rs15030710.

Gelabert, P.J., Montealegre, A.L., Lamelas, M.T., and Domingo, D., 2020. Forest structural diversity characterization in Mediterranean landscapes affected by fires using Airborne Laser Scanning data. *GIScience Remote Sens.* 57, 497–509, https://doi.org/10.1080/15481603.2020.1738060.

Hijmans, R., 2022. 'terra': Spatial Data Analysis. R Package Version 1.5-21. Available online: https://cran.r-project.org/package=terra (accessed on 13 June 2024).

Hillman, S., Wallace, L., Lucieer, A., Reinke, K., Turner, D., and Jones, S., 2021. A comparison of terrestrial and UAS sensors for measuring fuel hazard in a dry sclerophyll forest. *Int. J. Appl. Earth Obs. Geoinf.* 95, 102261, https://doi.org/10.1016/j.jag.2020.102261.

Hoffrén, R., Lamelas, M.T., de la Riva, J., Domingo, D., Montealegre, A.L., García-Martín, A., and Revilla, S., 2023a. Assessing GEDI-NASA system for forest fuels classification using machine learning techniques. *Int. J. Appl. Earth. Obs. Geoinf.* 116, 103175, https://doi.org/10.1016/j.jag.2022.103175.

Hoffrén, R., Lamelas, M.T., and de la Riva, J., 2023b. UAV-derived photogrammetric point clouds and multispectral indices for fuel estimation in Mediterranean forests. *Remote Sens. Appl. Soc. Environ.* 31, 100997, https://doi.org/10.1016/j.rsase.2023.100997.

Hoffrén, R., Lamelas, M.T., and de la Riva, J., 2024. Evaluation of handheld mobile laser scanner systems for the definition of fuel types in structurally complex Mediterranean forest stands. *Fire* 7, 59, https://doi.org/10.3390/fire7020059.

Hohner, A.K., Rhoades, C.C., Wilkerson, P., and Rosario-Ortiz, F.L., 2019. Wildfires alter forest watersheds and threaten drinking water quality. *Acc. Chem. Res.* 52, 1234–1244, https://doi.org/10.1021/acs.accounts.8b00670.

Hu, Y., Xu, X., Wu, F., Sun, Z., Xia, H., Meng, Q., Huang, W., Zhou, H., Gao, J., Li, W., *et al*., 2020. Estimating forest stock volume in Hunan Province, China, by integrating in situ plot data, Sentinel-2 images, and linear and machine learning regression models. *Remote Sens.* 12, 186, https://doi.org/10.3390/rs12010186.

Huesca, M., Riaño, D., and Ustin, S.L., 2019. Spectral mapping methods applied to LiDAR data: Application to fuel type mapping. *Int. J. Appl. Earth Obs. Geoinf.* 74, 159–168, https://doi.org/10.1016/j.jag.2018.08.020.

Hyyppä, E., Yu, X., Kaartinen, H., Hakala, T., Kukko, A., Vastaranta, M., and Hyyppä, J., 2020a. Comparison of backpack, handheld, under-canopy UAV, and above-canopy UAV laser scanning for field reference data collection in boreal forests. *Remote Sens.* 12, 3327, https://doi.org/10.3390/rs12203327

Hyyppä, E., Hyyppä, J., Hakala, T., Kukko, A., Wulder, M.A., White, J.C., Pyöräla, J., Yu, X., Wang, Y., Virtanen, J.P., *et al*., 2020b. Under-canopy UAV laser scanning for accurate forest field measurements. *ISPRS J. Photogramm. Remote Sens.* 164, 41–60, https://doi.org/10.1016/j.isprsjprs.2020.03.021.

Jakubowksi, M.K., Guo, Q., Collins, B., Stephens, S., and Kelly, M., 2013. Predicting surface fuel models and fuel metrics using LiDAR and CIR imagery in dense, mountainous forest. *Photogramm. Eng. Remote Sens.* 1, 37–49, https://doi.org/10.14358/PERS.79.1.37.

Jones, M.W., Abatzoglou, J.T., Veraverbeke, S., Andela, N., Lasslop, G., Forkel, M., Smith, A.J.P., Burton, C., Betts, R.A., van der Werf, G., *et al*., 2022. Global and regional trends and drivers of fire under climate change. *Rev. Geophys.* 60, e2020RG000726, https://doi.org/10.1029/2020RG000726

Kelly, L.T., Giljohann, K.M., Duane, A., Aquilué, N., Archibald, S., Batllori, E., Bennett, A.F., Buckland, S.T., Canelles, Q., Clarke, M.F., *et al*., 2020. Fire and biodiversity in the Anthropocene. *Science* 370, eabb0355, https://doi.org/10.1126/science.abb0355.

Kramer, H.A., Mockrin, M.H., Alexandre, P.M., and Radeloff, V.C., 2019. High wildfire damage in interface communities in California. *Int. J. Wildland Fire* 28, 641–650, https://doi.org/10.1071/WF18108.

Kuhn, M., 2008. Building predictive models in R using the caret package. *J. Stat. Softw.* 28, 1–26, https://doi.org/10.18637/jss.v028.i05.

Labenski, P., Ewald, M., Schmidtlein, S., and Fassnacht, F.E., 2022. Classifying surface fuel types based on forest stand photographs and satellite time series using deep learning. *Int. J. Appl. Earth Obs. Geoinf.* 109, 102799, https://doi.org/10.1016/j.jag.2022.102779.

Lasaponara, R. and Lanorte, A., 2006. Remotely sensed characterization of forest fuel types by using satellite ASTER data. *Int. J. Appl. Earth. Obs. Geoinf.* 9, 225–234, https://doi.org/10.1016/j.jag.20006.08.001.

Legge, S., Rumpff, L., Woinarski, J.C.Z., Whiterod, N.S., Ward, M., Southwell, D.G., Scheele, B.C., Nimmo, D.G., Lintermans, M., Geyle, H.M., *et al*., 2022. The conservation impacts of ecological disturbance: Time-bound estimates of population loss and recovery for fauna affected by the 2019–2020 Australian megafires. *Glob. Ecol. Biogeogr.* 31, 2085–2104, https://doi.org/10.1111/geb.13473.

Leite, R.V., Silva, C.A., Broadbent, E.N., do Amaral, C.H., Liesenberg, V., de Almeida, D.R.A., Mohan, M., Godinho, S., Cardil, A., Hamamura, C., *et al*., 2022. Large scale multi-layer fuel load characterization in tropical savanna using GEDI spaceborne LiDAR data. *Remote Sens. Environ.* 268, 112764, https://doi.org/10.1016/j.rse.2021.112764.

Levick, S.R., Whiteside, T., Loewensteiner, D.A., Rudge, M., and Bartolo, R., 2021. Leveraging TLS as a calibration and validation tool for MLS and ULS mapping of savanna structure and biomass at landscape-scales. *Remote Sens.* 13, 257, https://doi.org/10.3390/rs13020257.

Listopad, C.M.C.S., Masters, R.E., Drake, J., Weishampel, J., and Branquinho, C., 2015. Structural diversity indices based on airborne LiDAR as ecological indicators for managing highly dynamic landscapes. *Ecol. Indic.* 57, 268–279, https://doi.org/10.1016/j.ecolind.2015.04.017.

Loidi, J. (Ed.), 2017. The Ebro Basin. In *The Vegetation of the Iberian Peninsula. Plant and Vegetation*, Springer: Cham, Switzerland, Volume 12, pp. 513–547.

Marino, E., Ranz, P., Tomé, J.L., Noriega, M.Á., Esteban, J., and Madrigal, J., 2016. Generation of high-resolution fuel model maps from discrete airborne laser scanner and Landsat-8 OLI: A low-cost and highly updated methodology for large areas. *Remote Sens. Environ.* 187, 267–280, https://doi.org/10.1016/j.rse.2016.10.020.

McGaughey, R.J., 2021. FUSION/LDV: Software for LiDAR Data Analysis and Visualization v.4.21, USDA Forest Service: Washington, DC, USA.

Montealegre, A.L., Lamelas, M.T., de la Riva, J., García-Martín, A., and Escribano, F., 2015. A comparison of open-source LiDAR filtering algorithms in a Mediterranean forest environment. *IEEE J. Sel. Top. Appl. Earth Obs. Remote Sens.* 8, 4072–4085, https://doi.org/10.1109/JSTARS.2015.2436974.

Nicolau, A.P., Dyson, K., Saah, D., and Clinton, N., 2023. Accuracy assessment: Quantifying classification quality. In *Cloud-Based Remote Sensing with Google Earth Engine*, Cardille, J.A., Crowley, M.A., Saah, D., Clinton, N.E., Eds., Springer: Cham, Switzerland, pp. 135–145, https://doi.org/10.1007/978-3-031-26588-4_7.

Novo, A., Fariñas-Álvarez, N., Martínez-Sánchez, J., González-Jorge, H., Fernández-Alonso, J.M., and Lorenzo, H., 2020. Mapping forest fire risk—A case of study in Galicia (Spain). *Remote Sens.* 12, 3705, https://doi.org/10.3390/rs12223705.

Papatheodorou, I., Kitikidou, K., Stampoulidis, A., and Milios, E., 2023. Analyzing the impact of reforestation on forest fires and the economic outcome in an area in northern Greece: Should we reforest areas with conifers? Yes or no? *Ecol. Quest.* 34, 1–17, https://doi.org/10.12775/EQ.2023.052.

Pausas, J.G. and Keeley, J.E., 2021. Wildfires and global change. *Front. Ecol. Environ.* 19, 387–395, https://doi.org/10.1002/fee.2359.

Pausas, J.G., Llovet, J., Rodrigo, A., and Vallejo, R., 2008. Are wildfires a disaster in the Mediterranean basin?—A review. *Int. J. Wildland Fire* 17, 713–723, https://doi.org/10.1071/WF07151.

Phillips, C.A., Rogers, B.M., Elder, M., Cooperdock, S., Moubarak, M., Randerson, J.T., and Frumhoff, P.C., 2022. Escalating carbon emissions from North American boreal forest wildfires and the climate mitigation potential of fire management. *Sci. Adv.* 8, 17, https://doi.org/10.1126/sciadv.abl7161.

Ponomarev, E., Yakimov, N., Ponomareva, T., Yakubailik, O., and Conrad, S.G., 2021. Current trend of carbon emissions from wildfires in Siberia. *Atmosphere* 12, 559, https://doi.org/10.3390/atmos12050559

Prometheus, 1999. Management Techniques for Optimization of Suppression and Minimization of Wildfires Effects, System Validation, European Commission, DG XII, ENVIR & CLIMATE, Contract Number ENV4-CT98-0716, European Commission: Luxembourg.

Qi, Y., Coops, N.C., Daniels, L.D., and Butson, C.R., 2022. Assessing the effects of burn severity on post-fire tree structures using the fused drone and mobile laser scanning point clouds. *Front. Environ. Sci.* 10, 949442, https://doi.org/10.3389/fenvs.2022.949442.

R Core Team, 2020. R: A Language and Environment for Statistical Computing, R Foundation for Statistical Computing: Vienna, Austria. Available online: https://www.R-project.org (accessed on 13 June 2024).

Renslow, M., 2013. Manual of Airborne Topographic LiDAR, ASPRS: Bethesda, MD, USA, ISBN: 978-1570830976.

Revilla, S., Lamelas, M.T., Domingo, D., de la Riva, J., Montorio, R., Montealegre, A.L., and García-Martín, A., 2021. Assessing the potential of the DART model to discrete return LiDAR simulation—Application to fuel type mapping. *Remote Sens.* 13, 342, https://doi.org/10.3390/rs13030342.

Richards, J., Huser, R., Bevacqua, E., and Zscheischler, J., 2023. Insights into the drivers and spatiotemporal trends of extreme Mediterranean wildfires with statistical deep learning. *Artif. Intell. Earth Syst.* 2, e220095, https://doi.org/10.1175/AIEDS-D-22-0095.1.

Romero-Ramírez, F.J., Navarro-Cerrillo, R.M., Varo-Martínez, M.A., Quero, J.L., Doerr, S., and Hernández-Clemente, R., 2018. Determination of forest fuels characteristics in mortality-affected Pinus forests using integrated hyperspectral and ALS data. *Int. J. Appl. Earth. Obs. Geoinf.* 68, 157–167, https://doi.org/10.1016/j.jag.2018.01.003.

Roussel, J.R. and Auty, D., 2022. Airborne LiDAR Data Manipulation and Visualization for Forestry Applications. R Package Version 4.0.1. Available online: https://cran.r-project.org/package=lidR (accessed on 13 June 2024).

Roussel, J.R., Auty, D., Coops, N.C., Tompalski, P., Goodboy, T.R.H., Sánchez-Meador, A., Bourdon, J.F., de Boissieu, F., and Achim, A., 2020. 'lidR': An R package for analysis of Airborne Laser Scanning (ALS) data. *Remote Sens. Environ.* 251, 112061, https://doi.org/j.rse.2020.112061.

Ruffault, J., Curt, T., Moron, V., Trigo, R.M., Mouillot, F., Koutsias, N., Pimont, F., Martin-StPaul, N., Barbero, R., Dupuy, J.-L., *et al.*, 2020. Increased likelihood of heat-induced large wildfires in the Mediterranean *Basin. Sci. Rep.* 10, 13790, https://doi.org/10.1038/s41598-020-70069-z.

Shin, P., Sankey, T., Moore, M.M., and Thode, A.E., 2018. Evaluating unmanned aerial vehicle images for estimating forest canopy fuels in a Ponderosa pine stand. *Remote Sens.* 10, 1266, https://doi.org/10.3390/rs10081266.

Varol, T., Emir, T., Akgul, M., Ozel, H.B., Acar, H.H., and Cetin, M., 2020. Impacts of small-scale mechanized logging equipment on soil compaction in forests. *J. Soil Sci. Plant Nutr.* 20, 953–963, https://doi.org/10.1007/s42729-020-00182-5.

Wallace, L., Lucieer, A., Malenovský, Z., Turner, D., and Vopěnka, P., 2016. Assessment of forest structure using two UAV techniques: A comparison of airborne laser scanning and Structure from Motion (SfM) point clouds. *Forests* 7, 62, https://doi.org/10.3390/f7030062.

White, A.M. and Long, J.W., 2019. Understanding ecological contexts for active reforestation following wildfires. *New For.* 50, 41–56, https://doi.org/10.1007/s11056-018-9675-z.

Wilson, N., Bradstock, R., and Bedward, M., 2022. Influence of fuel structure derived from terrestrial laser scanning (TLS) on wildfire severity in logged forests. *J. Environ. Manag.* 302 Pt A, 114011, https://doi.org/10.1016/j.jenvman.2021.114011.

APPENDIX

Table A.1. Description and general characteristics of the forest plots. XY coordinates in ETRS89 / UTM zone 30N (EPSG: 25830). Part 1 of 3.

Sector	Plot name	FT	Plot center		UAV points/m^2 density	HMLS points/m^2 density
			X	Y		
Almudévar	al01	5	694602.4	4652067.8	562.11	71,594.08
	al02	5	694567.6	4652104.5	562.11	61,510.30
	al03	4	710134.0	4663293.6	502.80	55,084.31
	al04	4	710141.3	4663668.7	502.80	55,983.11
	al05	5	697105.5	4653417.9	457.56	-
	al06	5	697077.0	4653418.3	457.56	-
	al07	5	697017.0	4653403.3	457.56	-
	al08	5	697328.8	4653490.1	457.56	91,474.10
	al09	5	697275.2	4653516.2	457.56	69,930.07
Ayerbe	ay01	7	687724.6	4676577.7	548.62	-
	ay02	7	686539.2	4676302.0	527.17	-
	ay03	6	686345.4	4676281.1	527.17	-
	ay04	6	686687.0	4674577.9	549.93	133,259.23
	ay05	7	686571.7	4674322.0	484.65	-
	ay06	6	688450.4	4674202.7	408.93	89,334.00
	ay07	7	686360.6	4674755.4	402.53	-
	ay08	6	686536.4	4674651.8	549.93	84,663.50
	ay09	7	686777.5	4674151.0	484.65	-
	ay10	7	686827.2	4674370.8	336.32	-
	ay11	7	687030.2	4674287.7	336.32	-
	ay12	5	685055.4	4672393.5	487.08	29,699.16
	ay13	7	688074.2	4673849.8	443.70	-
	ay14	6	688185.8	4673837.0	443.70	-
	ay15	6	688256.4	4674080.0	408.93	80,750.19
	ay16	7	688792.3	4674281.6	506.80	115,322.61

Table A.1. Description and general characteristics of the forest plots. XY coordinates in ETRS89 / UTM zone 30N (EPSG: 25830). Part 2 of 3.

Sector	Plot name	FT	Plot center		UAV points/m^2 density	HMLS points/m^2 density
			X	Y		
Ayerbe	ay17	7	689248.8	4674261.2	406.49	131,697.66
	ay18	7	689238.5	4674206.1	406.49	-
	ay19	6	686878.8	4673256.3	459.62	119,540.63
	ay20	6	686703.7	4673179.9	459.62	84,514.25
	ay21	6	686995.7	4672946.4	311.16	-
	ay22	7	687240.4	4673227.3	351.69	77,658.80
	ay28	6	688371.2	4673218.0	489.35	82,040.58
	ay29	7	688737.6	4673129.7	426.31	85,566.76
	ay30	7	688775.1	4673342.4	292.70	78,094.99
	ay31	7	688609.8	4673178.1	426.31	78,879.46
	ay44	7	686251.9	4671350.2	457.55	-
	ay45	7	686273.1	4671283.0	457.55	-
	ay46	6	686986.9	4671460.5	453.52	-
	ay47	5	685130.0	4673135.5	644.98	31,830.43
	ay48	5	685134.6	4673047.1	644.98	-
	ay49	5	685076.3	4672599.0	487.08	52,189.62
	ay50	5	685122.5	4672511.9	487.08	24,966.82
Uncastillo	un02	5	643660.3	4693452.8	232.77	-
	un03	6	643147.3	4693675.1	330.96	-
	un04	3	643639.7	4694117.3	394.52	-
	un05	7	652269.5	4700453.3	306.03	-
	un11	3	643982.7	4699491.0	401.09	-
	un12	2	644240.8	4699753.6	401.09	46,152.96
	un13	7	645100.8	4694078.3	258.78	-
	un28	7	644296.6	4694614.6	350.39	-

Table A.1. Description and general characteristics of the forest plots. XY coordinates in ETRS89 / UTM zone 30N (EPSG: 25830). Part 3 of 3.

Sector	Plot name	FT	Plot center		UAV points/m^2 density	HMLS points/m^2 density
			X	Y		
Villarluengo	vi14	3	727270.3	4511291.6	286.69	49,447.92
	vi15	2	727036.2	4511166.4	344.58	35,912.14
	vi16	2	727080.8	4511157.8	344.58	47,463.93
	vi17	2	726201.4	4503645.7	520.54	26,659.39
	vi18	2	726118.3	4503470.2	520.54	42,036.27
	vi19	2	726672.8	4503511.0	737.29	17,187.46
	vi20	2	726746.0	4503541.1	737.29	18,689.68
	vi27	7	725543.4	4507042.2	386.36	-
	vi29	2	725332.8	4506874.6	426.13	31,546.16
	vi30	3	725369.2	4506806.6	426.13	43,004.04
	vi36	7	738378.0	4510231.1	425.54	-
	vi37	2	738317.9	4510185.8	425.54	-
	vi38	3	726062.4	4509797.7	570.69	50,681.73
	vi39	3	725818.5	4509536.0	441.26	36,774.11
	vi40	3	725846.4	4509684.0	441.26	32,018.89
	vi41	7	726150.4	4509715.6	570.69	68,006.40
Zuera	zu30	2	674321.2	4636134.8	448.03	47,760.41
	zu31	2	674042.8	4636569.9	458.81	77,218.45
	zu32	5	673137.1	4637107.1	478.08	23,244.28
	zu35	7	671227.6	4642052.5	903.85	-
	zu38 *	4	674071.5	4639208.6	822.62	21,633.29
	zu201	4	675701.7	4640029.0	305.40	49,040.58
	zu202	4	675677.7	4640049.3	305.40	85,760.62

* Plot of 10 m circular radius due to terrain constraints.

Table A.2. Number of pairs of Prometheus fuel types able to differentiate (value 1 means Dunn's test, $p \leq 0.05$) by the UAV variables. Part 1 of 4.

Variable	FT2 – FT3	FT2 – FT4	FT2 – FT5	FT2 – FT6	FT2 – FT7	FT3 – FT4	FT3 – FT5	FT3 – FT6	FT3 – FT7	FT4 – FT5	FT4 – FT6	FT4 – FT7	FT5 – FT6	FT5 – FT7	FT6 – FT7	Total pairs
Elev.strata..above.4.00..stddev			1	1	1		1	1	1	1	1	1				**9**
Elev.CV			1	1	1		1		1	1			1	1		**8**
Elev.L.kurtosis	1	1		1	1		1			1			1	1		**8**
Elev.P90			1	1	1		1		1	1	1	1				**8**
Elev.P95			1	1	1		1		1	1	1	1				**8**
Elev.P99			1	1	1		1		1	1	1	1				**8**
Elev.strata..above.4.00..mean			1	1	1		1		1	1	1	1				**8**
Elev.strata..above.4.00..mode			1	1	1		1	1	1	1		1				**8**
Elev.strata..above.4.00..median			1	1	1		1		1	1	1	1				**8**
Elev.maximum			1	1	1		1			1	1	1				**7**
Elev.stddev			1	1	1			1	1		1	1				**7**
Elev.variance			1	1	1			1	1		1	1				**7**
Elev.L2			1	1	1			1	1		1	1				**7**
Elev.L3			1	1	1		1	1	1	1						**7**
Elev.L.CV			1		1		1		1	1			1	1		**7**
Elev.P10			1	1	1		1		1	1			1			**7**
Elev.P20			1	1	1		1		1	1			1			**7**
Elev.P40			1	1	1		1	1	1	1						**7**
Elev.P70			1	1	1		1		1	1		1				**7**
Elev.P75			1	1	1		1		1	1		1				**7**
Elev.P80			1	1	1		1		1	1		1				**7**
Elev.SQRT.mean.SQ			1	1	1		1		1	1		1				**7**
Elev.CURT.mean.CUBE			1	1	1		1		1	1		1				**7**
Percentage.all.returns.above.4.00			1	1	1		1			1	1	1				**7**
All.returns.above.4.00			1	1	1		1			1	1	1				**7**
Elev.strata..above.4.00..total.return.count			1	1	1		1			1	1	1				**7**
Elev.strata..above.4.00..return.proportion			1	1	1		1			1	1	1				**7**
Elev.strata..above.4.00..max			1	1	1		1			1	1	1				**7**
Elev.strata..above.4.00..CV			1	1	1			1	1		1	1				**7**

Table A.2. Number of pairs of Prometheus fuel types able to differentiate (value 1 means Dunn's test, $p \leq 0.05$) by the UAV variables. Part 2 of 4.

Variable	FT2 – FT3	FT2 – FT4	FT2 – FT5	FT2 – FT6	FT2 – FT7	FT3 – FT4	FT3 – FT5	FT3 – FT6	FT3 – FT7	FT4 – FT5	FT4 – FT6	FT4 – FT7	FT5 – FT6	FT5 – FT7	FT6 – FT7	Total pairs
Elev.mean			1	1	1		1		1	1						**6**
Elev.kurtosis				1	1		1			1			1	1		**6**
Elev.AAD				1	1			1	1		1	1				**6**
Elev.L1			1	1	1		1		1	1						**6**
Elev.L.skewness			1	1	1		1		1	1						**6**
Elev.P50			1	1	1		1		1	1						**6**
Elev.P60			1	1	1		1		1	1						**6**
Canopy.relief.ratio			1	1	1		1		1	1						**6**
Percentage.first.returns.above.4.00			1	1	1					1	1	1				**6**
All.returns.above.4.00.Total.first.returns.100			1	1	1					1	1	1				**6**
First.returns.above.4.00			1	1	1					1	1	1				**6**
Percentage.all.returns.above.mean			1	1	1		1	1	1							**6**
All.returns.above.mean			1	1	1		1	1	1							**6**
Elev.strata..below.0.60..return.proportion			1	1	1		1		1	1						**6**
Profile.area			1	1	1		1		1	1						**6**
rumple_general			1	1	1			1			1	1				**6**
Elev.mode			1				1			1			1	1		**5**
Elev.IQ				1	1						1	1	1			**5**
Elev.skewness			1	1	1		1			1						**5**
Elev.MAD.median			1	1	1						1	1				**5**
Elev.MAD.mode			1	1	1			1	1							**5**
Elev.L4			1				1			1			1	1		**5**
Elev.P01			1	1	1		1		1							**5**
Elev.P05			1	1	1		1		1							**5**
Elev.P25			1	1	1		1			1						**5**
Elev.P30			1	1	1		1			1						**5**
Elev.strata..below.0.60..total.return.count			1	1	1		1		1							**5**
Elev.strata..below.0.60..max			1				1			1			1	1		**5**
Elev.strata..0.60.to.2.00..total.return.count		1					1			1			1	1		**5**

Table A.2. Number of pairs of Prometheus fuel types able to differentiate (value 1 means Dunn's test, $p \leq 0.05$) by the UAV variables. Part 3 of 4.

Variable	FT2 – FT3	FT2 – FT4	FT2 – FT5	FT2 – FT6	FT2 – FT7	FT3 – FT4	FT3 – FT5	FT3 – FT6	FT3 – FT7	FT4 – FT5	FT4 – FT6	FT4 – FT7	FT5 – FT6	FT5 – FT7	FT6 – FT7	Total pairs
Elev.strata..0.60.to.2.00..return.proportion		1					1			1			1	1		**5**
Elev.strata..0.60.to.2.00..min			1				1			1			1	1		**5**
rumple_0.60_2.00m				1	1			1					1	1		**5**
Percentage.first.returns.above.mean			1	1	1				1							**4**
Percentage.first.returns.above.mode				1	1								1	1		**4**
Percentage.all.returns.above.mode				1	1								1	1		**4**
All.returns.above.mean.Total.first.returns.100			1	1	1				1							**4**
All.returns.above.mode.Total.first.returns.100				1	1								1	1		**4**
First.returns.above.mean			1	1	1			1								**4**
Elev.strata..below.0.60..min							1			1			1	1		**4**
Elev.strata..below.0.60..mean					1					1			1	1		**4**
Elev.strata..below.0.60..stddev					1					1			1	1		**4**
Elev.strata..below.0.60..CV					1					1			1	1		**4**
Elev.strata..2.00.to.4.00..return.proportion	1						1			1				1		**4**
Elev.strata..2.00.to.4.00..min			1				1			1				1		**4**
Elev.strata..2.00.to.4.00..mean			1	1	1					1						**4**
Elev.strata..2.00.to.4.00..median			1	1	1					1						**4**
Elev.strata..2.00.to.4.00..stddev				1	1						1	1				**4**
LHDI		1		1	1									1		**4**
LHEI		1		1	1									1		**4**
rumple_below_0.60m		1								1			1	1		**4**
Elev.strata..below.0.60..skewness			1				1							1		**3**
Elev.strata..0.60.to.2.00..max							1			1				1		**3**
Elev.strata..0.60.to.2.00..mean			1								1		1			**3**
Elev.strata..0.60.to.2.00..median			1								1		1			**3**
Elev.strata..2.00.to.4.00..total.return.count	1						1							1		**3**
Elev.strata..2.00.to.4.00..max	1			1	1											**3**
rumple_above_4.00m	1							1	1							**3**
First.returns.above.mode				1	1											**2**

Table A.2. Number of pairs of Prometheus fuel types able to differentiate (value 1 means Dunn's test, $p \leq 0.05$) by the UAV variables. Part 4 of 4.

Variable	FT2 – FT3	FT2 – FT4	FT2 – FT5	FT2 – FT6	FT2 – FT7	FT3 – FT4	FT3 – FT5	FT3 – FT6	FT3 – FT7	FT4 – FT5	FT4 – FT6	FT4 – FT7	FT5 – FT6	FT5 – FT7	FT6 – FT7	Total pairs
Elev.strata..below.0.60..median													1	1		**2**
Elev.strata..0.60.to.2.00..mode													1	1		**2**
Elev.strata..0.60.to.2.00..CV													1	1		**2**
Elev.strata..0.60.to.2.00..skewness											1		1			**2**
Elev.strata..2.00.to.4.00..CV				1	1											**2**
Elev.strata..above.4.00..skewness	1						1									**2**
Elev.strata..above.4.00..kurtosis	1		1													**2**
rumple_2.00_4.00m						1	1									**2**
Elev.strata..below.0.60..mode													1			**1**
Elev.strata..0.60.to.2.00..stddev							1									**1**
Elev.strata..2.00.to.4.00..mode			1													**1**
Elev.strata..2.00.to.4.00..skewness										1						**1**
Elev.strata..above.4.00..min			1													**1**
Total.first.returns																**0**
Total.all.returns																**0**
Elev.strata..below.0.60..kurtosis																**0**
Elev.strata..0.60.to.2.00..kurtosis																**0**
Elev.strata..2.00.to.4.00..kurtosis																**0**
Total variables	**7**	**6**	**69**	**71**	**75**	**1**	**61**	**17**	**41**	**61**	**28**	**32**	**31**	**31**	**0**	

Table A.3. Confusion matrix of the SVM-L classification model of the UAV data.

Fuel types		**Predicted**						**Prod.'s accuracy**
		FT2	**FT3**	**FT4**	**FT5**	**FT6**	**FT7**	
Actual	**FT2**	**109**	20	0	0	0	0	84.50%
	FT3	1	**40**	0	19	0	1	65.57%
	FT4	0	0	**50**	0	0	0	100%
	FT5	0	0	0	**121**	0	11	91.67%
	FT6	0	0	0	0	**0**	0	0%
	FT7	0	10	0	0	120	**228**	63.69%
User's accuracy		99.09%	57.14%	100%	86.43%	0%	95.00%	

Table A.4. F-score (F) coefficient for each fuel type of the SVM-L classification model of the UAV data.

	FT2	**FT3**	**FT4**	**FT5**	**FT6**	**FT7**
F	0.91	0.61	1.00	0.89	0.00	0.76

Table A.5. Confusion matrix of the SVM-R classification model of the UAV data.

Fuel types		Predicted						Prod.'s accuracy
		FT2	**FT3**	**FT4**	**FT5**	**FT6**	**FT7**	
Actual	**FT2**	**101**	28	0	0	0	0	78.29%
	FT3	9	**32**	0	10	0	2	60.38%
	FT4	0	0	**41**	0	0	2	95.35%
	FT5	0	0	0	**118**	0	10	92.19%
	FT6	0	0	0	0	**97**	46	67.83%
	FT7	0	10	9	12	23	**180**	76.92%
User's accuracy		91.82%	45.71%	82.00%	84.29%	80.83%	75.00%	

Table A.6. F-score (F) coefficient for each fuel type of the SVM-R classification model of the UAV data.

	FT2	**FT3**	**FT4**	**FT5**	**FT6**	**FT7**
F	0.85	0.52	0.88	0.88	0.74	0.76

Table A.7. Confusion matrix of the SVM-L classification model of the UAV-HMLS data

Fuel types		Predicted						Prod.'s accuracy
		FT2	**FT3**	**FT4**	**FT5**	**FT6**	**FT7**	
Actual	**FT2**	**90**	10	0	0	0	0	90.00%
	FT3	10	**40**	10	10	0	1	56.34%
	FT4	0	0	**40**	0	0	9	81.63%
	FT5	0	0	0	**80**	0	0	100%
	FT6	0	0	0	0	**60**	18	76.92%
	FT7	0	0	0	0	10	**42**	80.77%
User's accuracy		90.00%	80.00%	80.00%	88.89%	85.71%	60.00%	

Table A.8. F-score (F) coefficient for each fuel type of the SVM-L classification model of the UAV-HMLS data.

	FT2	**FT3**	**FT4**	**FT5**	**FT6**	**FT7**
F	0.90	0.66	0.81	0.94	0.81	0.69

Table A.9. Confusion matrix of the SVM-R classification model of the UAV-HMLS data

Fuel types		Predicted						Prod.'s accuracy
		FT2	**FT3**	**FT4**	**FT5**	**FT6**	**FT7**	
Actual	**FT2**	**90**	10	0	0	0	0	90.00%
	FT3	10	**40**	9	0	0	2	65.57%
	FT4	0	0	**41**	0	0	8	83.67%
	FT5	0	0	0	**90**	0	0	100%
	FT6	0	0	0	0	**60**	9	86.96%
	FT7	0	0	0	0	10	**51**	83.61%
User's accuracy		90.00%	80.00%	82.00%	100%	85.71%	72.86%	

Table A.10. F-score (F) coefficient for each fuel type of the SVM-R classification model of the UAV-HMLS data.

	FT2	**FT3**	**FT4**	**FT5**	**FT6**	**FT7**
F	0.90	0.72	0.83	1.00	0.86	0.78

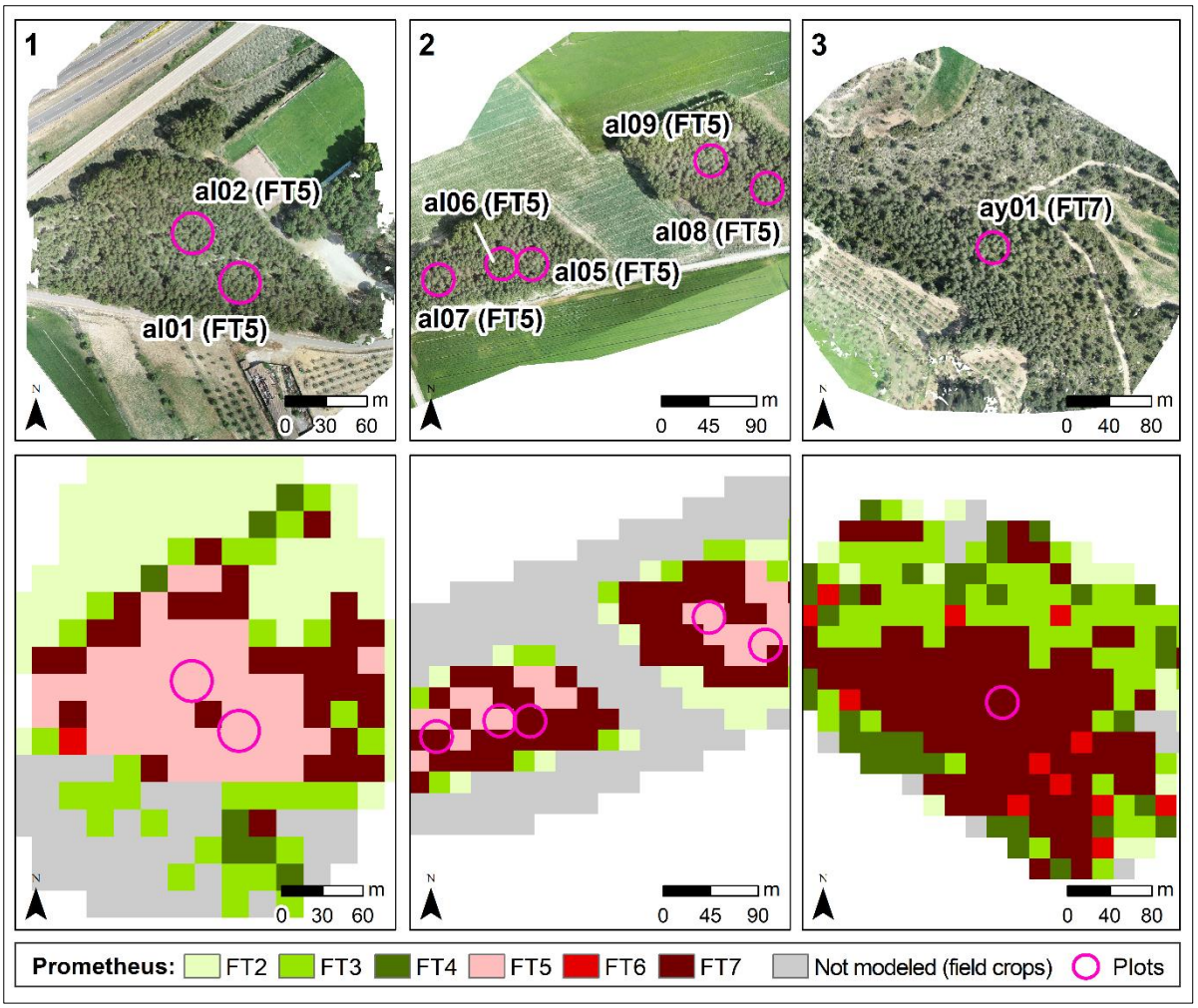

Figure A.1. Mapping of Prometheus fuel types from the best classification model (RF) of the UAV data at 20 m spatial resolution. (1) Plots "al01" and "al02". (2) Plots "al05", "al06", "al07", "al08", and "al09". (3) Plot "ay01".

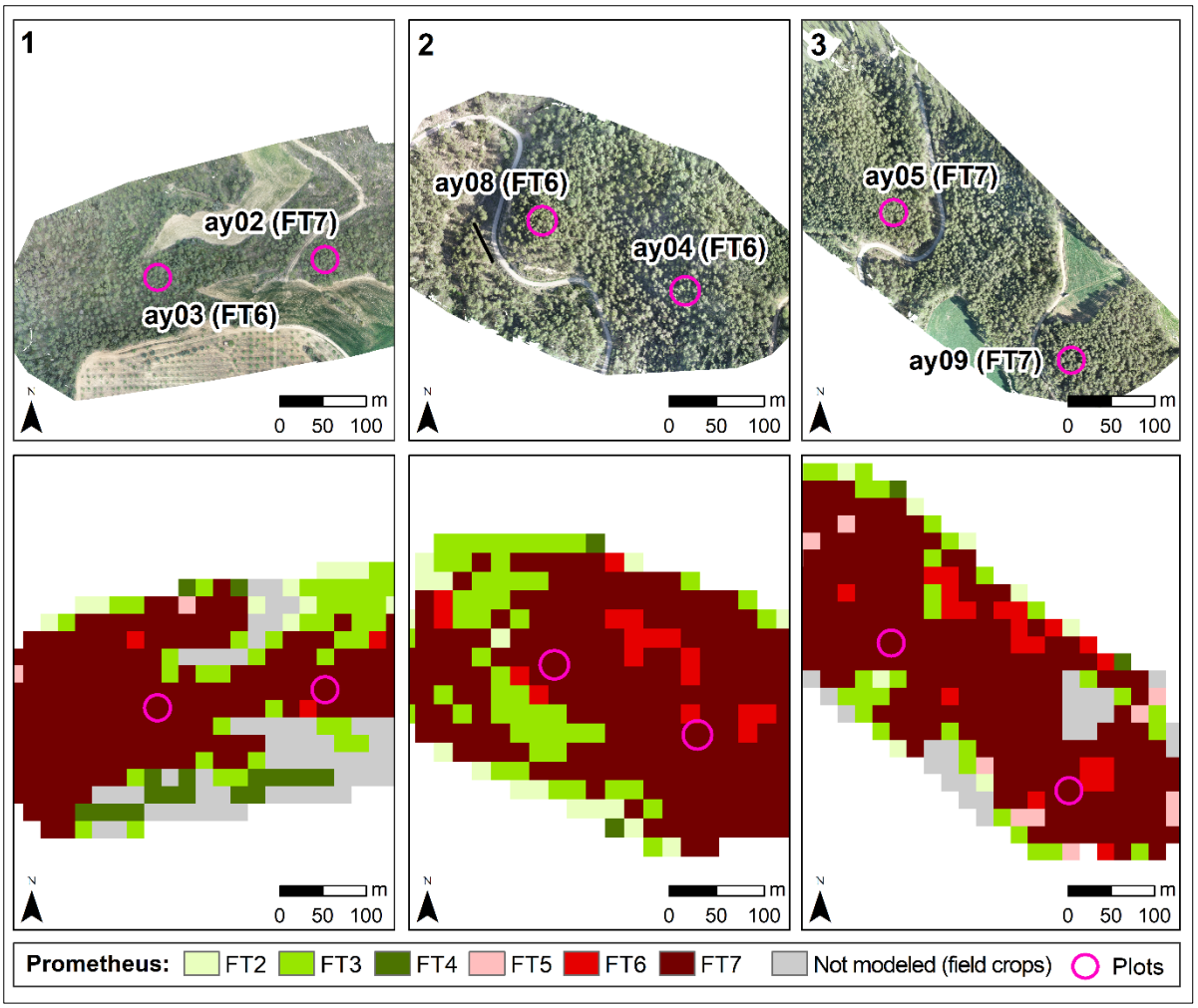

Figure A.2. Mapping of Prometheus fuel types from the best classification model (RF) of the UAV data at 20 m spatial resolution. (1) Plots "ay02" and "ay03". (2) Plots "ay04" and "ay08". (3) Plots "ay05" and "ay09".

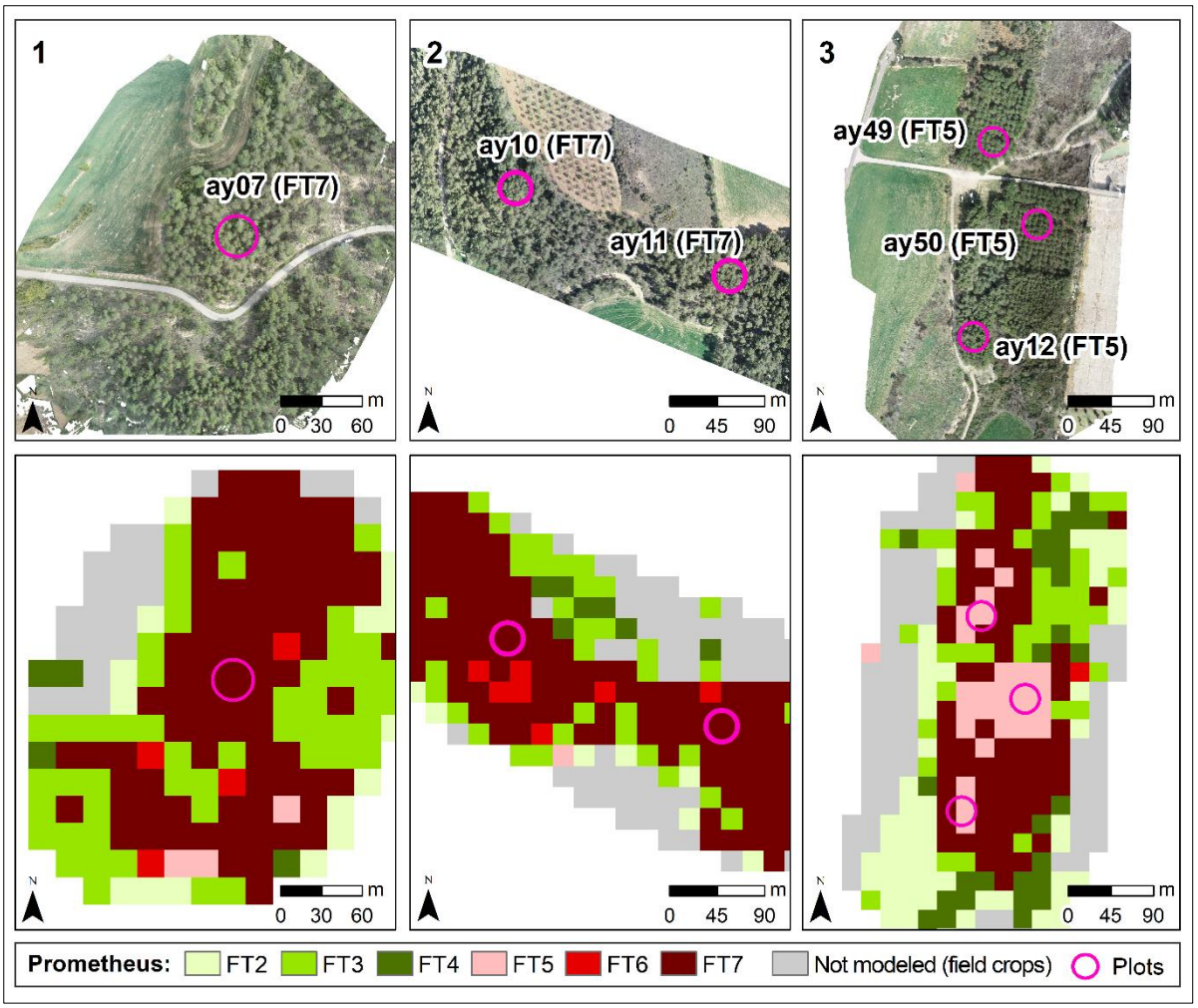

Figure A.3. Mapping of Prometheus fuel types from the best classification model (RF) of the UAV data at 20 m spatial resolution. (1) Plot "ay07". (2) Plots "ay10" and "ay11". (3) Plots "ay12", "ay49", and "ay50".

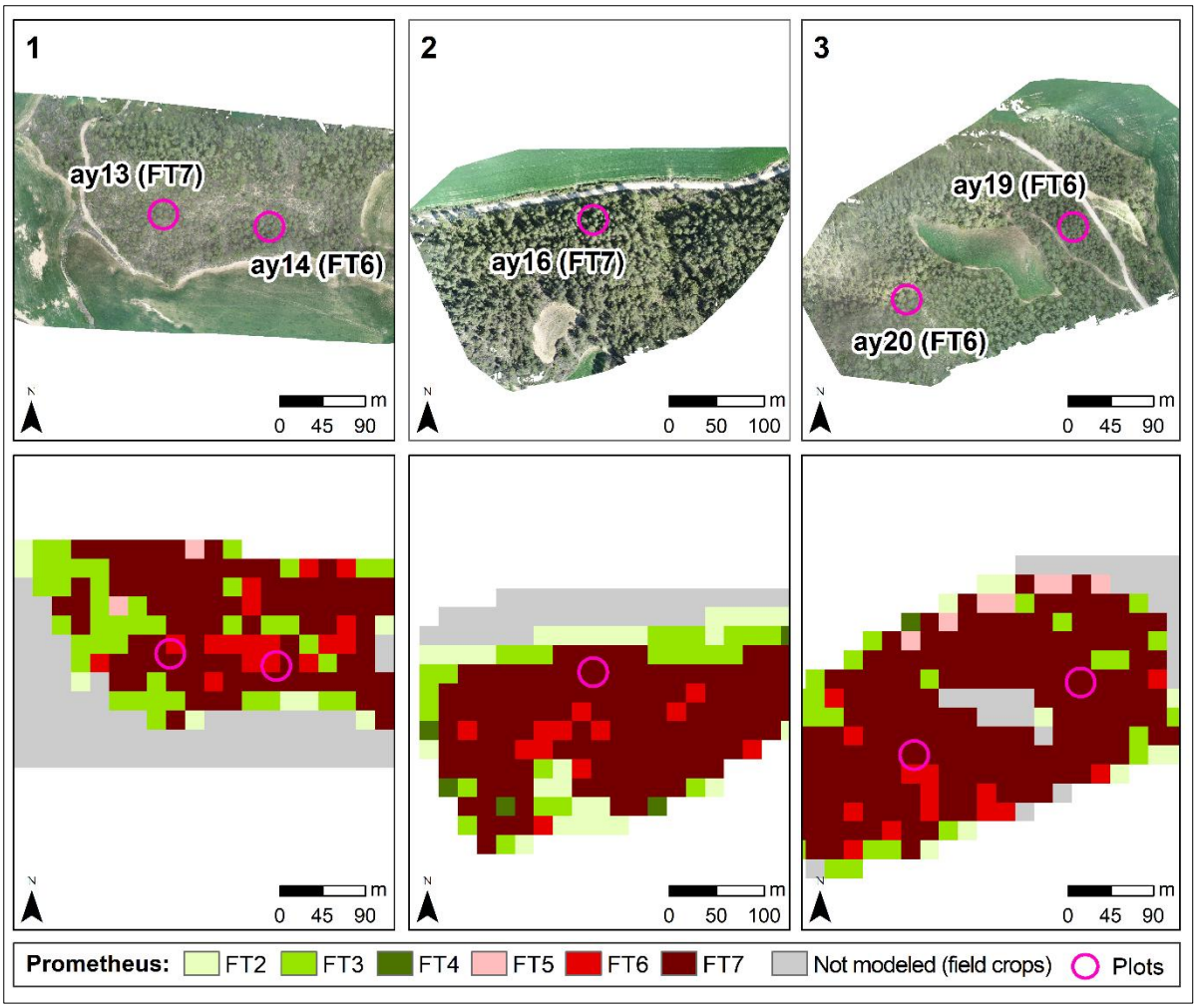

Figure A.4. Mapping of Prometheus fuel types from the best classification model (RF) of the UAV data at 20 m spatial resolution. (1) Plots "ay13" and "ay14". (2) Plot "ay16". (3) Plots "ay19" and "ay20".

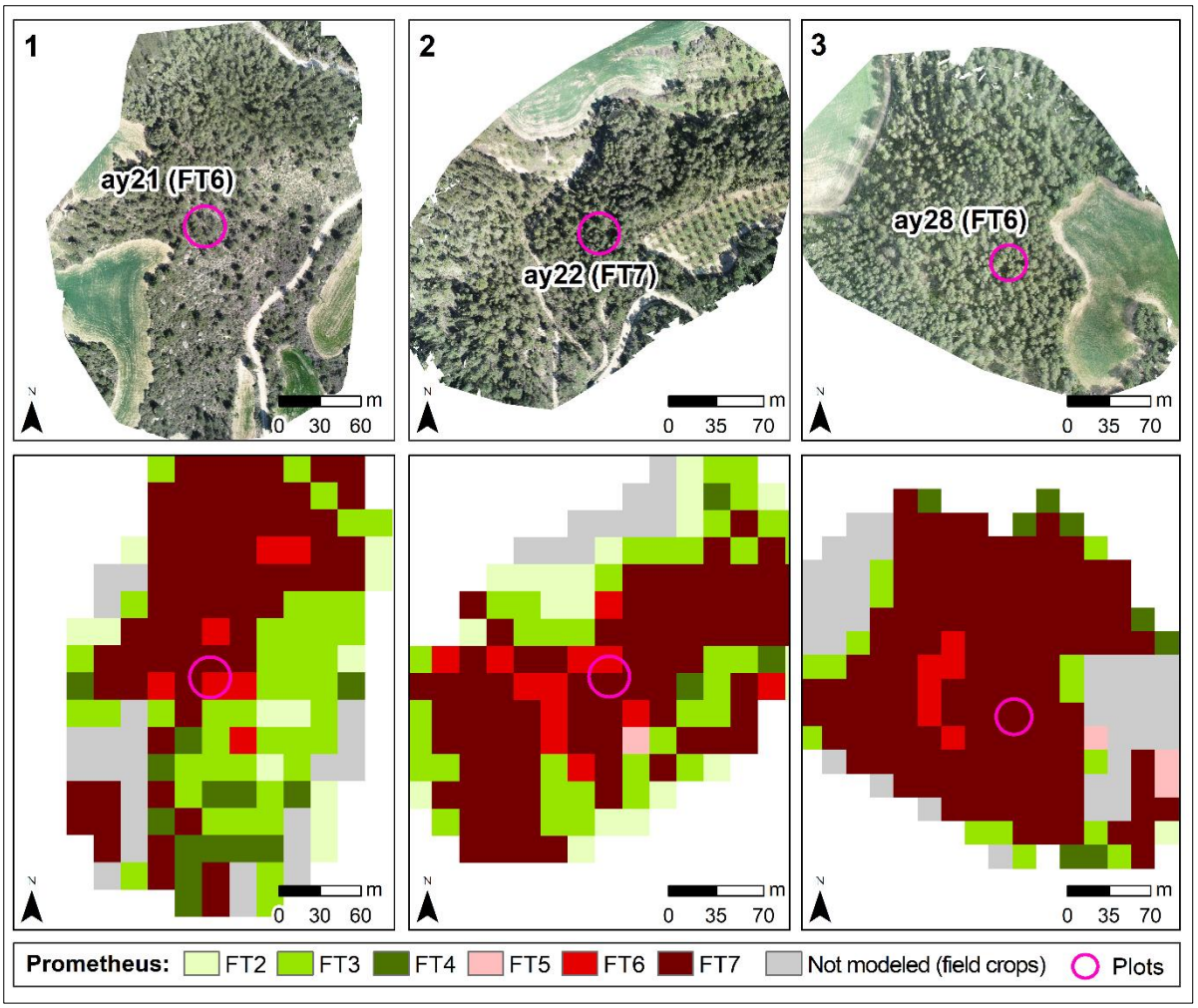

Figure A.5. Mapping of Prometheus fuel types from the best classification model (RF) of the UAV data at 20 m spatial resolution. (1) Plot "ay21". (2) Plot "ay22". (3) Plot "ay28".

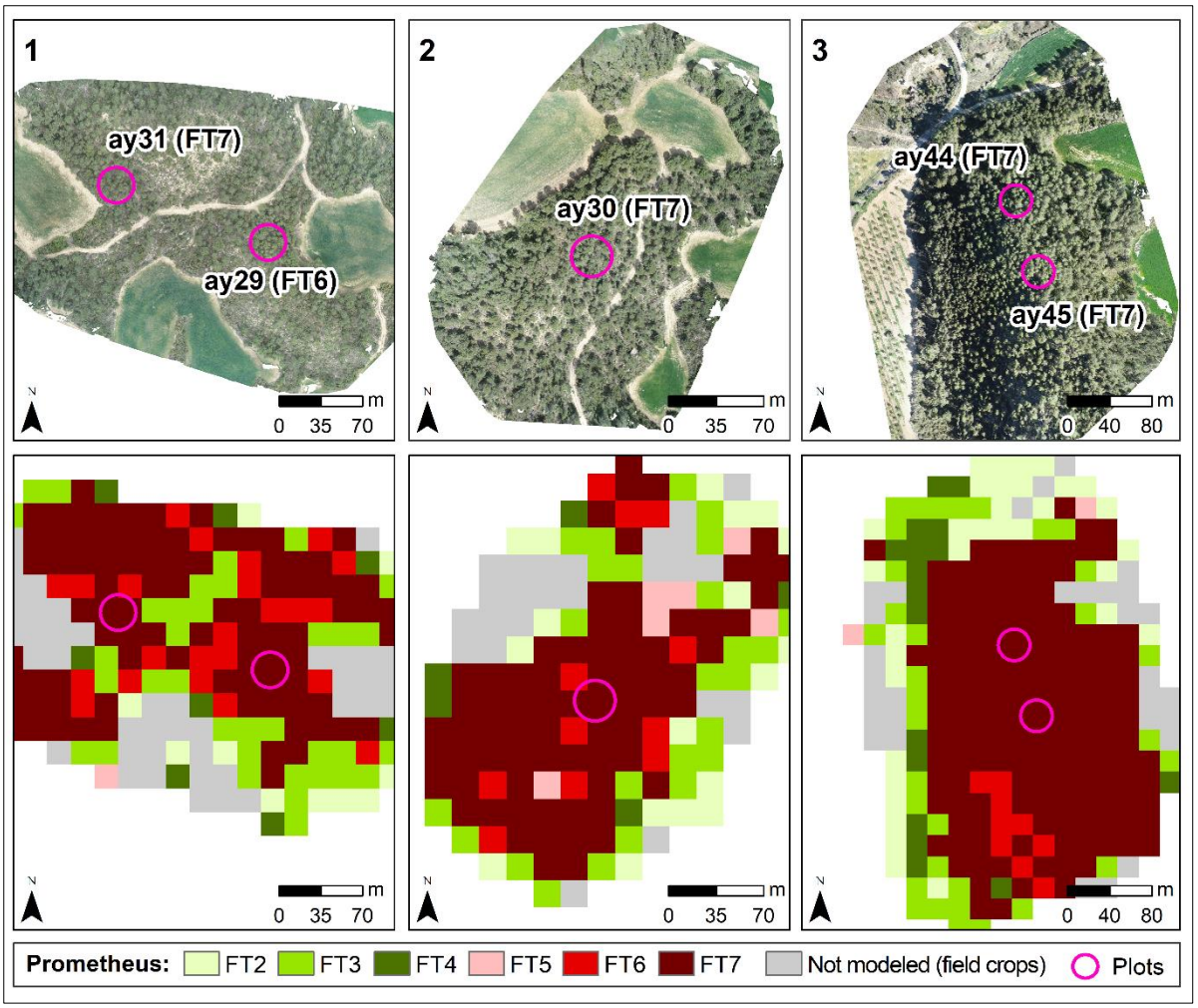

Figure A.6. Mapping of Prometheus fuel types from the best classification model (RF) of the UAV data at 20 m spatial resolution. (1) Plots "ay29" and "ay31". (2) Plot "ay30". (3) Plots "ay44" and "ay45".

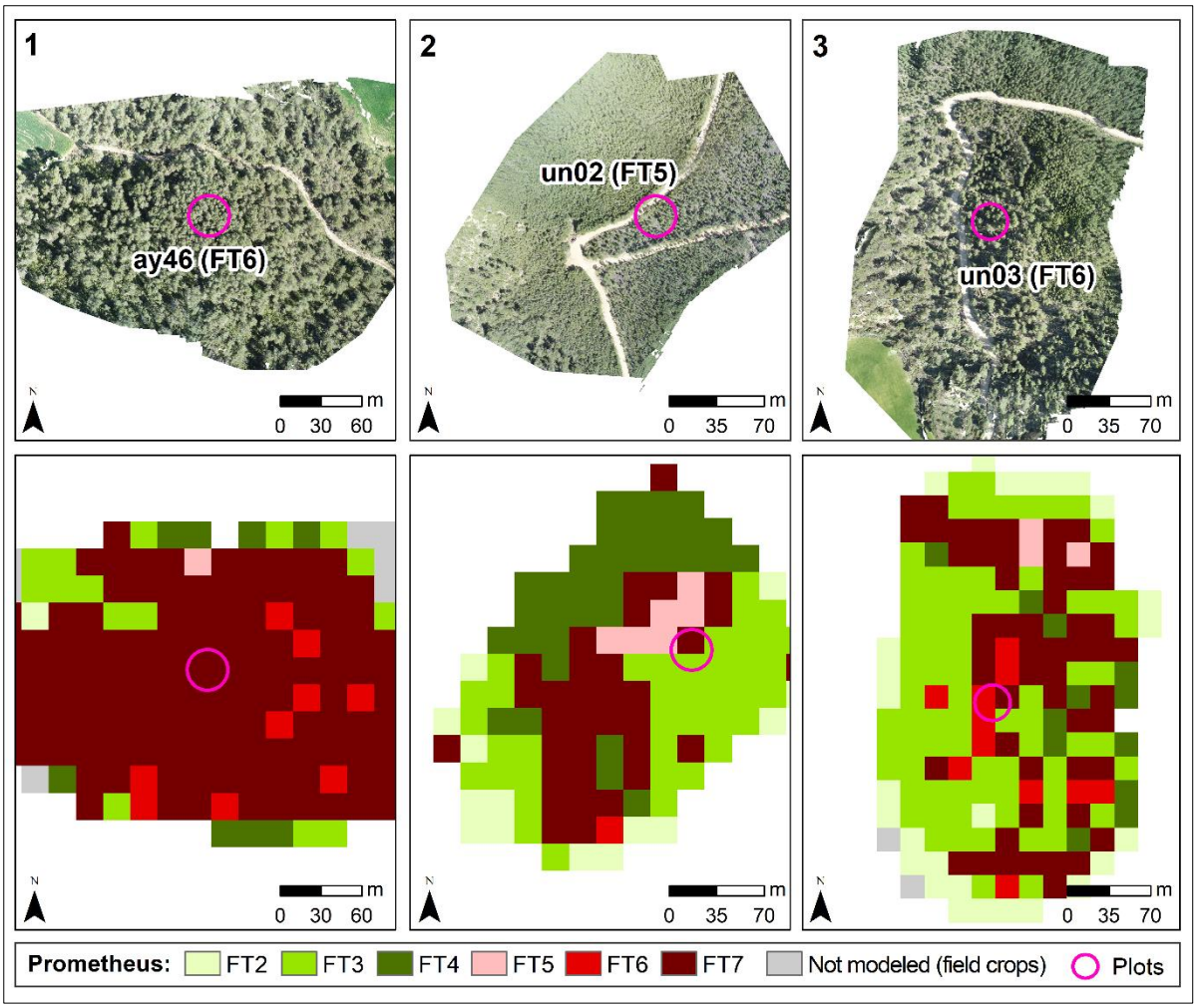

Figure A.7. Mapping of Prometheus fuel types from the best classification model (RF) of the UAV data at 20 m spatial resolution. (1) Plot "ay46". (2) Plot "un02". (3) Plot "un03".

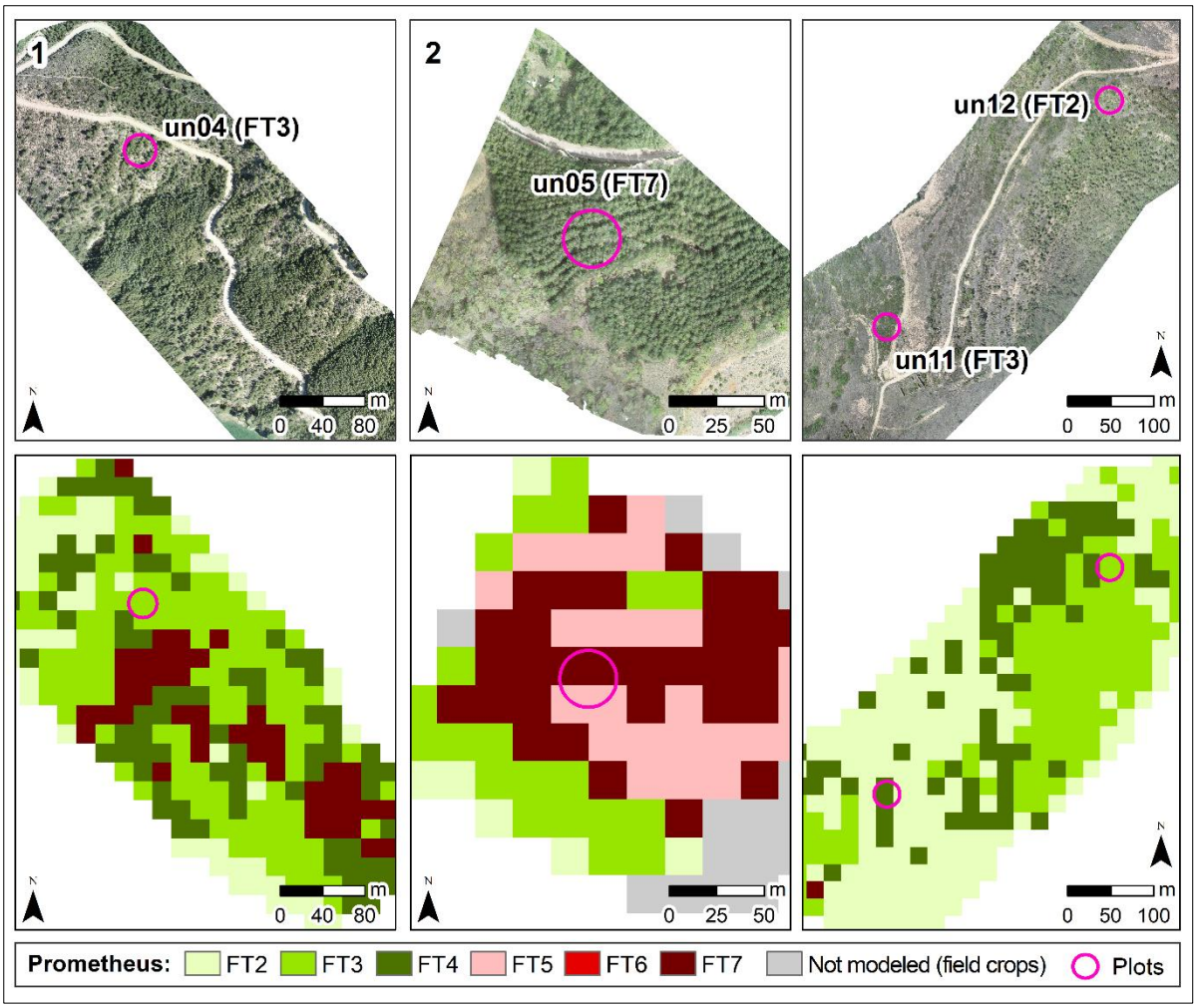

Figure A.8. Mapping of Prometheus fuel types from the best classification model (RF) of the UAV data at 20 m spatial resolution. (1) Plot "un04". (2) Plot "un05". (3) Plots "un11" and "un12".

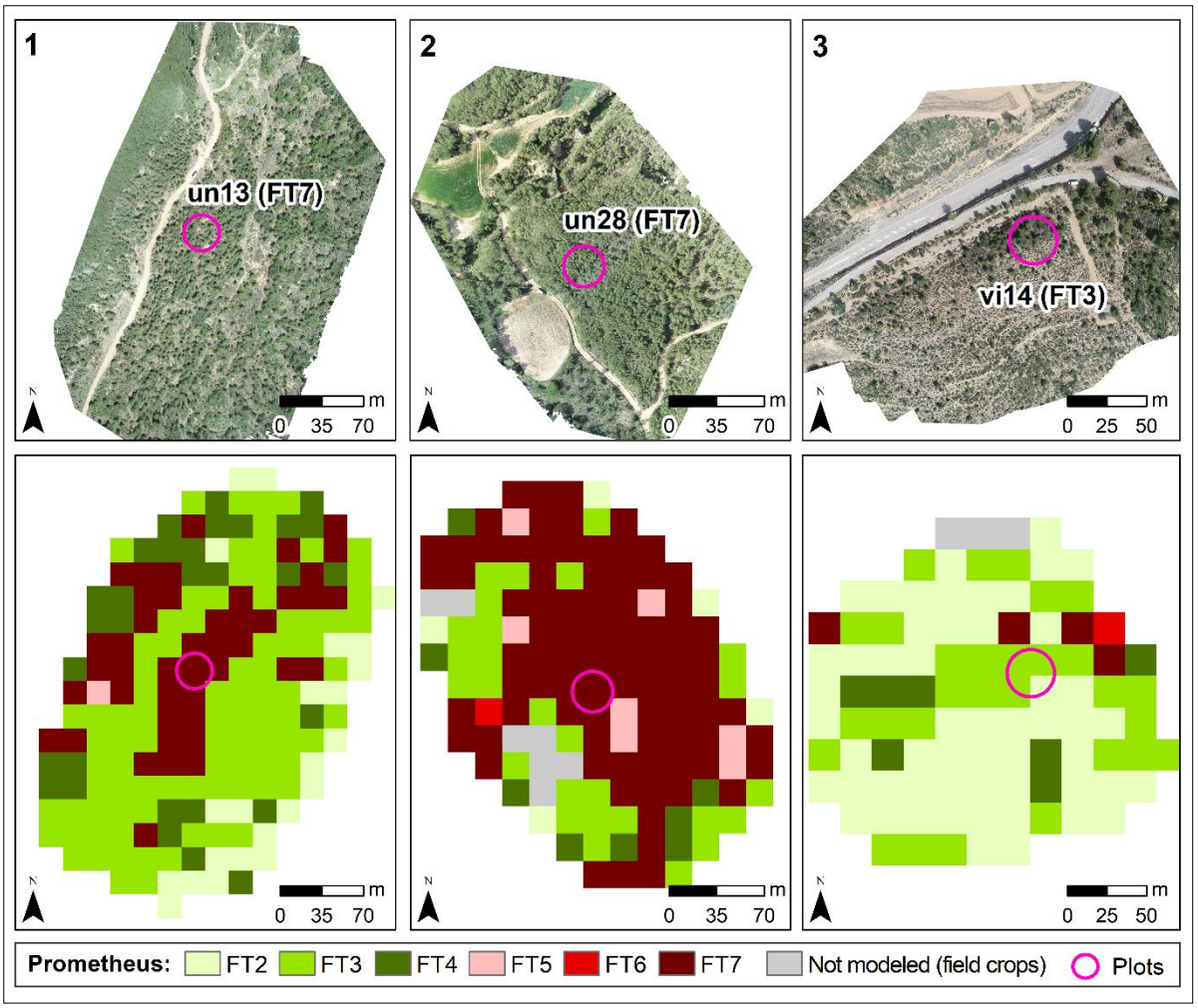

Figure A.9. Mapping of Prometheus fuel types from the best classification model (RF) of the UAV data at 20 m spatial resolution. (1) Plot "un13". (2) Plot "un28". (3) Plot "vi14".

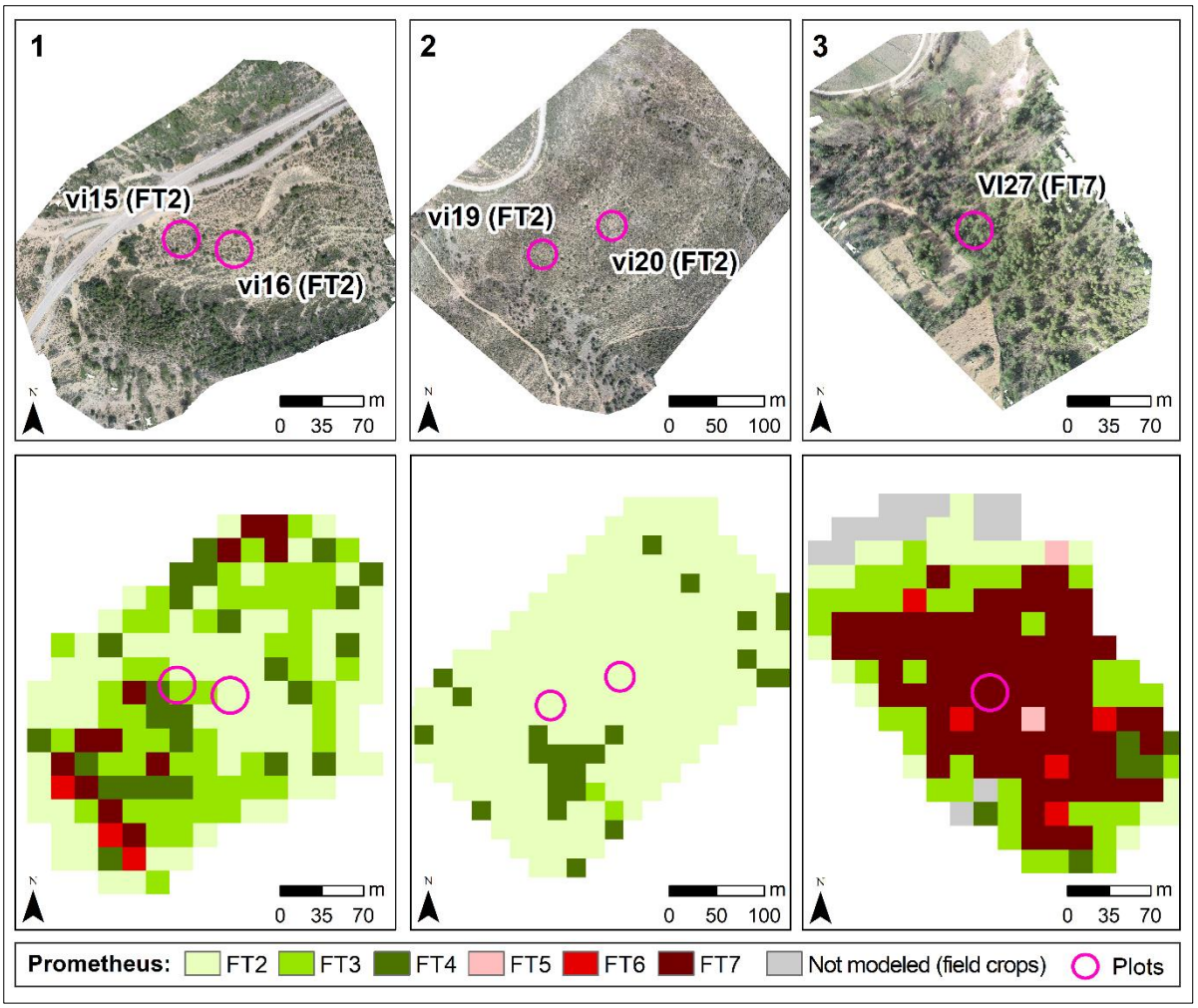

Figure A.10. Mapping of Prometheus fuel types from the best classification model (RF) of the UAV data at 20 m spatial resolution. (1) Plots "vi15" and "vi16". (2) Plots "vi19" and "vi20". (3) Plot "vi27".

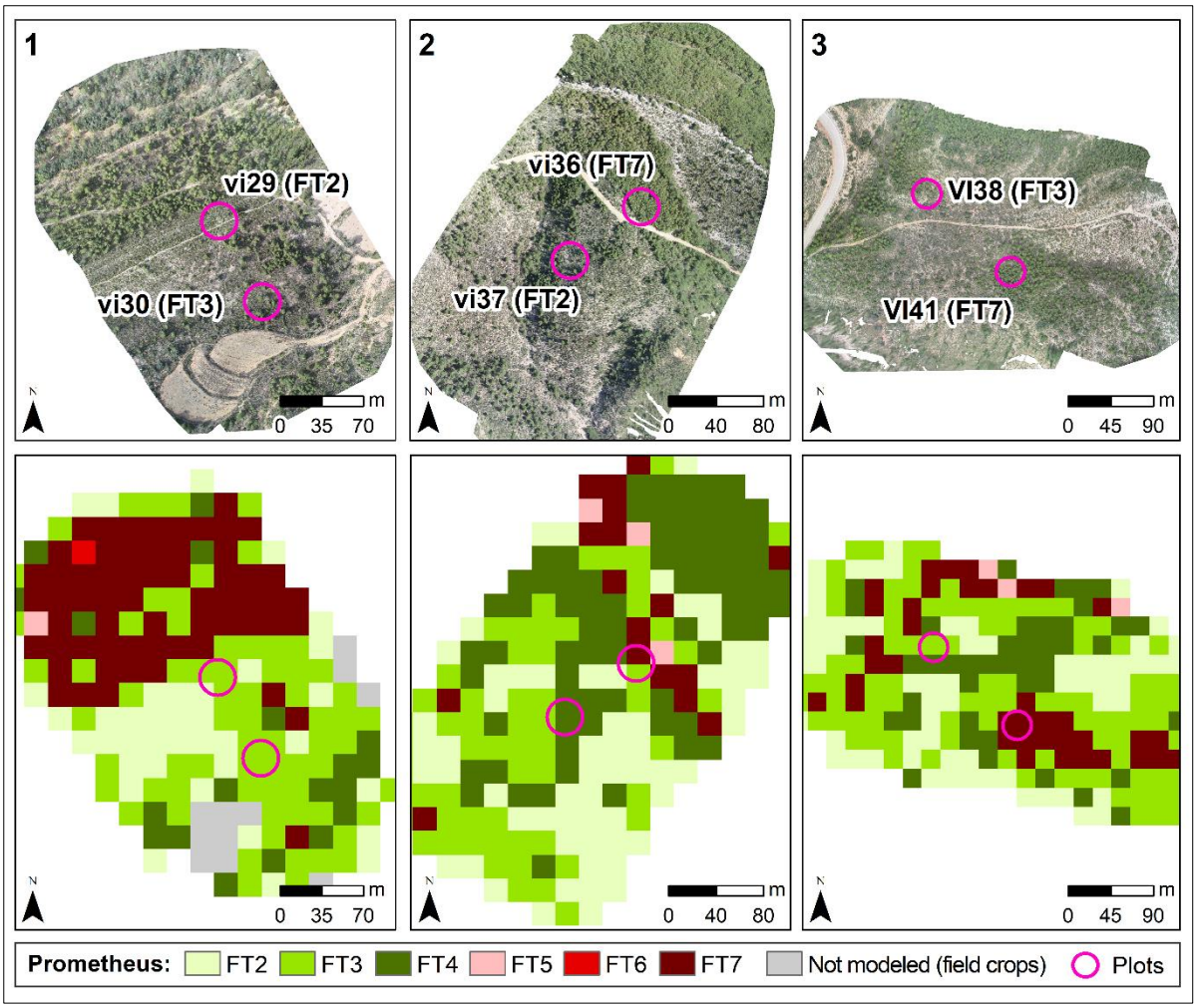

Figure A.11. Mapping of Prometheus fuel types from the best classification model (RF) of the UAV data at 20 m spatial resolution. (1) Plots "vi29" and "vi30". (2) Plots "vi36" and "vi37". (3) Plots "vi38" and "vi41".

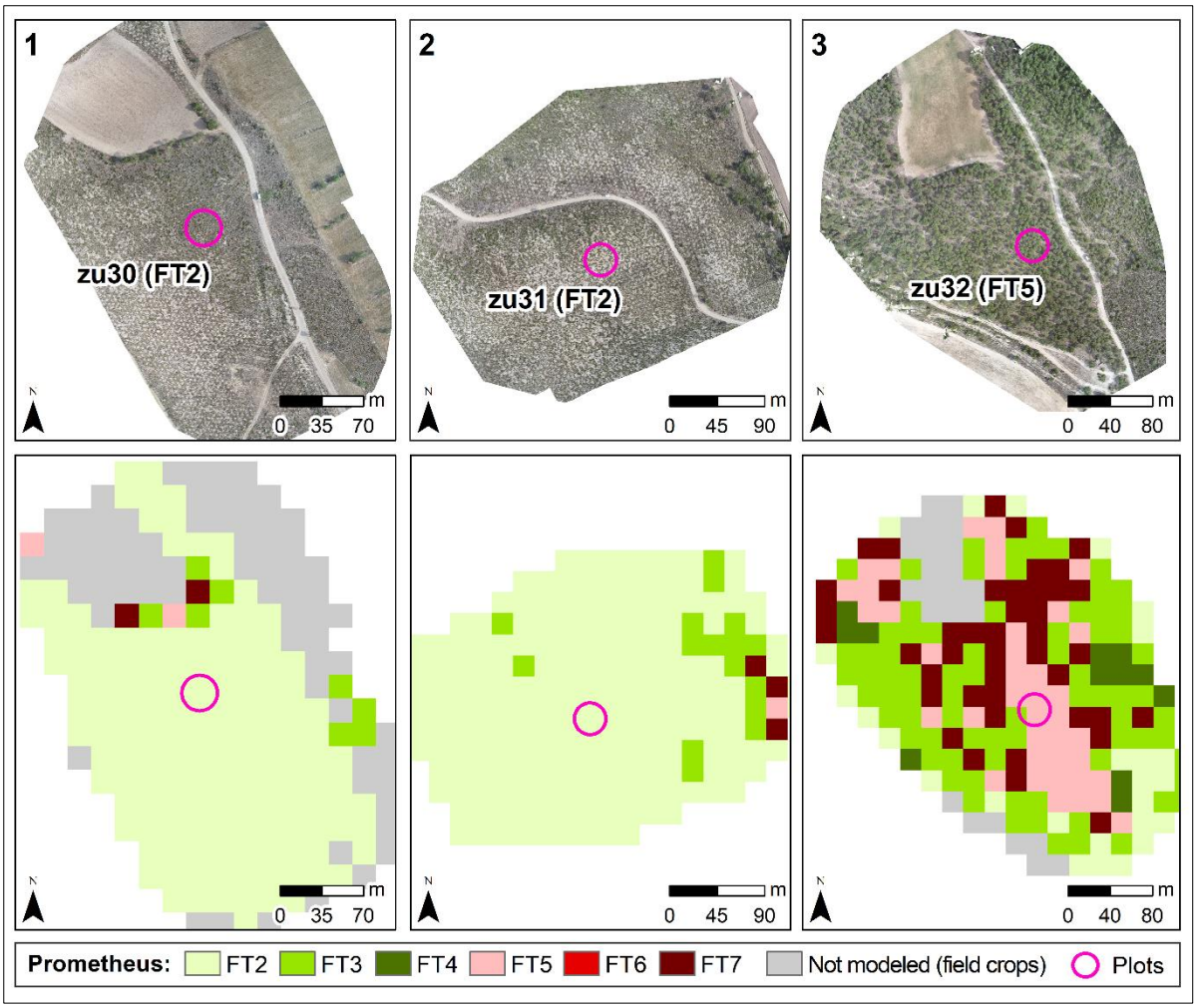

Figure A.12. Mapping of Prometheus fuel types from the best classification model (RF) of the UAV data at 20 m spatial resolution. (1) Plot "zu30". (2) Plot "zu31". (3) Plot "zu32".

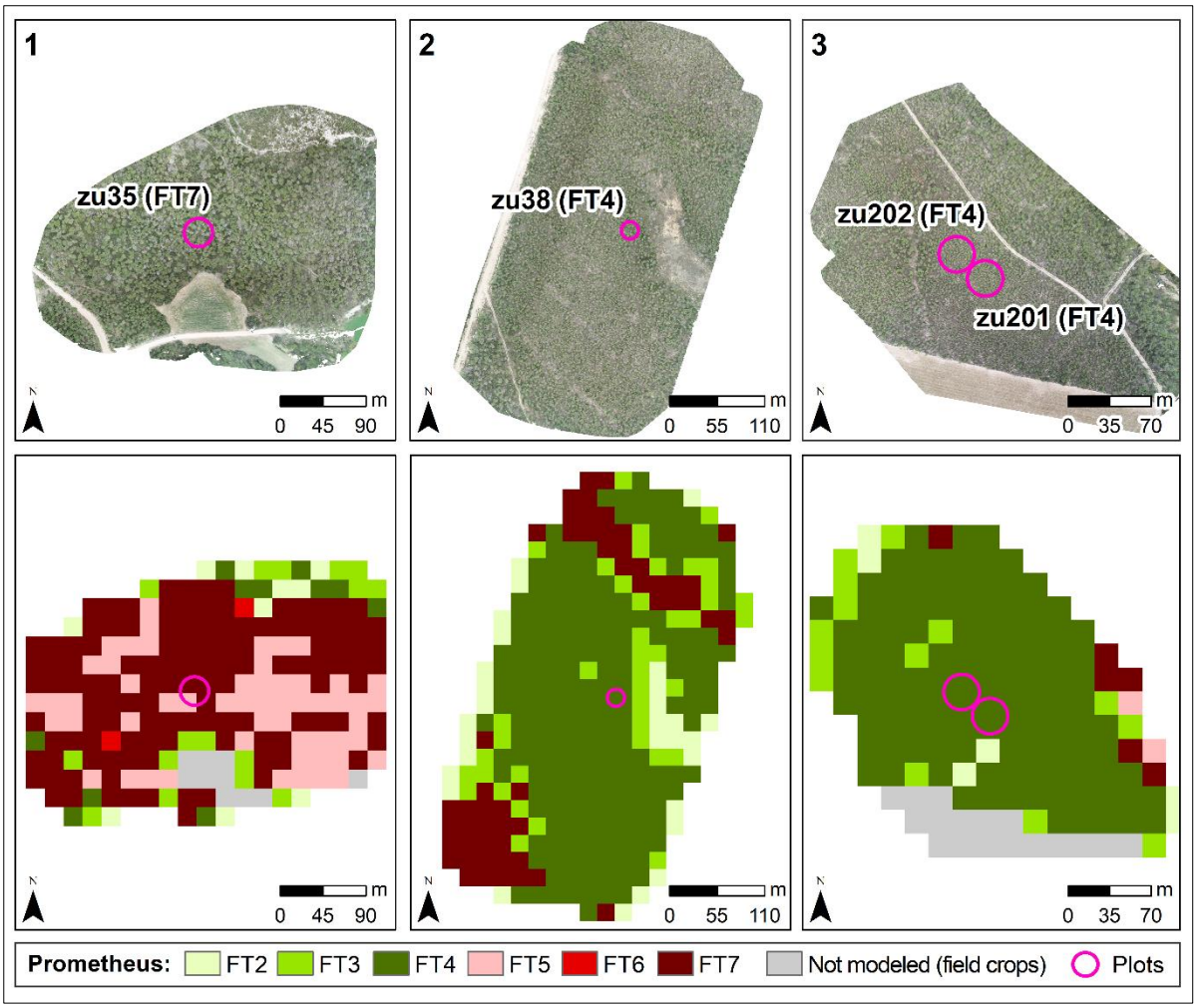

Figure A.13. Mapping of Prometheus fuel types from the best classification model (RF) of the UAV data at 20 m spatial resolution. (1) Plot "zu35". (2) Plot "zu38". (3) Plots "zu201" and "zu202".

CHAPTER 7

CAPABILITIES OF 3D REMOTE SENSING SYSTEMS FOR IMPROVED FUEL ESTIMATION

This chapter aims to provide a comprehensive discussion of the results obtained from the four remote sensing systems evaluated in the present PhD Thesis. Additionally, it incorporates systems that, while not directly assessed in the thesis, are highly relevant for enhancing forest fuel estimation. These include both commercial and non-commercial ALS systems, TLS systems, and the emerging ICESat-2/ATLAS SLS system. The discussion features a semi-quantitative analysis of different functionalities of each system, as mentioned in Section 2.8, focusing on three main components: intrinsic characteristics of the systems, data processing and analysis capabilities, and accuracy in estimating fuel types. Each functionality has been evaluated using a rating scale from 0 to 3, where 0 indicates a non-existent functionality, and 1, 2, and 3 represent low, medium, and high capacity functionalities of the assessed systems, respectively. It is important to note that the assessments have been conducted with consideration of the actual scale of forest fuel management work.

7.1. INTRINSIC CHARACTERISTICS OF THE SYSTEMS

The results of the analysis of the intrinsic characteristics of each system are presented in Table 7.1. The optical UAV has received the highest score (13) followed by non-commercial ALS systems and the UAV-LiDAR system (12), commercial ALS, HMLS and TLS systems (11), the ICESat-2/ATLAS SLS system (9), and the GEDI SLS system (6).

Table 7.1. Scores by functionalities of the intrinsic characteristics of the systems for effective forest fuel estimation.

Intrinsic characteristics of the systems	**SLS**		**ALS**		**UAVs**		**Ground-based**	
	GEDI	***ICESat2***	**Non-comm.**	**Comm.**	**Optical**	**LiDAR**	**HMLS**	**TLS**
Sampling density	1	1	2	3	3	3	3	3
Temporal resolution	0	2	1	2	3	3	3	3
Low economic cost	3	3	3	1	2	1	1	1
Spatial coverage	1	1	3	2	2	2	1	1
Accuracy of 3D location	1	2	3	3	3	3	3	3
Total	**6**	**9**	**12**	**11**	**13**	**12**	**11**	**11**

Sampling density

Sampling density refers to the number of points, pulses, or footprints recorded by the system per unit area. A higher sampling density provides more data and, consequently, greater detail of the recorded area. In this functionality, UAVs, ground-based laser scanner systems, and commercial ALS systems have received the highest ratings. Non-commercial ALS systems have obtained a medium score while SLS systems have obtained the lowest score.

UAVs typically produce highly dense three-dimensional point clouds. In this PhD Thesis, the optical UAV generated an average of 3,000 p/m^2 with a *SONY-WX* high-resoltution RGB camera, while the UAV-LiDAR system produced an average of 452 p/m^2 with the *DJI Zenmuse L1* sensor. However, the points generated by the optical UAV did not capture areas beneath the forest canopy, as these data were derived from two-dimensional zenithal images processed using the SFM photogrammetric technique. Therefore, although the optical UAV's point cloud density was higher, the UAV-LiDAR system offered the advantage of laser penetration through the forest canopy, allowing for the recording of vegetation within the forest and even the ground. Nevertheless, UAVs offer flexibility in adjusting the density of the point cloud. Thus, if desired, users can achieve higher point densities by adjusting flight parameters when obtaining the data, such as flight altitude, overlap between photographs, or flight paths and viewing angles (e.g., Domingo *et al*., 2019b; Crespo-Peremarch *et al*., 2020; Santos Santana *et al*., 2021; Lopes Bento *et al*., 2022; Swayze *et al*., 2022). Adjusting these parameters could enhance the sampling density and, subsequently, the accuracy of the final results.

On the other hand, the HMLS system used in this thesis produced three-dimensional point clouds with an exceptionally high density (63,148 p/m^2), similar to findings from previous studies using TLS systems (e.g., Crespo-Peremarch *et al*., 2020; Hillman *et al*., 2021; Wagers *et al*., 2021; Prendes *et al*., 2022; Torralba *et al*., 2022). Such density offered a highly detailed representation of the recorded forest area which enabled the delineation of the fuel types in structurally complex forest stands. Most ground-based laser scanner systems are equipped with high-precision sensors and high scanning frequencies, capable of covering distances of several hundred meters. TLS systems include the *Trimble TX8* (Crespo-Peremarch *et al*., 2020; Hillman *et al*., 2021), *Leica C10* (Wilson *et al*., 2021; Wagers *et al*., 2021); *RIEGL VZ-400i* (Klauberg *et al*., 2024; Tienaho *et al*., 2024), and *FARO Focus* (Alonso-Rego *et al*., 2020; Wallace *et al*., 2022), all of which can scan approximately 1 million points per second on average. HMLS systems primarily feature *GeoSLAM* sensors

(Bauwens *et al*., 2016; Del Perugia *et al*., 2019; Gollob *et al*., 2020; Forbes *et al*., 2022; Coskuner *et al*., 2023; Vatandaşlar *et al*., 2023), capable of scanning up to 300,000 points per second.

In the case of ALS, commercial systems typically produce medium-to-high dense point clouds, often exceeding 10 p/m^2 (e.g., Crespo-Peremarch *et al*., 2020; Donager *et al*., 2021b) and 40 p/m^2 (e.g., Guerra-Hernández *et al*., 2018), although Dai *et al.* (2019) reached up to 450 p/m^2 using a *RIEGL VQ-480-U* sensor. In contrast, non-commercial ALS systems, used for regional/national coverage, typically exhibit medium-to-low point densities. For example, Spain's first ALS national coverage (2008-2015) had an average density of 0.5 p/m^2, the second (2015-2022) increased to 1 p/m^2, and the third, which began in 2023, has an average density of 5 p/m^2 (ALS-PNOA: https://pnoa.ign.es/). Other countries fully covered with non-commercial ALS systems and freely available data are Denmark (4–5 p/m^2, https://gst.dk/), Estonia (2.1 p/m^2 in non-urban areas, https://geoportaal.maaamet.ee/), Finland (0.5–5 p/m^2, https://www.maanmittauslaitos.fi/), Latvia (1.5–4 p/m^2, https://www.lgia.gov.lv/), the Netherlands (6–10 p/m^2; https://www.ahn.nl/), Norway (0.5–5 p/m^2, https://hoydedata.no/), Poland (4–12 p/m^2; https://www.gugik.gov.pl/), and Switzerland (5–20 p/m^2, https://www.swisstopo.admin.ch/). In both commercial and non-commercial systems, the most commonly used ALS sensors are the *Leica ALS60*/*ALS80*, *RIEGL LMS Q780*, *RIEGL VQ-1560*, and *Teledyne Optech Galaxy*. These sensors feature scanning capacities of 1 to 2 million points per second, centimeter-level accuracy, and support multiple laser pulse returns.

Finally, the two SLS systems have received the lowest score due to their typical data collection method. The GEDI system scans the surface using discrete circular footprints with a diameter of 25 meters, generated by full continuous waveforms (Dubayah *et al*., 2020). ICESat-2/ATLAS collects data using a photon counting sensor that captures circular footprints measuring 70 meters in diameter (Neuenschwander and Pitts, 2019). These methods result in information gaps across the surface that can only be addressed through spatial interpolation and/or the use of auxiliary datasets (e.g., Potapov *et al*., 2021; Liu *et al*., 2022; Shendryk, 2022; Schwartz *et al*., 2024).

Temporal resolution

Temporal resolution indicates the system's ability to collect data from the same area at different times. Both UAVs, as well as the two ground-based laser scanner system, have received the highest ratings, as they offer complete

flexibility for data collection timing, provided there are no external factors such as adverse weather, inaccessible terrain, or wildfire that might impede data gathering. Therefore, their temporal resolution can be fully adjusted to meet the requirements of the study.

ALS systems have a relatively heterogeneous temporal resolution. Commercial systems have received a medium score because they offer flexibility comparable to that of UAVs. However, the main difference lies in the significantly higher economic cost of the flights, making it uncommon to systematically monitor a territory with such systems. Instead, they are typically used at specific times (e.g., Hilker *et al*., 2010; Dai *et al*., 2019) or after certain intervals as required (e.g., Marino *et al*., 2016). On the other hand, non-commercial ALS systems, which cover larger areas and are often developed by public administrations, generally have a low temporal resolution. These flights can occur several years apart, although very few countries have conducted multiple national coverages until now (e.g., Denmark, the Netherlands, or Spain). Consequently, a low score has been assigned to these systems.

The ICESat-2/ATLAS system has received a medium score because its heliosynchronous orbit allows a revisit time of 91 days (Neuenschwander and Pitts, 2019). This enables systematic data collection for the same footprint, although at a low temporal resolution. The GEDI system, due to the variable orbit of the ISS on which it is mounted, does not guarantee that a specific footprint will be revisited. In fact, in this thesis, none of the footprints within the Zuera study area (a total of 59,554 footprints) were revisited by the system; each footprint was unique in both time and space. As a result, it has been concluded that this functionality is non-existent for the GEDI system even though a given area is likely to contain multiple footprints recorded at different times.

Low economic cost

The low economic cost to the user determines the initial investment required to operate the system and obtain the information. The GEDI and ICESat-2/ATLAS systems have received the highest rating in this regard because they do not require an initial financial investment for acquiring the data, as it is freely available from various sources. The same rating has been assigned to non-commercial ALS systems, whose data are freely accessible and free of charge. In contrast, commercial ALS systems typically require a significant financial investment for data acquisition, which is why they have been assigned a low score.

Similarly, UAVs generally involve a high economic cost, with optical (i.e., photogrammetric) systems being less expensive than LiDAR systems (Mengiste *et al*., 2022). This principle has also been reflected in the present thesis; hence the optical UAV has been rated with a medium score and the UAV-LiDAR system with a low score. Some studies suggest that the lower economic cost of optical UAVs does not significantly affect their performance compared to LiDAR systems in estimating forest variables. For instance, Guerra-Hernández *et al*. (2018) obtained very similar estimates using an optical UAV compared to a non-commercial ALS, although they employed a cross-flight pattern for the UAV. Additionally, their study focused on a planted forest stand with lower heterogeneity than typical Mediterranean forest stands. On the other hand, Lamping *et al*. (2021) compared the performance of an optical UAV with LiDAR systems for estimating various forest attributes across heterogeneous temperate forests. To achieve this, they tested different viewing angles for UAV data collection, identifying the greatest challenges in areas with dense vegetation. In this thesis, however, the optical UAV were flown alone in a serpentine flight pattern with zenithal viewing angle in structurally complex forest stands, which might explain the lower performance in estimating the Prometheus fuel types compared to the UAV-LiDAR system. Moreover, the optical UAV required additional data alongside photogrammetric point clouds (i.e., multispectral images) to achieve high accuracy in fuel type classification, though it still did not match the results obtained by the UAV-LiDAR system. Therefore, users and managers should carefully consider the balance between cost and performance based on their investment capabilities and objectives. Additionally, depending on local regulations, there may be a requirement for an official UAV pilot certificate, which could entail further investment.

Finally, ground-based laser scanner systems have also received the lowest rating, as it typically requires a significant initial investment (e.g., Calders *et al*., 2020b; Mengiste *et al*., 2022; Loudermilk *et al*., 2023), although some authors suggest that these systems are becoming increasingly affordable (Gallagher *et al*., 2021).

Spatial coverage

Spatial coverage refers to the area that a system is capable of recording. In the present assessment, only non-commercial ALS systems have received a high rating, as they typically cover areas on a national scale. Commercial ALS systems, on the other hand, have received a medium rating since they generally cover smaller areas, mostly at the landscape scale (Hilker *et al*., 2010; Sheridan *et al*., 2014; Matikainen *et al*., 2017; Torralba *et al*., 2018) but occasionally

reaching regional scales (Marino *et al*., 2016; Dhargay *et al*., 2022), depending on the specific requirements of the study.

UAVs have also been rated with a medium score, as their data collection is restricted to local scales (i.e., forest stands), making their spatial coverage more localized. A UAV flight could cover up to 100 hectares of terrain (Sturdivant *et al*., 2017; Shin *et al*., 2018; Liao *et al*., 2021), although the exact coverage may vary depending on flight parameters, sensor type, terrain conditions, and accessibility (Ecke *et al*., 2022). Additionally, current UAV legislation may restrict the flight area due to proximity to certain facilities (e.g., airports, military bases, populated areas, etc.) or the distance a UAV can be flown from the operator. However, UAVs offer flexibility in data collection, allowing users to conduct multiple flights to cover relatively large areas. Fixed-wing UAVs can cover larger areas, but they require flat terrain nearby for landing. In contrast, quadcopter UAVs cover smaller areas than fixed-wing UAVs but can operate in complex terrain.

Regarding the ground-based laser scanner systems, both HMLS and TLS have received a low score due to their limited spatial coverage, which is very small (i.e., forest plot scale), especially for the time required for effective data collection, avoid occlusions, and accurately georeference the data (e.g., Vandendaele *et al*., 2022). Moreover, the time required to acquire data using TLS is often significantly longer compared to HMLS systems (Tommaselli *et al*., 2014; Di Stefano *et al*., 2021; Spadavecchia *et al*., 2023).

The two SLS systems have also been rated with the lowest score. Although they are satellite systems with global coverage, in the case of ICESat-2/ATLAS, and quasi-global coverage, in the case of GEDI (between latitudes 51.6º N and 51.6º S), the fact that its data are collected in discrete footprints makes it challenging to estimate fuels at an effective working scale. In this context, findings from Sothe *et al*. (2022) indicate that estimating spatially continuous forest variables with both GEDI and ICESat-2/ATLAS can be a challenging task, even when combined with other systems. However, other authors suggest that combining SLS data with other spaceborne-based products that provide spatially continuous data could facilitate continuous forest monitoring (Chen *et al*., 2022; Leite *et al*., 2022; Myroniuk *et al*., 2023), potentially enhancing subsequent fuel estimation.

Accuracy in 3D location

High accuracy in planimetric ("x" and "y" coordinates) and altimetric ("z" coordinate) location is crucial for accurately positioning objects recorded by

sensors and minimizing errors. ALS, UAVs, and ground-based laser scanner systems have received the highest scores due to their data capable of being obtained with sub-meter spatial accuracy. In contrast, the SLS systems have received the lowest score, primarily due to the significant geospatial uncertainty of its footprints.

ALS systems typically incorporate GNSS that enable the capture of data with sub-meter spatial accuracy, both for non-commercial (e.g., Gelabert *et al*., 2020; Koma *et al*., 2020; Assmann *et al*., 2022) and commercial (e.g., Donager *et al*., 2021b; Zhou *et al*., 2023) systems. However, in some cases, GCPs are required to achieve such accuracies (e.g., Torralba *et al*., 2018; Crespo-Peremarch *et al*., 2020). Furthermore, a study developed by Muhojoki *et al*. (2024) demonstrated that ALS systems can rival GNSS total stations in spatial accuracy.

In this PhD Thesis the UAV-LiDAR system's integration of RTK technology enabled direct acquisition of sub-meter accurate data during flights. In comparison, the optical UAV and HMLS system lacked this functionality, requiring the placement of multiple GCPs in the study areas. These GCPs, surveyed with a sub-meter precision GNSS station, were essential for later georeferencing the collected data. However, using GCPs increases field work time, as they must be placed at the edges of the study area and evenly spaced for optimal georeferencing (e.g., Crespo-Peremarch *et al*., 2020). On the other hand, RTK technology in the UAV-LiDAR system, along with PPK (*Post Processed Kinematic*) technology, allow immediate data acquisition with sub-meter accuracy. RTK requires a constant signal between the UAV and the base station throughout the flight (Bakuła *et al*., 2009), though this signal may be intermittently lost in closed environments like dense forests (Miller *et al*., 2021). PPK, however, applied location corrections during post-processing, making it a more reliable option, especially in challenging environments (e.g., Zhang *et al*., 2019; Eker *et al*., 2021; Miller *et al*., 2021). Ground-based laser scanner systems can also achieve sub-meter accuracy (Muhojoki *et al*., 2024), as demonstrated by the HMLS system used in this thesis. However, in most cases, the support of ground control points (GCPs) is necessary (Fol *et al*., 2023; Muhojoki *et al*., 2024).

Concerning the SLS systems, ICESat-2/ATLAS has received a medium score because, although its initial precision was estimated at 6.5 m (1σ) (Carabajal and Boy, 2020), subsequent analyses have demonstrated improved performance after applying laser and orbital variation calibrations, resulting in spatial precisions ranging from 2.5 to 4.4 m (Luthcke *et al*., 2021). On the other hand, GEDI has received the lowest score due to its high spatial uncertainty of its footprints, with

an estimated error of about 10 m (1σ) in 80% cases in the latest data release (version 2) (Dubayah *et al*., 2020; Roy *et al*., 2021; Tang *et al*., 2023). Consequently, to minimize this uncertainty, a new quality filter had to be developed in this thesis based on land cover homogeneity. Although several authors have proposed methods to mitigate GEDI's systematic geolocation error (e.g., Schleich *et al*., 2023; Shannon *et al*., 2024), many studies still accept this uncertainty in their analyses.

7.2. DATA PROCESSING AND ANALYSIS CAPABILITIES

The results of the data processing and analysis capabilities of each system are presented in Table 7.2. Both ALS systems have received the highest score (13) followed by the UAV-LiDAR system (12), the GEDI SLS system (11), the ICESat-2/ATLAS SLS system and the optical UAV (10), the HMLS system (9), and TLS systems (8).

Table 7.2. Scores by functionalities of the data processing and analysis capabilities of the analyzed systems for effective forest fuel estimation.

Data processing and analysis capabilities	**SLS**		**ALS**		**UAVs**		**Ground-based**	
	GEDI	***ICESat2***	**Non-Comm.**	**Comm.**	**Optical**	**LiDAR**	**HMLS**	**TLS**
Computational requirements	2	2	2	2	2	3	1	1
Processing accessibility	2	2	3	3	3	3	3	3
Intensity of field work	3	3	3	3	2	2	1	1
Pre-processing requirements	2	2	2	2	1	1	1	1
Accuracy in generating predictors	2	1	3	3	2	3	3	2
Total	**11**	**10**	**13**	**13**	**10**	**12**	**9**	**8**

Computation requirements

Computational requirements are crucial in determining the initial processing capacity of the data obtained. The UAV-LiDAR system has received the highest score because it did not require exceptional computational resources to generate point cloud files, as point clouds were recorded and created during data acquisition. However, the initial generated file sizes can be quite large. In

contrast, the optical UAV demanded more computational power and processing time than the UAV-LiDAR system, as found in the present thesis and in previous studies (e.g., Wallace *et al.*, 2016; Hillman *et al.*, 2021). This is the reason it has received medium score. Specifically, converting two-dimensional images into three-dimensional information requires significant computational resources. This process includes overlap analysis of the objects in the photographs, feature extraction, feature matching, generation of the photogrammetric point clouds, and georeferencing of the images, particularly if RTK/PPK technology is not available on the UAV, as in this thesis.

ALS systems have received a medium score because they can contain a large amount of information (Martijn *et al.*, 2019; Guerra-Hernández and Pascual, 2021), even in low-point-density non-commercial LiDAR datasets, as they usually cover extensive areas. Furthermore, the data is typically divided into tiles of a specific size (e.g., 1 km^2 in Denmark's national dataset or 2 km^2 in Spain's national dataset), making it necessary to work with a large number of tiles (e.g., Domingo *et al.*, 2020; Gelabert *et al.*, 2020; Assmann *et al.*, 2022; Cserép and Lindenbergh, 2023).

SLS systems have also been given a medium score because they can record vast amounts of data, as they are designed for spatial analysis at very large scales (even global scale). This results in large file sizes that demand high computational resources (e.g., Liu *et al.*, 2021a; Potapov *et al.*, 2021; Khalsa *et al.*, 2022; Holcomb *et al.*, 2023; Vangi *et al.*, 2023). In this thesis, even a relatively small study area contained a total of 59,554 footprints of the GEDI system. Each footprint included three different processing levels, and each one incorporating a large amount of data and metadata which further amplified the computation demands. Similarly, the study conducted by Liu *et al.* (2021a) in an area of approximately 7,000 km^2 resulted in 42,636 ICESat-2/ATLAS footprints and 90,472 GEDI footprints with valid measurements after applying several quality filters. Handling such a large amount of information poses a challenge for any computer.

Ground-based laser scanner systems have received the lowest score. Both TLS and HMLS systems generate a very large volume of data due to the extreme density of points acquired, necessitating more time and resources for the initial processing and georeferencing of the point clouds (e.g., Tao *et al.*, 2021; Molina-Valero *et al.*, 2022). This aspect has also been noted in the present thesis with the HMLS system. Nevertheless, it is worth noting that similar computation times between UAV-LiDAR and TLS systems has been reported by other authors (Hillman *et al.*, 2021).

Processing accessibility

Processing accessibility refers to the set of tools and techniques available for processing and analyzing the data obtained. In this functionality, ALS, UAVs and ground-based laser scanner systems have received the highest scores, while the SLS systems have earned a medium score. Therefore, none of the systems have received a low score, as there are numerous tools available for processing and analyzing three-dimensional data.

Many of these tools were initially developed for ALS data but are also applicable to any three-dimensional dataset, including those generated by UAVs and ground-based laser scanner systems. In this thesis, data from UAV-LiDAR system were initially processed using the proprietary software *DJI Terra* v.3.6.7 (DJI, Shenzhen, China), while optical UAV data were processed using *PIX4Dmapper* v.4.5.6 (PIX4D SA, Prilly, Switzerland). For the HMLS system, the proprietary software *GeoSLAM Connect* v.2.3.0 (GeoSLAM Ltd., Ruddington, UK) was utilized. For all three systems, the subsequent methodology for generating forest variables –including outlier filtering, ground point classification, DEM generation, height normalization, point cloud clipping to plots, and voxelization– was carried out using the open-source R environment, utilizing various packages capable of processing three-dimensional point clouds, regardless of whether they originate from ALS, UAVs, or ground-based systems. There are also alternative tools available for all these processes, including commercial solutions such as *Agisoft Metashape* (Agisoft LLC, St. Petersburg, Russia), *Terrasolid* (Terrasolid Ltd., Helsinki, Finland), *LiDAR360* (GreenValley International, Beijing, China), or the *LasTools* extension (rapidlasso GmbH, Gliching, Germany) for *ArcMap* (ESRI, 2019). There are also free tools such as *FUSION/LDV* (McGaughey, 2021), *3DFin* (Cabo *et al*., 2024), and various packages available for R or Python. Given this abundance of tools, several studies have compared the effectiveness of different software for processing three-dimensional remote sensing data. For instance, Kameyama and Sugiura (2021) found that *PIX4Dmapper* derived forest variables more accurately than *Agisoft Photoscan* and *Terra Mapper*. Similarly, a study by Jarahizadeh and Salehi (2024) showed that *DJI Terra* provided better overall results for tree point cloud generation and, along with *Agisoft Photoscan*, offered faster point cloud processing times than *PIX4Dmapper*.

Regarding the SLS systems, they have received a medium score due to the relatively limited number of tools available compared to discrete ALS, UAVs, and ground-based systems, particularly for working with raw full continuous waveform data. However, specific packages designed for GEDI and ICESat-

2/ATLAS data extraction and processing, particularly in R and Python environments, have been developed recently (e.g., Zhou and Popescu, 2016; Neumann *et al*., 2020; Silva *et al*., 2020; Liu *et al*., 2021; Silva and Hamamura, 2023; Vangi *et al*., 2023; Mouselimis, 2024), which have helped enhance its processing availability.

Intensity of field work

The intensity of field work is determined by the need to perform additional tasks in the field, which are essential for accurate data collection and, ultimately, for obtaining high-quality variables that allow for precise fuel type estimation. The SLS and ALS systems have received the highest score in this regard. GEDI and ICESat-2/ATLAS require minimal fieldwork to obtain the data, aside from sampling several footprints for validating the assigned fuel type. However, more intensive field work would be necessary for other objectives, such as sensor validation or biomass calculation (e.g., Fayad *et al*., 2021; Duncanson *et al*., 2022; Leite *et al*., 2022). ALS systems also require minimal fieldwork, except when conducting field inventories to assess the accuracy of the evaluated systems (Domingo *et al*., 2019a; Domingo *et al*., 2020) or when using GCPs to enhance the georeferencing of the ALS data (Crespo-Peremarch *et al*., 2020). UAV systems have earned medium scores because they require field visits for data collection. Additional tasks, such as surveying GCPs for later data georeferencing or accessing challenging locations due to flight plan requirements (e.g., flat areas for landing fixed-wing UAVs), may also increment the intensity of field work. However, UAVs generally demand less field work than ground-based laser scanner systems (e.g., Brede *et al*., 2017; Wieser *et al*., 2017; Slavík *et al*., 2020; Donager *et al*., 2021b). For this reason, the HMLS and TLS systems have received the lowest score, as data collection requires entering forest plots, a task that can be particularly challenging in densely vegetated and topographically complex areas. Additionally, data collection is often time-consuming, although HMLS systems tend to gather information more quickly than TLS systems, but requires more physical effort (Wilkes *et al*., 2017; Gollob *et al*., 2020).

Pre-processing requirements

Pre-processing requirements refer to the capacity and time needed by the user (learning curve) and the computer (processing power) to handle with the entire workflow, from raw data to the generation of predictor variables. None of the

systems have received a high score in this area, as no single system excels in processing the entire dataset easily.

The SLS systems have received a medium score because their data demand fewer processing resources compared to datasets with high-density three-dimensional information (i.e., data from UAVs and ground-based systems). GEDI and ICESat-2/ATLAS processing involves filtering out low-quality footprints, as indicated in their respective metadata, to ensure that only accurate footprints with derived predictor variables are used. However, if working directly with the raw data, additional noise decomposition and filtering processes would be necessary to obtain the desired variables.

ALS systems have also received a medium score, while UAVs and ground-based laser scanner systems have received low score. Although ALS systems follow the same workflow as UAVs and ground-based systems and utilize similar processing tools, the lower average density of the point clouds results in reduced processing requirement. In this regard, UAV, TLS, and HMLS data processing involves handling large amounts of information. These systems produce very dense point clouds and, in the case of UAVs, over relatively larger areas, leading to high processing requirements. One critical step in the three-dimensional point cloud workflow is the classification of ground points, as the quality of the DEMs, normalized heights, and predictor variables hinges on this process. Thus, it is crucial to select the most appropriate classification algorithm for the research objective and the available data to minimize processing time and to obtain high-quality variables. For instance, not all classification algorithms can handle very dense point clouds, especially those derived from ground-based laser systems, necessitating an additional step of point cloud decimation or homogenization (Anderson *et al*., 2006; Liu *et al*., 2018; Wallace *et al*., 2019; Wang *et al*., 2020; Braun *et al*., 2021b). This step is also implemented to eliminate bias caused by occlusion in ground-based laser scanner systems (Moriguchi, 2023).

Accuracy in generating predictors

Accuracy in generating predictor variables would be understood as a synthesis of the aforementioned functionalities, wherein a high capacity for field work, when required, coupled with significant computational and data pre-processing demands, culminates in the generation of precise predictor variables. However, the accuracy is also fundamentally dependent on the intrinsic characteristics of the system itself, including factors such as laser pulse frequency, the ability of the pulses to penetrate the vegetation canopy, and the density of the point cloud.

Thus, ALS, UAV-LiDAR, and HMLS systems have received the highest score due to their ability to capture high-resolution data, and their laser pulses' capacity to record information from the intermediate and lower strata of vegetation beneath the forest canopy. Furthermore, the availability of a diverse array of data processing tools for these systems throughout the workflow is essential for generating accurate predictor variables, particularly in the context of estimating fuel types. However, there are some challenges that can impact the accuracy of the predictor variables. For instance, Donager *et al*. (2021b) found some problems when using ALS for estimating tree height for trees with smaller diameters. Moreover, variables derived from UAV-LiDAR systems may occasionally lead to the overestimation of the Diameter at Breast Height (DBH) due to registration errors (Liang *et al*., 2019) or occlusions resulting from insufficient laser penetration (Pyörälä *et al*., 2018; Panagiotidis *et al*., 2022). However, in the present PhD Thesis, data obtained from the UAV-LiDAR system demonstrated strong overall performance in the classification of the Prometheus fuel types, utilizing a diverse array of forest variables (as detailed in Table 2 of Chapter 6).

For the HMLS system, the ability to generate vertical vegetation volume variables through high-resolution voxelization of the original three-dimensional point cloud was instrumental in successfully defining homogeneous distributions for each Prometheus fuel type in Chapter 5. The efficacy of HMLS systems in generating forest variables such as tree height, crown volume, DBH, and wood volume has also been corroborated by other studies (Vandendaele *et al*., 2022), alongside variables such as canopy cover and landscape metrics (Donager *et al*., 2021b). In contrast, TLS systems are more susceptible to occlusion issues, which can lead to an underestimation of structural variable values (Donager *et al*., 2021b). However, these occlusion problems can be mitigated by conducting a greater number of scans in different areas of the forest (Torralba *et al*., 2022), though this requires more time and effort for data acquisition. Therefore, TLS system have received a medium score.

The optical UAV has also been assigned a medium score, as variables derived from photogrammetric point clouds may underestimate vegetation situated below the forest canopy. In this thesis, the incorporation of multispectral information was critical to achieving a noteworthy level of accuracy in fuel type classification, suggesting a reduced predictive power of the variables derived from the photogrammetric point cloud compared to the UAV-LiDAR system. While some studies suggest that optical UAVs represent a cost-effective alternative for estimating forest variables (Shin *et al*., 2018), their efficacy in capturing the ground beneath dense canopies is lower when compared to LiDAR

data (Wallace *et al*., 2016). This limitation hinders the generation of accurate DEMs in densely forested areas, resulting in less detailed information about vegetation structure and necessitating the use of ancillary ground data, which, in the case of the present thesis, has proven to be satisfactory.

The GEDI system has also received a medium score as predictor variables are pre-generated at the footprint level within the respective data products, with quality indicators providing information on the reliability of these variables. On the other hand, ICESat-2/ATLAS, which also incorporates pre-generated variables with quality indicators, has received a low score due to greater uncertainties compared to GEDI (Sothe *et al*., 2022), as well as smaller number of available predictor variables. However, it is important to note that ICESat-2/ATLAS was not originally designed for forest analysis. In this thesis, the assessment of GEDI incorporated a range of structural variables for the estimation of the Prometheus fuel types, although the inclusion of multispectral information significantly enhanced fuel classification. This may be due to a lower predictive capacity of the variables, similar to the case with optical UAVs, or because the pre-generated predictors in the various GEDI products are insufficient for achieving high accuracy in classifying the Prometheus fuel types. Some authors have noted issues with the accuracy of SLS-derived variables for estimating forest structure. For instance, Dhargay *et al*. (2022) observed that GEDI's high percentile metrics (e.g., "RH99", "RH100") may be affected by noise, while lower percentile metrics (e.g., "RH50") may experience high laser waveform distortion or lower information density. Sothe *et al*. (2022) reported an average GEDI error of 4.20 m respect to ALS in forest canopy height when producing 250 m resolution maps. However, this study found that GEDI performed better than ICESat-2/ATLAS, although they emphasized the importance of considering the temporal shift of the data used in their analysis. Additionally, it has been noted that orographically complex areas lead to decreased accuracy of satellite variables. Potapov *et al*. (2021) found that slopes affect the estimation of tree cover using GEDI, while Tian and Shan (2021) reported lower uncertainty in the height of the ICESat-2/ATLAS "ATL08" product in flat areas compared to mountainous terrain.

7.3. ACCURACY IN ESTIMATING FUEL TYPES

The results of the analysis of the accuracy in estimating fuel types of each system are presented in Table 7.3. The ALS systems have received the highest score (14) followed by the UAV-LiDAR system (13), the optical UAV (12), the GEDI

SLS system (11), the HMLS and TLS systems (10), and the ICESat-2/ATLAS system (7).

Table 7.3. Scores by functionalities of the accuracy in estimating fuel types of the analyzed systems.

Accuracy in estimating fuel types	**SLS**		**ALS**		**UAVs**		**Ground-based**	
	GEDI	***ICESat2***	**Non-comm.**	**Comm.**	**Optical**	**LiDAR**	**HMLS**	**TLS**
Estimation of fuels	2	0	2	3	2	3	3	3
Multisensor integration	3	3	3	3	3	3	2	2
Multiplatform integration	3	3	3	3	3	3	3	3
Effective working scale	1	1	3	3	2	2	1	1
Capacity for forest fuels mapping	2	0	3	2	2	2	1	1
Total	**11**	**7**	**14**	**14**	**12**	**13**	**10**	**10**

Estimation of fuels

In this PhD Thesis, the Prometheus fuel types were classified using machine learning models, leveraging variables generated by the GEDI SLS system (Chapter 3) and both UAVs (Chapters 4 and 6). Additionally, the delineation of the Prometheus fuel types was possible through quantitative variables on the vertical volume of vegetation (Chapter 5), generated at a very high spatial resolution (5 cm^3) from HMLS voxelized point cloud. All systems evaluated in the present thesis have demonstrated adequate capabilities for classifying or defining fuel types; therefore, none has received a low score.

The UAV-LiDAR system has achieved the highest score due to its ability to classify fuel types with high accuracy using solely variables derived from the three-dimensional point cloud. Conversely, the optical UAV has received a medium score because its performance on classifying the fuels was lower, particularly when only variables derived from the photogrammetric point cloud were used. Although the incorporation of multispectral data alongside three-dimensional variables into the models improved the overall classification, it still did not match the overall accuracy obtained with the UAV-LiDAR systems' variables. The superior performance of the UAV-LiDAR system compared to the optical UAV can be attributed to the former's greater ability to generate

accurate predictor variables from the point cloud. The laser's capacity to penetrate the canopy is crucial for accurately estimating more complex fuel types, such as type 3 and type 6, which are intermediate types where the structural role of the shrubs and understory is highly significant. Another factor contributing to the lower performance of photogrammetric point clouds in estimating forest fuels may be the quality of the images obtained (Cao *et al*., 2019; Cova *et al*., 2023). This issue can lead to less accurate predictions of canopy density or canopy base height (Shin *et al*., 2018; Kelly *et al*., 2021), which may affect the accurate estimation of fuels. On the other hand, in this thesis, photogrammetric point clouds performed well for estimating surface fuels, such as grass (fuel type 1) and low shrubs (fuel type 2), aligning with findings from other studies (Eames *et al*., 2021; Cova *et al*., 2023).

The HMLS system's ability to define fuels has been rated highly, as it has demonstrated excellent capabilities in estimating the Prometheus fuel types in forest plots characterized by high structural heterogeneity. Similarly, TLS systems have received a high score. Previous studies have confirmed the effectiveness of ground-based laser scanners in successfully estimating forest fuels (e.g., Chen *et al*., 2016; Alonso-Rego *et al*., 2020; Wilson *et al*., 2021; Marcozzi *et al*., 2023). Furthermore, some studies have observed better performance of ground-based systems compared to optical UAVs for general forest fuel load estimation, although they found limited ability to accurately estimate the canopy fuel load (Arkin *et al*., 2021).

Regarding ALS, these systems have been widely used for forest fuel estimation. Commercial ALS systems have been awarded the highest rating, as they generally can provide denser three-dimensional point clouds compared to non-commercial ALS systems (e.g., Labenski *et al*., 2023), sometimes achieving densities comparable to those of UAV-LiDAR systems (Dai *et al*., 2019). This high point density allows for precise estimation of canopy fuels (Rocha *et al*., 2023), understory fuels and fuelbed depth (Labenski *et al*., 2023), and fuel types supported by multispectral data (Marino *et al*., 2016). Mihajlovksi *et al*. (2023) classified fuel types in Portugal with a maximum overall accuracy of 67% using only mean density ALS data (10 p/m^2) and the CART classification model. Non-commercial ALS systems, which generally do not achieve the same high point densities as their commercial counterparts, have received a medium rating. However, despite their lower to medium point densities, several studies demonstrate the capability of non-commercial ALS to accurately estimate fuels. For instance, García-Cimarras *et al*. (2021) achieved 81% overall accuracy in estimating changes in Prometheus fuel types using ALS-PNOA data and conditional rules. Revilla *et al*. (2021) classified the Prometheus fuel types with

88% and 91% accuracy using data simulated with the DART radiative transfer model (Gastellu-Etchegorry *et al*., 2015), validated with ALS-PNOA data from 2011 and 2016, respectively. Nevertheless, among the reviewed studies based on non-commercial ALS, the work by Domingo *et al*. (2020) stands out as the most comparable to the research presented in the thesis, although their study area was larger and more structurally heterogeneous and complex. In their study, the authors classified the Prometheus fuel types using machine learning models and predictor variables related to forest structure and diversity. Their best result was achieved with the SVM-R model, obtaining an overall accuracy of 59% when integrating ALS-PNOA and Sentinel-2 data. When only ALS variables were used, the SVM-L model achieved the highest performance, with an overall accuracy coefficient of 58%. While the characteristics of their study area should be taken into account, this work offers a solid basis for positively evaluating the results presented in Chapters 4 and 6, given the similarity in methodology.

The GEDI system has also received a medium score due to its good results in fuel classification when only variables provided by GEDI were used. However, similar to the optical UAV, the model performance was lower compared to the UAV-LiDAR system, although the inclusion of multispectral variables significantly improved the classification. Lastly, the ICESat-2/ATLAS system has been assigned a zero rating because, to date, no studies have been conducted using this system for fuel estimation, although it has been used for estimating forest structure attributes (Malambo and Popescu, 2021; Aktürk *et al*., 2023; Malambo and Popescu, 2024).

Multisensor integration

Multisensor integration refers to the synergies between three-dimensional data obtained from laser or photogrammetric systems and other non-laser-derived sources, such as two-dimensional optical images from passive sensors and Synthetic Aperture Radar (SAR)-derived data. This characteristic has been evaluated with the highest score for the SLS, ALS, and UAV systems, while ground-based laser scanner systems have received a medium score.

The GEDI system demonstrated particularly strong synergies with vegetation indices from Landsat-8 OLI imagery for the Prometheus fuel types classification. Numerous studies have confirmed the effectiveness of the integration of GEDI with multispectral images for estimating and mapping forest variables using Landsat (Potapov *et al*., 2021; Liang *et al*., 2023; Myroniuk *et al*., 2023; Vogeler *et al*., 2023), Sentinel-2 (Jiao *et al*., 2023), both Landsat and Sentinel-2 (Tsao *et al*., 2023), and VIIRS (Rishmawi *et al*., 2021) systems.

Research by Shendryk (2022) and Dwiputra *et al*. (2023) has demonstrated successful integration of GEDI, Sentinel-2, and SAR data from Sentinel-1 for estimating forest aboveground biomass and mapping tropical vegetation type distribution, respectively. Similarly, combining GEDI with SAR data from the TanDEM-X system has led to improved forest height estimation accuracy compared to using each system independently (Qi *et al*., 2019). The integration of GEDI and ICESat-2/ATLAS with SAR data, along with optical imageries, enabled the production of continuous canopy height maps in Canada (Sothe *et al*., 2022), although GEDI worked better than ICESat-2/ATLAS in this study. Nevertheless, ICESat-2/ATLAS also shows strong potential for integration with optical and SAR data. For instance, ICESat-2/ATLAS data can be combined with Landsat-8 OLI imagery to enhance estimates of aboveground biomass and carbon pools in dryland ecosystems (Glenn *et al*., 2016), as well as with optical and SAR data to estimate emissions from forest biomass burning (Liu and Popescu, 2022) and to map forest canopy height (Luo *et al*., 2023; Malambo and Popescu, 2024; Mansouri *et al*., 2024).

The fusion of ALS data and optical imagery has also proven to be highly effective for estimating vegetation structure and composition (Labenski *et al*., 2023), as well as for identifying forest fuels, whether using Landsat (Marino *et al*., 2016), Sentinel-2 (Domingo *et al*., 2020) or both systems combined (Crespo-Calvo *et al*., 2023). The findings of Adhikari *et al*. (2020) suggest that integrating low-density ALS data, such as those from non-commercial sources, with optical imagery could achieve accuracies comparable to those obtained using high-density ALS data alone. Additionally, the inclusion of airborne hyperspectral data has been shown to improve results in the identification and mapping of forest fuels (Romero-Ramírez *et al*., 2018). However, Mihajlovski *et al*. (2023) found no improvement when combining ALS data with Sentinel-2 optical imagery, and Sentinel-1 and PALSAR-2/ALOS-2 SAR data for classifying fuel types in Portugal.

In this thesis, the fusion of variables from photogrammetric point clouds and optical UAV-derived multispectral imagery improved the estimation of the Prometheus fuel types. The effectiveness of combining these two data sources for forest analysis has been observed in other studies as well (e.g., Shen *et al*., 2019; Xu *et al*., 2020; Liu *et al*., 2021b; Reilly *et al*., 2021). Regarding UAV-LiDAR system, although this thesis did not explore the fusion of its data with optical imagery, it is reasonable to conjecture that integrating both datasets would yield satisfactory results, based on the positive outcomes with the optical UAV and findings from previous studies (e.g., Briechie *et al*., 2020; Shendryk *et al*., 2020; Liu *et al*., 2021c). However, experimental validation would be

necessary to confirm this hypothesis, as well as the generally positive results observed when merging optical data with three-dimensional SLS and ALS data.

Finally, the ground-based laser scanner systems have received a medium score. The reason for not assigning the highest score is that ground-based systems are often used as ground-truth for variables obtained through other remote sensing systems, rather than as a synergetic support to enhance the accuracy of the results. For example, Mulatu *et al*. (2019) evaluated the accuracy of vegetation indices and SAR satellite data in measuring forest structure parameters, using TLS data and field-observed measurements as references. On the other hand, Taneja *et al*. (2023) used ALS, optical satellite imagery, and climate and soil data to validate a predictive model based on fuel hazard metrics obtained through TLS. The authors found that the TLS-validated model demonstrated greater predictive power compared to model based on in-situ observation. It can be hypothesized, therefore, that HMLS data could also serve as ground-truth for other remote sensing data sources to estimate various fuel attributes. Moreover, incorporating auxiliary remotely sensed data would highlight the superior accuracy of HMLS metrics in comparison to in-situ observations. However, given the current lack of studies, more research is needed to explore these possibilities.

Multiplatform integration

Multiplatform laser or photogrammetric integration refers to the combination of three-dimensional data obtained from different laser or photogrammetric systems sources. In this section, all systems have received high scores.

This thesis did not merge GEDI data with other three-dimensional information but several studies have demonstrated its effectiveness. The fusion of GEDI and ICESat-2/ATLAS systems has proven to be beneficial for estimating various vegetation attributes. For instance, it enhances the accuracy of forest aboveground biomass estimates compared to when each system is used independently (Silva *et al*., 2021). Additionally, ALS data have served as a reference for validating both SLS systems, revealing that GEDI provides more accurate canopy height estimates than ICESat-2/ATLAS. The latter tends to overestimate the canopy height in low shrublands while underestimating the forest canopy height in nearly all forest ecosystems (Liu *et al*., 2021a). Furthermore, integrating data from GEDI and ALS has enabled the assessment of forest dynamics in three rapidly growing forest ecosystems (Guerra-Hernández and Pascual, 2021) and facilitated estimates of aboveground forest

biomass (Dorado-Roda *et al*., 2021). Therefore, it can be hypothesized that such integration would be beneficial for forest fuel estimation

The fusion of ALS and ground-based laser scanner systems significantly enhances estimates of tree diameter distribution (Vastaranta *et al*., 2014; Kankare *et al*., 2015), biomass (Hauglin *et al*., 2014), and three-dimensional crown structure (Paris *et al*., 2017). This integration also improves predictive mapping of vegetation structural components in Mediterranean forests (Puletti *et al*., 2021) and leads to more accurate predictions of canopy fuel variables in Atlantic pine stands (Alonso-Rego *et al*., 2021). Furthermore, the independent integration of ALS data with TLS and HMLS increases the accuracy of estimating tree height and crown projection area radius (Giannetti *et al*., 2018), which would ultimately allow for better estimates of forest fuels.

The integration of UAV-LiDAR data with the HMLS data for fuel estimation has also proven to be highly effective, according to the results presented in Chapter 6. The fusion of these systems enhanced fuel estimation across the entire forest structure, as UAVs tend to capture better the aerial part of vegetation, while HMLS systems are better in estimating the intermediate and lower parts of vegetation. In this regard, Fekry *et al*. (2022) reported improved estimates of tree height and volume when integrating data from UAV-LiDAR and TLS compared to using each system separately. Similarly, Qi *et al*. (2022) demonstrated that the combination of UAV-LiDAR and HMLS data is highly effective in quantifying forest structure post-fire. In this thesis, positive results were also achieved through the integration of photogrammetric point clouds with ancillary ALS data, enabling the generation of DEMs to normalize photogrammetric point cloud heights and produce structural and textural variables. These findings are consistent with those of previous studies (e.g., Graham *et al*., 2020; Yoshii *et al*., 2022).

Effective working scale

The effectiveness of remote sensing systems in accurately estimating fuel types may be compromised if their operational scale is not suitable for forest fuel management. In this context, while SLS and ground-based laser scanner systems have demonstrated capabilities in fuel estimation, their operational scales might not be ideal for practical forest management. This is the reason why they have received low scores. The scale of GEDI and ICESat-2/ATLAS allows for fuel estimation on a broad level, such as regional (Duncanson *et al*., 2020; Malambo and Popescu, 2021; Quirós *et al*., 2021; Leite *et al*., 2022; Narine *et al*., 2022; Myroniuk *et al*., 2023; Schwartz *et al*., 2024), national (Neuenschwander *et al*.,

2020; Fayad *et al*., 2021; Shendryk, 2022; Gao *et al*., 2023; Vangi *et al*., 2023), continental (Rishmawi *et al*., 2021; Feng *et al*., 2023; Mandl *et al*., 2023), or global scales (Potapov *et al*., 2021; Duncanson *et al*., 2022; Lang *et al*., 2022), but may not be as practical for fire management by local administrations, although they offer valuable insights into the general distribution of fuels across extensive areas, serving as essential baseline information for subsequent forest fuel management activities at more effective operational scales. Conversely, the scale of TLS and HMLS systems is highly localized, limiting fuel management to individual forest plots.

On the other hand, ALS systems have received a high score due to the operational scale at which the data is capture. While ALS can operate at a local level (Matikainen *et al*., 2017), their most common application is at landscape scales (Montealegre *et al*., 2014; Lindgren *et al*., 2015; Gelabert *et al*., 2020; Guerra-Hernández *et al*., 2022; Pascual *et al*., 2023), making it highly effective for identifying fuels and implementing appropriate fuel management strategies.

UAV systems have received a medium score due to their more local scale, which similarly restricts forest management to smaller areas. However, the flexibility offered by UAVs in data collection, regardless of possible flight restrictions, coupled with potential technological advancements (e.g., improved battery life, increased speed, etc.), could expand their operational scale to cover larger areas, thereby making them more effective for forest management purposes. Moreover, based on the positive results obtained in this thesis and numerous previous studies referenced above, integrating multiple three-dimensional systems would facilitate scaling up from the local level of UAVs to broader landscape management scales. UAVs enable the collection of forest information with high accuracy while providing greater temporal flexibility and faster data collection compared to other remote sensing systems and traditional forest inventories based on field work. In this context, UAV data could serve as ground-truth, similar to TLS and HMLS, allowing for the spatialization of results over larger areas using systems that operate at more effective spatial scales for forest management, such as ALS systems.

Capacity for forest fuel mapping

The capability for generating forest fuel maps has been rated as high for non-commercial ALS systems; medium for GEDI, commercial ALS, and UAVs; low for ground-based laser scanner systems; and non-existent for ICESat-2/ATLAS.

Non-commercial ALS systems typically cover large areas with high and consistent resolution, making them highly effective for efficient forest fuel management. Their fuel mapping capabilities, both independently and in combination with other remote sensing data sources, are very robust (e.g., Romero-Ramírez *et al*., 2018; Domingo *et al*., 2020; García-Cimarras *et al*., 2021; Crespo-Calvo *et al*., 2023). In contrast, commercial ALS systems have been assigned a medium score because, while they offer the same or even better benefits as non-commercial ALS systems in terms of resolution and accuracy for fuel spatialization, they usually cover smaller areas, limiting their capacity to map fuels over larger regions.

GEDI offers the potential for fuel mapping over large areas, albeit at resolutions of several meters (Leite *et al*., 2022). Myroniuk *et al*. (2023) mapped forest fuels at 1 km^2 spatial resolution; however, information gaps arose due to factors such as high uncertainty or lack of footprints, the presence of clouds, or the orbital dynamics of the ISS. These issues could be mitigated by interpolation techniques or by waiting for the system to record a larger number of footprints (Patterson *et al*., 2019). Additionally, combining GEDI with other sensors could facilitate vegetation mapping at medium scales (Dwiputra *et al*., 2023). In the case of ICESat-2/ATLAS, it has received a zero score due to the absence of forest fuel mapping studies involving this system to date.

UAVs enable fuel mapping at scales more effective for fuel management, typically at the meter level. However, as discussed earlier, the area that a UAV can cover is relatively small, necessitating an extension of coverage to spatialize the results over larger areas or multisensor integration.

Ground-based laser scanner systems face greater limitations for mapping fuels over extensive areas, as data collection is typically conducted at the forest plot scale. Some researchers have successfully generated mappings in small forest areas using ground-based laser systems (e.g., Ritter *et al*., 2017) and in combination with UAV data (Pierzchała *et al*., 2018). Nonetheless, large-area mapping could be achieved by integrating TLS and ALS data (Puletti *et al*., 2021).

7.4. IMPLICATIONS FOR FOREST FUEL MANAGEMENT

The semi-quantitative analysis presented here is intended to serve as a reference for the improvement of forest fuel management. Table 7.4 presents the final scores for each of the evaluated systems. The non-commercial ALS systems used in national coverage has achieved the highest score (39) followed by commercial

ALS (38), the UAV-LiDAR system (37), the optical UAV (35), the HMLS system (30), TLS systems (29), the GEDI SLS system (28), and the ICESat-2/ATLAS SLS system (26).

Table 7.4. Scores by the components assessed of each system for effective forest fuel estimation.

	SLS		**ALS**		**UAVs**		**Ground-based**	
	GEDI	***ICESat2***	**Non-comm.**	**Comm.**	**Optical**	**LiDAR**	**HMLS**	**TLS**
Intrinsic characteristics of the systems	6	9	12	11	13	12	11	11
Data processing and analysis capabilities	11	10	13	13	10	12	9	8
Accuracy in estimating fuel types	11	7	14	14	12	13	10	10
Total	**28**	**26**	**39**	**38**	**35**	**37**	**30**	**29**

ALS systems have received the highest scores, with non-commercial ALS rated one point higher due to its better intrinsic characteristics. These systems exhibit strong capabilities across all three components analyzed. One key advantage of LIDAR sensors is their ability to penetrate the forest canopy, allowing the collection of valuable data from within the forest interior, particularly the intermediate and lower strata, including shrubs, grass, and even the ground. This makes it possible to estimate structural features of vegetation and produce accurate DEMs for height normalization. While ALS typically operates with low to medium-high point density, studies have shown that even low-density ALS data can yield accurate forest fuel estimation. On the other hand, one of the main limitations of ALS systems is their temporal resolution. Non-commercial systems often require extended periods for site revisits (if new coverage is planned), whereas commercial ALS systems can be tailored to meet the user's needs. However, the high economic cost of commercial ALS flights can limit the frequency of revisits. Another advantage when working with three-dimensional point clouds data, applicable to ALS, UAVs, and ground-based laser scanner systems, is the wide array of freely accessible tools available for processing. Moreover, these tools are likely to increase in number and improve in performance in the future. Lastly, it is important to highlight the high potential of ALS for forest fuel estimation, its ability to integrate with other remote

sensing sensors (e.g., optical, SAR, or other laser platforms), and its effectiveness in delivering results at scales suitable for forest management.

The UAV-LiDAR system has also demonstrated exceptional capabilities across all three components analyzed. Its ability to classify and map fuels, as shown in Chapter 6, has been very satisfactory and balanced across all fuel types, using a simple methodology at every step. As in ALS systems, the ability of LiDAR sensors to penetrate the canopy ensures the capture of parts of the understory and even the ground, thereby fully capturing the structure of forest fuels. However, UAV-LiDAR differs from ALS in that it provides a higher point cloud density, which allows for more detailed information on vegetation structure. This capability allows for the generation of very accurate predictor variables. The operational scale of UAVs might be considered well-suited for fuel management, enabling coverage of local areas and the possibility of scaling up to landscape scales making multiple flights or, especially, through the integration with ALS data. In addition, UAVs allow users complete flexibility in data collection over different time periods, provided there are no external constraints (e.g., meteorological conditions, wildlife, or local restrictions on UAV flights). This temporal flexibility allows for systematic updates on the status and structure of fuels and enables the generation of updated maps of fuel types in a given forest area of interest. Furthermore, capturing data with UAVs does not require significant time and effort for field work. The main drawback of UAV-LiDAR systems nowadays are their high economic costs, although these systems might become more affordable in the near future. Likewise, it is expected that ongoing technological advancements in UAVs and remote sensing sensors will improve the performance of these instruments and facilitate the management of forest fuels.

Optical UAVs share many benefits with UAV-LiDAR systems except for the ability to capture data within the forest canopy. This could represent a significant limitation in dense forest areas, as these systems could not reliably record the complete vertical structure of fuels. In this PhD Thesis, the classification models showed good overall performance, although some difficulties were observed in correctly classifying the intermediate fuel types of both shrub and tree strata (i.e., types 3 and 6, respectively). The UAV-LiDAR system also encountered some issues in this respect, but the improvement in the classification of these types was substantial. Another challenge of optical UAVs with respect to LiDAR data is the greater computing resources required to generate photogrammetric point clouds from two-dimensional photographs. In contrast, optical UAVs have the advantage of being able to obtain multispectral images that, as demonstrated in this PhD Thesis and in other previous studies, have proven to be a very valuable

complement to three-dimensional point clouds for fuel identification. Nevertheless, the main and most evident advantage of optical UAVs over UAV-LiDAR systems is their lower economic cost, making them accessible to a broader audience.

Ground-based laser scanner systems allow managers to record forest fuels with extreme detail, providing highly accurate fuel estimates. However, this precision comes with a high computational load and processing time. Similar to UAVs, ground-based systems offer temporal flexibility for data capture, enabling frequently updated data. They typically require a significant initial financial investment. In addition, preprocessing tools for raw data are often commercial and provided by the same company that manufactures the instrument. For typical point cloud processing, tools similar to those used for optical UAVs or discrete-return LiDAR systems can be employed, although many are not specifically designed for ground-based LiDAR systems, which could introduce potential errors. One of the main limitations of ground-based systems is the considerable time required for data capture, especially when using TLS, and the resulting smaller area covered compared to UAVs. Thus, HMLS systems could be more suitable for recording data in dense forest plots to avoid occlusion issues. Furthermore, ground-based systems could act as supplementary support to other platforms, such as UAVs or ALS. The results obtained in this PhD Thesis demonstrate that HMLS systems can be highly effective for determining a specific fuel type at forest plot scale in structurally complex forest stands. This would enable forest managers to better establish the ground-truth for fuel type classification models using other remote sensing systems and produce more accurate and updated fuel maps.

SLS systems offer the potential for large-scale fuel estimation and mapping. They offer global coverage (quasi-global in the case of GEDI), with freely accessible data, eliminating the need for extensive field work. However, the structural information is derived from discrete footprints with significant spatial uncertainty, which is higher in GEDI, although it is possible that this issue will be improve in the near future. Although ICESat-2/ATLAS footprints are revisited every 91 days, GEDI footprints are unique not only in space but in time, as they are not systematically revisited due to the variable orbit of the ISS. This means it is almost impossible to study the temporal evolution of fuel in the same footprint and to produce updated maps of fuel types periodically using GEDI. However, it is possible to revisit a specific area by using multiple GEDI footprints from different time points and applying spatial interpolation processes. Furthermore, the GEDI system is currently suspended although it can be reactivated, but its operational lifespan is expected to be limited to the year

2030. Finally, an important aspect to consider is the positive results obtained, both in this thesis and in the reviewed studies, when SLS data are combined with optical satellite imagery and SAR data for estimating vegetation structural parameters and various forest fuels attributes. Passive satellite systems, such as Landsat or Sentinel-2, enable systematic monitoring of vegetation over time. Their integration with GEDI or ICESat-2/ATLAS could offer valuable auxiliary and periodical information on the physiological state of forest fuels, which could serve as a foundation for subsequent forest fuel management at landscape scales.

CHAPTER 8

CONCLUSIONS AND FURTHER WORK

8.1. MAIN CONCLUSIONS

Reducing the risk of wildfires is essential for conserving natural forest resources, preserving biodiversity, and promoting rural development. The threats posed by climate change, land abandonment, and wild reforestation make the efficient management of forests an essential objective for land and environmental development. Remote sensing provides valuable information on the state and distribution of vegetation in forests, serving as a powerful tool for the development of forecasting, prevention, and mitigation plans of fire risk. The *Strategic Guidelines for the Management of Wildfires in Spain* emphasize the need to integrate technological advances and land management across different spatial scales in order to reduce the risk and negative effects of wildfires on ecosystems, while at the same time adapting ecosystems and population to the occurrence of fire. In this context, a critical task for wildfire prevention is to explore new remote sensing systems at different scales to understand their capabilities and limitations to improve forest fuel identification and, therefore, better estimate the behavior and spread of fire on forest masses.

In this PhD Thesis, the capability of four emerging multiscale and three-dimensional remote sensing systems for estimating the Prometheus fuel types has been evaluated. Additionally, the integration capabilities of these systems with satellite and proximal optical imagery have been examined, as well as the synergies resulting from combining multiple three-dimensional systems. Fuels have been identified using two effective techniques: machine learning classification models and high-resolution quantitative data of the vertical volume of fuel. Machine learning models applied to GEDI, optical UAV, and UAV-LiDAR data successfully classified the Prometheus fuel types with high overall accuracy, with RF showing greater effectiveness than SVM for classification, and observing positive results when three-dimensional data were combined with multispectral indices. However, certain limitations were noted in distinguishing between similar fuel types, primarily due to the intrinsic characteristics of the systems analyzed. This issue could be solved by integrating data from different three-dimensional systems, in particular LiDAR data from UAV and HMLS. On the other hand, the vertical fuel volume quantitative data enhanced the differentiation of fuel types in forest areas with high structural complexity, owing to the very high point density provided by the HMLS system and the voxelization of the point clouds.

The highest accuracy in fuel classification was achieved by combining data from the UAV-LiDAR and HMLS systems. This effectiveness stemmed not only from

the very high point density provided by both sensors but also from their distinct data recording methods. The UAV-LiDAR system captured data from a zenith angle, allowing it to record the aerial parts of vegetation (i.e., tree crowns and upper parts of shrubs) with greater precision, as these were the first elements to interact with the laser. Conversely, the HMLS system recorded data from the ground, capturing the understory and the intermediate and lower strata of vegetation first, thus providing detailed information on these lower layers. As a result, the combination of both systems enabled accurate recording of the entire vertical structure of fuels, significantly enhancing the estimation of vertical continuity of understory fuels, which is a crucial factor for the precise identification of the Prometheus fuel types. However, it should be noted that the UAV-LiDAR system itself provided good overall accuracy without requiring HMLS data. Moreover, it was effective with a limited number of variables related to the structure and diversity of forest vegetation. In turn, the optical UAV yielded somewhat lower precision in the classification of the fuel types and it was required the inclusion of vegetation indices generated from multispectral images recorded by the UAV. Although the integration of optical UAV data with HMLS data has not been tested in this thesis, it can be hypothesized that this combination would enhance the estimation of the Prometheus fuel types based on the results obtained from the data integration of UAV-LiDAR and HMLS systems, as well as the successful results of ALS-LiDAR data integration from the PNOA project for height normalization of the photogrammetric point cloud. The GEDI SLS system effectively classified the Prometheus fuels; however, similar to the optical UAV, fuel classification improved significantly when vegetation indices were incorporated, in this case, from Landsat-8 OLI multispectral images. Integrating GEDI data with proximal platforms like UAVs or ground-based laser scanner systems to improve fuels classification is not feasible, not only due to the geolocation uncertainty of the GEDI footprints and the large number of said footprints, but just because the work scale of both platforms is very different. Conversely, combining GEDI with ALS systems could be effective, as their working scales are compatible, as well as with other existing SLS data, such as ICESat-2/ATLAS currently, or EDGE in the near future.

The semi-quantitative analysis of the four systems evaluated in this thesis, along with other contemporary systems relevant for forest management (ALS, TLS, and the ICESat-2/ATLAS SLS system), has highlighted the advantages of ALS, particularly non-commercial systems. ALS operates effectively at a landscape scale, making it well-suited for forest management tasks, with excellent data processing capabilities and high accuracy in fuel estimation. However, the

ratings for optical and LiDAR UAVs suggest they could rival ALS systems. In fact, they possess capabilities of a similar intrinsic nature or, in the case of UAV-LiDAR systems, superior to ALS, as indicated by the scores given in the analysis. In this context, UAV-LiDAR systems emerge as a strong alternative to ALS for forest fuel estimation, providing information with unprecedented spatial resolution. At the same time, they can become a significant support for ALS systems, as the high-precision data obtained with UAV-LiDAR systems can serve as ground-truth for the subsequent spatialization of results over larger areas using ALS systems, which operate at a more operational landscape level. On the other hand, optical UAVs lag in terms of the accuracy of fuel predictor variables, as their three-dimensional point clouds are derived from aerial photographs and, therefore, have a lower capacity to detect the strata beneath the tree canopy in areas of very dense vegetation. Nonetheless, their economic cost is much lower than that of UAV-LiDAR systems, which makes the trade-off between cost and performance an important factor to consider. Ground-based systems rank below UAVs in terms of performance for effective fuel management. However, their potential lies more in utilizing their extremely accurate ground-truth data for estimating fuels using other remote sensing systems. Consequently, they can serve as excellent substitutes for traditional forest inventory based on field work, as they operate at the forest plot scale and enable relatively fast data collection in the case of HMLS systems. Nonetheless, their high economic cost remains their primary drawback. Finally, SLS systems have received the lowest scores, with GEDI outperforming ICESat-2/ATLAS, considering that the initial objective of the latter was not the analysis of forest ecosystems. SLS systems provide a broad overview of fuel distribution across large areas, which, when combined with satellite passive sensors, can yield valuable systematic information on fuel status. Their main utility lies in using this information as a foundation for understanding the general distribution of fuels, allowing land managers to have a starting point for conducting forestry work at more appropriate scales for fuel management.

The main conclusions for each of the specific objectives detailed in Chapter 1 (Table 1.2) are as follows:

a. *Evaluate the performance of machine learning classification models for classifying Prometheus fuel types.*
    - The RF and SVM models successfully classified the Prometheus fuel types across the platforms evaluated for fuel classification. In all cases, RF showed equal or better performance than SVM. The models created with UAV-LiDAR data were also successfully spatialized.

- Some common limitations were observed in both UAV models regarding the classification accuracy of types 3 and 6, which correspond to the intermediate types of shrub and tree strata, respectively. These confusions were particularly significant when using optical UAV data, whereas they were quite minor using variables from the UAV-LiDAR system. Incorporating HMLS data into the UAV-LiDAR model nearly eliminated these confusions entirely.
- The prior selection of variables, essential for creating parsimonious models with explanatory power, was effectively performed using the Spearman's rank correlation coefficient, the Kruskal-Wallis H test, and the Dunn's test for multiple comparisons.

b. *Assess the capability of SLS systems to identify fuel types independently and in combination with optical images from satellites for improved fuel type classification.*
   - The use of height percentile metrics, canopy profile indices, and quantitative aboveground biomass data from the GEDI SLS system allowed to classify the Prometheus fuel types with an overall accuracy of 61.54% using RF and SVM-R models.
   - The fusion of structural data from GEDI with vegetation indices from Landsat-8 OLI multispectral images resulted in very good performance for fuel classification, achieving an overall accuracy of 83.71% with RF.
   - The fuel type that showed the worst performance in the models was type 4, which was mainly confused with type 3 and, to a lesser extent, with type 2. These confusions may be attributed to the observed GEDI data reduced performance in capturing information from the shrub and herbaceous strata. Type 4 was also confused with type 7, likely due to the observed tendency of GEDI to overestimate vegetation heights. Finally, the absence of type 6 data does not allow for any assessment of GEDI's ability to classify this fuel type.

c. *Explore the potential of integrating Digital Elevation Models (DEMs) generated from ALS data to normalize the heights of UAV photogrammetric point clouds.*
   - The generation of DEMs at different spatial resolutions from ALS-LiDAR data from the PNOA project allowed for the normalization of photogrammetric point cloud heights and resolved the issue of the absence of ground points in the photogrammetric data.
   - The point cloud normalized to the DEM of 0.50 m spatial resolution performed best for identifying the Prometheus fuel types when

photogrammetric point clouds and multispectral data were combined. On the other hand, the point cloud normalized to the DEM of 1 m spatial resolution was optimal for identifying the fuels when only point cloud data were used.

d. *Evaluate the capability of optical UAVs in identifying fuel types using structural, textural, and multispectral variables.*

- The best classification of the Prometheus fuel types was achieved by combining photogrammetric point clouds obtained with the RGB sensor and vegetation indices from the images acquired with the multispectral sensor, resulting in an overall accuracy of 71% with the RF model.
- When structural and textural variables were generated from multispectral photogrammetric point clouds, which had lower point density than those generated from the RGB sensor, the Prometheus types were classified with an overall accuracy of 66% with the RF model. Although this model's performance was lower, only a single flight would be necessary to obtain multispectral point clouds, assuming RGB and multispectral data cannot be obtained simultaneously. In this context, the user should evaluate whether reducing the time spent on data acquisition is worth accepting a generally lower model accuracy.
- The absence of multispectral variables in the models reduced the performance of the classification, thus yielding an overall accuracy of 64% using only structural and textural variables from the RGB photogrammetric point clouds. Therefore, when possible, it should be recommended to use multispectral data in conjunction with structural and/or textural data, as also seen in the GEDI models, as it provides additional information on the state of forest fuels, which aids in distinguishing the Prometheus fuel types.

e. *Evaluate the effectiveness of HMLS systems in delineating fuel types within structurally complex forest stands.*

- The HMLS system enabled the delineation of the Prometheus fuel types and corrected misestimated types in field observations caused by the high structural heterogeneity of fuels. This was achieved by quantifying the fuel volume in height strata with very high spatial resolution (5 cm), revealing common distributions for each fuel type. This facilitated the identification of specific Prometheus fuel types even in structurally complex forest plots and the construction of a more robust ground-truth.
- The extreme density of the point clouds obtained with the HMLS system was successfully processed and analyzed by transforming them into 5

cm^3 voxels. Furthermore, voxelization process enabled the quantification of the volume of fuel.

f. Assess the efficacy of UAV-LiDAR systems in classifying and mapping fuel types and evaluate the integration of HMLS data.

- The evaluated UAV-LiDAR system effectively classified the Prometheus fuel types using structural variables and forest diversity indices. The RF model delivered the best results, achieving an overall accuracy of 81.28%.
- The integration of quantitative fuel volume variables from the HMLS system into the UAV-LiDAR models significantly enhanced all classification models tested, almost entirely eliminating confusion between the fuel types. The RF model achieved the best results, with an overall accuracy of 95.05%.
- The mapping of the fuel types was feasible only with variables derived from UAV-LiDAR system, as the HMLS captured information solely within the forest plots and immediate surroundings. This limitation affects the use of HMLS systems for improving the mapping of fuel types across large areas. Despite this, the UAV-LiDAR models alone demonstrated good overall performance, with satisfactory mapping of all fuel types except type 6, which was predominantly categorized as type 7.

8.1. CONCLUSIONES PRINCIPALES

La reducción del riesgo de incendios forestales es esencial para conservar los recursos naturales forestales, preservar la biodiversidad y promover el desarrollo rural. Las amenazas que plantean el cambio climático, el abandono de las tierras y la reforestación silvestre hacen de la gestión eficiente de los bosques un objetivo fundamental para el desarrollo territorial y medioambiental. La teledetección proporciona una valiosa información sobre el estado y la distribución de la vegetación en los sistemas forestales, sirviendo como una potente herramienta para el desarrollo de planes de previsión, prevención y mitigación del riesgo de incendios. Las *Orientaciones Estratégicas para la Gestión de Incendios Forestales en España* enfatizan la necesidad de integrar los avances tecnológicos y la gestión del territorio a diferentes escalas espaciales para reducir el riesgo y los efectos negativos de los incendios forestales sobre los ecosistemas y, al mismo tiempo, adaptar los ecosistemas y la población a la ocurrencia de incendios. En este contexto, una tarea crucial para la prevención

de los incendios forestales es explorar nuevos sistemas de teledetección a distintas escalas para entender mejor sus capacidades y limitaciones para mejorar la identificación de los combustibles forestales y, por tanto, estimar mejor el comportamiento y propagación del fuego en las masas forestales.

En esta tesis se ha evaluado la capacidad de cuatro sistemas emergentes de teledetección multiescala y tridimensional para estimar los tipos de combustible Prometheus. Además, se ha examinado la capacidad de integración de estos sistemas con imágenes ópticas satelitales y proximales, así como las sinergias resultantes de combinar múltiples sistemas tridimensionales. Los combustibles han sido identificados utilizando dos técnicas efectivas: modelos de clasificación basados en *machine learning* y datos cuantitativos de alta resolución del volumen vertical del combustible. Los modelos de *machine learning* aplicados a los datos GEDI, UAV óptico y UAV-LiDAR clasificaron con éxito los tipos de combustible Prometheus con exactitudes generales altas, mostrando RF una mayor eficacia que SVM para la clasificación, y observando resultados positivos al combinar datos tridimensionales con índices multiespectrales. Sin embargo, se observaron ciertas limitaciones al distinguir entre tipos de combustible similares, debido principalmente a las características intrínsecas de los sistemas analizados. Este problema podría ser resuelto integrando datos de diferentes sistemas tridimensionales, en particular entre datos LiDAR procedentes de UAV y HMLS. Por otra parte, los datos cuantitativos del volumen vertical de combustible mejoraron la diferenciación de los tipos de combustible en zonas forestales de gran complejidad estructural, gracias a la altísima densidad de puntos proporcionada por el sistema HMLS y a la voxelización de dichas nubes de puntos.

La mayor precisión en la clasificación de los combustibles se consiguió combinando los datos de los sistemas UAV-LiDAR y HMLS. Esta efectividad se debió no sólo a la altísima densidad de puntos proporcionada por ambos sensores, sino también a sus distintos métodos de registro de datos. El sistema UAV-LiDAR capturó los datos desde un ángulo cenital, lo que le permitió registrar las partes aéreas de la vegetación (i.e., las copas de los árboles y las partes superiores de los arbustos) con mayor precisión, ya que estos eran los primeros elementos que interactuaban con el láser. Por otro lado, el sistema HMLS registró los datos desde el suelo, capturando primero el sotobosque y los estratos intermedios e inferiores de la vegetación, proporcionado así información detallada de estas capas inferiores. Como resultado, la combinación de ambos sistemas permitió un registro preciso de la totalidad de la estructura vertical de los combustibles, mejorando significativamente la estimación de la continuidad vertical de los combustibles del sotobosque, un factor muy importante para la

identificación precisa de los tipos de combustible Prometheus. No obstante, cabe señalar que el sistema UAV-LiDAR por sí mismo proporcionó buenas precisiones generales sin necesidad de usar datos HMLS. Además, fue eficaz con un número limitado de variables relacionadas con la estructura y la diversidad de la vegetación forestal. Por su parte, el UAV óptico alcanzó una precisión algo menor en la clasificación de los tipos de combustible, requiriendo la inclusión de índices de vegetación generados a partir de imágenes multiespectrales registradas por el UAV. Aunque en esta tesis no se ha probado la integración de datos ópticos UAV con datos HMLS, cabe plantear la hipótesis de que esta combinación mejoraría la estimación de los tipos de combustible Prometheus, dados los resultados obtenidos de la integración de datos UAV-LiDAR y HMLS, así como los resultados satisfactorios observados al integrar datos ALS-LiDAR del proyecto PNOA para la normalización de las alturas de la nube de puntos fotogramétrica. El sistema SLS GEDI clasificó satisfactoriamente los combustibles Prometheus; sin embargo, de manera similar al UAV óptico, la clasificación de los combustibles mejoró significativamente cuando se incorporaron índices de vegetación, en este caso, de imágenes multiespectrales de Landsat-8 OLI. La integración de datos GEDI con plataformas proximales como los UAVs o los sistemas láser terrestres para mejorar la clasificación de los combustibles no es factible, no sólo por la incertidumbre de geolocalización existente en las huellas de GEDI y el gran número de dichas huellas, sino porque la escala de trabajo de ambas plataformas muy diferentes. Por el contrario, la combinación de GEDI con sistemas ALS sí podría ser eficaz, ya que sus escalas de trabajo son compatibles, así como con otros datos SLS existentes, como ICESat-2/ATLAS en la actualidad o EDGE en un futuro próximo.

El análisis semicuantitativo de los cuatro sistemas evaluados en la tesis, junto con otros sistemas contemporáneos relevantes para la gestión forestal (sistemas ALS, TLS y ICESat-2/ATLAS), ha puesto de manifiesto las ventajas de los ALS, en particular de los sistemas no comerciales. Los ALS funcionan de forma efectiva a escala de paisaje, lo que los convierte en muy adecuados para tareas de gestión forestal, con una excelente capacidad de procesamiento de los datos y una gran precisión en la estimación de los combustibles. Sin embargo, las valoraciones de los UAVs ópticos y LiDAR sugieren que estos podrían rivalizar con los sistemas ALS. De hecho, poseen capacidades de naturaleza intrínseca similares o, en el caso de los sistemas UAV-LiDAR, superiores, como indican las puntuaciones otorgadas en el análisis. En este contexto, los sistemas UAV-LiDAR surgen como una fuerte alternativa a los ALS para la estimación del combustible forestal, proporcionando información con una resolución espacial

sin precedentes. Al mismo tiempo, pueden convertirse en un apoyo muy importante para los sistemas ALS, ya que los datos de alta precisión obtenidos con los sistemas UAV-LiDAR pueden actuar como verdad-terreno para la espacialización posterior de los resultados a áreas más grandes utilizando sistemas ALS, que operan a una escala más operativa de paisaje. Por otro lado, los UAV ópticos languidecen en cuanto a la precisión de las variables predictoras del combustible ya que sus nubes de puntos tridimensionales proceden de fotografías aéreas y, por tanto, tienen menor capacidad de detectar los estratos situados bajo las copas de los árboles en zonas de vegetación muy densa. No obstante, su coste económico es mucho menor que el de los sistemas UAV-LiDAR, lo que convierte el equilibrio entre costo y rendimiento en un factor importante a considerar. Los sistemas terrestres se sitúan por debajo de los UAVs en cuanto a rendimiento para una gestión eficaz de los combustibles. No obstante, su potencial reside más bien en la utilización de sus datos extremadamente precisos sobre el terreno para estimar los combustibles mediante otros sistemas de teledetección. En consecuencia, pueden servir como excelentes sustitutos de los inventarios forestales tradicionales basados en el trabajo de campo, ya que operan a escala de parcela forestal y permiten obtener datos de una manera relativamente rápida en el caso de los sistemas HMLS. Sin embargo, su elevado coste económico sigue siendo su principal inconveniente. Por último, los sistemas SLS han recibido las puntuaciones más bajas, superando GEDI a ICESat-2/ATLAS, considerando que el objetivo inicial de este último no era el análisis de ecosistemas forestales. Los sistemas SLS proporcionan una visión general de la distribución del combustible en grandes áreas que, combinada con sensores pasivos satelitales, puede arrojar una valiosa información sistemática sobre el estado de los combustibles. Su principal utilidad radica en el uso de esta información como base para conocer la distribución general de los combustibles, permitiendo a los gestores del territorio disponer de un punto de partida para realizar trabajos forestales a escalas más adecuadas para la gestión del combustible.

Las principales conclusiones para cada objetivo específico, detallados en el Capítulo 1 (Tabla 1.2), son las siguientes:

a *Evaluar el rendimiento de los modelos de clasificación machine learning para clasificar los tipos de combustible Prometheus*.

- Los modelos RF y SVM clasificaron satisfactoriamente los tipos de combustible Prometheus en todas las plataformas evaluadas para clasificar combustibles. En todos los casos, RF mostró igual o mejor

rendimiento que SVM. Los modelos creados con datos UAV-LiDAR fueron asimismo satisfactoriamente espacializados.

- Algunas limitaciones comunes fueron observadas en ambos modelos UAV relacionadas con la precisión de la clasificación de los tipos 3 y 6, que corresponden con tipos intermedios de estratos arbustivos y arbóreos, respectivamente. Estas confusiones fueron particularmente significativas cuando se usaron datos del UAV óptico, mientras que fueron menores usando variables del sistema UAV-LiDAR. La incorporación de datos HMLS en el modelo UAV-LiDAR eliminó casi por completo estas confusiones.
- La selección previa de variables, esencial para crear modelos parsimoniosos con poder explicativo, se llevó a cabo satisfactoriamente usando el coeficiente de correlación de Spearman, el test H de Kruskal-Wallis y el test de Dunn de comparaciones múltiples.

b Valorar la capacidad de los sistemas SLS para identificar tipos de combustible de forma independiente y en combinación con imágenes ópticas satelitales para mejorar la clasificación de los tipos de combustibles.

- El uso de métricas de percentiles de altura, índices del perfil del dosel y datos cuantitativos de la biomasa aérea superficial del sistema SLS GEDI permitió clasificar los tipos de combustibles Prometheus con una exactitud general del 61,54% usando modelos RF y SVM-R.
- La fusión de la información estructural de GEDI con índices de vegetación procedentes de imágenes multiespectrales de Landsat-8 OLI dio como resultado un muy buen rendimiento de la clasificación del combustible, logrando una exactitud general del 83,71% con RF.
- El tipo de combustible que mostró un peor rendimiento en los modelos fue el tipo 4, que fue confundido principalmente con el tipo 3 y, en menor medida, con el tipo 2. Estas confusiones podrían atribuirse a un menor rendimiento observado de los datos GEDI para capturar información de los estratos arbustivos y herbáceos. El tipo 4 también fue confundido con el tipo 7, probablemente debido a la tendencia observada de GEDI a sobrestimar las alturas de la vegetación. Finalmente, la ausencia de datos del tipo 6 no permite hacer ninguna valoración sobre la capacidad de GEDI para clasificar este tipo de combustible.

c *Explorar el potencial de integrar Modelos Digitales de Elevaciones (MDEs) generados a partir de datos ALS para normalizar las alturas de las nubes de puntos fotogramétricas.*

- La generación de MDEs a diferentes resoluciones espaciales procedentes de datos ALS-LiDAR del proyecto PNOA permitió la normalización de las alturas de las nubes de puntos fotogramétricas y solucionó el problema de la ausencia de puntos de suelo en los datos fotogramétricos.
- La nube de puntos normalizada con el MDE de 0,50 m de resolución espacial mostró un mejor rendimiento para identificar los tipos de combustible Prometheus cuando se combinaron las nubes de puntos fotogramétricas y los datos multiespectrales. Por otro lado, la nube de puntos normalizada con el MDE de 1 m de resolución espacial fue óptima para identificar los combustibles cuando sólo se usaron datos procedentes de la nube de puntos.

d *Evaluar la capacidad de los UAVs ópticos para identificar tipos de combustible utilizando variables estructurales, texturales y multiespectrales.*

- La mejor clasificación de los tipos de combustible Prometheus fue alcanzada al combinar la nube de puntos fotogramétrica obtenida del sensor RGB y los índices de vegetación procedentes de imágenes adquiridas con el sensor multiespectral, dando como resultado una exactitud general del 71% con el modelo RF.
- Cuando las variables estructurales y texturales fueron generadas a partir de la nube de puntos fotogramétrica del sensor multiespectral, de menor densidad de puntos que la generada con el sensor RGB, los tipos Prometheus fueron clasificados con una exactitud general del 66% con el modelo RF. Aunque el rendimiento del modelo fue menor, sólo sería necesario un único vuelo para obtener nubes de puntos multiespectrales, asumiendo que los datos RGB y multiespectrales no pueden ser obtenidos de manera simultánea. En este contexto, el usuario debería de evaluar si la reducción del tiempo dedicado a la adquisición de datos justifica la aceptación de una exactitud del modelo más baja.
- La ausencia de variables multiespectrales en los modelos redujo el rendimiento de la clasificación, dando como resultado una exactitud general del 64% al utilizar únicamente variables estructurales y texturales de las nubes de puntos fotogramétricas del sensor RGB. Por lo tanto, cuando sea posible, sería recomendable utilizar datos multiespectrales junto con datos estructurales y/o texturales, como se observó también en los modelos de GEDI, ya que proporcionan

información adicional sobre el estado de los combustibles forestales, ayudando a distinguir los tipos de combustible Prometheus.

e *Evaluar la eficacia de los sistemas HMLS para definir tipos de combustible en parcelas forestales estructuralmente complejas*.

- El sistema HMLS posibilitó la definición de los tipos de combustible Prometheus y corrigió los tipos mal estimados en las observaciones de campo causados por la alta heterogeneidad estructural de los combustibles. Esto se consiguió al cuantificar el volumen de combustible en estratos de altura con una resolución muy alta (5 cm), desvelando distribuciones comunes para cada tipo de combustible. Esto facilitó la identificación de tipos de combustible Prometheus específicos incluso en parcelas forestales estructuralmente complejas y la construcción de una verdad-terreno más robusta.
- La extrema densidad de las nubes de puntos obtenidas con el sistema HMLS fue procesada y analizada con éxito al transformarlas en vóxeles de 5 cm^3. Además, el proceso de voxelización permitió cuantificar el volumen de combustible.

f *Valorar la eficacia de los sistemas UAV-LiDAR para clasificar y espacializar tipos de combustible y evaluar la integración con datos HMLS*.

- El sistema UAV-LiDAR evaluado clasificó eficazmente los tipos de combustible Prometheus utilizando variables estructurales e índices de diversidad forestal. El modelo RF proporcionó los mejores resultados, alcanzando una exactitud general del 81,28%.
- La integración de variables cuantitativas del volumen del combustible del sistema HMLS en los modelos UAV-LiDAR mejoró sustancialmente todos los modelos de clasificación probados, eliminando casi por completo la confusión entre los tipos de combustible. El modelo RF alcanzó los mejores resultados, con una exactitud general del 95,05%.
- La cartografía de los tipos de combustible fue factible únicamente con variables derivadas del sistema UAV-LiDAR, ya que el HMLS capturó información únicamente dentro de las parcelas forestales y sus entornos más inmediatos. Esta limitación afecta el uso de los sistemas HMLS para mejorar la cartografía de los tipos de combustible en grandes áreas. A pesar de esto, los modelos UAV-LiDAR por sí solos demostraron un buen rendimiento general, con una cartografía satisfactoria de todos los tipos de combustible, excepto el tipo 6, que fue predominantemente categorizado como tipo 7.

8.2. FUTURE RESEARCH PROPOSALS

All the remote sensing systems evaluated in this PhD Thesis have demonstrated capabilities for improving the estimation and classification of the Prometheus fuel types. However, more research is needed to further improve the efficiency of forest fuel management. Climate change presents an uncertain future, potentially leading to greater climatic extremes and more devastating wildfires. The ongoing trend of rural abandonment, particularly in Mediterranean environments, is especially concerning, as it results in an increase of fuel loads and continuity between understory and canopy fuels. These factors, along with continuous advancements in remote sensing systems, processing and analysis tools, and statistical methods, highlight several potential future research proposals.

In this PhD Thesis, classification models based on machine learning, a well-established technique in forest studies, have been developed. The application of more advanced statistical techniques that have emerged in recent years, like deep learning, could provide more accurate results in fuel classification. Among deep learning methods, neural networks and generative networks could offer potential for classifying images and, similarly, forest variables from three-dimensional point clouds related to forest fuels.

New ongoing satellite remote sensing systems that will be operational in the near future, anticipated to offer enhanced performance, should be evaluated for their potential to improve forest fuel estimation. The EDGE system, currently under development and designed for forest ecosystems, will incorporate advanced scanning technologies and offer systematic, global coverage. Additionally, it is likely that passive satellite systems, which are continuously updated, will provide increasingly detailed data on Earth's forest ecosystems. Similarly, ongoing advancements in proximal remote sensing, particularly with UAVs, may enable greater area coverage in less time and increase point density, thereby providing more detailed fuel information over larger areas. Applying the methods used in this thesis, as well as new proposals presented in this section to the next generation of UAVs, supposes an opportunity to further enhance the identification and mapping of forest fuels.

UAV data can be acquired using various methods, allowing operators to adjust parameters such as flight height, type of mapping, overlap between photographs, and scan angle, among others. While the parameters employed in this PhD Thesis were adjusted based on prior experience and prior research, a detailed examination of their influence on improving fuel identification is necessary. This

could be particularly relevant for enhancing data acquisition with optical UAVs, which face limitations compared to UAV-LiDAR systems, especially in capturing understory fuels and the ground in dense forest areas.

Finally, given the positive results achieved by combining three-dimensional information with multispectral images for fuel identification, exploring the use of dual UAV systems equipped with both LiDAR sensor and multispectral camera would be valuable. The use of multispectral LiDAR systems may also be of great interest, allowing to capture in a single instrument the three-dimensional information of the forest and the spectral characteristics of the vegetation. Such an approach could enable the simultaneous acquisition of both types of information quickly and effectively, potentially leading to more accurate identification of fuel types.

8.2. LÍNEAS DE TRABAJO FUTURAS

Todos los sistemas de teledetección evaluados en esta tesis han demostrado su capacidad para mejorar la estimación y clasificación de los tipos de combustible Prometheus. No obstante, es necesario seguir investigando para mejorar la gestión eficiente de los combustibles forestales. El cambio climático presenta un futuro incierto, que puede conducir a mayores extremos climáticos y a incendios forestales más devastadores. La actual tendencia de abandono rural, particularmente en los entornos mediterráneos, es especialmente preocupante, ya que resulta en un aumento de la carga de combustible y de la continuidad entre los combustibles de sotobosque y de copas. Estos factores, junto con los continuos avances en los sistemas de teledetección, las herramientas de procesado y análisis y los métodos estadísticos, ponen de manifiesto varias posibles propuestas de investigación futuras.

En esta tesis se han generado modelos de clasificación basados en *machine learning*, una técnica reconocida en estudios forestales. La aplicación de técnicas estadísticas más avanzadas que han surgido en los últimos años, como el *deep learning*, podría proporcionar resultados más precisos en la clasificación de combustibles. Entre los métodos de *deep learning*, las redes neuronales y las redes generativas podrían ofrecer potencial para clasificar imágenes y, del mismo modo, variables forestales procedentes de nubes de puntos tridimensionales relacionadas con los combustibles forestales.

Los nuevos sistemas de teledetección satelitales en curso que estarán operativos en un futuro próximo, y que se prevé que ofrezcan un mayor rendimiento, deberían de evaluarse por su potencial para mejorar la estimación de los

combustibles forestales. El sistema EDGE, actualmente en desarrollo y diseñado para ecosistemas forestales, incorporará tecnologías avanzadas de escaneado y ofrecerá una cobertura sistemática global. Además, es probable que los sistemas satelitales pasivos, continuamente en actualización, proporcionen datos cada vez más detallados de los ecosistemas forestales terrestres. Del mismo modo, los avances que se están produciendo en la teledetección proximal, especialmente con los vehículos aéreos no tripulados, pueden permitir una mayor cobertura de áreas en menos tiempo y aumentar la densidad de puntos, proporcionando así información más detallada sobre los combustibles en áreas más extensas. La aplicación de los métodos utilizados en la presente tesis, así como las nuevas propuestas presentadas en esta sección a la siguiente generación de UAVs, supone una oportunidad para mejorar aún más la identificación y cartografía de los combustibles forestales.

Los datos de los UAV pueden adquirirse utilizando diversos métodos, permitiendo a los operadores ajustar parámetros como la altura de vuelo, el tipo de cartografía, el solapamiento entre fotografías y el ángulo de visión, entre otros. Aunque los parámetros empleados en esta tesis se ajustaron basándose en experiencia previa y en investigaciones previas, es necesario un examen más detallado de su influencia en la mejora de la identificación de combustibles. Esto podría ser particularmente relevante para mejorar la adquisición de datos con UAV ópticos, que se enfrentan a limitaciones respecto a los sistemas UAV-LiDAR, especialmente en la captura de los combustibles del sotobosque y del suelo en zonas forestales densas.

Por último, dados los resultados positivos obtenidos al combinar información tridimensional con imágenes multiespectrales para la identificación de los combustibles, sería valioso explorar el uso de sistemas UAV duales equipados tanto con sensor LiDAR como con cámara multiespectral. También puede ser de gran interés el uso de sistemas LiDAR multiespectrales, que permitan capturar en un único instrumento la información tridimensional del bosque y las características espectrales de la vegetación. Este enfoque permitiría la adquisición simultánea de ambos tipos de información de manera rápida y eficaz, posibilitando una identificación más precisa de los tipos de combustible.

REFERENCES

A

Abdollahi, A. and Yebra, M., 2023. Forest fuel type classification: Review of remote sensing techniques, constraints and future trends. *Journal of Environmental Management* 342, 118315. https://doi.org/10.1016/j.jenvman.2023.118315.

Abram, N.J., Henley, B.J., Gupta, A.S., Lippmann, T.J.R., Clarke, H., Dowdy, A.J., Sharples, J.J., Nolan, R.H., Zhang, T., Wooster, M.J., Wurtzel, J.B., Meissner, K.J., Pitman, A.J., Ukkola, A.M., Murphy, B.P., Tapper, N.J., and Boer, M.M., 2021. Connections of climate change and variability to large and extreme forest fires in southeast Australia. *Communications Earth & Environment* 2, 8. https://doi.org/10.1038/s43247-020-00065-8.

Adedapo, S.M. and Zurqani, H.A., 2024. Evaluating the performance of various interpolation techniques on Digital Elevation Models in highly dense forest vegetation environment. *Ecological Informatics* 81, 102646. https://doi.org/10.1016/j.ecoinf.2024.102646.

Adhikari, H., Valbuena, R., Pellikka, P.K.E., and Heiskanen, J., 2020. Mapping forest structural heterogeneity of tropical montane forests remnants from airborne laser scanning and Landsat time series. *Ecological Indicators* 108, 105739. https://doi.org/10.1016/j.ecolind.2019.105739.

Ahearn, S.C., 1988. Combining laplacian images of different spatial frequencies (scales): Implications for remote-sensing image analysis. *IEEE Transactions on Geoscience and Remote Sensing* 26(6), 826-831.

Aktürk, E., Popescu, S.C., and Malambo, L., 2023. ICESat-2 for canopy cover estimation at large-scale on cloud-based platform. *Sensors* 23(7), 3394. https://doi.org/10.3390/s23073394.

Albini, F., 1976. Estimating wildfire behavior and effects. In USDA Forest Service, Intermountain Forest and Range Experiment Station, General Technical Report INT-30.

Aldred, A.H. and Bonnor, G.M., 1985. Application of airborne lasers to forest surveys. Petawawa National Forestry Institute. Canadian Forestry Service, Information Report PI-X-51.

Alonso-Benito, A., Arroyo, L.A., Arbelo, M., Hernández-Leal, P., and González-Calvo, A., 2012. Pixel and object-based classification approaches for mapping forest fuel types in Tenerife island from ASTER data. International *Journal of Wildland Fire* 22(3), 306-317. https://doi.org/10.1071/WF11068.

Alonso-Rego, C., Arellano-Pérez, S., Cabo, C., Ordóñez, C., Álvarez-González, J.G., Díaz-Varela, R.A., and Ruiz-González, A.D., 2020. Estimating fuel loads and structural characteristics of shrub communities by using Terrestrial Laser Scanning. *Remote Sensing* 12(22), 3704. https://doi.org/10.3390/rs12223704.

Améztegui, A., Brotons, L., and Coll, L., 2010. Land-use changes as major drivers of mountain pine (Pinus uncinata Ram.) expansion in the Pyrenees. *Global Ecology and Biogeography* 19, 632-641. https://doi.org/10.1111/j.1466-8238.2010.00550.x.

Andersen, H.E., McGaughey, R.J., and Reutebuch, S.E., 2005. Estimating forest canopy fuel parameters using LiDAR data. *Remote Sensing of Environment* 94, 441-449. https://doi.org/10.1016/j.rse.2004.10.013.

Anderson, E.S., Thompson, J.A., Crouse, D.A., and Austin, R.E., 2006. Horizontal resolution and data density effects on remotely sensed LiDAR-based DEM. *Geoderma* 132(3-4), 406-415. https://doi.org/10.1016/j.geoderma.2005.06.004.

Arkin, J., Coops, N.C., Daniels, L.D., and Plowright, A., 2021. Estimation of vertical fuel layers in tree crowns using high density LiDAR data. *Remote Sensing* 13(22), 4598. https://doi.org/10.3390/rs13224598.

Arroyo, L.A., Healey, S.P., Cohen, W.B., Cocero, D., and Manzanera, J.A., 2006. Using object-oriented classification and high-resolution imagery to map fuel types in a Mediterranean region. *Journal of Geophysical Research* 111, G04S04. https://doi.org/10.1029/2005JG000120.

Arroyo, L.A., Pascual, C., and Manzanera, J.A., 2008. Fire models and methods to map fuel types: The role of remote sensing. *Forest Ecology and Management* 256, 1239-1252. https://doi.org/10.1016/j.foreco.2008.06.048.

Ascoli, D., Moris, J.V., Marchetti, M., and Sallustio, L., 2021. Land use change towards forests and wooded land correlates with large and frequent wildfires in Italy. *Annals of Silvicultural Research* 46(2), 177-188. https://doi.org/10.12899/asr-2264.

Ascoli, D., Vacchiano, G., Scarpa, C., Arca, B., Barbati, A., Elia, M., Esposito, A., Garfi, V., Lovreglio, R., Mariota, P., Marchetti, M., Marchi, E., Meytre, S., Ottaviano, M., Pelizzaro, G., Rizzolo, R., Sallustio, L., Salis, M., Sirca, C., Valese, E., Ventura, A., and Bacciu, V., 2022. Harmonized dataset of surface fuels under Alpine, temperate and Mediterranean conditions in Italy. A synthesis supporting fire management. *iForest - Biogeosciences and Forestry* 13, 513-522. https://doi.org/10.3832/ifor3587-013.

Ashowrth, A., Evans, D.L., Cooke, W.H., Londo, A., Collins, C., and Neuenschwander, A., 2010. Predicting southeastern forest canopy heights and fire fuel models using GLAS data. *Photogrammetric Engineering & Remote Sensing* 76(8), 915-922.

Assmann, J.J., Moeslund, J.E., Treier, U.A., and Normand, S., 2022. EcoDes-DK15: high-resolution ecological descriptors of vegetation and terrain derived from Denmark's national Airborne Laser Scanning data set. *Earth System Science Data* 14(2), 823-844. https://doi.org/10.5194/essd-14-823-2022.

Axelsson, P., 2000. DEM generation from laser scanner data using adaptive TIN models. *International Archive of Photogrammetry and Remote Sensing* 23, 110-117.

B

Bakuła, M., Oszczak, S., and Pelc-Mieczkowska, R., 2009. Performance of RTK positioning in forest conditions: Case study. *Journal of Surveying Engineering* 135(3), 125-130. https://doi.org/10.1061/(ASCE)0733-9453(2009)135:3(125).

Barnes, E.M., Clarke, T.R., and Richards, S.E., 2000. Coincident detection of crop water stress, nitrogen status and canopy density using ground-based multispectral data. *Proceedings of the 5th International Conference on Precision Agriculture and Other Resource Managements*. 16-19 July, Bloomington, MN, USA.

Barton, J., Gorte, B., Eusuf, M.S.R.S., and Zlatanova, S., 2020. A voxel-based method to estimate near-surface and elevated fuel from dense lidar point clouds for hazard reduction burning. In *Proceedings of the 13th Geoinformation for Disaster Management Conference*. ISPRS Annals of the Photogrammetry, Remote Sensing and Spatial Information Sciences, VI-3/W1-2020. Sydney, Australia.

Bauwens, S., Bartholomeus, H., Calders, K., and Lejeune, P., 2016. Forest inventory with terrestrial LiDAR: A comparison of static and hand-held mobile laser scanning. *Forests* 7, 127. https://doi.org/10.3390/f7060127.

Beck, J., Wirt, B., Armston, J., Hofton, M., Luthcke, S., and Tang, H., 2021. Global Ecosystem Dynamics Investigation (GEDI) Level 2 User Guide, Version 2.0.

Beland, M., Parker, G., Sparrow, B., Harding, D., Chasmer, L., Phinn, S., Antonarakis, A., and Strahler, A., 2019. On promoting the use of LiDAR systems in forest ecosystem research. *Forest Ecology and Management* 450, 117484. https://doi.org/10.1016/j.foreco.2019.117484.

Benson, A., Greenlee, J., and Langenheim, J., 1982. Assessment of wildland fuel hazards in Big Basin Redwoods State Park, California. In *Proceedings of the 5th International Symposium on Computer-Assisted Cartography*. Crystal City, VI, USA.

Bergen, K.M., Goetz, S.J., Dubayah, R., Henebry, G.M., Hunsaker, C.T., Imhoff, M.L., Nelson, R.F, Parker, G.G., and Radeloff, V.C., 2009. Remote sensing of vegetation 3-D structure for biodiversity and habitat: Review and implications for LiDAR and radar spaceborne missions. *Journal of Geophysical Research: Biogeosciences* 114, G2. https://doi.org/10.1029/2008JG000883.

Blackburn, R.C., Buscaglia, R., and Sánchez-Meador, A.J., 2021. Mixtures of airborne LiDAR-based approaches improve predictions of forest structure. *Canadian Journal of Forest Research* 51(8), 1106-1116. https://doi.org/10.1139/cjfr-2020-0506.

Braun, A.Ch., Fassnacht, F., Valencia, D., and Sepulveda, M., 2021a. Consequences of land-use change and the wildfire disaster of 2017 for the central Chilean biodiversity hotspot. *Regional Environmental Change* 21, 37. https://doi.org/10.1007/s10113-021-01756-4.

Braun, J., Braunová, H., Suk, T., Michal, O., Petovský, P., and Kuric, I., 2021b. Structural and geometrical vegetation filtering. Case study on mining area point cloud acquired by UAV Lidar. *Acta Montanistica Slovaca* 26(4), 661-674. https://doi.org/10.46544/AMS.v26i4.06.

Brede, B., Lau, A., Bartholomeus, H.M., and Kooistra, L., 2017. Comparing RIEGL RiCOPTER UAV LiDAR derived canopy height and DBH with terrestrial LiDAR. *Sensors* 17(10), 2371. https://doi.org/10.3390/s17102371.

Bretar, F., Chauve, A., Mallet, C., and Jutzi B., 2008. Managing full waveform LiDAR data: A challenging task for the forthcoming years. In *Proceedings of the ISPRS Congress 2008*, Beijing, China.

Briechie, S., Krzystek, P., and Vosselman, G., 2020. Classification of tree species and standing dead trees by fusing UAV-based LiDAR data and multispectral imagery in the 3D deep neural network PointNet++. *ISPRS Annals of the Photogrammetry, Remote Sensing and Spatial Information Sciences* V-2-2020, 203-2010. https://doi.org/10.5194/isprs-annals-V-2-2020-203-2020.

Burgan, R.E. and Shasby, M.B., 1984. Mapping broad-area fire potential from digital fuel, terrain, and weather data. *Journal of Forestry* 82(4), 228-231.

C

Cabo, C., Laino, D., Janvier, R., Prendes, C., Ordoñez, C., Nikanovas, T., Doerr, S., and Santin, C., 2024. 3DFin: A software for 3D forest inventory in terrestrial point clouds. EGU General Assembly 2024, Vienna, Austria. https://doi.org/10.5194/egusphere-egu24-12375.

Calders, K., Jonckheere, I., Nightingale, J., and Vastaranta, M., 2020a. Remote sensing technology applications in forestry and REDD+. *Forests* 11, 188. https://doi.org/10.3390/f11020188.

Calders, K., Adams, J., Armston, J., Bartholomeus, H., Bauwens, S., Bentley, L.P., Chave, J., Danson, F.M., Demol, M., Disney, M., Gaulton, R., Moorthy, S.M.K., Levick, S.R., Saarinen, N., Schaaf, C., Stovall, A., Terryn, L., Wilkes, P., and Verbeeck, H., 2020b. Terrestrial laser scanning in forest ecology: Expanding the horizon. *Remote Sensing of Environment* 251, 112102. https://doi.org/10.1016/j.rse.2020.112102.

Cao, L., Liu, H., Fu, X., Zhang, Z., Shen, X., and Ruan, H., 2019. Comparison of UAV LiDAR and Digital Aerial Photogrammetry point clouds for estimating forest structural attributes in subtropical planted forests. *Forests* 10(2), 145. https://doi.org/10.3390/f10020145.

Carabajal, C.C. and Boy, J.P., 2020. ICESat-2 altimetry as geodetic control. *The International Archives of Photogrammetry, Remote Sensing and Spatial Information Sciences* XLIII-B3-2020, 1299-1306. https://doi.org/10.5194/isprs-archives-XLIII-B3-2020-1299-2020.

Carbone, A., Spiller, D., and Laneve, G., 2023. Fuel type mapping using a CNN-based remote sensing approach: A case study in Sardinia. *Fire* 6, 395. https://doi.org/10.3390/fire6100395.

Casbeer, D.W., Beard, R.W., McLain, T.W., Li, S.M., and Mehra, R.K., 2005. Forest fire monitoring with multiple small UAVs. In *Proceedings of the American Control Conference 2005*, Portland, OR, USA. https://doi.org/10.1109/ACC.2005.1470520.

Chen, C., Li, Y., Li, W., and Dai, H., 2013. A multiresolution hierarchical classification for filtering airborne LiDAR data. *ISPRS Journal of Photogrammetry and Remote Sensing* 82, 1-9. https://doi.org/10.1016/j.isprsjprs.2013.05.001

Chen, T., Song, C., Luo, S., Ke, L., Liu, K., and Zhu, J., 2022. Monitoring global reservoirs using ICESat-2: Assessment on spatial coverage and application potential. *Journal of Hydrology* 604, 127257. https://doi.org/10.1016/j.jhydrol.2021.127257

Chen, Y., Zhu, X., Yebra, M., Harris, S., and Tapper, N., 2016. Strata-based forest fuel classification for wild fire hazard assessment using terrestrial LiDAR. *Journal of Applied Remote Sensing* 10(4), 046025. https://doi.org/10.1117/1.JRS.10.046025.

Chirici, G., Scotti, R., Montaghi, A., Barbati, A., Cartisano, R., López, G., Marchetti, M., McRoberts, R.E., Olsson, H., and Corona, P., 2013. Stochastic gradient boosting classification trees for forest fuel types mapping through airborne laser scanning and IRS LISS-III imagery. *International Journal of Applied Earth Observation and Geoinformation* 25, 87-97. https://doi.org/10.1016/j.jag.2013.04.006.

Chuvieco, E. and Congalton, R.G., 1989. Application of remote sensing and Geographic Information Systems to forest fire hazard mapping. *Remote Sensing of Environment* 29(2), 147-159. https://doi.org/10.1016/0034-4257(89)90023-0.

Chuvieco, E. and Salas, J., 1996. Mapping the spatial distribution of forest fire danger using GIS. *International Journal of Geographical Information Systems* 10(3), 333-345. https://doi.org/10.1080/02693799608902082.

Chuvieco, E., 2008. Teledetección ambiental. La observación de la Tierra desde el Espacio. Editorial Ariel, S.A., Barcelona, Spain. ISBN: 978-84-344-8073-3.

Chuvieco, E., 2009. Earth observation of wildland fires in Mediterranean ecosystems. Springer Berlin, Heidelberg, Germany. ISBN: 978-3-642-01753-7. https://doi.org/10.1007/978-3-642-01754-4.

Cohen, W.B., 1989. Potential utility of the TM Tasseled Cap multispectral data transformation for crown fire hazard assessment. In Proceedings of the Agenda for the 90's. Technical Papers 1989 ASPRS/ACSM Annual Convention, Baltimore, MD, USA.

Cosentino, M., 1977. Fuel mapping in relation to the management of brushlands and timberlands in Mendocino County, California. Berkeley. Space Sciences Laboratory.

Coskuner, K.A., Vatandaşlar, C., Ozturk, M., Harman, I., Bilgili, E., Karahalil, U., Berber, T., and Gormus, E.T., 2023. Estimating Mediterranean stand fuel characteristics using handheld mobile laser scanning technology. *International Journal of Wildland Fire* 32(9), 1347-1363. https://doi.org/10.1071/WF23005.

Cova, G.R., Prichard, S.J., Rowell, E., Drye, B., Eagle, P., Kennedy, M.C., and Nemens, D.G., 2023. Evaluating close-range photogrammetry for 3D understory fuel characterization and biomass prediction in pine forests. *Remote Sensing* 15(19), 4837. https://doi.org/10.3390/rs15194837.

Crespo-Calvo, R., Varo-Martínez, M.A., Ruiz-Gómez, F., Ariza-Salamanca, A.J., and Navarro-Cerrillo, R.M., 2023. Improvements of fire fuels attributes maps by integrating field inventories, low density ALS, and satellite data in complex Mediterranean forests. *Remote Sensing* 15(8), 2023. https://doi.org/10.3390/rs15082023.

Crespo-Peremarch, P., Piotr, T., Coops, N.C., and Ruiz, L.A., 2018. Characterizing understory vegetation in Mediterranean forests using full-waveform airborne laser scanning data. *Remote Sensing of Environment 217*, 400-413. https://doi.org/10.1016/j.rse.2018.08.033.

Crespo-Peremarch, P., Torralba, J., Carbonell-Rivera, J.P., and Ruiz, L.A., 2020. Comparing the generation of DTM in a forest ecosystem using TLS, ALS and UAV-DAP, and different software tools. *The International Archives of the Photogrammetry, Remote Sensing and Spatial Information Sciences*, Volume XLIII-B3-2020, 575-582. https://doi.org/10.5194/isprs-archives-XLIII-B3-2020-575-2020.

Cserép, M. and Lindenbergh, R., 2023. Distributed processing of Dutch AHN laser altimetry changes of the built-up area. *International Journal of Applied Earth Observation and Geoinformation* 116, 103174. https://doi.org/10.1016/j.jag.2022.103174.

Cuadrat, J.M., 2004. El clima de Aragón. In Peña J.L., Longares, L.A., and Sánchez, M. (eds), *Geografía Física de Aragón. Aspectos Generales y Temáticos*. Universidad de Zaragoza e Institución Fernando el Católico. ISBN: 84-96214-29-X. Zaragoza, Spain.

Cuadrat, J.M., Saz, M.Á., and Vicente, S.M., 2007. Atlas Climático de Aragón. Servicio de Información y Educación Ambiental, Dirección General de Calidad Ambiental y Cambio Climático, Departamento de Medio Ambiente, Gobierno de Aragón: Zaragoza, Spain.

D

Dai, W., Yang, B., Liang, X., Dong, Z., Huang, R., Wang, Y., and Li, W., 2019. Automated fusion of forest airborne and terrestrial point clouds through canopy density analysis. *ISPRS Journal of Photogrammetry and Remote Sensing* 156, 94-107. https://doi.org/10.1016/j.isprsjprs.2019.08.008.

Deeming, J.E., Lancaster, J.W., Fosberg, M.A., Furman, R.W., and Schroeder, M.J., 1972. The National Fire-Danger Rating System. USDA Forest Service Research Paper RM-84. Intermountain Forest and Range Experiment Station.

Deeming, J.E., Burgan, R.E., and Cohen, J.D., 1977. National Fire-Danger Rating System - 1978, General Technical Report INT-GTR-39. Ogden, UT. USDA Forest service, Intermountain Forest and Range Experiment Station.

Del Perugia, B., Giannetti, F., Chirici, G., and Travaglini, D., 2019. Influence of scan density on the estimation of single-tree attributes by hand-held mobile laser scanning. *Forests* 10(3), 277. https://doi.org/10.3390/f10030277.

Dhargay, S., Lyell, C.S., Brown, T.P., Inbar, A., Sheridan, G.J., and Lane, P.N.J., 2022. Performance of GEDI space-borne LiDAR for quantifying structural variation in temperate forests of south-eastern Australia. *Remote Sensing* 14, 3615. https://doi.org/10.3390/rs14153615.

Di Stefano, F., Chiappini, S., Gorreja, A., Balestra, M., and Pierdicca, R., 2021. Mobile 3D scan LiDAR: a literature review. *Geomatics, Natural Hazards and Risk* 12(1), 2387-2429. https://doi.org/10.1080/19475705.2021.1964617.

Domingo, D., Lamelas, M.T., Montealegre, A.L., and de la Riva, J., 2017. Comparison of regression models to estimate biomass losses and CO_2 emissions using low-density airborne laser scanning data in a burnt Aleppo pine forest. European Journal of *Remote Sensing* 50(1), 384-396. https://doi.org/10.1080/22797254.2017.1336067.

Domingo, D., Lamelas, M.T., Montealegre, A.L., García-Martín, A., and de la Riva, J., 2018. Estimation of total biomass in Aleppo pine forest stands applying parametric and nonparametric methods to low-density airborne laser scanning data. *Forests* 9, 158-175. https://doi.org/10.3390/f9040158.

Domingo, D., 2019. Characterization of Mediterranean Aleppo pine forest using low-density ALS data. PhD Thesis. University of Zaragoza, Spain. https://zaguan.unizar.es/record/99288/files/?ln=en.

Domingo, D., Montealegre, A.L., Lamelas, M.T., García-Martín, A., de la Riva, J., Rodríguez-Puerta, F., and Alonso, R., 2019a. Quantifying forest residual biomass in Pinus halepensis Miller stands using Airborne Laser Scanning data. *GIScience and Remote Sensing* 56(8), 1210-1232. https://doi.org/10.1080/15481603.2019.1641653.

Domingo, D., Ole-Orka, H., Næsset, E., Kachamba, D., and Gobakken, T., 2019b. Effects of UAV image resolution, camera type, and image overlap on accuracy of biomass predictions in a tropical woodland. *Remote Sensing* 11(8), 948. https://doi.org/10.3390/rs11080948.

Domingo, D., de la Riva, J., Lamelas, M.T., García-Martín, A., Ibarra, P., Echeverría, M., and Hoffrén, R., 2020. Fuel type classification using airborne laser scanning and Sentinel 2 data in Mediterranean forest affected by wildfires. *Remote Sensing* 12(21), 1-22. https://doi.org/10.3390/rs12213660.

Donager, J., Sankey, T.Ts., Sánchez-Meador, A.J., Sankey, J.B., and Springer, A., 2021a. Integrating airborne and mobile lidar data with UAV photogrammetry for rapid assessment of changing forest snow depth and cover. *Science of Remote Sensing* 4, 100029. https://doi.org/10.1016/j.srs.2021.100029.

Donager, J., Sánchez-Meador, A.J., and Blackburn, R.C., 2021b. Adjudicating perspectives on forest structure: How do airborne, terrestrial, and mobile LiDAR-derived estimates compare? *Remote Sensing* 13(12), 2297. https://doi.org/10.3390/rs13122297.

Dorado-Roda, I., Pascual, A., Godinho, S., Silva, C.A., Botequim, B., Rodríguez-Gonzálvez, P., González-Ferreiro, E., and Guerra-Hernández, J., 2021. Assessing the accuracy of GEDI data for canopy height and aboveground biomass estimates in Mediterranean forests. *Remote Sensing* 13(12), 2279. https://doi.org/10.3390/rs13122279.

Dougherty, E.R., Peltz, J.B., Sand, F.M., and Lent, A., 1992. Morphological image segmentation by local granulometric size distributions. *Journal of Electronic Imaging* 1(1). https://doi.org/10.1117/12.55174.

Drake, J.B., Dubayah, R., Knox, R.G., Clark, D.B., and Blair, J.B., 2002. Sensitivity of large-footprint LiDAR to canopy structure and biomass in a neotropical rainforest. *Remote Sensing of Environment* 81(2-3), 378-392. https://doi.org/10.1016/S0034-4257(02)00013-5.

Dubayah, R., Blair, J.B., Goetz, S., Fatoyinbo, L., Hansen, M., Healey, S., Hofton, M., Hurtt, G., Kellner, J., Luthcke, S., Armston, J., Tang, H., Duncanson, L., Hancock, S., Jantz, P., Marselis, S., Patterson, P.L., Qi W., and Silva, C., 2020. The Global Ecosystem Dynamics Investigation: High-resolution laser ranging of the Earth's forests and topography. *Science of Remote Sensing* 1, 100002. https://doi.org/10.1016/j.srs.2020.100002.

Duncanson, L., Dubayah, R., Cook, B.D., Rosette, J., and Parker, G., 2015. The importance of spatial detail: Assessing the utility of individual crown information and scaling approaches for LiDAR-based biomass density estimation. *Remote Sensing of Environment* 168, 102-112. https://doi.org/10.1016/j.rse.2015.06.021.

Duncanson, L., Neuenschwander, A., Hancock, S., Thomas, N., Fatoyinbo, T., Simard, M., Silva, C.A., Armston, J., Luthcke, S.B., Hofton, M., Kellner, J.R., and Dubayah, R., 2020. Biomass estimation from simulated GEDI, ICESat-2 and NISAR across environmental gradients in Sonoma County, California. *Remote Sensing of Environment* 242, 111779. https://doi.org/10.1016/j.rse.2020.111779.

Duncanson, L., Kellner, J.R., Armston, J., Dubayah, R., Minor, D.M., Hancock, S., Healey, S.P., Patterson, P.L., Saarela, S., Marselis, S., Silva, C.E., Bruening J., Goetz, S.J., Tang, H., Hofton, M., Blair, J.B., Luthcke, S., Fatoyinbo, L., *et al*., 2022. Aboveground biomass density models for NASA's Global Ecosystem Dynamics Investigation (GEDI) lidar mission. *Remote Sensing of Environment* 270, 112845. https://doi.org/10.1016/j.rse.2021.112845.

Dunn, O.J., 1964. Multiple comparisons using rank sums. *Technometrics* 6(3), 241-252. https://doi.org/10.1080/00401706.1964.10490181.

Dupuy, J.L., Fargeon, H., Martin-StPaul, N., Pimont, F., Ruffault, J., Guijarro, M., Hernando, C., Madrigal, J., and Fernandes, P., 2020. Climate change impact on future wildfire danger and activity in southern Europe: a review. *Annals of Forest Science* 77, 35. https://doi.org/10.1007/s13595-020-00933-5.

Dwiputra, A., Coops, N.C., and Schwartz, N.B., 2023. GEDI waveform metrics in vegetation mapping –a case of study from a heterogeneous tropical forest landscape. *Environmental Research Letters* 18(1), 015007. https://doi.org/10.1088/1748-9326/acad8d.

E

Eames, T., Russell-Smith, J., Yates, C., Edwards, A., Vernooij, R., Ribeiro, N., Steinbruch, F., and van der Werf, G.R., 2021. Instantaneous pre-fire biomass and fuel load measurements from multi-spectral UAS mapping in southern African savannas. *Fire* 4(1), 2. https://doi.org/10.3390/fire4010002.

Ecke, S., Dempewolf, J., Frey, J., Schwaller, A., Endres, E., Klemmt, H.J., Tiede, D., and Seifert, T., 2022. UAV-based forest health monitoring: A systematic review. *Remote Sensing* 14(13), 3205. https://doi.org/10.3390/rs14133205.

Eker, R., Alkan, E., and Aydin, A., 2021. A comparative analysis of UAV-RTK and UAV-PPK methods in mapping different surface types. *European Journal of Forest Engineering* 7(1), 12-25. https://doi.org/10.33904/ejfe.938067.

Eusuf, M.S.R.S., Barton, J., Gorte, B., and Zlatanova, S., 2020. Volume estimation of fuel load for hazard reduction burning: first results to a voxel approach. In *Proceedings of the XXIV ISPRS Congress*. The International Archives of the Photogrammetry, Remote Sensing and Spatial Information Sciences, XLIII-B3-2020. Nice, France.

Evans, J.S. and Hudak, A.T., 2007. A multiscale curvature algorithm for classifying discrete return LiDAR in forested environments. *IEEE Transactions on Geoscience and Remote Sensing* 45(4), 1029-1038. https://doi.org/10.1109/TGRS.2006.890412.

𝔉

Faber, A. and Förstner, W., 1999. Scale characteristics of local autocovariances for texture segmentation. *International Archives of Photogrammetry and Remote Sensing* 32(7), 4-3.

FAO and Plan Bleu, 2018. State of Mediterranean forests 2018. Food and Agriculture Organization of the United Nations, Rome, Italy, and Plan Bleu, Marseille, France. ISBN: 978-92-5-131047-2.

FAO and UNEP, 2020. The State of the World's Forests 2020: Forests, biodiversity and people. Rome, Italy. https://doi.org/10.4060/ca8642en.

Farwell, L.S., Gudex-Cross, D., Anise, I.E., Bosch, M.J., Olah, A.M., Radeloff, V.C., Razenkova, E., Rogova, N., Silveira, E.M.O., Smith, M.M., and Pidgeon, A.M., 2021. Satellite image texture captures vegetation heterogeneity and explains patterns of bird richness. *Remote Sensing of Environment* 253, 112175. https://doi.org/10.1016/j.rse.2020.112175.

Fayad, I., Baghdadi, N., Bailly, J.S., Barbier, N., Goud, V., El Hajj, M., Fabre, F., and Bourgine, B., 2014. Canopy height estimation in French Guiana with LiDAR ICESat/GLAS data using Principal Components Analysis and Random Forest regressions. *Remote Sensing* 6, 11883-11914. https://doi.org/10.3390/rs61211883.

Fayad, I., Baghdadi, N., Alcarde Alvares, C., Stape, J.L., Bailly, J.S., Scolforo, H.F., Cegatta, I.R., Zribi, M., and Le Maire, G., 2021. Terrain slope effect on forest height and wood volume estimation from GEDI data. *Remote Sensing* 13(11), 2136. https://doi.org/10.3390/rs13112136.

Fekry, R., Yao, W., Cao, L., and Shen, X., 2022. Ground-based/UAV-LiDAR data fusion for quantitative structure modeling and tree parameters retrieval in subtropical planted forest. *Forest Ecosystems* 9, 100065. https://doi.org/10.1016/j.fecs.2022.100065.

Fernández-Sarría, A., Martínez, I., Velázquez-Martí, B., Sajdak, M., Estornell, J., and Recio, J.A., 2013. Different methodologies for calculating crown volumes of Platanus hispanica trees using terrestrial laser scanner and a comparison with classical dendrometric measurements. *Computers and Electronics in Agriculture* 90, 176-185. http://doi.org/10.1016/j.compag.2012.09.017.

Feng, T., Duncanson, L., Montesano, P., Hancock, S., Minor, D., Guenther, E., and Neuenschwander, A., 2023. A systematic evaluation of multi-resolution ICESat-2 ATL08 terrain and canopy heights in boreal forests. *Remote Sensing of Environment* 291, 113570. https://doi.org/10.1016/j.rse.2023.113570.

Filin, S. and Pfeifer, N., 2006. Segmentation of airborne laser scanning data using a slope adaptive neighborhood. *ISPRS Journal of Photogrammetry and Remote Sensing* 60, 71-80. https://doi.org/10.1016/j.isprsjprs.2005.10.005.

Fogarty, L.G., Pearce, H.G., Catchpole, W.R., and Alexander, M.E., 1998. Adoption vs. Adaptation: Lessons from applying the Canadian Forest Fire Danger Rating system in New Zealand. In *Proceedings of the 3rd International Conference on Forest Fire Research and 14th Conference on Fire and Forest Meteorology*, 1011-1028. Luso, Coimbra, Portugal.

Fol, C.R., Kükenbrink, D., Rehush, N., Murtiyoso, A., and Griess, V.C., 2023. Evaluating state-of-the-art 3D scanning methods for stem-level biodiversity inventories in forests. *International Journal of Applied Earth Observation and Geoinformation* 122, 103396. https://doi.org/10.1016/j.jag.2023.103396.

Foody, G.M., Boyd, D.S., and Cutler, M.E.J., 2003. Predictive relations of tropical forest biomass from Landsat TM data and their transferability between regions. *Remote Sensing of Environment* 85(4), 463-474. https://doi.org/10.1016/S0034-4257(03)00039-7.

Forbes, B., Reilly, S., Clark, M., Ferrell, R., Kelly, A., Krause, P., Matley, C., O'Neil, M., Villasenor, M., Disney, M.I., Wilkes, P., and Bentley, L.P., 2022. Comparing remote sensing and field-based approaches to estimate ladder fuels and predict wildfire burn severity. *Frontiers in Forest and Global Change* 5. https://doi.org/10.3389/ffgc.2022.818713.

Francini, S., D'Amico, G., Vangi, E., Borghi, C., and Chirici, G., 2022. Integrating GEDI and Landsat: Spaceborne LiDAR and four decades of optical imagery for the analysis of forest disturbances and biomass change in Italy. *Sensors* 22, 2015. https://doi.org/10.3390/s22052015.

Franco-Aliaga, T., 2010. Geografía de España (física, humana y económica). Editorial Proyectos Corydon. ISBN: 978-84-614-5358-0. Madrid, Spain.

Frandsen, W.H., 1971. Fire spread through porous fuels from the conservation of energy. *Combustion and Flame* 16(1), 9-16. https://doi.org/10.1016/S0010-2180(71)80005-6.

Fréjaville, T. and Curt, T., 2017. Seasonal changes in the human alteration of fire regimes beyond the climate forcing. *Environmental Research Letters* 12, 035006. https://doi.org/10.1088/1748-9326/aa5d23.

G

Gajardo, J., García, M., and Riaño, D., 2014. Applications of Airborne Laser Scanning in Forest Fuel Assessment and Fire Prevention. In Maltamo, M., Næsset, E., Vauhkonen, J. (eds), *Forestry Applications of Airborne Laser Scanning. Managing Forest Ecosystems* 27. Springer, Dordrecht, The Netherlands. https://doi.org/10.1007/978-94-017-8663-8_22.

Gallagher, M.R., Maxwell, A.E., Guillén, L.A., Everland, A., Loudermilk, E.L., and Skowronski, N.S., 2021. Estimation of plot-level burn severity using Terrestrial Laser Scanning. *Remote Sensing* 13(20), 4168. https://doi.org/10.3390/rs13204168.

Gao, B.C., 1996. NDWI – a Normalized Difference Water Index for remote sensing of vegetation liquid water from space. *Remote Sensing of Environment* 58(3), 257-266. https://doi.org/10.1016/S0034-4257(96)00067-3.

Gao, S., Zhu, J., and Fu, H., 2023. A rapid and easy way for national forest heights retrieval in China using ICESat-2/ATL08 in 2019. *Forests* 14(6), 1270. https://doi.org/10.3390/f14061270.

García, M., Popescu, S., Riaño, D., Zhao, K., Neuenschwander, A., Agca, M., and Chuvieco, E., 2012. Characterization of canopy fuels using ICESat/GLAS data. *Remote Sensing of Environment* 123, 81-89. https://doi.org/10.1016/j.rse.2012.03.018.

García-Cimarras, A., Manzanera, J.A., and Valbuena, R., 2021. Analysis of Mediterranean vegetation fuel type changes using multitemporal LiDAR. *Forests* 12(3), 335. https://doi.org/10.3390/f12030335.

García-Gutiérrez, J., González-Ferreiro, E., Riquelme-Santos, J.C., Miranda, D., Diéguez-Aranda, U., and Navarro-Cerrillo, R.M., 2013. Evolutionary feature selection to estimate forest stand variables using LiDAR. *International Journal of Applied Earth Observation and Geoinformation* 26, 119-131. http://doi.org/10.1016/j.jag.2013.06.005.

Gastellu-Etchegorry, J.P., Yin, T., Lauret, N., Cajgfinger, T., Gregoire, T., Grau, E., Feret, J.B., Lopes, M., Guilleux, J., Dedieu, G., Malenovský, Z., Cook, B.D., Morton, D., Rubio, J., Durrieu, S., Cazanave, G., Martin, E., and Ristorcelli, T., 2015. Discrete Anisotropic Radiative Transfer (DART5) for modeling airborne and satellite spectroradiometer and LiDAR acquisitions of natural and urban landscapes. *Remote Sensing* 7(2), 1667-1701. https://doi.org/10.3390/rs70201667

Gelabert, P.J., Montealegre, A.L., Lamelas, M.T., and Domingo, D., 2020. Forest structural diversity characterization in Mediterranean landscapes affected by fires using Airborne Laser Scanning data. *GIScience and Remote Sensing* 57(4), 497-509. https://doi.org/10.1080/15481603.2020.1738060.

Giannetti, F., Puletti, N., Quatrini, V., Travaglini, D., Bottalico, F., Corona, P., and Chirici, G., 2018. Integrating terrestrial and airborne laser scanning for the assessment of single-tree attributes in Mediterranean forest stands. *European Journal of Remote Sensing* 51(1), 795-807. https://doi.org/10.1080/22797254.2018.1482733.

Gitelson, A.A., Kaufman, Y.J., and Merzlyak, M.N., 1996. Use of a green channel in remote sensing of global vegetation from EOS-MODIS. *Remote Sensing of Environment* 58, 289-298. https://doi.org/10.1016/S0034-4257(96)00072-7.

Gitelson, A.A., Gritz, Y., and Merzlyak, M.N., 2003. Relationships between leaf chlorophyll content and spectral reflectance and algorithms for non-destructive chlorophyll assessment in higher plant leaves. *Journal of Plant Physiology* 160, 271-282. https://doi.org/10.1078/0176-1617-00887.

Glenn, N.F., Neuenschwander, A., Vierling, L.A., Spaete, L., Li, A., Shinneman, D.J., Pilliod, D.S., Arkle, R.S., and McIlroy, S.K., 2016. Landsat 8 and ICESat-2: Performance and potential synergies for quantifying dryland ecosystem vegetation cover and biomass. *Remote Sensing of Environment* 185, 233-242. https://doi.org/10.1016/j.rse.2016.02.039.

Gollob, C., Ritter, T., and Nothdurft, A., 2020. Forest inventory with long range and high-speed Personal Laser Scanning (PLS) and Simultaneous Localization and Mapping (SLAM) technology. *Remote Sensing* 12(9), 1509. https://doi.org/10.3390/rs12091509.

González de Vega, S., de las Heras, J., and Moya, D., 2016. Resilience of Mediterranean terrestrial ecosystems and fire severity in semiarid areas: Responses of Aleppo pine forests in the short, mid, and long term. *Science of the Total Environment* 573, 1171-1177, https://doi.org/10.1016/j.scitotenv.2016.03.115.

González-Ferreiro, E., Diéguez-Aranda, U., Crecente-Campo, F., Barreiro-Fernández, L., Miranda, D., and Castedo-Dorado, F., 2014. Modelling canopy fuel variables for Pinus radiata D. Don in NW Spain with low-density LiDAR data. *International Journal of Wildland Fire* 23(3), 350-362. https://doi.org/10.1071/WF13054.

Graham, A.N.V., Coops, N.C., Tompalski, P., Plowright, A., and Wilcox, M., 2020. Effect of ground surface interpolation methods on the accuracy of forest attribute modelling using unmanned aerial systems-based digital aerial photogrammetry. *International Journal of Remote Sensing* 41(9), 3287-3306. https://doi.org/10.1080/01431161.2019.1694722.

Guerra-Hernández, J. and Pascual, A., 2021. Using GEDI LiDAR data and airborne laser scanning to assess height growth dynamics in fast-growing species: A showcase in Spain. *Forest Ecosystems* 8, 14. https://doi.org/10.1186/s40663-021-00291-2.

Guerra-Hernández, J., González-Ferreiro, E., Monleón, V.J., Faias, S.P., Tomé, M., and Díaz-Varela, R.A., 2017. Use of multi-temporal UAV-derived imagery for estimating individual tree growth in Pinus pinea stands. *Forests* 8, 300. https://doi.org/10.3390/f8080300.

Guerra-Hernández, J., Cosenza, D.N., Rodriguez, L.C.E., Silva, M., Tomé, M., Díaz-Varela, R.A., and González-Ferreiro, E., 2018. Comparison of ALS- and UAV(SfM)-derived high-density point clouds for individual tree detection in Eucalyptus plantations. *International Journal of Remote Sensing* 39(15-16), 5211-5235. https://doi.org/10.1080/01431161.2018.1486519.

Guerra-Hernández, J., Botequim, B., Bujan, S., Jurado-Varela, A., Molina-Valero, J.A., Martínez-Calvo, A., and Pérez-Cruzado, C., 2022. Interpreting the uncertainty of model-based and design-based estimation in downscaling estimates from NFI data: a case-study in Extremadura (Spain). GIScience and *Remote Sensing* 59(1), 686-704. https://doi.org/10.1080/15481603.2022.2051383.

Guo, Q., Li, W., Yu, H., and Alvarez, O., 2010. Effects of topographic variability and lidar sampling density on several DEM interpolation methods. *Photogrammetric Engineering and Remote Sensing* 76(6), 701-702. https://doi.org/10.14358/PERS.76.6.701.

H

Haas, A., Matheron, G., and Serra, J., 1967. Morphologie Mathématique et granulométries en place. *Les Annales des Mines* 12, 768-782.

Haralick, R.M., Shanmugam, K., and Dinstein, I., 1973. Textural features for image classification. *IEEE Transactions on Systems, Man, and Cybernetics* 6, 610-621.

Hauglin, M., Gobakken, T., Astrup, R., Ene, L., and Næsset, E., 2014. Estimating single-tree crown biomass of Norway spruce by Airborne Laser Scanning: A comparison of methods with and without the use of Terrestrial Laser Scanning to obtain the ground reference data. *Forests* 5(3), 384-403. https://doi.org/10.3390/f5030384.

Hermosilla, T., Coops, N.C., Ruiz, L.A., and Moskal, L.M., 2014. Deriving pseudo-vertical waveforms from small-footprint full-waveform LiDAR data. *Remote Sensing Letters* 5(4), 332-341. https://doi.org/10.1080/2150704X.2014.903350.

Hershey, J.L., McDill, M.E., Miller, D.A., Holderman, B., and Michael, J.H., 2022. A voxel-based individual tree stem detection method using airborne LiDAR in mature northeastern U.S. forests. *Remote Sensing* 14, 806. https://doi.org/10.3390/rs14030806.

Hilker, T., van Leeuwen, M., Coops, N.C., Wulder, M.A., Newnham, G.J., Jupp, D.L.B., and Culvenor, D.S., 2010. Comparing canopy metrics derived from terrestrial and airborne laser scanning in a Douglas-fir dominated forest stand. *Trees* 24, 819-832. https://doi.org/10.1007/s00468-010-0452-7.

Hillman, S., Wallace, L., Lucieer, A., Reinke, K., Turner, D., and Jones, S., 2021. A comparison of terrestrial and UAS sensors for measuring fuel hazard in a dry sclerophyll forest. *International Journal of Applied Earth Observation and Geoinformation* 95, 102261. https://doi.org/10.1016/j.jag.2020.102261.

Höfle, B., Hollaus, M., Lehner, H., Pfeifer, N., and Wagner, W., 2008. Area-based parametrization of forest structure using full-waveform airborne laser scanning data. In *Proceedings of SilviLaser 2008, 8th International Conference on LiDAR Applications in Forest Assessment and Inventory*. Edinburgh, UK.

Hofton, M. and Blair, J.B., 2019. Algorithm Theoretical Basis Document (ATBD) for GEDI Transmit and Receive Waveform Processing for L1 and L2 Products, Version 1.0. NASA Goddard Space Flight Center, Greenbelt, MD, USA.

Holcomb, A., Mathis, S.V., Coomes, D.A., and Keshav, S., 2023. Computational tools for assessing forest recovery with GEDI shots and forest change maps. *Science of Remote Sensing* 8, 100106. https://doi.org/10.1016/j.srs.2023.100106.

Hollaus, M., Mücke, W., Roncat, A., Pfeifer, N., and Briese, C., 2014. Full-waveform airborne laser scanning systems and their possibilities in forest applications. In Maltamo, M., Næsset, E., Vauhkonen, J. (eds), *Forestry Applications of Airborne Laser Scanning: Managing Forest Ecosystems* 27. Springer, Dordrecht, The Netherlands. https://doi.org/10.1007/978-94-017-8663-8_3.

Hudak, A.T., Bright, B.C., Pokswinski, S.M., Loudermilk, E.L., O'Brien, J.J., Hornsby, B.S., Klauberg, C., and Silva, C.A., 2016. Mapping forest structure and composition from low-density LiDAR for informed forest, fuel, and fire management at Eglin Air Force Base, Florida, USA. *Canadian Journal of Remote Sensing* 42(5), 441-427. https://doi.org/10.1080/07038992.2016.1217482.

Huete, A.R., 1988. A Soil-Adjusted Vegetation Index (SAVI). *Remote Sensing of Environment* 25, 295-309. https://doi.org/10.1016/0034-4257(88)90106-X.

J

James, F.C. and Wamer, N.O., 1982. Relationships between temperate forest bird communities and vegetation structure. *Ecology* 63, 159-171. https://doi.org/10.2307/1937041.

Jarahizadeh, S. and Salehi, B., 2024. A comparative analysis of UAV photogrammetric software performance for forest 3D modeling: A case study using Agisoft Photoscan, PIX4DMapper, and DJI Terra. *Sensors* 24(1), 286. https://doi.org/10.3390/s24010286.

Jarron, L.R., Coops, N.C., MacKenzie, W.H., Tompalski, P., and Dykstra, P., 2020. Detection of sub-canopy forest structure using airborne LiDAR. *Remote Sensing of Environment* 244, 111770. https://doi.org/10.1016/j.rse.2020.111770.

Jiao, Y., Wang, D., Yao, X., Wang, S., Chi, T., and Meng, Y., 2023. Forest emissions reduction assessment using optical satellite imagery and space LiDAR fusion for carbon stock estimation. *Remote Sensing* 15(5), 1410. https://doi.org/10.3390/rs15051410.

Johnson, M.C. and Peterson, D.L., 2005. Forest fuel treatments in western North America: Merging silviculture and fire management. *The Bark Beetles, Fuels, and Fire Bibliography* 126.

Jones, M.W., Smith, A.J.P., Betts, R., Canadell, J.G., Prentice, I.C., and Le Quéré, C., 2020. Climate change increases the risk of wildfires. *ScienceBrief*, January 2020.

Julesz, 1962. Visual pattern discrimination. *IRE Transactions on Information Theory* 8(2), 84-92.

K

Kakoulaki, G., Martínez, A., and Florio, P., 2021. Non-commercial Light Detection and Ranging (LiDAR) data in Europe. EUR 30817 EN. Publications Office of the European Union, Luxembourg. ISBN: 978-92-76-41150-5. https://doi.org/10.2760/212427.

Kameyama, S. and Sugiura, K., 2021. Effects of differences in Structure from Motion software image processing of Unmanned Aerial Vehicle photography and estimation of crown area and tree height in forests. *Remote Sensing* 13(4), 626. https://doi.org/10.3390/rs13040626.

Kankare, V., Vauhkonen, J., Holopainen, M., Vastaranta, M., Hyyppä, J., Hyyppä, H., and Alho, P., 2015. Sparse density, leaf-off airborne laser scanning data in aboveground biomass component prediction. *Forests* 6(6), 1839-1857. https://doi.org/10.3390/f6061839.

Kantola, T., Vastaranta, M., Yu, X., Lyytikainen-Saarenmaa, P., Holopainen, M., Talvitie, M., Kaasalainen, S., Solberg, S., and Hyyppä, J., 2010. Classification of defoliated trees using tree-level airborne laser scanning data combined with aerial images. *Remote Sensing* 2, 2665-2679. https://doi.org/10.3390/rs2122665.

Kauth, R.J. and Thomas, G.S., 1976. The Tasseled Cap—A graphic description of the spectral-temporal development of agricultural crops as seen by Landsat. *Proceedings of the Symposium on Machine Processing of Remotely Sensed Data*, 29 June-1 July 1976, Purdue University, West Lafayette, IN, USA.

Kellner, J.R., Armston, J., and Duncanson, L., 2022. Algorithm Theoretical Basis Document for GEDI footprint aboveground biomass density. *Earth and Space Science* 10(4), e2022EA002516. https://doi.org/10.1029/2022EA002516.

Kelly, A., Reilly, S., Forbes, B., Krause, P., Cooper, Z., Bentley, L.P., Clark, M., and Blesius, L., 2021. Evaluating canopy fuels in northern California oak woodlands and mixed-conifer forests using 3D data from Unoccupied Aerial Systems and Airborne Laser Scanners. *AGU Fall Meeting 2021*, B35A-1424. New Orleans, LA, USA.

Khalsa, S.J.D., Borsa, A., Nandigam, V., Phan, M., Lin, K., Crosby, C., Fricker, H., Baru, C., and López, L., 2022. OpenAltimetry – rapid analysis and visualization of spaceborne altimeter data. *Earth Science Informatics* 15, 1471-1480. https://doi.org/10.1007/s12145-020-00520-2.

Klauberg, C., Hudak, A.T., Silva, C.A., Lewis, S.A., Robichaud, P.R., and Jain, T.B., 2019. Characterizing fire effects on conifers at tree level from airborne laser scanning and high-resolution, multispectral satellite data. *Ecological Modelling* 412, 108820. https://doi.org/10.1016/j.ecolmodel.2019.108820.

Koma, Z., Seijmonsbergen, A.C., and Kissling, D., 2020. Classifying wetland-related land cover types and habitats using fine-scale LiDAR metrics derived from country-wide Airborne Laser Scanning. *Remote Sensing in Ecology and Conservation* 7(1), 80-96. https://doi.org/10.1002/rse2.170.

Kourtz, P.H., 1977. An application of Landsat digital technology to forest fire fuel type mapping. In *ERIM Proceedings of the 11th International Symposium on Remote Sensing of Environment* 2.

Kraus, K. and Pfeifer, N., 1998. Determination of terrain models in wooded areas with airborne laser scanner data. *ISPRS Journal of Photogrammetry and Remote Sensing* 53, 193-203.

Kristensen, T., Næsset, E., Ohlson, M., Bolstad, P.V., and Kolka, R., 2015. Mapping above- and below-ground carbon pools in boreal forests: The case for airborne LiDAR. *PLoS ONE* 10, e0138450. https://doi.org/10.1371/journal.pone.0138450.

Kruskal, W.H. and Wallis, W.A., 1952. Use of ranks in one-criterion variance analysis. *Journal of the American Statistical Association* 47, 260.

Kumar, S., Sara, R., Singh, J., Agrawal, S., and Kushwaha, S.P.S., 2018. Spaceborne PolInSAR and ground-based TLS data modeling for characterization of forest structural and biophysical parameters. *Remote Sensing Applications: Society and Environment* 11, 241-253. https://doi.org/10.1016/j.rsase.2018.07.010.

Kupidura, P., 2019. The comparison of different methods of texture analysis for their efficacy for land use classification in satellite imagery. *Remote Sensing* 11, 1233. https://doi.org/10.3390/rs11101233.

L

Labenski, P., Ewald, M., Schmidtlein, S., Heinsch, F.A., and Fassnacht, F.E., 2023. Quantifying surface fuels for fire modelling in temperate forests using airborne lidar and Sentinel-2: potential and limitations. *Remote Sensing of Environment* 295, 113711. https://doi.org/10.1016/j.rse.2023.113711.

Lamping, J.E., Zald, H.S.J., Madurapperuma, B.D., and Graham, J., 2021. Comparison of low-cost commercial unpiloted Digital Aerial Photogrammetry to Airborne Laser Scanning across multiple forest types in California, USA. *Remote Sensing* 13(21), 4292. https://doi.org/10.3390/rs13214292.

Lang, N., Kalischek, N., Armston, J., Schindler, K., Dubayah, R., and Wegner, J.D., 2022. Global canopy height regression and uncertainty estimation from GEDI LIDAR waveforms with deep ensembles. *Remote Sensing of Environment* 268, 112760. https://doi.org/10.1016/j.rse.2021.112760.

Lasaponara, R., Lanorte, A., and Pignatti, S., 2006. Characterization and mapping of fuel types for the Mediterranean ecosystems of Pollino National Park in southern Italy by using hyperspectral MIVIS data. *Earth Interactions* 10, 13.

Lechner, A.M., Foody, G.M., and Boyd, D.S., 2020. Applications in remote sensing to forest ecology and management. *One Earth* 2, 405-412. https://doi.org/10.1016/j.oneear.2020.05.001.

Lecigne, B., Delagrange, S., and Messier, C., 2018. Exploring trees in three dimensions: VoxR, a novel voxel-based R package dedicated to analyzing the complex arrangement of tree crowns. *Annals of Botany* 121, 589-601. https://doi.org/10.1093/aob/mcx095.

Lefsky, M.A., Cohen, W.B., Acker, S.A., Spies, T.A., Parker, G.G., and Harding D., 1998. LiDAR remote sensing of forest canopy structure and related biophysical parameters at H.J. Andrews Experimental Forest, Oregon, USA. *IGARSS '98. Sensing and Managing the Environment*. IEEE International Geoscience and Remote Sensing. Symposium Proceedings. Seattle, WA, USA. https://doi.org/10.1109/IGARSS.1998.691367.

Lefsky, M.A., Harding, D., Cohen, W.B., Parker, G., and Shugart, H.H., 1999. Surface LiDAR remote sensing of basal area and biomass in deciduous forests of Eastern Maryland, USA. *Remote Sensing of Environment* 67(1), 83-98. https://doi.org/10.1016/S0034-4257(98)00071-6.

Lefsky, M.A., Cohen, W.B., Parker, G.G., and Harding D.J., 2002. LiDAR remote sensing for ecosystem studies. *BioScience* 52(1), 19-30.

Lefksy, M.A., Harding, D.J., Keller, M., Cohen, W.B., Carabajal, C.C., del Bom Espirito-Santo, F., Hunter, M.O., and de Oliveira Jr., R., 2005. Estimates of forest canopy height and aboveground biomass using ICESat. *Geophysical Research Letters* 32, 22. https://doi.org/10.1029/2005GL023971.

Leite, R.V., Silva, C.A., Broadbent, E.N., do Amaral, C.H., Liesenberg, V., de Almeida, D.R.A., Mohan, M., Godinho, S., Cardil, A., Hamamura, C., de Faria, B.L., Brancalion, P.H.S., Hirsch, A., Marcatti, G.E., Dalla Corte, A.P., Zambrano, A.M.A., da Costa, M.B.T., Matricardi, E.A.T., da Silva, A.L., *et al*., 2022. Large scale multilayer fuel load characterization in tropical savanna using GEDI spaceborne LiDAR data. *Remote Sensing of Environment* 268, 112764. https://doi.org/10.1016/j.rse.2021.112764.

Li, X., Li, L., Ni, W., Mu, X., Wu, X., Laurin, G.V., Vangi, E., Sterenczak, K., Chirici, G., Yu, S., and Huang, H., 2024. Validating GEDI tree canopy cover product across forest types using co-registered aerial LiDAR data. *ISPRS Journal of Photogrammetry and Remote Sensing* 207, 326-337. https://doi.org/10.1016/j.isprsjprs.2023.11.024.

Li, Y., Bu, R., Sun, M., Wu, W., Di, X., and Chen, B., 2018. PointCNN: Convolution on X-transformed points. In *Proceedings of the 32nd Conference on Neural Information Processing Systems (NeurIPS 2018)*. Montréal, Canada.

Liang, X., Wang, Y., Pyörälä, J., Lehtomäki, M., Yu, X., Kaartinen, H., Kukko, A., Honkavaara, E., Issaoui, A.E.I., Nevalainen, O., Vaaja, M., Virtanen, J.P., Katoh, M., and Deng, S., 2019. Forest in situ observations using unmanned aerial vehicle as an alternative of terrestrial measurements. *Forest Ecosystems* 6, 20. https://doi.org/10.1186/s40663-019-0173-3.

Liao, J., Zhou, J., and Yang, W., 2021. Comparing LiDAR and SfM digital surface models for three land cover types. *Open Geosciences* 13(1), 497-504. https://doi.org/10.1515/geo-2020-0257.

Lin, S., Zhang, H., Liu, S., Gao, G., Li, L., and Huang, H., 2023. Characterizing post-fire forest structure recovery in the Great Xing'an Mountain using GEDI and time series Landsat data. *Remote Sensing* 15, 3107. https://doi.org/10.3390/rs15123107.

Lin, X. and Zhang, J., 2014. Segmentation-based filtering of airborne LiDAR point clouds by progressive densification of terrain segments. *Remote Sensing* 6, 1294-1326. https://doi.org/10.3390/rs6021294.

Lindgren, N., Christensen, P., Nilsson, B., Åkerholm, M., Allard, A., Reese, H., and Olsson H., 2015. Using optical satellite data and airborne LiDAR data for nationwide sampling survey. *Remote Sensing* 7(4), 4253-4267. https://doi.org/10.3390/rs70404253.

Listopad, C.M.C.S., Masters, R.E., Drake, J., Weishampel, J., and Branquinho, C., 2015. Structural diversity indices based on airborne LiDAR as ecological indicators for managing highly dynamic landscapes. *Ecological Indicators* 57, 268-279. http://doi.org/10.1016/j.ecolind.2015.04.017.

Liu, M. and Popescu, S., 2022. Estimation of biomass burning emissions by integrating ICESat-2, Landsat 8, and Sentinel-1 data. *Remote Sensing of Environment* 280, 113172. https://doi.org/10.1016/j.rse.2022.113172.

Liu, A., Cheng, X., and Chen, Z., 2021a. Performance evaluation of GEDI and ICESat-2 laser altimeter data for terrain and canopy height retrievals. *Remote Sensing of Environment* 264, 112571. https://doi.org/10.1016/j.rse.2021.112571.

Liu, H., Xiao, P., Zhang, X., Zhou, X., Li, J., and Guo, R., 2021c. Object-based island green cover mapping by integrating UAV multispectral image and LiDAR data. *Journal of Applied Remote Sensing* 15(3), 034512. https://doi.org/10.1117/1.JRS.15.034512.

Liu, H.Q. and Huete, A.R., 1995. A feedback based modification of the NDVI to minimize canopy background and atmospheric noise. *IEEE Transactions on Geoscience and Remote Sensing* 33, 457-465. https://doi.org/10.1109/TGRS.1995.8746027.

Liu, J., Shen, X., Cao, L., Wang, G., and Cao, F., 2018. Estimating forest structural attributes using UAV-LiDAR data in Ginkgo plantations. *ISPRS Journal of Photogrammetry and Remote Sensing* 146, 465-482. https://doi.org/10.1016/j.isprsjprs.2018.11.001.

Liu, K., Wang, A., Zhang, S., Zhu, Z., Bi, Y., Wang, Y., and Du, X., 2021b. Tree species diversity mapping using UAS-based digital aerial photogrammetry point clouds and multispectral imageries in a subtropical forest invaded by moso bamboo (Phyllostachys edulis). *International Journal of Applied Earth Observation and Geoinformation* 104, 102587. https://doi.org/10.1016/j.jag.2021.102587.

Liu, X., Su, Y., Hu, T., Yang, Q., Liu, B., Deng, Y., Tang, H., Tang, Z., Fang, J., and Guo, Q., 2022. Neural network guided interpolation for mapping canopy height of China's forests by integrating GEDI and ICESat-2 data. *Remote Sensing of Environment* 269, 112844. https://doi.org/10.1016/j.rse.2021.112844.

Longares, L.A., 2004. Variedad biogeográfica del territorio aragonés. In Peña J.L., Longares, L.A., and Sánchez, M. (eds), *Geografía Física de Aragón. Aspectos Generales y Temáticos*. Universidad de Zaragoza e Institución Fernando el Católico. ISBN: 84-96214-29-X. Zaragoza, Spain.

Lopes Bento, N., Araújo E Silva Ferraz, G., Alexandre Pena Barata, R., Santos Santana, L., Diennevan Souza Barbosa, B., Conti, L., *et al.*, 2022. Overlap influence in images obtained by an unmanned aerial vehicle on a digital terrain model of altimetric precision. *European Journal of Remote Sensing* 55(1), 263-276. https://doi.org/10.1080/22797254.2022.2054028.

Loudermilk, E.L., Pokswinski, S., Hawley, C.M., Maxwell, A., Gallagher, M.R., Skowronski, N.S., Hudak, A.T., Hoffman, C., and Hiers, J.K., 2023. Terrestrial laser scan metrics predict surface vegetation biomass and consumption in a frequently burned southeastern U.S. ecosystem. *Fire* 6(4), 151. https://doi.org/10.3390/fire6040151.

Luo, Y., Qi, S., Liao, K., Zhang, S., Hu, B., and Tian, Y., 2023. Mapping the forest height by fusion of ICESat-2 and multi-source remote sensing imagery and topographic information: A case of study in Jiangxi province, China. *Forests* 14(3), 454. https://doi.org/10.3390/f14030454.

Luthcke, S.B., Thomas, T.C., Pennington, T.A., Rebold, T.W., Nicholas, J.B., Rowlands, D.D., Gardner, A.S., and Bae, S., 2021. ICESat-2 pointing calibration and geolocation performance. *Earth and Space Science* 8(3), e2020EA001494. https://doi.org/10.1029/2020EA001494.

M

MacArthur, R.H. and MacArthur, J.W., 1961. On bird species diversity. *Ecology* 42, 594-598. https://doi.org/10.2307/1932254.

Maclean, G.A. and Krabill, W.B., 1986. Gross-merchantable timber volume estimation using an Airborne LiDAR System. *Canadian Journal of Remote Sensing* 12(1), 7-18. https://doi.org/10.1080/07038992.1986.10855092.

Magnussen, S. and Wulder, M.A., 2012. Post-fire canopy height recovery in Canada's boreal forests using Airborne Laser Scanner (ALS). *Remote Sensing* 4, 1600-1616. https://doi.org/10.3390/rs4061600.

Malambo, L. and Popescu, S., 2021. Assessing the agreement of ICESat-2 terrain and canopy height with airborne LiDAR over US ecozones. *Remote Sensing of Environment* 266, 112711. https://doi.org/10.1016/j.rse.2021.112711.

Malambo, L. and Popescu, S., 2024. Mapping vegetation canopy height across the contiguous United States using ICESat-2 and ancillary datasets. *Remote Sensing of Environment* 309, 114226. https://doi.org/10.1016/j.rse.2024.114226.

Malambo, L., Popescu, S.C., Murray, S.C., Putman, E., Pugh, N.A., Horne, D.W., Richardson, G., Sheridan, R., Rooney, W.L., Avant, R., Vidrine, M., McCutchen, B., Baltensperger, D., and Bishop, M., 2018. Multitemporal field-based plant height estimation using 3D point clouds generated from small unmanned aerial systems high-resolution imagery. *International Journal of Applied Earth Observation and Geoinformation* 64, 31-42. https://doi.org/10.1016/j.jag.2017.08.014.

Mandl, L., Stritih, A., Siedl, R., Ginzler, C., and Senf, C., 2023. Spaceborne LiDAR for characterizing forest structure across scales in the European Alps. *Remote Sensing in Ecology and Conservation* 9(5), 599-614. https://doi.org/10.1002/rse2.330.

Mansouri, J., Jafari, M., and Dehkordi, A.T., 2024. Continuous mapping of forest canopy height using ICESat-2 data and a weighted kernel integration of multi-temporal multi-source remote sensing data aided by Google Earth Engine. *Environmental Science and Pollution Research* 31, 49757-49779. https://doi.org/10.1007/s11356-024-34415-2.

Marcozzi, A.A., Johnson, J.V., Parsons, R.A., Flanary, S.J., Seielstad, C., and Downs J.Z., 2023. Application of LiDAR derived fuel cells to wildfire modeling at laboratory scale. *Fire* 6(10), 394. https://doi.org/10.3390/fire6100394.

Marino, E., Ranz, P., Tomé, J.L., Noriega, M.Á., Esteban, J., and Madrigal, J., 2016. Generation of high-resolution fuel model maps from discrete airborne laser scanner and Landsat-8 OLI: a low-cost and highly updated methodology for large areas. *Remote Sensing of Environment* 187, 267-280. https://doi.org/10.1016/j.rse.2016.10.020.

Marselis, S.M., Kreil, P., Chase, J.M., and Dubayah, R., 2022. The use of GEDI canopy structure for explaining variation in tree species richness in natural forests. *Environmental Research Letters* 17, 045003. https://doi.org/10.1088/1748-9326/ac583f.

Martijn, L., Meijerink, S., and Ezeiza, J., 2019. Detect illegal buildings based on LiDAR point cloud data. https://event.cwi.nl/lsde/2019/results/group02.pdf. (Accessed on Sep 27, 2024).

Matikainen, L., Karila, K., Hyppä, J., Litkey, P., Puttonen, E., and Ahokas, E., 2017. Object-based analysis of multispectral Airborne Laser Scanner data for land cover classification and map updating. *ISPRS Journal of Photogrammetry and Remote Sensing* 128, 298-313. https://doi.org/10.1016/j.isprsjprs.2017.04.005.

Maturana, D. and Scherer, S., 2015. VoxNet: A 3D convolutional neural network for real-time object recognition. In *Proceedings of IEEE/RSJ International Conference on Intelligent Robots and Systems (IROS)*. Hamburg, Germany.

McArthur, A.G., 1967. Fire behavior in Eucalypt forest. Forestry and Timber Bureau, Australia.

McFeeters, S.K., 1996. The use of the Normalized Difference Water Index (NDWI) in the delineation of open water features. *International Journal of Remote Sensing* 17(7), 1425-1432. https://doi.org/10.1080/01431169608948714.

McGaughey, R.J., 2021. FUSION/LDV: Software for LIDAR data analysis and visualization v.4.21. USDA Forest Service, Washington DC, USA.

Means, J.E., Acker, S.A., Harding, D.J., Blair, J.B., Lefsky, M.A., Cohen, W.B., Harmon, M.E., and McKee W.A., 1999. Use of large-footprint scanning airborne lidar to estimate forest stand characteristics in the Western Cascades of Oregon. *Remote Sensing of Environment* 67(3), 298-308. https://doi.org/10.1016/S0034-4257(98)00091-1.

Mediterranean Experts on Climate and environmental Change (MedECC), 2020. Climate and environmental change in the Mediterranean Basin: Current situation and risks for the future. First Mediterranean Assessment Report. ISBN: 978-2-9577416-0-1. https://doi.org/10.5281/zenodo.7224821.

Mengiste, E., Prieto, S.A., and García de Soto, B., 2022. Comparison of TLS and photogrammetric 3D data acquisition techniques: Considerations for developing countries. *Proceedings of the 39th ISARC*, 491-494. Bogotá, Colombia. https://doi.org/10.22260/ISARC2022/0067.

Merrill, D.F. and Alexander, M.E., 1987. Glossary of forest fire management terms, 4th Edition. National Research Council of Canada, Canadian Committee on Forest Fire Management. Ottawa, Canada.

Mihajlovski, B., Fernandes, P.M., Pereira, J.M.C., and Guerra-Hernández, J., 2023. Comparing forest understory fuel classification in Portugal using discrete airborne laser scanning data and satellite multi-source remote sensing data. *Fire* 6(9), 327. https://doi.org/10.3390/fire6090327.

Miller, W.A. and Johnston, D.C., 1985. Comparison of fuel maps produced using MSS and AVHRR data. Pecora 10, Remote Sensing in Forest and Range Resource Management. U.S. Geological Survey. Fort Collins, CO, USA.

Miller, Z.M., Hupy, J., Chandrasekaran, A., Shao, G., and Fei, S., 2021. Application of postprocessing kinematic methods with UAS remote sensing in forest ecosystems. *Journal of Forestry* 119(5), 454-466. https://doi.org/10.1093/jofore/fvab021.

Mitri, G.H., Nader, M., and Salloum, L., 2011. Fuel type mapping in the Mediterranean region of North Lebanon using object-based image analysis of ASTER imagery. In San-Miguel-Ayanz, J., Gitas, I., Camia, A., and Oliveira, S. (eds), *Advances in Remote Sensing and GIS Applications in Forest Fire Management. From Local to Global Assessments. Proceedings of the 8th International EARSeL FF-SIG Workshop*. Stresa, Italy.

Molina-Valero, J.A., Martínez-Calvo, A., Ginzo Villamayor, M.J., Novo Pérez, M.A., Álvarez-González, J.G., Montes, F., and Pérez-Cruzado, C., 2022. Operationalizing the use of TLS in forest inventories: The R package FORTLS. *Environmental Modelling & Software* 150, 105337. https://doi.org/10.1016/j.envsoft.2022.105337.

Montealegre, A.L., Lamelas, M.T., Tanase, M.A., and de la Riva, J., 2014. Forest fire severity assessment using ALS data in a Mediterranean environment. *Remote Sensing* 6, 4240-4265. https://doi.org/10.3390/rs6054240.

Montealegre, A.L., Lamelas, M.T., and de la Riva, J., 2015. Interpolation routines assessment in ALS-derived Digital Elevation Models for forestry applications. *Remote Sensing* 7, 8631-8654. https://doi.org/10.3390/rs70708631.

Montealegre, A.L., Lamelas, M.T., de la Riva, J., García-Martín, A., and Escribano, F., 2016. Use of low point density ALS data to estimate stand-level structural variables in Mediterranean Aleppo pine forest. *Forestry* cpw008. https://doi.org/10.1093/forestry/cpw008.

Montealegre, A.L., Lamelas, M.T., García-Martín, A., de la Riva, J., and Escribano, F., 2017. Using low-density discrete Airborne Laser Scanning data to assess the potential carbon dioxide emission in case of a fire event in a Mediterranean pine forest. *GIScience and Remote Sensing* 54(5), 721-740. https://doi.org/10.1080/15481603.2017.1320863.

Moriguchi, K., 2023. Estimation of fractal dimension of trees using LiDAR point data with sequential data decimation. *Remote Sensing of Environment* 295, 113722. https://doi.org/10.1016/j.rse.2023.113722.

Mouselimis, L., 2024. IceSat2R: ICESat-2 altimeter data using R. R package version 1.0.6. https://CRAN.R-project.org/package=IceSat2R. (Accessed on Sep 27, 2024).

Muhojoki, J., Hakala, T., Kukko, A., Kaartinen, H., and Hyyppä, J., 2024. Comparing positioning accuracy of Mobile Laser Scanning systems under a forest canopy. *Science of Remote Sensing* 9, 100121. https://doi.org/10.1016/j.srs.2024.100121.

Mulatu, K.A., Decuyper, M., Brede, B., Kooistra, L., Reiche, J., Mora, B., and Herold, M., 2019. Linking terrestrial LiDAR scanner and conventional forest structure measurements with multi-modal satellite data. *Forests* 10(3), 291. https://doi.org/10.3390/f10030291.

Myroniuk, V., Zibtsev, S., Bogomolov, V., Goldammer, J.G., Soshenskyi, O., Levchenko, V., and Matsala, M., 2023. Combining Landsat time series and GEDI data for improved characterization of fuel types and canopy metrics in wildfire simulation. *Journal of Environmental Management* 345, 118736. https://doi.org/10.1016/j.jenvman.2023.118736.

𝔑

Næsset, E., 1997. Estimating timber volume of forest stands using airborne laser scanner data. *Remote Sensing of Environment* 61(2), 246-253. https://doi.org/10.1016/S0034-4257(97)00041-2.

Næsset, E., Gobakken, T., Bollandsås, O.M., Gregoire, T.G., Nelson, R., and Ståhl, G., 2013. Comparison of precision of biomass estimates in regional field sample surveys and airborne LiDAR-assisted surveys in Hedmark County, Norway. *Remote Sensing of Environment* 130, 108-120. https://doi.org/10.1016/j.rse.2012.11.010.

Nandy, S., Srinet, R., and Padalia, H., 2021. Mapping forest height and aboveground biomass by integrating ICESat-2, Sentinel-1, and Sentinel-2 data using Random Forest algorithm in northwest Himalayan foothills of India. *Geophysical Research Letters* 48(14), e2021GL093799. https://doi.org/10.1029/2021GL093799.

Narine, L.L., Popescu, S., Neuenschwander, A., Zhou, T., Srinivasan, S., and Harbeck, K., 2019. Estimating aboveground biomass and forest canopy cover with simulated ICESat-2 data. *Remote Sensing of Environment* 224, 1-11. https://doi.org/10.1016/j.rse.2019.01.037.

Narine, L., Malambo, L., and Popescu, S., 2022. Characterizing canopy cover with ICESat-2: A case study of southern forests in Texas and Alabama, USA. *Remote Sensing of Environment* 281, 113242. https://doi.org/10.1016/j.rse.2022.113242.

Nelson, R., Krabill, W., and Maclean, G., 1984. Determining forest canopy characteristics using airborne laser data. *Remote Sensing of Environment* 15(3), 201-212. https://doi.org/10.1016/0034-4257(84)90031-2.

Nelson, R., Krabill, W., and Tonelli, J., 1987. Estimating forest biomass and volume using airborne laser data. *Remote Sensing of Environment* 24(2), 247-267. https://doi.org/10.1016/0034-4257(88)90028-4.

Nelson, R., Oderwald, R., and Gregoire, T.G., 1997. Separating the ground and airborne laser sampling phases to estimate tropical forest basal area, volume, and biomass. *Remote Sensing of Environment* 60(3), 311-326. https://doi.org/10.1016/S0034-4257(96)00213-1.

Neuenschwander, A. and Pitts, K., 2019. The ATL08 land and vegetation product for the ICESat-2 mission. *Remote Sensing of Environment* 221, 247-259. https://doi.org/10.1016/j.rse.2018.11.005.

Neuenschwander, A., Guenther, E., White, J.C., Duncanson, L., and Montesano, P., 2020. Validation of ICESat-2 terrain and canopy heights in boreal forests. *Remote Sensing of Environment* 251, 112110. https://doi.org/10.1016/j.rse.2020.112110.

Neumann, T.A., Brenner, A., Hancock, D., Robbins, J., Saba, J., Harbeck, K., Gibbons, A., Lee, J., Luthcke, S.B., Rebold, T., *et al*., 2021. ATLAS/ICESat-2 L2A Global Geolocated Photon Data (ATL03, Version 5). [Data Set]. Boulder, Colorado USA. NASA National Snow and Ice Data Center Distributed Active Archive Center. https://doi.org/10.5067/ATLAS/ATL03.005. (Accessed on Sep 27, 2024).

Nilsson, M., 1996. Estimation of tree heights and stand volume using an Airborne LiDAR System. *Remote Sensing of Environment* 56(1), 1-7. https://doi.org/10.1016/0034-4257(95)00224-3.

Ollero, A., Martínez de Dios, J.R., and Merino, L., 2006. Unmanned aerial vehicles as tools for forest-fire fighting. *Forest Ecology and Management* 234, Supplement S263. https://doi.org/10.1016/j.foreco.2006.08.292.

Olsson, H., Egberth, M., Engberg, J., Fransson, J., Pahlén, T. G., Hagner, O., Holmgren, J., Joyce, S., Magnusson, M., Nilsson, B., Nilsson, M., Olofsson K., Reese, H., and Wallerman, J., 2005. Current and emerging operational uses of remote sensing in Swedish forestry. In *Proceedings of the 5th Annual Forest Inventory and Analysis Symposium*. New Orleans, LA, USA.

Ottmar, R.D., Sandberg, D.V., Riccardi, C.L., and Prichard, S.J., 2007. An overview of the Fuel Characteristic Classification System - Quantifying, classifying, and creating fuelbeds for resource planning. *Canadian Journal of Forest Research* 37(12), 2383-2393. https://doi.org/10.1139/X07-077.

Özyeşil, O., Voroninski, V., Basri, R., and Singer, A., 2017. A survey of structure from motion. *Acta Numerica* 26, 305-364. https://doi.org/10.1017/S096249291700006X.

P

Panagiotidis, D., Abdollahnejad, A., and Slavík, M., 2022. 3D point cloud fusion from UAV and TLS to assess temperate managed forest structures. *International Journal of Applied Earth Observation and Geoinformation* 112, 102917. https://doi.org/10.1016/j.jag.2022.102917.

Papatheodorou, I., Kitikidou, K., Stampoulidis, A., and Milios, E., 2023. Analyzing the impact of reforestation on forest fires and the economic outcome in an area in northern Greece. Should we reforest areas with conifers? Yes or no? *Ecological Questions* 34(2), 1-17. https://doi.org/10.12775/EQ.2023.052.

Paris, C., Kelbe, D., van Aardt, J., and Bruzzone, L., 2017. A novel automatic method for the fusion of ALS and TLS LiDAR data for robust assessment of tree crown structure. *IEEE Transactions on Geoscience and Remote Sensing* 55(7), 3679-3693. https://doi.org/10.1109/TGRS.2017.2675963.

Pascual, A., Godinho, S., and Guerra-Hernández, J., 2023. Integrated LiDAR-supported valuation of biomass and litter in forest ecosystems. A showcase in Spain. *Science of the Total Environment* 897, 165364. https://doi.org/10.1016/j.scitotenv.2023.165364.

Pastor, F., Valiente, J.A., and Khodayar, S., 2020. A warming Mediterranean: 38 years of increasing sea surface temperature. *Remote Sensing* 12, 2687. https://doi.org/10.3390/rs12172687.

Patterson, P.L., Healy, S.P., Ståhl, G., Saarela, S., Holm, S., Andersen, H.E., Dubayah, R., Duncanson, L., Hancock, S., Armston, J., Kellner, J.R., Cohen, W.B., and Yang, Z., 2019. Statistical properties of hybrid estimators proposed by GEDI – NASA's Global Ecosystem Dynamics Investigation. *Environmental Research Letters* 14, 065007. https://doi.org/10.1088/1748-9326/ab18df.

Pausas, J.G. and Fernández-Muñoz, S., 2012. Fire regime changes in the Western Mediterranean Basin: from fuel-limited to drought-driven fire regime. *Climatic Change* 110, 215-226. https://doi.org/10.1007/s10584-011-0060-6.

Pausas, J.G. and Keeley, J.E., 2021. Wildfires and global change. *Frontiers in Ecology and the Environment* 19(7), 387-395. https://doi.org/10.1002/fee.2359.

Peña, J.L. and Lozano, M.V., 2004. Las unidades del relieve aragonés. In Peña J.L., Longares, L.A., and Sánchez, M. (eds), *Geografía Física de Aragón. Aspectos Generales y Temáticos*. Universidad de Zaragoza e Institución Fernando el Católico. ISBN: 84-96214-29-X. Zaragoza, Spain.

Peñuelas, J. and Sardans, J., 2021. Global change and forest disturbances in the Mediterranean Basin: Breakthroughs, knowledge gaps, and recommendations. *Forests* 12, 603. https://doi.org/10.3390/f12050603.

Peterson, B.E., 2005. Canopy fuels inventory and mapping using large-footprint LiDAR. PhD Thesis. University of Maryland. College Park, MD, USA.

Peterson, B.E., Nelson, K., and Wylie, B., 2013. Towards integration of GLAS into a national fuel mapping program. *Photogrammetric Engineering & Remote Sensing* 79(2), 175-183.

Pierce, K.B., Ohmann, J.L., Wimberly, M.C., Gregory, M.J., and Fried, J.S., 2009. Mapping wildland fuels and forest structure for land management: a comparison of nearest neighbor imputation and other methods. *Canadian Journal of Forest Research* 39(10), 1901-1916. https://doi.org/10.1139/X09-102.

Pierzchała, M., Giguère, P., and Astrup, R., 2018. Mapping forests using an unmanned ground vehicle with 3D LiDAR and graph-SLAM. *Computers and Electronics in Agriculture* 145, 217-225. https://doi.org/10.1016/j.compag.2017.12.034.

Pingel, T.J., Clarke, K.C., and McBride, W.A., 2013. An improved simple morphological filter for the terrain classification of airborne LiDAR data. *ISPRS Journal of Photogrammetry and Remote Sensing* 77, 21-30. https://doi.org/10.1016/j.isprsjprs.2012.12.002.

Potapov, P., Li, X., Hernández-Serna, A., Tyukavina, A., Hansen, M.C., Kommareddy, A., Pickens, A., Turubanova, S., Tang, H., Silva, C.E., Armston, J., Dubayah, R., Blair, J.B., and Hofton, M., 2021. Mapping global forest canopy height through integration of GEDI and Landsat data. *Remote Sensing of Environment* 253, 112165. https://doi.org/10.1016/j.rse.2020.112165.

Prendes, C., Canga, E., Ordóñez, C., Majada, J., Acuña, M., and Cabo, C., 2022. Automatic assessment of individual stem shape parameters in forest stands from TLS point clouds: Application in Pinus pinaster. *Forests* 13(3), 431. https://doi.org/10.3390/f13030431.

Prometheus, 1999. Management techniques for optimization of suppression and minimization of wildfires effects. System Validation. European Commission, DG XII, ENVIR & CLIMATE. European Commission, Luxembourg. Contract Number ENV4-CT98-0716.

Puletti, N., Grotti, M., Masini, A., Bracci, A., and Ferrara, C., 2021. Enhancing wall-to-wall forest structure mapping through detailed co-registration of Airborne and Terrestrial Laser Scanning data in Mediterranean forests. *Ecological Informatics* 67, 101497. https://doi.org/10.1016/j.ecoinf.2021.101497.

Puliti, S., Ole-Orka, H., Gobakken, T., and Næsset, E., 2015. Inventory of small forest areas using an unmanned aerial system. *Remote Sensing* 7, 9632-9654. https://doi.org/10.3390/rs70809632.

Pyne, S.J., 2009. The human geography of fire: a research agenda. *Progress in Human Geography* 33(4), 443-446. https://doi.org/10.1177/0309132508101598.

Pyörälä, J., Liang, X., Vastaranta, M., Saarinen, N., Kankare, V., Wang, Y., Holopainen, M., and Hyyppä, J., 2018. Quantitative assessment of Scots pine (Pinus sylvestris L.) whorl structure in a forest environment using Terrestrial Laser Scanning. *IEEE Journal of Selected Topics in Applied Earth Observations and Remote Sensing* 11(10), 3598-3607. https://doi.org/10.1109/JSTARS.2018.2819598.

Q

Qi, C.R., Su, H., Mo, K., and Guibas L.J., 2017a. PointNet: Deep Learning on point sets for 3D classification and segmentation. In *Proceedings of the IEEE Conference on Computer Vision and Pattern Recognition*, Honolulu, HI, USA.

Qi, C.R., Yi, L., Su, H., and Guibas, L.J., 2017b. PointNet++: Deep hierarchical feature learning on point sets in a metric space. In *Proceedings of the 31st Conference on Neural Information Processing Systems (NIPS 2017)*, Long Beach, CA, USA.

Qi, W., Saarela, S., Armston, J., Ståhl, G., and Dubayah, R., 2019. Forest biomass estimation over three distinct forest types using TanDEM-X InSAR data and simulated GEDI lidar data. *Remote Sensing of Environment* 232, 111283. https://doi.org/10.1016/j.rse.2019.111283.

Qi, Y., Coops, N.C., Daniels, L.D., and Butson, C.R., 2022. Assessing the effects of burn severity on post-fire tree structures using the fused drone and mobile laser scanning point clouds. *Frontiers in Environmental Sciences* 10. https://doi.org/10.3389/fenvs.2022.949442.

Quirós, E., Polo, M.A., and Fragoso-Campón, L., 2021. GEDI elevation accuracy assessment: A case study of southwest Spain. *IEEE Journal of Selected Topics in Applied Earth Observations and Remote Sensing* 14, 5285-5299. https://doi.org/10.1109/JSTARS.2021.3080711.

R

R Core Team, 2022. R: A language and environment for statistical computing. R Foundation for Statistical Computing. Vienna, Austria.

Rabii, H.A., 1979. An investigation of the utility of Landsat 2 MSS data to the fire-danger rating area, and forest fuel analysis within Crater Lake National Park, Oregon. Oregon State University, USA.

Ranson, K.J., Sun, G., Kovacs, K., and Kharuk, V.I., 2004. Use of ICESat GLAS data for forest disturbance studies in central Siberia. *IGARSS 2004. Proceedings of the IEEE International Geoscience and Remote Sensing Symposium*. Anchorage, AK, USA. https://doi.org/10.1109/IGARSS.2004.1370722.

Reilly, S., Clark, M.L., Bentley, L.P., Matley, C., Piazza, E., and Menor, I.O., 2021. The potential of multispectral imagery and 3D point clouds from Unoccupied Aerial Systems (UAS) for monitoring forest structure and the impacts of wildfire in Mediterranean-climate forests. *Remote Sensing* 13(19), 3810. https://doi.org/10.3390/rs13193810.

Remondino, F., Spera, M.G., Nocerino, E., Menna, F., and Nex, F., 2014. State-of-the-art in high density image matching. *The Photogrammetric Record* 29(146), 144-166. https://doi.org/10.1111/phor.12063.

Revilla, S., Lamelas, M.T., Domingo, D., de la Riva, J., Montorio, R., Montealegre, A.L., and García-Martín, A., 2021. Assessing the potential of the DART model to discrete return LiDAR simulation. Application to fuel type mapping. *Remote Sensing* 13(3), 1-21. https://doi.org/10.3390/rs13030342.

Riaño, D., Chuvieco, E., Salas, J., Palacios-Orueta, A., and Bastarrika, A., 2002. Generation of fuel type maps from Landsat TM images and ancillary data in Mediterranean ecosystems. *Canadian Journal of Forest Research* 32(8), 1301-1315. https://doi.org/10.1139/x02-052.

Rishmawi, K., Huang, C., and Zhan, X., 2021. Monitoring key forest structure attributes across the conterminous United States by integrating GEDI LiDAR measurements and VIIRS data. *Remote Sensing* 13(3), 442. https://doi.org/10.3390/rs13030442.

Ritter, T., Schwarz, M., Tockner, A., Leisch, F., and Nothdurft, A., 2017. Automatic mapping of forest stands based on three-dimensional point clouds derived from Terrestrial Laser-Scanning. *Forests* 8(8), 265. https://doi.org/10.3390/f8080265.

Roberts, K.C., Lindsay, J.B., and Berg, A.A., 2019. An analysis of ground-point classifiers for terrestrial LiDAR. *Remote Sensing* 11, 1915. https://doi.org/10.3390/rs11161915.

Rocha, K.D., Silva, C.A., Cosenza, D.N., Mohan, M., Klauberg, C., Schlickmann, M.B., Xia, J., Leite, R.V., de Almeida, D.R.A., Aktins, J.W., Cardil, A., Rowell, E., Parsons, R., Sánchez-López, N., Prichard, S.J., and Hudak, A.T., 2023. Crown-level structure and fuel load characterization from airborne and terrestrial laser scanning in a longleaf pine (Pinus palustris Mill.) forest ecosystem. *Remote Sensing* 15(4), 1002. https://doi.org/10.3390/rs15041002.

Rodrigues, M., de la Riva, J., Domingo, D., Lamelas, M.T., Ibarra, P., Hoffrén, R., and García-Martín, A., 2024. An empirical assessment of the potential of post-fire recovery of tree-forest communities in Mediterranean environments. *Forest Ecology and Management* 552, 121587. https://doi.org/10.1016/j.foreco.2023.121587.

Rodríguez-Puerta, F., Alonso, R., Pérez-Rodríguez, F., Águeda, B., Martín-García, S., Martínez-Rodrigo, R., and Lizarralde, I., 2020. Comparison of machine learning algorithms for wildland-urban interface fuelbreak planning integrating ALS and UAV-borne LiDAR data and multispectral images. *Drones* 4, 21. https://doi.org/10.3390/drones4020021.

Romero-Ramírez, F.J., Navarro-Cerrillo, R.M., Varo-Martínez, M.A., Quero, J.L., Doerr, S., and Hernández-Clemente, R., 2018. Determination of forest fuels characteristics in mortality-affected Pinus forests using integrated hyperspectral and ALS data. *International Journal of Applied Earth Observation and Geoinformation* 68, 157-167. https://doi.org/10.1016/j.jag.2018.01.003.

Rothermel, R.C. and Anderson, H.E., 1966. Fire spread characteristics determined in the laboratory. US Forest Service, Research paper INT-30. Intermountain Forest and Range Experiment Station, Ogden, UT.

Rothermel, R.C., 1972. A mathematical model for predicting fire spread in wildland fuels. USDA Forest Service, Research Paper INT-115, Intermountain Forest and Range Experiment Station, Ogden, UT.

Rouse, J.W., Haas, R.H., Schell, J.A., and Deering, D.W., 1974. Monitoring vegetation systems in the Great Plains with ERTS. Third ERTS-1 Symposium NASA, NASA SP- 351, Washington DC, 309-317.

Roussel, J.R. and Auty, D, 2022. Airborne LiDAR data manipulation and visualization for forestry applications. R Package Version 4.0.1.

Rowell, A. and Moore, P.F., 2000. Global review of forest fires. Forests for Life Programme Unit, WWF International. Gland, Switzerland.

Rowell, E., Loudermilk, E.L., Hawley, C., Pokswinski, S., Seilestad, C., Queen, L., O'Brien, J.J., Hudak, A.T., Goodrick, S., and Hiers J.K., 2020. Coupling terrestrial laser scanning with 3D fuel biomass sampling for advancing wildlands fuels characterization. *Forest Ecology and Management* 462, 117945. https://doi.org/10.1016/j.foreco.2020.117945.

Roy, D.P., Kashongwe, H.B., and Armston, J., 2021. The impact of geolocation uncertainty on GEDI tropical forest canopy height estimation and change monitoring. *Science of Remote Sensing* 4, 100024. https://doi.org/10.1016/j.srs.2021.100024.

Roy, P.S., Sharma, K.P., and Jain, A., 1996. Stratification of density in dry deciduous forest using satellite remote sensing digital data – an approach based on spectral indices. *Journal of Bioscience* 21(5), 723-734. https://doi.org/10.1007/BF02703148.

Ruffault, J. and Mouillot, F., 2015. How a new fire-suppression policy can abruptly reshape the fire-weather relationship. *Ecosphere* 6(10), 199. https://doi.org/10.1890/ES15-00182.1.

Ruffault, J., Curt, T., Moron, V., Trigo, R.M., Mouillot, F., Koutsias, N., Pimont, F., Martin-StPaul, N., Barbero, R., Dupuy, J.L., Russo, A., and Belhadj-Khedher, C., 2020. Increased likelihood of heat-induced large wildfires in the Mediterranean Basin. *Scientific Reports* 10, 13790, https://doi.org/10.1038/s41598-020-70069-z.

Ruiz, L.A., Recio, J.A., Crespo-Peremarch, P., and Sapena, M., 2016. An object-based approach for mapping forest structural types based on low-density LiDAR and multispectral imagery. *Geocarto International* 33(5), 443-457. https://doi.org/10.1080/10106049.2016.1265595.

Ruiz, L.A., Crespo-Peremarch, P., and Torralba, J., 2018. Aplicación del LiDAR full-waveform en la modelización de combustibilidad de la cubierta arbóreo y el sotobosque. 3er taller del Grupo de Incendios Forestales de la AET: LiDAR aplicado a los incendios forestales. Alcalá de Henares, Spain.

S

Saarela, S., Holm, S., Healey, S.P., Andersen, H.E., Petersson, H., Prentius, W., Patterson, P.L., Næsset, E., Gregoire, T.G., and Ståhl, G., 2018. Generalized hierarchical model-based estimation for aboveground biomass assessment using GEDI and Landsat data. *Remote Sensing* 10, 1832. https://doi.org/10.3390/rs10111832.

Saatchi, S.S., Harris, N.L., Brown, S., Lefsky, M.A., Mitchard, E.T.A., Salas, W., Zutta, B.R., Buermann, W., Lewis, S.L., Hagen, S., Petrova, S., White, L., Silman, M., and Morel, A., 2011. Benchmark map of forest carbon stocks in tropical regions across three continents. In *Proceedings of the National Academy of Sciences* 108, 24.

Salach, A., Bakuła, K., Pilarska, M., Ostrowski, W., Górski, K., and Kurczyński, Z., 2018. Accuracy assessment of point clouds from LiDAR and dense image matching acquired using the UAV platform for DTM creation. *ISPRS International Journal of Geo-Information* 7(9), 342. https://doi.org/10.3390/ijgi7090342.

San-Miguel-Ayanz, J., Durrant, T., Boca, R., Maianti, P., Libertà, G., Jacome Felix Oorn, D., Branco, A., De Rigo, D., Suárez-Moreno, M., Ferrari, D., Roglia, E., Scionti, N., Scionti, N., Broglia, M., Onida, M., Tristan, A., and Loffler, P., 2023. Forest fires in Europe, Middle East and North Africa 2022. Publications Office of the European Union, Luxembourg. https://doi.org/10.2760/348120.

Sandberg, D.V., Ottmar, R.D., and Cushon, G., 2001. Characterizing fuels in the 21st Century. *International Journal of Wildland Fire* 10, 381-387.

Santos Santana, L., Araújo E Silva Ferraz, G., Bedin Marin, D., Dienevam Souza Barbosa, B., Mendes Dos Santos, L., Ferreira Ponciano Ferraz, P., *et al*., 2021. Influence of flight altitude and control points in the georeferencing of images obtained by unmanned aerial vehicle. *European Journal of Remote Sensing* 54(1), 59-71. https://doi.org/10.1080/22797254.2020.1845104.

Schleich, A., Durrieu, S., Soma, M., and Vega, C., 2023. Improving GEDI footprint geolocation using a high-resolution digital elevation model. *IEEE Journal of Selected Topics in Applied Earth Observation and Remote Sensing* 16, 7718-7732. https://doi.org/10.1109/JSTARS.2023.3298991.

Schwartz, M., Ciais, P., Ottlé, C., de Truchis, A., Vega, C., Fayad, I., Brandt, M., Fensholt, R., Baghdadi, N., Morneau, F., Morin, D., Guyon, D., Dayau, S., and Wigneron, J.P., 2024. High-resolution canopy height map in the Landes forest (France) based on GEDI, Sentinel-1, and Sentinel-2 data with a deep learning approach. *International Journal of Applied Earth Observation and Geoinformation* 128, 103711. https://doi.org/10.1016/j.jag.2024.103711.

Scott, J.H. and Burgan, R.E., 2005. Standard Fire Behavior Fuel Models: A comprehensive set for use with Rothermel's surface fire spread model. USDA Forest Service, Rocky Mountain Research Station. General Technical Report RMRS-GTR-153.

Seielstad, C.A., 2003. Using LiDAR remote sensing to estimate forest fuels. PhD Thesis. University of Montana, USA.

Shannon, E.S., Finley, A.O., Hayes, D.J., Noralez, S.N., Weiskittel, A.R., Cook, B.D., and Babcock, C., 2023. Quantifying and correcting geolocation error in spaceborne LiDAR forest canopy observations using high spatial accuracy data: A Bayesian model approach. *Environmetrics* 35, e2840, https://doi.org/10.1002/env.2840.

Shen, X., Cao, L., Yang, B., Xu, Z., and Wang, G., 2019. Estimation of forest structural attributes using spectral indices and point clouds from UAS-based multispectral and RGB imageries. *Remote Sensing* 11(7), 800. https://doi.org/10.3390/rs11070800.

Shendryk, Y., Sofonia, J., Garrard, R., Rist, Y., Skocaj, D., and Thorburn, P., 2020. Fine-scale prediction of biomass and leaf nitrogen content in sugarcane using UAV LiDAR and multispectral imaging. *International Journal of Applied Earth Observation and Geoinformation* 92, 102177. https://doi.org/10.1016/j.jag.2020.102177.

Shendryk, Y., 2022. Fusing GEDI with Earth Observation data for large area aboveground biomass mapping. *International Journal of Applied Earth Observation and Geoinformation* 115, 103108. https://doi.org/10.1016/j.jag.2022.103108.

Sheridan, R.D., Popescu, S.C., Gatziolis, D., Morgan, C.L.S., and Ku, N.W., 2014. Modeling forest aboveground biomass and volume using airborne LiDAR metrics and forest inventory and analysis data in the Pacific northwest. *Remote Sensing* 7(1), 229-255. https://doi.org/10.3390/rs70100229.

Shin, P., Sankey, T., Moore, M.M., and Thode, A.E., 2018. Evaluating unmanned aerial vehicle images for estimating forest canopy fuels in a Ponderosa pine stand. *Remote Sensing* 10, 1266. https://doi.org/10.3390/rs10081266.

Sillmann, J., Kharin, V.V., Zwiers, F.W., Zhang, X., and Bronaugh, D., 2013. Climate extreme indices in the CMIP5 multimodel ensemble: Part 2. Future climate projections. *Journal of Geophysical Research: Atmospheres* 118, 2473-2493. https://doi.org/10.1002/jgrd.50188.

Silva, C.A. and Hamamura, C., 2023. ICESat2VegR: An R package for NASA's Ice, Cloud, and Elevation satellite (ICESat-2) data processing and visualization for land and vegetation applications. https://github.com/carlos-alberto-silva/ICESat2VegR. (Accessed on Sep 27, 2024).

Silva, C.A., Klauberg, C., Hudak, A.T., Vierling, L.A., Liesenberg, V., Carvalho, S.P.C., and Rodríguez, L.C.E., 2016. A principal components approach for predicting the stem volume in Eucalyptus plantations in Brazil using airborne LiDAR data. *Forestry* 89, 422-433. https://doi.org/10.1093/forestry/cpw016.

Silva, C.A., Hamamura, C., Valbuena, R., Hancock, S., Cardil, A., Broadbent, E.N., de Almeida, D.R.A., Silva Junior, C.H.L., and Klauberg, C., 2020. rGEDI: An R package for NASA's Global Ecosystem Dynamics Investigation (GEDI) data visualization and processing. https://github.com/carlos-alberto-silva/rGEDI. (Accessed on Sep 27, 2024).

Silva, C.A., Duncanson, L., Hancock, S., Neuenschwander, A., Thomas, N., Hofton, M., Fatoyinbo, L., Simard, M., Marshak, C.Z., Armston, J., Lutchke, S., and Dubayah, R., 2021. Fusing simulated GEDI, ICESat-2 and NISAR data for regional aboveground biomass mapping. *Remote Sensing of Environment* 253, 112234. https://doi.org/10.1016/j.rse.2020.112234.

Sithole, G. and Vosselman, G., 2001. Filtering of laser altimetry data using a slope adaptive filter. *International Archives of Photogrammetry, Remote Sensing and Spatial Information Sciences* 34, 3/W4, 203-210.

Sithole, G. and Vosselman, G., 2004. Experimental comparison of filter algorithms for bare-Earth extraction from airborne laser scanning point clouds. *ISPRS Journal of Photogrammetry and Remote Sensing* 59, 85-101. https://doi.org/10.1016/j.isprsjprs.2004.05.004.

Slavík, M., Kuželka, K., Modlinger, R., Tomášková, I., and Surový, P., 2020. UAV laser scans allow detection of morphological changes in tree canopy. *Remote Sensing* 12(22), 3829. https://doi.org/10.3390/rs12223829.

Snavely, N., Seitz, S.M., and Szeliski, R., 2008. Modeling the world from Internet photo collections. *International Journal of Computer Vision* 80, 189-210. https://doi.org/10.1007/s11263-007-0107-3.

Sothe, C., Gonsamo, A., Lourenço, R.B., Kurz, W.A., and Snider, J., 2022. Spatially continuous mapping of forest canopy height in Canada by combining GEDI and ICESat-2 with PALSAR and Sentinel. *Remote Sensing* 14(20), 5158. https://doi.org/10.3390/rs14205158.

Spadavecchia, C., Belcore, E., Grasso, N., and Piras, M., 2023. A fully automatic forest parameters extraction at single-tree level: A comparison of MLS and TLS applications. *The International Archives of Photogrammetry, Remote Sensing and Spatial Information Sciences* XLVIII-1/W1-2023, 457-463. https://doi.org/10.5194/isprs-archives-XLVIII-1-W1-2023-457-2023.

Spearman, C., 1904. The proof and measurement of association between two things. *The American Journal of Psychology* 15(1), 72-101.

Stephens, S.L., Moghaddas, J.J., Edminster, C., Fiedler, C.E., Haase, S., Harrington, M., Keeley, J.E., Knapp, E.E., McIver, J.D., Metlen, K., Skinner, C.N., and Youngblood, A., 2009. Fire treatment effects on vegetation structure, fuels, and potential fire severity in western U.S. forests. *Ecological Applications* 19(2), 305-320.

Stephens, S.L., McIver, J.D., Boerner, R.E.J., Fettig, C.J., Fontaine, J.B., Hartsough, B.R., Kennedy, P.L., and Schwilk, D.W., 2012. The effects of forest fuel-reduction treatments in the United States. *Bioscience* 62, 549-560. https://doi.org/10.1525/bio.2012.62.6.6.

Sturdivant, E.J., Lentz, E.E., Thieler, E.R., Farris, A.S., Weber, K.M., Remsen, D.P., Miner, S., and Henderson, R.E., 2017. UAS-SfM for coastal research: Geomorphic feature extraction and land cover classification from high-resolution evaluation and optical imagery. *Remote Sensing* 9(10), 1020. https://doi.org/10.3390/rs9101020.

Sujit, P.B., Kingston, D., and Beard, R., 2007. Cooperative forest fire monitoring using multiple UAVs. In *Proceedings of the IEEE Conference on Decision and Control*, New Orleans, LA, USA. https://doi.org/10.1109/CDC.2007.4434345.

Swayze, N.C., Tinkham, W.T., Creasy, M.B., Vogeler, J.C., Hoffman, C.M., and Hudak, A.T., 2022. Influence of UAS flight altitude and speed on aboveground biomass prediction. *Remote Sensing* 14(9), 1989, https://doi.org/10.3390/rs14091989.

𝕿

Taneja, R., Wallace, L., Hillman, S., Reinke, K., Hilton, J., Jones, S., and Hally, B., 2023. Up-scaling fuel hazard metrics derived from Terrestrial Laser Scanning using a machine learning model. *Remote Sensing* 15(5), 1273. https://doi.org/10.3390/rs15051273.

Tang, H., Dubayah, R., Swatantran, A., Hofton, M., Sheldon, S., Clark, D.B., and Blair, J.B., 2012. Retrieval of vertical LAI profiles over tropical rain forests using waveform LiDAR at La Selva, Costa Rica. *Remote Sensing of Environment* 124, 242-250. https://doi.org/10.1016/j.rse.2012.05.005.

Tang, H. and Armston, J., 2019. Algorithm Theoretical Basis Document (ATBD) for GEDI L2B Footprint Canopy Cover and Vertical Profile Metrics, Version 1.0. Goddard Space Flight Center, Greenbelt, MD, USA.

Tang, H., Stoker, J., Lutchke, S., Armston, J., Lee, K., Blair, J.B., and Hofton, M., 2023. Evaluating and mitigating the impact of systematic geolocation error on canopy height measurement performance of GEDI. *Remote Sensing of Environment* 291, 113571. https://doi.org/10.1016/j.rse.2023.113571.

Tao, S., Labrière, N., Calders, K., Fischer, F.J., Rau, E.P., Plaisance, L., and Chave, J., 2021. Mapping tropical forest trees across large areas with lightweight cost-effective terrestrial laser scanning. *Annals of Forest Science* 78, 103. https://doi.org/10.1007/s13595-021-01113-9.

Taylor, S.W., Pike, R., and Alexander, M.E., 1996. Field guide to the Canadian Forest Fire Behavior Prediction (FBP) System. Canadian Forest Service, Northern Forestry Centre. Edmonton, Alberta, Canada.

Tian, X. and Shan, J., 2021. Comprehensive evaluation of the ICESat-2 ATL08 terrain product. *IEEE Transactions on Geoscience and Remote Sensing* 59(10), 8195-8209. https://doi.org/10.1109/TGRS.2021.3051086.

Tienaho, N., Saarinen, N., Yrttimaa, T., Kankare, V., and Vastaranta, M., 2024. Quantifying fire-induced changes in ground vegetation using bitemporal terrestrial laser scanning. *Silva Fennica* 58(3), 23061. https://doi.org/10.14214/sf.23061.

Tommaselli, A.M.G., Moraes, M.V.A., Silva, L.S.L., Rubio, M.F., Carvalho, G.J., and Tommaselli, J.T.G., 2014. Monitoring marginal erosion in hydroelectric reservoirs with terrestrial mobile laser scanner. *International Archive of Photogrammetry, Remote Sensing and Spatial Information Sciences* XL-5, 589-596. https://doi.org/10.5194/isprsarchives-XL-5-589-2014.

Torralba, J., Crespo-Peremarch, P., and Ruiz, L.A., 2018. Assessing the use of discrete, full-waveform LiDAR and TLS to classify Mediterranean forest species composition. *Revista de Teledetección* 52, 27-40. https://doi.org/10.4995/raet.2018.11106.

Torralba, J., Carbonell-Rivera, J.P., Ruiz, L.A., and Crespo-Peremarch, P., 2022. Analyzing TLS scan distribution and point density for the estimation of forest stand structural parameters. *Forests* 13(12), 2115. https://doi.org/10.3390/f13122115.

Tsao, A., Nzewi, I., Jayeoba, A., Ayogu, U., and Lobell, D.B., 2023. Canopy height mapping for plantations in Nigeria using GEDI, Landsat, and Sentinel-2. *Remote Sensing* 15(21), 5162. https://doi.org/10.3390/rs15215162.

Turco, M., Bedía, J., Di Liberto, F., Fiorucci, P., von Hardenberg, J., Koutsias, N., Llasat, M.C., Xystrakis, F., and Provenzale, A., 2016. Decreasing fires in Mediterranean Europe. *PLoS ONE* 11(3), e0150663. https://doi.org/10.1371/journal.pone.0150663.

𝔙

Vandendaele, B., Martin-Ducup, O., Fournier, R.A., Pelletier, G., and Lejeune, P., 2022. Mobile laser scanning for estimating tree structural attributes in a temperature hardwood forest. *Remote Sensing* 14(18), 4522. https://doi.org/10.3390/rs14184522.

Vangi, E., D'Amico, G., Francini, S., and Chirici, G., 2023. GEDI4R: an R package for NASA's GEDI level 4A data downloading, processing and visualization. *Earth Science Informatics* 16, 1109-1117. https://doi.org/10.1007/s12145-022-00915-3.

Vastaranta, M., Saarinen, N., Kankare, V., Holopainen, M., Kaartinen, H., Hyyppä, J., and Hyyppä, H., 2014. Multisource single-tree inventory in the prediction of tree quality variables and logging recoveries. *Remote Sensing* 6(4), 3475-3491. https://doi.org/10.3390/rs6043475.

Vatandaşlar, C., Seki, M., and Zeybek, M., 2023. Assessing the potential of Mobile Laser Scanning for stand-level forest inventories in near-natural forests. *Forestry: An International Journal of Forest Research* 96(4), 448-464. https://doi.org/10.1093/forestry/cpad016.

Vincent, L., 1996. Opening trees and local granulometries. In *Proceedings of Mathematical Morphology and Its Applications to Signal Processing*. Georgia, USA.

Vogeler, J.C., Fekety, P.A., Elliott, L., Swayze, N.C., Filippelli, S.K., Barry, B., Holbrook, J.D., and Vierling, K.T., 2023. Evaluating GEDI data fusions for continuous characterizations of forest wildlife habitat. *Frontiers in Remote Sensing* 4. https://doi.org/10.3389/frsen.2023.1196554.

Vosselman, G., 2000. Slope based filtering of laser altimetry data. *International Archives of Photogrammetry and Remote Sensing* 33, B3/2, 935-942.

Vosselman, G. and Maas, H.G., 2010. Airborne and Terrestrial Laser Scanning. Whittles Publishing.

W

Wagers, S., Castilla, G., Filiatrault, M., and Sánchez-Azofeifa, G.A., 2021. Using TLS-measured tree attributes to estimate aboveground biomass in small black spruce trees. *Forests* 12(11), 1521. https://doi.org/10.3390/f12111521.

Wallace, L., Lucieer, A., Malenovský, Z., Turner, D., and Vopěnka, P., 2016. Assessment of forest structure using two UAV techniques: a comparison of Airborne Laser Scanning and Structure from Motion (SfM) point clouds. *Forests* 7(3), 62. https://doi.org/10.3390/f7030062.

Wallace, L., Bellman, C., Hally, B., Hernández, J., Jones, S., and Hillman, S., 2019. Assessing the ability of image based point clouds captured from a UAV to measure the terrain in the presence of canopy cover. *Forests* 10(3), 284. https://doi.org/10.3390/f10030284.

Wallace, L., Hillman, S., Hally, B., Taneja, R., White, A., and McGlade, J., 2022. Terrestrial laser scanning: An operational tool for fuel hazard mapping? *Remote Sensing* 5(4), 85. https://doi.org/10.3390/fire5040085.

Wang, C.K. and Tsen, Y.H., 2010. DEM generation from airborne LiDAR data by an adaptive dual-directional slope filter. In Wagner W., Székely, B. (eds), *ISPRS TC VII Symposium - 100 Years ISPRS*. Vienna, Austria.

Wang, C., Zhang, W., Ji, Y., Marino, A., Li, C., Wang, L., Zhao, H., and Wang, M., 2024. Estimation of aboveground biomass for different forest types using data from Sentinel-1, Sentinel-2, ALOS PALSAR-2, and GEDI. *Forests* 15(3), 401. https://doi.org/10.3390/f15030401.

Wang, Y., Fan, Z., and You, Y., 2020. Application research of earth volume calculation based on 3D laser point cloud data. *IOP Conference Series: Materials Science and Engineering* 780, 032050. https://doi.org/10.1088/1757-899X/780/3/032050.

Whelan, A.W., Cannon, J.B., Bigelow, S.W., Rutledge, B.T., and Sánchez-Meador, J., 2023. Improving generalized models of forest structure in complex forest types using area- and voxel-based approaches from lidar. *Remote Sensing of Environment* 284, 113362. https://doi.org/10.1016/j.rse.2022.113362.

White, J.C., Coops, N.C., Wulder, M.A., Vastaranta, M., Hilker, T., and Tompalski, P., 2016. Remote sensing technologies for enhancing forest inventories: a review. *Canadian Journal of Remote Sensing* 42(5), 619-641. https://doi.org/10.1080/07038992.2016.1207484.

Wieser, M., Mandlburger, G., Hollaus, M., Otepka, J., Glira, P., and Pfiefer, N., 2017. A case study of UAS borne laser scanning for measurement of tree stem diameter. *Remote Sensing* 9(11), 1154. https://doi.org/10.3390/rs9111154.

Wilkes, P., Lau, A., Disney, M., Calders, K., Burt, A., González de Tanago, J., Bartholomeus, H., Brede, B., and Herold, M., 2017. Data acquisition considerations for Terrestrial Laser Scanning of forest plots. *Remote Sensing of Environment* 196, 140-153. https://doi.org/10.1016/j.rse.2017.04.030.

Wilson, N., Bradstock, R., and Bedward, M., 2021. Detecting the effects of logging and wildfire on forest fuel structure using Terrestrial Laser Scanning (TLS). *Forest Ecology and Management* 488, 119037. https://doi.org/10.1016/j.foreco.2021.119037.

Wulder, M.A., Bater, C.W., Coops, N.C., Hilker, T., and White, J.C., 2008. The role of LiDAR in sustainable forest management. *The Forestry Chronicle* 84(6), 807-826. https://doi.org/10.5558/tfc84807-6.

𝔛

Xanthopoulos, G., Caballero, D., Galante, M., Alexandrian, D., Rigolot, E., and Marzano, R., 2006. Forest fuels management in Europe. In *Fuels Management-How to Measure Success: Conference Proceedings*. USDA Forest Service, Portland, OR, USA.

Xi, Y., Tian, Q., Zhang, W., Zhang, Z., Tong, X., Brandt, M., and Fensholt, R., 2022. Quantifying understory vegetation density using multi-temporal Sentinel-2 and GEDI LiDAR data. *GIScience and Remote Sensing* 59(1), 2068-2083. https://doi.org/10.1080/15481603.2022.2148338.

Xu, D., Wang, H., Xu, W., Luan, Z., and Xu, X., 2021. LiDAR applications to estimate forest biomass at individual tree scale: Opportunities, challenges, and future perspectives. *Forests* 12, 550. https://doi.org/10.3390/f12050550.

Xu, Z., Shen, X., Cao, L., Coops, N.C., Goodbody, T.R.H., Zhong, T., Zhao, W., Sun, Q., Ba, S., Zhang, Z., and Wu, X., 2020. Tree species classification using UAS-based digital aerial photogrammetry point clouds and multispectral imageries in subtropical natural forests. *International Journal of Applied Earth Observation and Geoinformation* 92, 102173. https://doi.org/10.1016/j.jag.2020.102173.

Y

Yoshii, T., Matsumura, N., and Lin, C., 2022. Integrating UAV-SfM and airborne LiDAR point cloud data to plantation forest feature extraction. *Remote Sensing* 14(7), 1713. https://doi.org/10.3390/rs14071713.

Z

Zellweger, F., Morsdorf, F., Purves, R.S., Braunisch, V., and Bollmann, K., 2014. Improved methods for measuring forest landscape structure: LiDAR complements field-based habitat assessment. *Biodiversity Conservation* 23, 289-307. https://doi.org/10.1007/s10531-013-0600-7.

Zhang, H., Aldana-Jague, E., Clapuyt, F., Wilken, F., Vanacker, V., and van Oost, K., 2019. Evaluating the potential of post-processing kinematic (PPK) georeferencing for UAV-based structure-from-motion (SfM) photogrammetry and surface change detection. *Earth Surface Dynamics* 7, 807-827. https://doi.org/10.5194/esurf-7-807-2019.

Zhang, K., Chen, S.C., Whitman, D., Shyu, M.L., Yan, J., and Zhang, C., 2003. A progressive morphological filter for removing nonground measurements from airborne LiDAR data. *IEEE Transactions on Geoscience and Remote Sensing* 41(4), 872-882.

Zhang, W., Qi, J., Wan, P., Wang, H., Xie, D., Wang, X., and Yan, G., 2016. An easy-to-use airborne LiDAR data filtering method based on cloth simulation. *Remote Sensing* 8, 501. https://doi.org/10.3390/rs8060501.

Zhou, T. and Popescu, S.C., 2019. waveformlidar: An R package for waveform LiDAR processing and analysis. *Remote Sensing* 11(21), 2552. https://doi.org/10.3390/rs11212552.

Zhou, J., Guo, R.Y., Sun, M., Di, T.T., Wang, S., Zhai, J., and Zhao, Z., 2017. The effects of GLCM parameters on LAI estimation using texture values from Quickbird satellite imagery. *Scientific Reports* 7, 7366. https://doi.org/10.1038/s41598-017-07951-w.

Zhou, R., Sun, H., Ma, K., Tang, J., Chen, S., Fu, L., and Liu, Q., 2023. Improving estimation of tree parameters by fusing ALS and TLS point cloud data based on canopy gap shape feature points. *Drones* 7(8), 524. https://doi.org/10.3390/drones7080524.

APPENDIX: PHD THESIS PAPERS METRICS

This section presents the publication references that constitute the PhD Thesis body, the Impact Factor of the journal, and the task performed by the authors in each study. The PhD candidate, Raúl Hoffrén, is the first author and responsible for each one of the published articles. This research works will not be part of any other PhD Thesis by paper compendium.

Hoffrén, R., Lamelas, M.T., de la Riva, J., Domingo, D., Montealegre, A.L., García-Martín, A., and Revilla, S., 2023. Assessing GEDI-NASA system for forest fuels classification using machine learning techniques. *International Journal of Applied Earth Observation and Geoinformation* 116, 103175.
In this work the PhD candidate, Raúl Hoffrén, is responsible for most of the work, including the acquisition and preprocessing of GEDI and Landsat data, the analysis of the structural metrics, the generation of the ground-truth, the performing of the classification models, and the writing of the original manuscript. Dr. María Teresa Lamelas and Dr. Juan de la Riva are responsible for the methodological development and, along with Dr. Darío Domingo, Dr. Antonio Luis Montealegre, Dr. Alberto García-Martín, and Mr. Sergio Revilla, the reviewing of the analyses performed and the manuscript writing.

I.F. 2023	I.F. 5 years	JCR category	Order number	Quartile
7.6	7.5	Remote Sensing	6 of 62	Q1

Hoffrén, R., Lamelas, M.T., and de la Riva, J., 2023. UAV-derived photogrammetric point clouds and multispectral indices for fuel estimation in Mediterranean forests. *Remote Sensing Applications: Society and Environment* 31, 100997.
In this work the PhD candidate, Raúl Hoffrén, is responsible for most of the work, having performed the field campaigns, the acquisition, processing and analysis of the data, the statistical analyses, and the writing of the original manuscript. Dr. María Teresa Lamelas and Dr. Juan de la Riva are responsible for the methodological development and the reviewing of the analyses performed and the manuscript writing, as well as co-responsible for the field campaigns.

I.F. 2023	I.F. 5 years	JCR category	Order number	Quartile
3.8	-	Remote Sensing	21 of 62	Q2

Hoffrén, R., Lamelas, M.T., and de la Riva, J., 2024. Evaluation of handheld mobile laser scanner systems for the definition of fuel types in structurally complex Mediterranean forest stands. *Fire* 7 (2), 59.

In this work the PhD candidate, Raúl Hoffrén, is responsible for most of the work, having performed the field campaigns, the acquisition, processing, and analysis of the data, and the writing of the original manuscript. Dr. María Teresa Lamelas and Dr. Juan de la Riva are responsible for the methodological development and the reviewing of the analyses performed and the manuscript writing, as well as co-responsible for the field campaigns.

I.F. 2023	I.F. 5 years	JCR category	Order number	Quartile
3.0	3.4	Forestry	11 of 69	Q1

Hoffrén, R., Lamelas, M.T., and de la Riva, J., 2024. Classification and mapping of fuels in Mediterranean forest landscapes using a UAV-LiDAR system and integration possibilities with handheld mobile laser scanner systems. *Remote Sensing* 16 (18), 3536.

In this work the PhD candidate, Raúl Hoffrén, is responsible for most of the work, having performed the field campaigns, the acquisition, processing, and analysis of the data, the statistical and spatial analyses, and the writing of the original manuscript. Dr. María Teresa Lamelas and Dr. Juan de la Riva are responsible for the methodological development and the reviewing of the analyses performed and the manuscript writing, as well as co-responsible for the field campaigns.

I.F. 2023	I.F. 5 years	JCR category	Order number	Quartile
4.2	4.9	Geosciences, Multidisciplinary	34 of 253	Q1
		Remote Sensing	16 of 62	Q2